GHENT UNIVERSITY

FACULTY OF SCIENCES

Atomic Layer Deposition of Metals and Metal Oxides - Towards the Synthesis of Bimetallic Materials

Ranjith K. Ramachandran

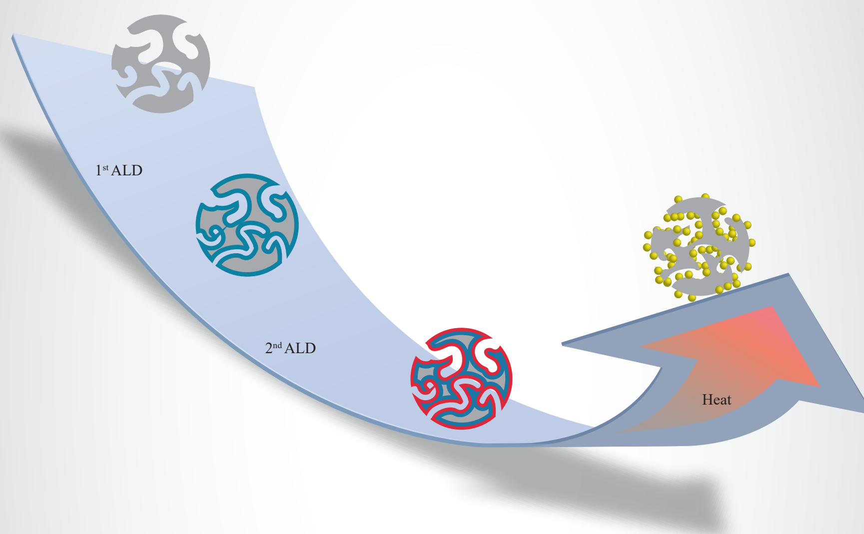

Thesis submitted for the degree of Doctor in Sciences: Chemistry

Academic year: 2016 - 2017

Promotors:
Prof. Dr. Christophe Detavernier
Dr. Hilde Poelman

Ghent University
Faculty of Sciences
Department of Solid State Sciences
Krijgslaan 281/S1, 9000 Ghent, Belgium

Atomic Layer Deposition of Metals and Metal Oxides - Towards the Synthesis of Bimetallic Materials

Ranjith K. Ramachandran

Promotors: Prof. Dr. Christophe Detavernier
Dr. Hilde Poelman

Members of the Jury:

Prof. Dr. Patrick Bultinck (UGent, chair)
Prof. Dr. Klaartje De Buysser (UGent)
Dr. Jolien Dendooven (UGent)
Prof. Dr. Anjana Devi (Ruhr-Universitat Bochum, Germany)
Prof. Dr. ir. W.M.M. Erwin Kessels
(Technische Universiteit Eindhoven, The Netherlands)
Prof. Dr. ir. Guy B. Marin (UGent)
Prof. Dr. ir. Johan A. Martens (K.U. Leuven)

Thesis submitted for the degree of
Doctor in Sciences: Chemistry
January 2017

Dedicated to my family...

Preface

This PhD thesis is focused on the development of new Atomic Layer Deposition (ALD) processes for metals and metal oxides, which are relevant for catalysis, and the synthesis of bimetallic materials. This research was started in September 2011, and results obtained up to September 2016 are included. Most of the experimental works were carried out at the Department of Solid State Sciences at Ghent University, in the CoCooN research group of professor Christophe Detavernier. The synchrotron based characterizations, X-ray Absorption Spectroscopy (XAS) and Gracing-Incidence Small-Angle X-ray Spectroscopy (GISAXS), were performed at the SAMBA beam line of the SOLEIL synchrotron (Saint-Aubin, France) and at the DUBBLE beamline of the ESRF synchrotron facility (Grenoble, France), respectively. The data were analyzed, thanks to the collaboration with the Laboratory for Chemical Technology (LCT) of Ghent University for the XAS part, and thanks to Dr. Jolien Dendooven for analyzing and interpreting the GISAXS data. The catalytic results presented in this thesis were only obtained thanks to the collaboration with LCT and the Centre for Surface Chemistry and Catalysis (COK) of the University of Leuven.

Most of the results obtained during this work have been published in peer-reviewed journals and the thesis is mainly written based on these publications. The main findings are summarized and discussed in the context of related literature, in the beginning of each chapter preceding the respective paper(s). I have put much effort in summarizing the work in a comprehensive and attractive way and I hope you will enjoy reading this thesis.

Ranjith K R
Ghent, January 2017

Acknowledgements

Undertaking this PhD has been a truly life-changing experience for me and it would not have been possible to do without the support and guidance that I received from many people. By this time, I have worked with a great number of people who contributed directly or indirectly to the research and making of the thesis. It is a pleasure to convey my gratitude to all of them in my humble acknowledgment.

First and foremost, I would like to express my gratitude to my promotor Professor Dr. Christophe Detavernier for valuable advice, helpful discussion, careful reviewing of manuscripts, and continuous encouragement. His guidance helped me in all the time of research and writing of this thesis. I deeply respect his endless curiosity and Intellectual humility for science. I am grateful to you for your wholehearted support, insightful guidance which will continue to inspire me in all the way through. Also, I greatly appreciate my promotor Dr. Hilde Poelman for her kind advice and the fruitful discussions. Her careful reviewing and valuable suggestions helped me a lot in improving manuscripts and this thesis. I still remember the day when you showed me the Eiffel tower for the first time. I was really excited, but you were even excited to make sure that I see it. Thank you for being so friendly.

Apart from my promoters, I would like to thank my colleagues in CoCooN group who helped significantly during the thesis. First of all, I want to express my sincere appreciation to Jolien for fruitful discussion and helpful advice. You constantly supported me throughout my research and I am sure that the manuscripts we wrote together wouldn't have been that perfect without your help. I am very impressed with your attitude for research, which always been an example to me. Davy and Geert, the most humble persons I ever met, you were always ready to dedicate your time whenever I needed help in any aspect of the research. Kilian, the coolest person in the lab, you taught me how to work with vacuum systems and thank you for helping me to deal with XPS results. Liesje, the person in our group whom I met first, thank you for the discussions that we had throughout and showing me how to work with the EP set up. Thank you Amit for helping me a lot not only in research but also personally. Thank you Shaoren for your advice and it was great pleasure hearing about interesting Chinese culture. Delphine, thank you for always taking an initiative to bring back an 'informal' group discussion in to English, when all others eventually slip in to Dutch. And, next time I'll definitely convince you that"Cricket" indeed is a game! Wouter, as we started our research

career together, we had a lot of opportunities to discuss different topics. Your extra-curricular activities are always an inspiration to me. I am really thankful to you for helping me to solve all the LaTeX related issues. Thank you Felix and Jan for helping me with the old and new IXRD softwares. Thank you Kevin for always making time to solve the LabvieW related issues. We always had a list of issues after each synchrotron campaign and you were always happy to solve them. Karl, you were always ready to transfer more samples to Leuven and thank you for sharing your valuable experiences in the research. Thomas, the 'IT specialist', thank you very much for helping me to get all the data back when my computer was crashed, it wouldn't have been that easy without your help. Thank you Michiel for helping me with FTIR measurements. Matthias and Eduardo, we had a lot of academic and cultural discussions. I will never forget the days we spent together for the synchrotron campaigns, we had a lot of fun together. I also would like to thank Jakob, Jeroen, Tareq, Veronique, Andreas for their support. Last, but not least, I would like to thank my officemates, Bob, Boris, Filip, Liao and Ken, for making my each day memorable. We always worked in a positive and informal atmosphere. Thank you Bob for helping me with all the software related things, which even included configuring my new laptop! Thank you Boris and Filip for always being ready to translate my Dutch files. We had a lot of memorable moments together.

I would like to thank my colleagues from the LCT research group, for the nice collaboration. Mathias, the night shifts that we had together during the synchrotron campaigns were always exciting and we had a lot of fun. Thank you very much for explaining the XAS results and it always amazed me how you express them in the manuscript. Vladimir, thank you for making time, in your busy schedule, to carry out the catalytic experiments on my samples. Evgeniy and Aditya, thank you for the nice discussions. I would like to thank Gina from KU Leuven for the catalysis experiments. I would like to thank Prof. Guy B Marin and Prof. Johan A Martens for their kind advice and valuable suggestions. I would like to thank Prof. Patrick Bultinck for being the chairman of my PhD jury and all my PhD examination jury members for the insightful comments and encouragement, which helped to improve the thesis.

I would like to thank the technical staffs, Olivier, Nico, Stefan, Gilbert and Jo for providing the best possible service. Thank you Olivier for the interesting talks we had during SEM measurements. Special thanks goes to our Secretaries, Elly, Kristof and Wouter, you were always ready to help in any possible way. I would like to thank all other colleagues and professors in S1 for their friendly behavior. I would like to thank the beamline scientists, Emiliano Fonda from SAMBA (SOLEIL, Paris) and Wim Bras and Daniel Hermida Merino from DUBBLE (ESRF, Grenoble) for their support.

Besides my colleagues, I would like to acknowledge my friends in Ghent and Leuven. Sambhu, words are not enough to express how supportive you were throughout the last five years of my life. We had countless memorable moments and fun during these years. Thank you for all your supports and love. Sreeyettan,

no one else has inspired me in my life like you did. I still remember your words, when I was confused in taking decision between quitting the position at CUSAT and coming to Belgium, that “You have to take risk at some point, and if you cannot do it at this age, it may never happen”, which completely changed my life. Thank you for being there to solve any problems, and I always feel relaxed after talking to you. Joice achacha, you are an example for everyone who wish to excel in their research career, thank you for your love, care and inspiration. Thank you Krishna chechi, kalyani, Nithya chechi, Ivanu and Andrew for the love and care.

There is also a big group of people who made me feel at home in Belgium, my lovely friends Mohan chettan, Latha chechi, Aravind, Vinayan chettan, Ajitha chechi, Nikitha, Nithika, Jubi chettan, Merin chechi, Joan, Sandeep chettan, Parvathy chechi, Sidharth, Aditya, Biju chettan, Preji chechi, Aaron, Vinay chettan, Santhi chechi, Avanthika, Applonia chechi, Aju chettan, Ann, Maju chettan, Sneha chechi, Nimisha chechi, Jineesh, Nathan, Vinod chettan, Resmi chechi, Febin, Thanzi, Saira, Aysha, Shaneesh, Ishaan, Zahia, Deepak, Sreeraj, Radhika, John, Shibin and so many. Thank you all.

I am thankful to all my dear friends and beloved teachers in Calicut University and SNGS College, Pattambi, for their love and care. I am thankful to Dr. P.A. Joy and Dr. T. Ajithkumar at NCL, Pune for their advice and support. I would like to thank my friends in NCL Pune, Kuttettan, Rejiyettan, Rahulettan, Rennychayan, Vipin chettan, Dasettan, for their encouragement and support. I also would like to thank all my friends in my village for being there and supporting me.

Without the support of my lovely family, I wouldn’t have been able to come over to Belgium and do my PhD here. I would like to express my deep sense of gratitude to my parents. Thank you amma and achan for the support you gave me over the past years. Without your support and encouragement, I would not have reached here. Your hopes in me were what sustained me throughout. I am thankful to my dear sister Rajitha, brother in law Sunil and their children my lovely Nandhuttan and Nandhuttii for their love and support. I am thankful to my sweet ammamma (late) for her love and care. Thanks to my father in law, mother in law, Jiju, Liju, Jyothi and cutie Aamikutty for their love and care. Thanks to my cousins and all other family members for their support and care. Finally, and most importantly, I would like to thank my wife Jiji. Your constant support, encouragement and unconditional love were undoubtedly the bedrock upon which the past six years of my life have been built. Thank you for your endless love and care.

Thanks to almighty for all blessings.

Ranjith K. R.
Gent, January 2017

Table of contents

Preface i

Acknowledgements iii

English summary xi

Nederlandstalige samenvatting xiii

1 Introduction 1
- 1.1 Atomic Layer deposition 1
  - 1.1.1 Characteristics of ALD processes 2
- 1.2 ALD for Catalysis 7
  - 1.2.1 Motivation 7
  - 1.2.2 ALD in supported catalyst design 7
    - 1.2.2.1 Metal oxide ALD for Catalysis 8
    - 1.2.2.2 Metal ALD for Catalysis 15
- 1.3 Goals and Outline of the Thesis 19

2 Experimental 29
- 2.1 Thin film deposition by ALD 29
  - 2.1.1 Substrates for ALD 29
  - 2.1.2 ALD Precursors and reactants 29
  - 2.1.3 ALD Setup 30
- 2.2 Characterization methods 31
  - 2.2.1 Spectroscopic Ellipsometry (SE) 31
  - 2.2.2 Mass Spectrometry (MS) 32
  - 2.2.3 Scanning Electron Microscopy (SEM) and Energy Dispersive X-ray Spectroscopy (EDX) 32
  - 2.2.4 Atomic Force Microscopy (AFM) 33
  - 2.2.5 X-ray Photoelectron Spectroscopy (XPS) 34
  - 2.2.6 X-ray Absorption and X-ray Fluorescence Spectroscopy (XAS and XRF) 34
  - 2.2.7 X-ray Diffractometry (XRD) 37
  - 2.2.8 X-ray Reflectivity (XRR) 38
  - 2.2.9 Grazing-Incidence Small-Angle X-ray Scattering (GISAXS) 38

2.2.10 Transmission Electron Microscopy (TEM) 39

3 Process development for the ALD of Pt and MO_x (M = Ga, In and Fe) 43

3.1 Importance of Pt and Pt ALD in catalysis 43

3.2 Importance of Metal oxides and Metal oxide ALD in catalysis . . 45

3.3 Catalytic applications 51

3.3.1 Case study I: Bifunctional hydroconversion catalyst *via* atomic layer deposition of platinum 51

3.3.2 Case study II: Introduction of acid sites in an all-silica - COK-14 zeolite by Ga-ALD and its catalytic activation. . 53

Paper I: Low Temperature Atomic Layer Deposition of Platinum using (methylcyclopentadienyl)Trimethylplatinum and Ozone 63

Paper II: Plasma enhanced atomic layer deposition of Ga_2O_3 thin films 75

Paper III: Low temperature atomic layer deposition of crystalline In_2O_3 films 91

Paper III - supplementary information: Low temperature atomic layer deposition of crystalline In_2O_3 films 103

Paper IV: Plasma enhanced atomic layer deposition of Fe_2O_3 thin films 107

Paper IV - supplementary information: Plasma enhanced atomic layer deposition of Fe_2O_3 thin films 121

4 ALD based synthesis of noble and non-noble metal containing bimetallic alloys 125

4.1 Introduction 125

4.2 ALD for the synthesis of bimetallic materials 126

Paper V: Atomic Layer Deposition Route to Tailor Nanoalloys of Noble and Non-Noble Metals 129

Paper V - supplementary information: Atomic Layer Deposition Route to Tailor Nanoalloys of Noble and Non-Noble Metals 145

Paper VI: Size- and Composition-Controlled Pt-Sn Bimetallic Nanoparticles Prepared by Atomic Layer Deposition 155

Paper VI - supplementary information: Size- and Composition-Controlled Pt-Sn Bimetallic Nanoparticles Prepared by Atomic Layer Deposition 165

5 Conclusions and suggestions for future work 169

List of abbreviations **175**

List of Figures **177**

List of Tables **181**

List of publications **183**

English summary

Atomic Layer Deposition (ALD), a thin film deposition technique, has revolutionized the field of semiconductor industry. By now, ALD has emerged as a powerful deposition tool in various other fields such as catalysis, photovoltaics, sensors, polymers, fuel cells and batteries. In particular, in the field of heterogeneous catalysis, it is now emerging as an impressive method for designing and modifying the catalysts (and catalyst supports) at the nanoscale level through precise control over the structure and composition. This thesis work can be divided into three parts: 1) developing new processes for the ALD of metals and metal oxides, that are relevant for catalysis, 2) developing a method for the synthesis of bimetallic materials, containing both noble and non-noble metals, by combining different ALD processes and finally 3) testing the feasibility of the developed methods in supported catalyst preparation. Since different ALD processes have to be eventually combined for the synthesis of bimetallic materials, processes with wide ALD temperature window were targeted when developing the processes.

The newly developed ALD processes are described in chapter 3 of this thesis. In total four ALD processes have been developed for the deposition of metallic Pt and the oxides of Ga, In and Fe, which are of importance in the field of catalysis, especially for hydrocarbon conversion reactions. A very well-known Pt precursor, $Me_3PtCpMe$, is used for the Pt ALD in combination with ozone as reactant. Compared to the existing Pt ALD processes, this novel process enables the deposition of metallic Pt at very low temperatures ranging from 100 - 300 °C. This could be beneficial for the deposition of Pt on temperature sensitive materials. Another cyclopentadienyl based precursor called tertiary-butyl ferrocene (TBF) is used in combination with oxygen plasma for the deposition of iron oxide. The advantage of this precursor over the commonly used ferrocene precursor is that it is a liquid and vaporizes at lower temperatures. Gallium and indium oxides are deposited using β-diketonate based precursors, $Ga(TMHD)_3$ and $In(TMHD)_3$, respectively. The exceptional stability and low cost make β-diketonate precursors highly interesting. Both processes use O_2 plasma as reactant and exhibit a wide temperature window of 100 - 400 °C.

The second goal of this thesis work was to develop a new method for the synthesis of different bimetallic materials by combining respective ALD processes. Supported Pt nanoparticles alloyed with In, Ga or Sn have proven to be highly selective catalysts for the dehydrogenation of propane to propylene. In particular, a Pt-Sn-based catalyst is used worldwide in the industrial dehydrogenation process

Oleflex (UOP). However, despite the success of current dehydrogenation technologies, there are still opportunities for further enhancement of the catalyst stability and efficiency. This requires an in-depth understanding of the relation between the structural and electronic properties of the alloyed Pt phase and the catalytic performance. Such insights are closely related to the availability of methodologies that can tailor the composition and morphology of the bimetallic catalysts at the atomic scale.

Even though ALD has shown its potential for the synthesis of bimetallic materials, so far it has been limited to the synthesis of bimetallic alloys containing only noble metals. The main challenge here is the lack of favorable ALD chemistries for the deposition of non-noble metals like Ga, In *etc.* in their elemental state. In this work, a novel ALD based methodology is developed for the controlled synthesis of bimetallic alloys containing both noble and non-noble metals. In this synthesis method, first a bilayer consisting of the materials of interest is deposited by ALD, which is then subjected to a temperature programmed reduction (TPR) under hydrogen atmosphere. Real time information on the formation of different bimetallic alloy phases can be obtained by using *in situ* X-ray diffraction measurements during TPR. A detailed description of this novel method is given and demonstrated by taking Pt-In and Pt-Ga systems as examples.

Finally, the feasibility of the developed methods (ALD and bimetallic synthesis) in synthesizing different supported catalyst materials was investigated. Pt ALD was employed for introducing Pt into a ZSM-5 zeolite support for the synthesis of a bifunctional catalyst. In a second experiment, catalytic activity was induced in a purely siliceous -COK-14 zeolite by introducing catalytically active acidic gallium species by gallium oxide ALD. Both these catalysts were then tested for decane hydroconversion reaction. A Pt-In bimetallic catalyst was prepared in a mesoporous silica support by employing the newly developed bimetallic synthesis method and was tested for the well-known propane dehydrogenation reaction. The details of the catalytic experiments are reported in chapters 3 and 4 respectively.

Nederlandstalige samenvatting –Summary in Dutch–

Atoomlaagafzetting (ALD) is een dunne film depositietechniek die voor een ware evolutie zorgde binnen de halfgeleiderindustrie. De dag van vandaag wordt de ALD techniek ook ingezet in tal van andere toepassingsgebieden zoals katalyse, fotovoltaische zonnecellen, sensoren, polymeren, brandstofcellen en batterijen. In het domein van de heterogene katalyse ontpopt ALD zich momenteel tot een uiterst krachtige methode voor het ontwikkelen en modificeren van katalysatoren (en dragermaterialen) op nanometerschaal met precieze controle over de materiaalstructuur en -samenstelling. Deze thesis bestaat uit 3 delen: 1) ontwikkelen van nieuwe processen voor ALD van metalen en metaaloxides die relevant zijn voor katalytische processen, 2) ontwikkelen van een methode voor de synthese van bimetalen, die zowel een edel- als een niet-edelmetaal bevatten, door combinatie van verschillende ALD processen en 3) testen van de ontwikkelde methodes en materialen voor toepassingen in heterogene katalyse.

De nieuw ontwikkelde ALD processen zijn beschreven in hoofdstuk 3 van deze thesis. In totaal werden vier ALD processen ontwikkeld voor de afzetting van metallisch Pt en oxides van Ga, In en Fe. Deze materialen zijn belangrijk in katalyse, in het bijzonder voor de omzettingsreacties van koolwaterstoffen. Voor de afzetting van Pt werd een alom gebruikte Pt precursor, $Me_3PtCpMe$, gecombineerd met ozon als een nieuw reactant. In vergelijking met de bestaande Pt ALD processen laat dit nieuwe proces toe om Pt af te zetten in een ruimer temperatuurvenster, 100 - 300 °C. De mogelijkheid om Pt af te zetten bij deze lage temperaturen kan een voordeel bieden wanneer Pt nodig is op temperatuurgevoelige materialen. Voor de afzetting van ijzeroxide werd een tweede cyclopentadienyl-gebaseerde precursor gebruikt, namelijk tertiary-butyl ferrocene (TBF), in combinatie met zuurstofplasma. Het voordeel van deze precursor ten opzichte van het normaal gebruikte ferroceen is dat TBF een vloeistof is die verdampt bij lagere temperaturen. Galliumoxide en indiumoxide werden afgezet met behulp van diketonaat-precursoren, respectievelijk $Ga(TMHD)_3$ en $In(TMHD)_3$. De uitzonderlijke stabiliteit en de lage kost maken dit type precursoren zeer interessant voor toepassingen. Beide ALD processen gebruiken zuurstofplasma als reactant en zijn gekenmerkt door een breed temperatuurvenster van 100 - 400 °C.

Het tweede doel van deze thesis was om een nieuwe methode te ontwikkelen voor de synthese van bimetalen door de respectieve ALD processen te combineren.

Pt nanodeeltjes, gelegeerd met In, Ga of Sn afgezet op een dragermateriaal, zijn zeer selectieve katalysatoren voor de dehydrogenatie van propaan tot propyleen. Pt-Sn katalysatoren worden wereldwijd gebruikt in het industriele Oleflex dehydrogenatieproces (UOP). Ondanks het succes van deze technologie is er nog steeds ruimte voor verbetering van de stabiliteit en efficintie van de gebruikte katalysatoren. Dit laatste vereist een diepgaand begrip van de relatie tussen de structuur en elektronische eigenschappen van de gelegeerde Pt materialen en hun katalytische eigenschappen. Deze inzichten kunnen enkel verworven worden als er methodes beschikbaar zijn om bimetallische materialen te synthetiseren met precieze controle over de samenstelling en morfologie, en dat op atomaire schaal.

Hoewel het potentieel van ALD voor de synthese van bimetalen al eerder werd aangetoond, was dit tot nog toe beperkt tot combinaties van twee edelmetalen. De voornaamste uitdaging om dit verder uit te breiden naar niet-edelmetalen is het gebrek aan betrouwbare ALD processen voor de afzetting van niet-edelmetalen zoals Ga, In, enz. in hun elementaire vorm. In dit werk werd een alternatieve methode ontwikkeld voor de gecontroleerde vorming van bimetaallegeringen die zowel een edel- als een niet-edelmetaal bevatten. Hierbij wordt eerst een dubbellaag (bilaag) bestaande uit de twee relevante materialen (edelmetaal en niet-edelmetaaloxide) afgezet, gevolgd door temperatuur-geprogrammeerde reductie (TPR) in waterstof. Via in situ X-stralen diffractie tijdens TPR werd real time informatie verkregen over de vorming van verschillende bimetaallegeringen. De thesis geeft een gedetailleerde beschrijving van deze methode met voorbeelden van Pt-In en Pt-Ga legeringen.

Tenslotte werd de toepasbaarheid van de ontwikkelde ALD methodes in katalyse onderzocht. ALD van Pt werd gebruikt om Pt te introduceren in een ZSM-5 zeoliet dragermaterial teneinde een bifunctionele katalysator te bekomen. In een tweede experiment werd een puur silicaatmateriaal, -COK-14 zeoliet, katalytisch actief gemaakt door zure gallium sites te introduceren via ALD. Beide katalysatoren werden getest voor hydroconversie (hydrogenerend kraken) van n-decaan. De katalytische activiteit van een Pt-In bimetallische katalysator afgezet op een mesoporeus silica dragermateriaal werd bepaald voor de gekende propaan dehydrogenatie reactie. De details van de katalytische experimenten worden respectievelijk besproken in hoofdstukken 3 en 4.

1

Introduction *

1.1 Atomic Layer deposition

Atomic layer deposition (ALD) is a thin film growth technique that enables the deposition of metal oxides, nitrides, sulfides, and metals in a layer-by-layer fashion, i.e. the deposition of one (sub-)monolayer of material per process cycle. The atomic level thickness control and extreme conformal nature of coating make it a potential tool for depositing uniform and conformal films on complex three-dimensional topographies. In recent years, ALD has been established as a key coating technique for advanced nano-electronics and its application has been exploited in various other fields such as catalysis, photovoltaics, sensors, fuel cells and batteries.

ALD was originally developed and introduced worldwide with the name Atomic Layer Epitaxy (ALE) in the late 1970s,[1] motivated by the need for a deposition method for thin-film electroluminescent (TFEL) flat-panel displays.[2] For such an application, high-quality dielectric and luminescent films are required on large-area substrates. Later, in the beginning of 2000 the name was changed to ALD, as most of the films grown by ALD are in fact amorphous without showing any epitaxial structure with respect to the underlying substrate.[3] The renaissance of ALD began in the mid-1990s, with the interest focused on silicon-based microelectronics. Shrinking device dimensions and increasing aspect ratios in integrated circuits (IC) demanded thin-film deposition techniques which can produce very thin, con-

*Accepted as a book chapter (Section 1.1 & 1.2): Ramachandran, R. K.; Detavernier, C., Dendooven, J.; *Nanotechnology in catalysis - Applications in the chemical industry, energy research, and environment protection*, WILEY-VCH publications

formal films with control of the thickness and composition at the atomic level, which could be accomplished by the self-limiting aspect of ALD.[4;5] During the same decade (90's) several researchers also demonstrated the capability of ALD to produce high surface area catalyst materials[6–9] and this potential of ALD continues to be explored nowadays.[10;11] Apart from the above mentioned applications, by now, ALD has emerged as a promising technique in various other fields such as photovoltaics,[12–14] sensors,[15;16] polymers,[17–22] fuel cells[23–25] and batteries.[26–29]

ALD is basically a chemical vapour deposition (CVD) technique that relies on saturating and irreversible, separated gas-solid reactions, which are repeated in a cyclic manner. One ALD cycle consists typically of four steps, as schematically illustrated in **Figure 1.1**, for an ideal ALD process. I) exposure to the first reactant (Reactant A), typically a metal reactant, II) purge or evacuation to remove the unreacted molecules and gaseous by-products, III) exposure to the second reactant (Reactant B), typically a non-metal reactant and IV) second purge or evacuation to remove the unreacted molecules and gaseous by-products. These four steps can be repeated to produce more ALD cycles. Often in an ALD chemistry the metal compound is referred to as precursor and the non-metal compound as reactant.

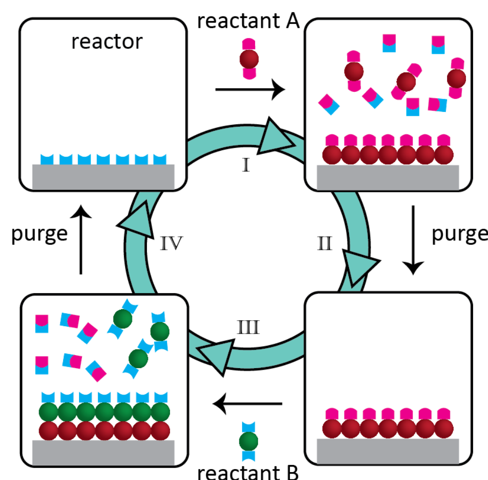

Figure 1.1. *Schematic illustration of ALD reaction cycle.*

1.1.1 Characteristics of ALD processes

The ALD process is characterised by four characteristic features called saturation, linearity, temperature window and conformality. The defining feature of an ideal ALD process is its saturative growth, which means that the reaction between the reactant molecule and the substrate must be self-limiting and the presence of excess precursor beyond what is necessary for the saturation of all accessible (sometimes, not all the surface sites are accessible due to the steric constraints imposed by the

precursor ligands) surface sites must not lead to additional film growth. A natural consequence of this self-limiting behavior is linearity, meaning that the film thickness increases by a fixed amount with each ALD cycle and the growth can be expressed as growth per cycle (GPC) instead of time. **Figure 1.2**(a) shows the saturated growth curves with the tetrakis(dimethylamino)tin (TDMASn)/H_2O process[30] for the deposition of SnO_2 at 100 °C. It is clear from the graph that a 2 s pulse of both TDMASn and H_2O is enough to obtain a saturated growth, and that a larger exposure to the precursor or reactant vapor does not result in any further deposition. This in turn results in a linear increase in the thickness of SnO_2, as shown in **Figure 1.2**(b), where the thickness was measured by ellipsometry over a wide range of ALD cycles.

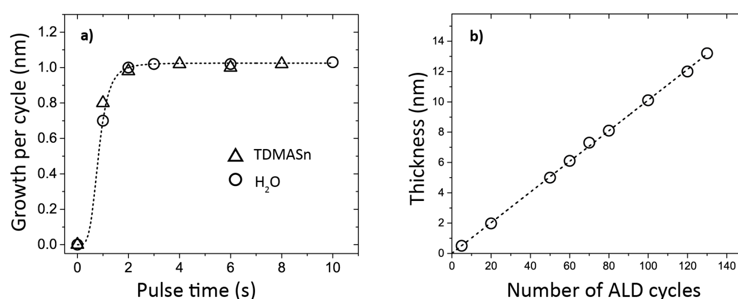

Figure 1.2. *(a) Saturation of the SnO_2 growth against the exposure time of the Sn precursor (TDMASn) (triangles) and H_2O (circles) at 100 °C. (b) Linear growth of the SnO_2 on a SiO_2 surface at 100 °C. Every ALD cycle results in the deposition of the same amount of SnO_2.*

An ideal ALD process will result in the deposition of one monolayer of the material per cycle as shown in **Figure 1.1**. However, an ideal ALD process is rarely observed. In reality, the deposited ALD material in each cycle is less than a monolayer, either because of the lack of insufficient active species on the substrate, or due to steric hindrance of bulky ligands which prevent the precursor from reacting with all the available active sites. In this case, further film growth can occur in three different ways as shown in **Figure 1.3**. a) Two-dimensional growth: the deposited material settles always in the lowest unfilled material layer and one monolayer of the ALD-grown material covers the substrate completely, b) island growth: the new material units are preferentially deposited on the ALD-grown material and c) random deposition: a statistical growth mode, where the new material units are deposited with an equal probability on all surface sites. For detailed information on different growth mode, the reader is referred to the review article by R. L. Puurunen.[4]

For each ALD process, there is usually a temperature regime within which self-limiting growth can be achieved. This temperature range is often called the temperature window (**Figure 1.4**). Below and above the temperature window an uncontrolled growth can occur due to several reasons. At low temperatures, the

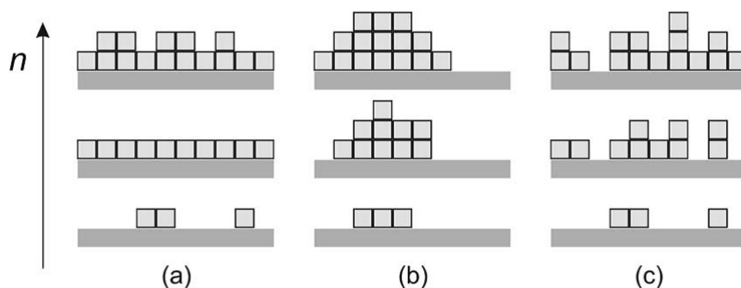

Figure 1.3. *Schematic illustration with increasing number of reaction cycles n of selected growth modes possible in ALD: a) two-dimensional growth, b) island growth and, c) random deposition. (Reproduced from Ref.[4])*

self-limiting growth can be affected by a decrease in growth rate as the degree of thermal activation becomes insufficient to sustain effective surface reactions. Alternatively, an increase in growth behavior may also be observed as a result of precursor condensation and/or physisorption leading to the association of multiple monolayers of precursor which cannot be removed by purging the reactor. High temperatures will also destroy the self-limiting growth either by increasing the growth rate due to the thermal decomposition of the precursor or by decreasing the growth rate by favoring the desorption of chemisorbed species from the surface. Ideally, within the temperature window the growth rate of an ALD process would remain independent on the change in temperature (**Figure 1.4**, red line parallel to X -axis). However, many ALD processes exhibit a temperature-dependent saturated growth even within the temperature window, as exemplified in **Figure 1.4** (circles) for the ALD growth of SnO_2, where the growth rate was found to decrease with increasing temperature.[30;31] This occurs typically if the number of reactive surface sites affects the amount of chemisorbed species and if increasing the temperature decreases the number of reactive surface sites. A detailed description of this temperature-dependent saturated growth can be found in reference.[4] Generally, for most of the ALD processes using metalorganic precursors, the temperature window falls in the range of 100 - 350 °C.

A second consequence of the self-limiting surface chemistry is that it enables ALD to coat extremely complex 3D morphologies with excellent conformality[†], and makes ALD insensitive to differences in precursor flux, meaning that the growth rate is the same everywhere in the ALD reaction chamber. This is in contrast to flux-controlled deposition methods, such as physical and chemical

[†]Conformality is the ability to coat a surface structure with a uniform thickness. As such, it is a consequence of the self-limiting surface reactions of an ALD process, which enables the conformal coating of high aspect ratio complex (3D) structures with uniform film thickness. This is often expressed in terms of step coverage, the ratio of the film thickness at the top to the film thickness at the bottom of the feature. When an ALD coating did not reach the bottom of the feature, the conformality can be expressed in terms of ‘coated aspect ratio’, which is the aspect ratio of the structure up to where the film thickness is still 50% of the film thickness at the top.

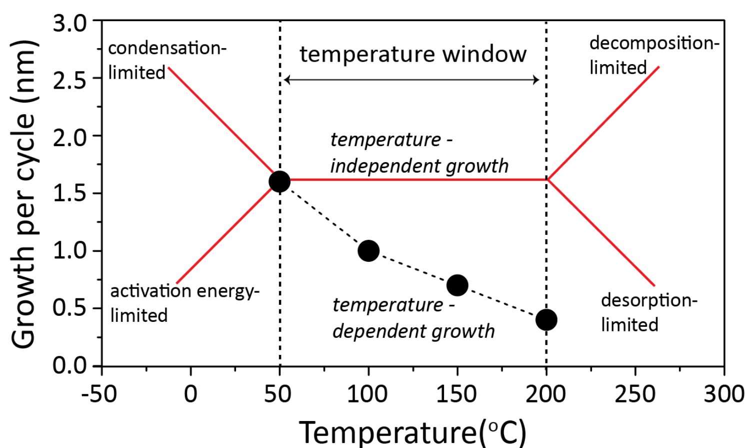

Figure 1.4. *The solid lines describe a general ALD temperature window. The red line parallel to the X-axis shows the temperature-independent saturated growth. Circles show the temperature-dependent saturated growth rate of SnO_2 as a function of deposition temperature.*

vapour deposition (PVD and CVD), where material is mainly deposited in the direction of the flux. This conformal nature of ALD has been extensively explored in microelectronic industry for coating trench structures, as illustrated by the cross-sectional scanning electron microscopy (SEM) image in **Figure 1.5**(a), where high aspect ratio silicon trench structures are coated conformally with 300 nm Al_2O_3.[32] The self-limiting nature also enables the precursor molecules to diffuse into narrow pores until they encounter an active site and thereby coat the pores with great uniformity, which is extremely useful for catalyst synthesis. For example, **Figure 1.5**(b) and (c) show the TEM images of a TiO_2 coated zeotile-4 material (with main hexagonal pores of 8-10 nm diameter and small slit-like side pores of 2-4 nm).[33] The dark outer rim observed in the TEM images can be ascribed to the infiltration of TiO_2 material in the slit-like mesopores. **Figure 1.5**(b) shows the top view of the main hexagonal pores, where the TiO_2 coating is seen as the black spots (green arrow). **Figure 1.5**(c) is a parallel cut to the main channels. The dark area corresponding to TiO_2 deposition in the direction of main pores (white arrows) was about 150 nm, while in perpendicular directions (green arrows) penetration was limited to about 50 nm due to the narrower mesopores.

The success of ALD relies on the availability of suitable precursors.[34–37] In general, the most important characteristics of ALD precursors are good volatility, thermal stability, and high reactivity. The precursor must be sufficiently stable (thermodynamically or energetically) to volatilize and reach the surface of interest without decomposition, that is, the bond between the metal (M) and the ligand (L) must have an adequate strength. However, if the precursor is too stable or the M-L bond is too strong, the precursor may be unreactive (kinetically stable), since a

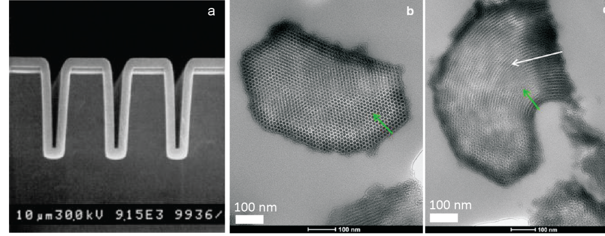

Figure 1.5. *(a) Cross-sectional SEM image of an Al_2O_3 ALD film with a thickness of 300 nm on a Si wafer with a trench structure. (Reprinted with permission from Ref.[32] Copyright 1999 John Wiley & Sons). Cross-sectional TEM images revealing (b) the spreading of TiO_2 deposited in a Zeotile-4 powder particle and (c) the penetration of the TiO_2 deposition in the hexagonal mesopores (white arrow) and in the smaller slit-like mesopores (green arrow). The Zeotile-4 material was subjected to 30 TDMAT/H_2O ALD cycles with a TDMAT exposure time of 90 s. (Adapted with permission from Ref.[33] Copyright 2012 American Chemical Society)*

high activation energy will be required to break the M-L bond for the reaction with the surface to occur. So, a precursor with moderate M-L bond strength is preferred to ensure sufficient volatility, thermal stability and reactivity.

Consider an ALD process where a metal organic precursor, ML_n, reacts with water. The reaction proceeds *via* two successive half reactions: 1) reaction of ML_n with the surface hydroxyl groups of the substrate (Eq. 1.1) and 2) subsequent reaction with water (Eq. 1.2).

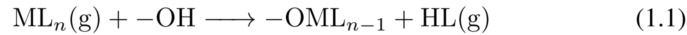

$$\mathrm{ML}_n(\mathrm{g}) + -\mathrm{OH} \longrightarrow -\mathrm{OML}_{n-1} + \mathrm{HL}(\mathrm{g}) \qquad (1.1)$$

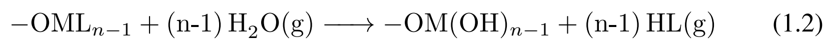

$$-\mathrm{OML}_{n-1} + \text{(n-1)}\,\mathrm{H_2O}(\mathrm{g}) \longrightarrow -\mathrm{OM(OH)}_{n-1} + \text{(n-1)}\,\mathrm{HL}(\mathrm{g}) \qquad (1.2)$$

Based on the above reaction mechanism, a successful ALD process is feasible if the conditions listed in the **Table 1.1** are satisfied in terms of the bond strength of different chemical species involved.

Requirement for the ALD process	Bond strength requirement
Precursor should have sufficient volatility and thermal stability	M-L bond should be sufficiently strong
Precursor/reactant should aggressively react with the surface groups and the byproducts should be volatile and unreactive	The bond strengths should be in the following order: M-L $<$ H-L $>$ O-H

Table 1.1. *Feasibility of an ALD process based on the bond strength of different chemical species involved.*

1.2 ALD for Catalysis

1.2.1 Motivation

Catalysts are the workhorses of chemical transformations in the industry. Approximately 85-90 % of the products of the chemical industry are made in catalytic processes, which include petroleum refining, chemical upgrading, automobile exhaust treatment and fuel cells.[38] A catalyst offers an alternative, energetically favorable mechanism to the non-catalytic reaction, thus enabling processes to be carried out under industrially feasible conditions of pressure and temperature. Heterogeneous catalysts with the catalytic active materials (metal/metal oxide nanoparticles) dispersed on high surface area solid materials such as mesoporous silica, metal oxide, zeolite and carbon are the preferred form in most industrial processes, since the catalyst can be easily separated from reaction products. In some cases, the support material itself can also provide an additional catalytic function that further improves the overall performance of the catalyst.

Supported metal catalysts are often prepared by a combination of different operations such as (I) introduction of metal salts on the support by impregnation, co-precipitation and deposition precipitation, (II) drying and calcination, and (III) activation under a reducing atmosphere.[39;40] These methods quite often result in a non-uniform distribution of the active phase on the support, which leads to a low selectivity to desired products. Deactivation of the metal catalyst due to sintering (the formation of larger metal particles at high temperature)[41;42] and coking (the blocking of the active surface by the accumulation of carbon)[41;43–45] is another major problem in the case of supported catalysts. In many cases, they can also occur simultaneously. Coke formation can be prevented by passivating the active metal with traces of sulfur, tin, *etc.* or by alloy formation.[46–48] The sintering of metal nanoparticles at high temperatures can be prevented by over-coating them with inorganic oxide such as mesoporous silica, tin oxide, or zirconia.[49–52] These are often obtained by methods such as chemical vapour deposition or grafting, where the shell thickness is poorly controlled. The challenge of simultaneously improving catalytic activity, selectivity, and stability of the supported metal catalysts demands an advanced synthesis method with precise control at the atomic level.

1.2.2 ALD in supported catalyst design

Due to its self-limiting features in each deposition cycle, ALD can provide a possible method to design and modify catalysts at the nanoscale through precise control over the structure and composition of the underlying support, the catalytic active sites, and the protective layer. Suntola and co-workers demonstrated the suitability of ALD for coating porous high surface area materials in the early 1990s.[8;53] Since then ALD has shown its great potential in advanced catalysts synthesis. The possibilities of ALD in supported catalyst design are schematically illustrated in the **Figure 1.6**.

Figure 1.6(a) shows the schematic cross section of a single pore in a porous support. Figure 1.6(b) represents the introduction of highly dispersed catalytically active centers inside the pores using metal oxide ALD.[8;54–58] In this case either a few ALD cycles are applied or thicker ALD films are deposited and subjected to a post deposition annealing to break up the layer. Unlike metal oxides, ALD of metals (especially noble metals) on oxide surfaces often shows a delay in the nucleation during the initial stages of growth, which results in the formation of discrete, three-dimensional nanoparticles.[4] Also, noble metals show a tendency to grow preferably on top of noble metals rather than on the oxide surfaces.[59] By exploiting these growth behaviors, nanoparticles of single (monometallic) and mixed (bimetallic) noble metals can be synthesized. **Figure 1.6**(c) shows the formation of monometallic nanoparticles, while **Figure 1.6** (d) and (e) show the introduction of bimetallic noble metal nanoparticles into the porous support. In the case of bimetallic nanoparticles two different approaches are possible: 1) a core-shell nanoparticle can be obtained by performing two ALD processes one after the other (**Figure 1.6**(d)). The thickness of the core and the outer shell can be precisely controlled by the number of ALD cycles.[59;60] 2) A mixed (alloy) nanoparticle can be obtained in a supercycle approach where the ALD processes for the individual metals are alternated (Figure 1.6(e)). The composition of the resulting alloy can be tuned by the relative number of ALD cycles.[61] Another possibility of ALD in catalysis is the introduction of a protective layer over the metallic nanoparticles to stabilize them against sintering and coke formation[62–66] (**Figure 1.6**(f)). The layer is dense and continuous on the support, and acts as a physical barrier for the nanoparticles. On the particles, the layer shows some porosity (formed either during ALD or by post-ALD annealing) thus making the active material accessible. ALD can also be used to modify the support material prior to the introduction of the active particles. In **Figure 1.6**(g), the atomic level thickness control of ALD is exploited to precisely tune the pore size of the support material, which can enhance the selectivity of the catalyst.[67;68]

In the following sections, examples are provided for the different ALD approaches depicted in the schematic picture based on a literature survey and in each case, one of the examples is discussed in detail.

1.2.2.1 Metal oxide ALD for Catalysis

Among materials deposited by ALD, metal oxides are the most predominant because of their early applications as thin film insulators and semiconductors for microelectronics.[4;59] For catalytic applications, the conformal deposition allows the creation of well-defined oxide catalysts over intricate morphologies with high surface area. ALD of metal oxides has been used for the creation of catalytic sites, photocatalysis, tuning the substrate morphology and for depositing protecting over-layers on other catalytic materials. Due to their unique acid-base and redox properties, metal oxides have been widely used in a broad range of catalytic reactions.

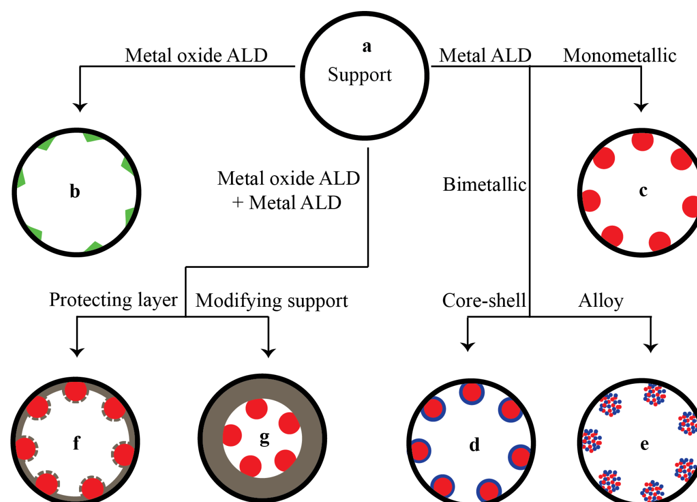

Figure 1.6. *Possibilities of ALD in supported catalyst design: (a) Porous support, (b) Introducing catalytic sites on the pore walls, Introducing catalytic (c) monometallic, (d) bimetallic core-shell and (e) bimetallic alloy nanoparticles on the pore walls, (f) Stabilizing catalytic nanoparticles with an ALD over-layer, (g) Tuning pore size of the support prior to the introduction of catalytic nanoparticles.*

Introducing catalytically active sites: Performing one or only a few ALD cycles can produce an exceptionally uniform coverage of well dispersed metal oxide surface species with high catalytic activity. For example, catalytically active Co_x [8;54;55] and VO_x [56] species were introduced into different silica and alumina supports by ALD.

In 2011, Sree *et al.* demonstrated that the ALD process using TMA and H_2O is suited for the incorporation of Al species to increase the acidity and thereby enhance the catalytic activity in mesoporous zeolites and ordered micro/mesoporous zeotile-4 material.[57] More recently, this method was extended to introduce catalytically active aluminum species on a purely siliceous zeolite (-COK-14) with intersecting 10- and 12-membered rings of tetrahedral pore systems.[58;69] The interrupted -COK-14 zeolite framework was prepared by degermanation of UTL zeolite, onto which the aluminum species were introduced by five cycles of alumina ALD. ^{27}Al MAS NMR revealed a distribution of aluminum coordination in the Al-ALD treated, ammonium-exchanged COK-14 sample of *ca.* 21% tetrahedral Al, *ca.* 19% pentacoordinated or distorted tetrahedral Al, and 60% octahedral extra-framework Al. According to EDX the Si/Al atomic ratio was around 50. Combining NMR and EDX data, the framework Si/Al atomic ratio was estimated to be *ca.* 240. Interestingly, this modification causes a permanent conversion of the originally interrupted framework of -COK-14 to a fully connected OKO type framework (**Figure 1.7**(a)), and generates new acid sites which are catalytically active for hydrocracking of n-decane. The catalytic activity of Pt-loaded all-silica

and Pt-loaded aluminosilicate COK-14 was investigated in the hydroconversion of n-decane. The conversion of n-decane is plotted against reaction temperature in **Figure 1.7**(b). Hydroisomerisation and hydrocracking of a long n-alkane are bifunctional catalytic processes in which the dehydrogenation and hydrogenation is catalyzed by the noble metals, while the carbon-carbon bonds of the n-alkane are rearranged on acid sites. The results showed that the purely siliceous COK-14 lacking Brønsted acid sites was inactive, while the bifunctional Pt-loaded aluminosilicate COK-14 having Brønsted acid sites was active and complete conversion of n-decane was achieved at a reaction temperature of 310 °C. In this way aluminum oxide ALD has been used for both modifying/stabilizing the support and introducing catalytically active centers.

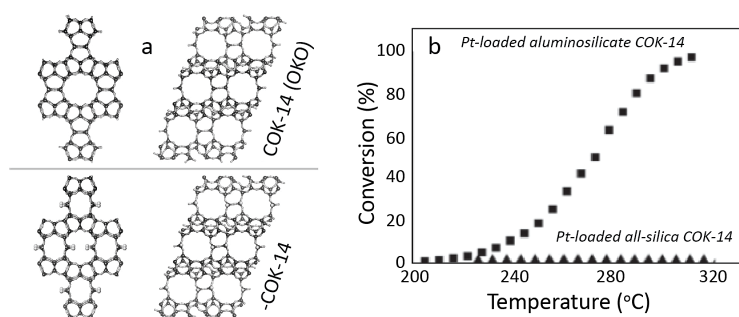

Figure 1.7. *(a) Framework of COK-14 (OKO framework type) (top) and -COK-14 zeolite (bottom), viewed along the 12-MR pores (left) and 10-MR pores (right). (b) Conversion of n-decane against reaction temperature on Pt-loaded all-silica COK-14 (triangle) and Pt-loaded aluminosilicate COK-14 (squares) (reaction conditions: P_{H2}/P_{C10} = 214, W/F^{o} = 980 kg s mol^{-1}, P = 0.45 MPa) (Adapted from Ref[58] with permission from The Royal Society of Chemistry).*

Photocatalysis: The possibility of depositing photocatalytic oxide layers by ALD onto nanostructured supports has drawn considerable attention in recent years. This application requires precise control over the composition, structure, and thickness of the photocatalytic oxide layers. Deng *et al.* recently demonstrated ALD based synthesis of highly photoactive, self-supported anatase TiO_2 nanoparticle chains using multi-walled carbon nanotubes (MWCNTs) as sacrificial templates.[70] MWCNTs supported on a planar silicon substrate were first coated with thin TiO_2 layers using 100 cycles of the tetrakis- (dimethylamino)titanium, TDMAT/O_3 ALD process. **Figure 1.8**(a) shows scanning electron microscopy (SEM) images of a MWCNTs sample after coating with 100 cycles of the TiO_2 ALD process. The transmission electron microscopy (TEM) image of some of the coated CNTs that were extracted from the MWCNT forest is shown in **Figure 1.8**(b), which illustrates that the ALD coating resulted in a uniform TiO_2 layer surrounding most of the MWCNTs. The sample was then heated in air at a ramp rate of 1 °C per minute from room temperature to 850 °C, which resulted

in the removal of carbon from the MWCNTs and the formation of free standing anatase TiO_2 nanoparticles (∼12 nm diameter) with an ultrahigh surface area (137 cm^2/cm^2 of substrate), as revealed by SEM and TEM measurements (**Figures 1.8** (c) and (d)). The obtained porous film, consisting of anchored anatase nanoparticle chains, provides a large surface area and a sufficiently porous arrangement to allow gas molecules to diffuse, adsorb and react on the active surfaces. The photocatalytic activity of these forests of TiO_2 nanoparticle chains was evaluated for the degradation of acetaldehyde under UV light. Air spiked with different concentrations of acetaldehyde was flowed over the sample at a total flow rate of 400 $cm^3 min^{-1}$ and the evolution of the acetaldehyde concentration, as well as that of CO_2 as the degradation product was continuously monitored using on-line FTIR spectroscopy. The moment the UV-A lamp is switched on, acetaldehyde starts degrading into CO_2 and water as can be seen in the **Figure 1.9**, where the change in the reactor outlet concentrations of acetaldehyde and CO_2 for an inlet concentration of 25 ppmv is displayed. This method is furthermore extendable to various metal oxides with different carbonaceous template materials, as illustrated by several authors.[70–72]

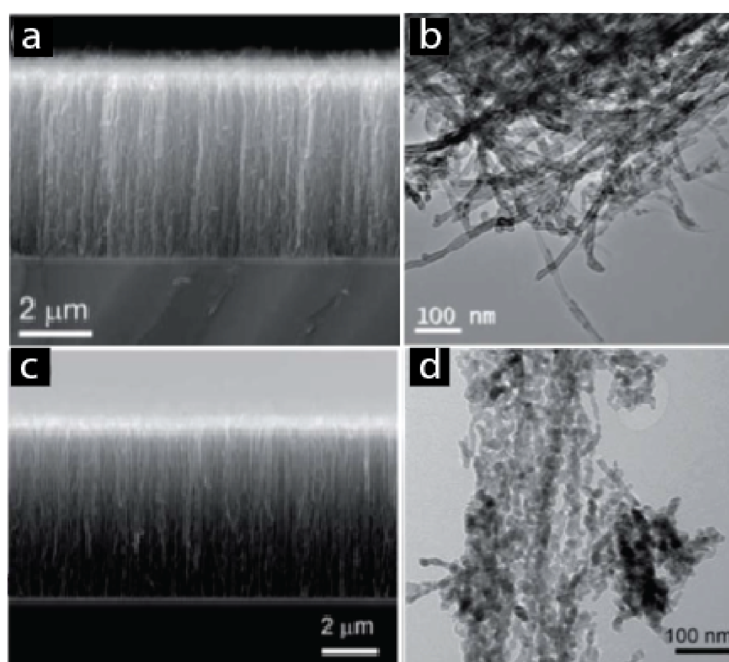

Figure 1.8. *SEM (a, c) and TEM (b, d) images of 6 μm MWCNTs after 100 ALD cycles of TiO_2 (top) and the TiO_2 nanoparticle chains (bottom) after annealing the same film in air at 500 °C for 3 hours. (Adapted from Ref[70] with permission from The Royal Society of Chemistry)*

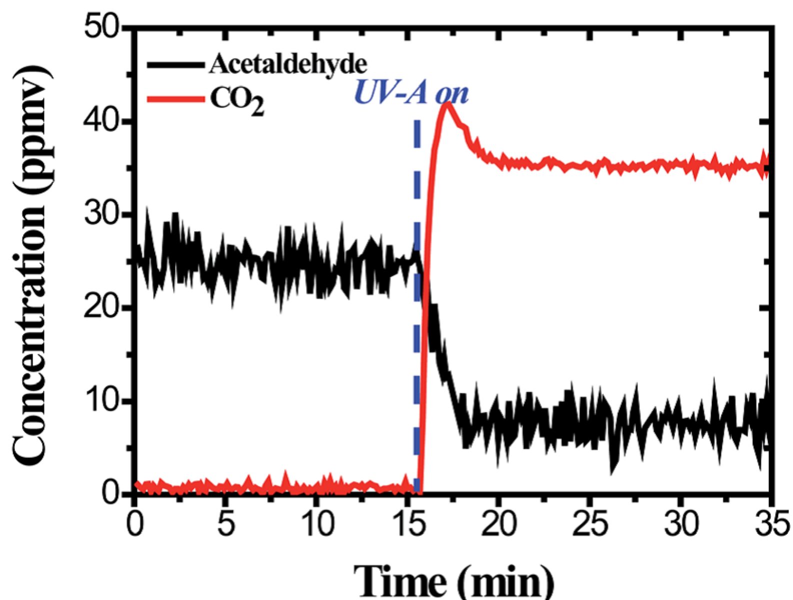

Figure 1.9. *Reactor outlet concentrations of acetaldehyde (black curve) and CO_2 (red curve) during the photocatalytic test on TiO_2 nanoparticle chains. The moment the UV-A lamp is switched on is indicated with the dashed blue line. (Adapted from Ref*[70] *with permission from The Royal Society of Chemistry)*

Tuning the substrate morphology: The morphology of the support material plays a crucial role in heterogeneous catalysis. For example, the pore size of mesoporous materials has been found to have a great influence in the catalytic activity and selectivity.[73] The potential of ALD for modifying the catalyst support has been investigated in detail by several researchers. For example, Dendooven *et al.* demonstrated the use of HfO_2 ALD[67] for tuning the pore size of mesoporous titania film containing ink-bottle shaped pores.[74] The mesoporous titania film was synthesized on a planar silicon substrate by spin coating a solution of titanium precursor and polymeric templates. Ellipsometric porosimetry (EP) measurements revealed that the titania film contained ink-bottle shaped mesopores with an average pore diameter of 6.8 nm and an average neck size of 4.8 nm. The mesoporous film was then coated with HfO_2 using 30 cycles of the tetrakis-(ethylmethylamino)hafnium (TEMAHf)/H_2O ALD process at 200 °C.[67]

After ALD coating, the film was characterized by using quantitative electron tomography. A 3D image of the HfO_2 coated mesopores was reconstructed from a series of 2D TEM images acquired at different tilt angles. **Figure 1.10**(a) shows a 3D volume rendering of the porous film. To examine the inner structure in more detail, slices were made through the 3D reconstruction (**Figure 1.10**(b)). Dark areas represent voids, light grey zones correspond to the HfO_2 coating and dark grey zones to the titania pore walls. The conformal deposition of an ultrathin

HfO_2 layer (2.2 ± 0.5 nm) was confirmed throughout the whole mesoporous film.

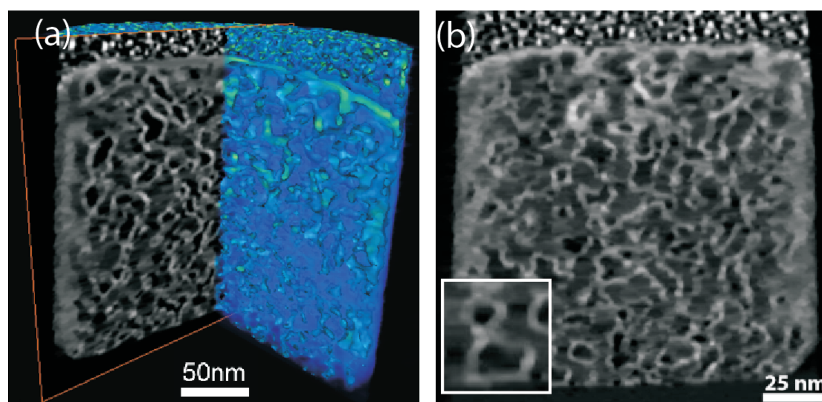

Figure 1.10. *Electron tomography reconstructions of a thin HfO_2 ALD layer deposited in a mesoporous titania film (initial porosity: 30 %, thickness: 120 nm). a) 3D volume rendering of the mesoporous material coated with HfO_2 (blue/green) and the cross section through the 3D reconstruction (grey). b) XZ-orthoslice through the 3D reconstruction with HfO_2 coating in light gray, titania matrix in dark gray and voids in black. The inset shows conformally coated ink-bottleshaped mesopores. (Adapted with permission from Ref[74]. Copyright 2012 American Chemical Society)*

A schematic representation of the conformal coating of ink-bottle mesopores by ALD is given in **Figure 1.11**(a-d). The pore walls are uniformly coated in a layer-by-layer fashion until the size of the neck becomes too small for the precursor molecules to enter the pores (**Figure 1.11**(b,c)). After that, coating proceeds only on top of the coated ink-bottle mesopores (**Figure 1.11**(d)). This was studied in detail using *in situ* synchrotron-based XRF measurements.[75] **Figure 1.11**(e) shows the Hf XRF intensity against the number of ALD cycles for deposition on the porous film as well as on a planar SiO_2 reference substrate. The XRF intensities were normalized to the incident beam intensity that was measured right before each XRF measurement. During the initial ALD cycles (ca. 19), the XRF intensity increased faster in the mesoporous film than on the planar substrate, indicating the deposition of HfO_2 on the internal surface of the porous thin film. With progressing number of ALD cycles, the slope of the XRF curve for the mesoporous film became more similar to the slope obtained for ALD on the planar reference sample, which suggests that the pore necks became too narrow to enable diffusion of the TEMAHf precursor, and that ALD continued on top of the coated mesoporous film. This was confirmed by the x-ray reflectivity measurement, which revealed a growth rate of 0.12 nm per cycle for the TEMAHf/H_2O process on the planar substrate. Assuming a similar growth rate in the titania ink-bottle pores, 19 ALD cycles would result in a 2.3 nm thick coating, which in turn reduces the size of the ink-bottle neck to 0.3 nm, less than half of the estimated kinetic diameter of the TEMAHf molecule (ca. 0.7 nm).

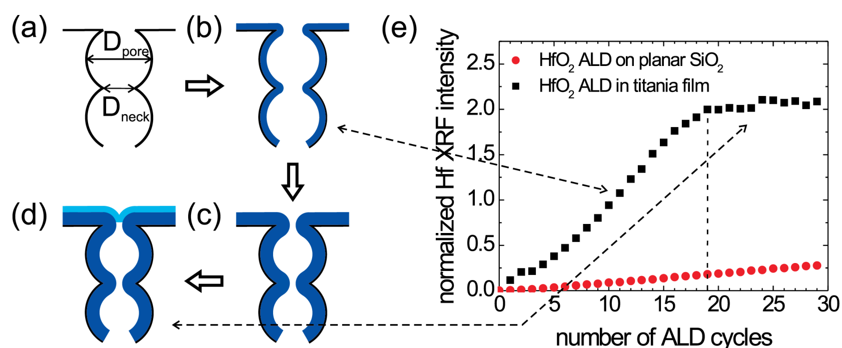

Figure 1.11. *(a - d) Schematic representation of conformal ALD in ink-bottle mesopores. (e) In situ XRF during HfO_2 ALD on a planar SiO_2 substrate and on a mesoporous titania film: Hf Lα (7.9 keV) peak area against the number of ALD cycles. (Reproduced with permission from Ref[74]. Copyright 2012 American Chemical Society)*

Protective coating: Another important application of ALD in catalysis is the protective coating. For example, a thin Al_2O_3 ALD overcoat was reported to protect Pd catalysts from coking and/or sintering in high-temperature reactions.[62] Feng *et al.* showed the effectiveness of a sub-nanometer thick Al_2O_3 over-layer to prevent sintering of supported Pd nanoparticles up to 500 °C.[63] The protective layer was found to preferentially nucleate at corners, steps and edges of the Pd nanoparticles, while keeping the more active Pd(111) facets accessible for methanol conversion. Lu *et al.* found that a thick Al_2O_3 ALD overcoat (∼8 nm) on Pd nanoparticles can increase the resistance toward coke formation in the oxidative dehydrogenation of ethane.[62] They proposed that the ALD generated layers preferentially coat the defect sites of Pd NPs, which are believed to be active for coke formation. O'Neill *et al.* also found that the overcoating of Cu with Al_2O_3 by ALD can suppress the deactivation of Cu caused by sintering and leaching of the metal under trickle bed conditions.[64] Recently, Baktash *et al.* reported 5 cycles of Al_2O_3 ALD overcoat on a Ni based catalyst strongly inhibited the sintering and enhanced its catalytic activity compared to an uncoated catalyst at elevated temperatures (700 - 800 °C).[65] Zhang *et al.* compared the effect of ALD deposited Al_2O_3 and TiO_2 overcoat on copper chromite catalysts for selective hydrogenation of furfural and found that the TiO_2 overcoats substantially increased the stability without affecting the activity towards hydrogenation. On the other hand the Al_2O_3 overcoat reduced the activity while increasing the stability of the catalyst.[66] Recently, Lee *et al.* found that a thin ALD TiO_2 coating successfully stabilizes cobalt particles supported on TiO_2 for aqueous-phase hydrogenation (APH) reactions by preventing leaching and sintering of cobalt.[76]

1.2.2.2 Metal ALD for Catalysis

In heterogeneous catalysis, metal nanoparticles have been used for over a century.[77] Industrial catalysts containing about 1 nm sized Pt-particles on chlorinated alumina were introduced in the 1960s.[78] The control over the nanoparticle size and shape is of fundamental importance for catalysis, where ALD has already shown its immense potential.[11;79–81] Unlike the continuous film growth of metal oxide ALD, metal ALD often forms islands of metal during the initial cycles. For example, **Figure 1.12** shows the SEM image of Pt islands formed using the ($MeCpPtMe_3$)/O_3 process on silicon. This peculiar growth behaviour has been exploited by several research groups for the fabrication of different catalytic nanoparticles containing a single metal (monometallic) or two different metals (bimetallic). **Table 1.2** and **Table 1.3** summarizes a selection of papers illustrating the variety of ALD processes that have been explored for the synthesis on mono- and bimetallic nanoparticles, respectively, while in the coming paragraphs, an example is demonstrated for the ALD based synthesis of both mono- and bimetallic nanoparticles.

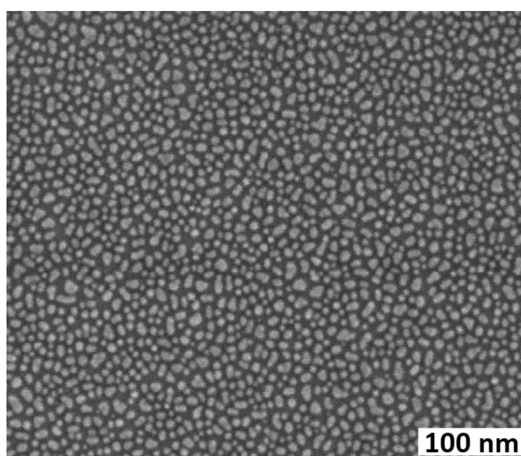

Figure 1.12. *SEM image of nanoparticles formed on a flat silicon substrate using the ($MeCpPtMe_3$)/O_3 process.*

Monometallic nanoparticles by ALD: Recently, in collaboration with the Department of Inorganic and Physical Chemistry (COMOC) of Ghent University, we demonstrated the synthesis of monometallic Pt nanoparticles within MIL-101-Cr, a MOF with inner pore diameters of approximately 25-35 Å and with a thermal stability up to 300 °C, by using $MeCpPtMe_3$ and O_3 at 150 °C.[82–84] The obtained Pt@MIL-101 materials were characterized by means of N_2 adsorption and XRD measurements showing that the framework of the MIL-101-Cr host material was well preserved during the ALD deposition. TEM analysis (**Figure 1.13**(a)) con-

firmed the deposition of highly dispersed Pt nanoparticles with sizes determined by the MIL-101-Cr pore sizes. The Pt@MIL-101 material was examined as catalyst in the hydrogenation of different linear and cyclic olefins at room temperature showing full conversion for each substrate (up to 100 %, **Figure 1.13**(c)). Moreover, under solvent free conditions, full conversion of the substrate was observed with no change in the selectivity.

Metal	ALD process (Precursor/reactant)	Support	Catalytic application	References
Pt	$(MeCpPtMe_3)/O_2$	Carbon aerogel(CA)	Oxidation of CO	ref [23]
		Carbon nanotubes (CNT), CNT/graphene hybrid	In fuel cell	ref [85;86]
		Graphene, Nitrogen-doped graphene	Methanol oxidation, Fuel cell	ref [87;88]
	$(MeCpPtMe_3)/O_3$	Metal organic framework (MIL101)	Hydrogenation of hydrocarbons	ref [83]
	$(MeCpPtMe_3)/O_2$ or H_2	Alumina	Oxidative dehydrogenation of propane	ref [89]
Pd	$Pd(hfac)_2$/Formalin	Porous alumina	Hydrogen sensor, Methanol decomposition	ref [90;91]
		TiO_2 nanotubes	Electrooxidation of ethanol	ref [92]
		Porous carbon, Activated carbon	Lithium-O_2 battery, Hydrogenation of nitrobenzene	ref [93;94]
	$Pd(thd)_2/O_2$	Porous carbon	Alcohol oxidation	ref [95]
Cu	$Cu(thd)_2$/Air/H_2	Silica	Water-gas shift reaction	ref [96–98]
Ni	$NiCp_2/H_2$	Porous silica gel/silica naoparticles	Chemoselective reduction of nitroarenes	ref [99]
		Alumina	Hydrogenolysis and hydrogenation reactions	ref [100;101]

Table 1.2. *Supported monometallic nanoparticles by ALD.*

Bimetallic nanoparticles by ALD: For the successful deposition of a bimetallic material the second metal should selectively grow on the first metal but not on the support, which can be obtained in different ways such as tuning the reaction conditions or manipulating the surface of the support. For example, Weber *et al.* demonstrated the successful deposition of Pd/Pt core/shell nanoparticles by reducing the partial pressure of O_2 during Pt ALD.[59;60] For ALD of Pd, the plasma-assisted process employing $Pd(hfac)_2$ and H_2 plasma at a substrate temperature of 100 °C was used,[102] and as expected, it starts with a nucleation delay of 100 cycles (**Figure 1.14**(a)). The Pt ALD was performed using $MeCpPtMe_3$ and O_2 gas at 300 °C.[103]

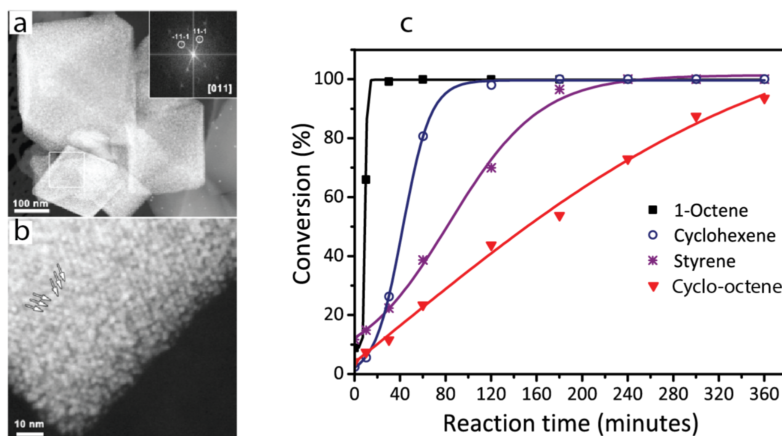

Figure 1.13. *a) Overview ADF-STEM image of MIL-101 crystals heavily loaded with Pt nanoparticles by 120 ALD cycles. The inset Fourier transform pattern of the region indicated by the white rectangle evidences that the MIL-101 material remains crystalline, even after heavy Pt loading, and is imaged along the [011] zone axis orientation. b) HR ADF-STEM image of a heavily Pt-loaded MIL-101 particle. The ordering of the Pt nanoparticles follows the pore structure of MIL-101. c) Conversion patterns using Pt@MIL-101-Cr-120 cycles as a catalyst and 1-octene (black), cyclohexene (blue), styrene (purple) or cyclooctene (red) as the substrate. Reaction conditions: 25 mmol of substrate, 0.05 mmol of catalyst, RT, 6 bar of* H_2.

A low oxygen partial pressure of approximately 1 Pa was used for the selective growth of Pt on Pd with no growth on Al_2O_3 [104] as shown in the **Figure 1.14**(b). **Figure 1.14**(c) schematically illustrates the concept of the two-step ALD process to deposit the Pd/Pt core/shell system. To deposit Pd nanoparticles 200 ALD cycles were employed, onto which 50 ALD cycles of Pt were applied to selectively cover the Pd cores. The synthesized Pd/Pt nanoparticles were characterized using probe corrected STEM-HAADF imaging. As shown in **Figure 1.14**(d), the contrast between the Pd core and the Pt shell is well recognizable, proving the selective growth of Pt on the Pd core. The STEM-HAADF images also revealed an average shell thickness of approximately 0.8 nm for particles with a total diameter of approximately 5 nm. An energy-dispersive x-ray spectroscopy (EDX) mapping of such an ensemble of Pd/Pt core/shell structured NPs is shown in **Figure 1.14**(e), which reveals that Pd (in green) is confined to the center of the NPs, while Pt (in red) is best visible at the NPs' edge. Furthermore, the authors succeeded in precisely nanotailoring the dimensions of the core and shell separately.[60]

Bimetal	ALD process (Precursor/reactant)	Support	Catalytic application	References
Pd/Pt core/shell	$Pd(hfac)_2/H_2$plasma+ $(MeCpPtMe_3)/O_2$	Alumina		ref [59;60]
	$Pd(hfac)_2$/Formalin + $(MeCpPtMe_3)/O_2$	Silicon with native oxide modified by self-assembled monolayers		ref [105]
	$Pd(hfac)_2/H_2$ + $(MeCpPtMe_3)/O_2$	Alumina, Titania, Zirconia		ref [61]
Pd/Pt alloy	$MeCpPtMe_3/O_2/H_2$ + $Pd(hfac)_2/H_2/O_2$	Alumina, Titania, Zirconia		ref [61]
Ru/Pt core/shell	$Ru(EtCp)_2/O_2/H_2$ + $MeCpPtMe_3/O_2$	Alumina, Titania, Zirconia		ref [61]
Ru/Pt alloy	$Ru(EtCp)_2/O_2/H_2$ + $MeCpPtMe_3/O_2/H_2$	Alumina, Titania, Zirconia		ref [61]
Ru/Pd core/shell	$Ru(EtCp)_2/O_2/H_2$ + $Pd(hfac)_2/H_2$	Alumina, Titania, Zirconia		ref [61]
Ru/Pd alloy	$Ru(EtCp)_2/O_2/H_2$ + $Pd(hfac)_2/H_2$	Alumina, Titania, Zirconia		ref [61]
Ru/Pt alloy	$Ru(EtCp)_2/O_2$ + $MeCpPtMe_3/O_2$	N-doped CNTs, Spherical alumina nanoparticles, Silicon	Direct methanol fuel cell, CO and Methanol oxidation, Methanol decomposition	ref [106–109]
Ir/Pt alloy	$Ir(acac)_3/O_2$ + $MeCpPtMe_3/O_2$	Silicon, Fused quartz, Glass, Porous anaodized alumina	Electrochemical sensing	ref [16;110]
Au/Pd core/shell	$Pd(hfac)_2/H_2$ on Au particles	Silica	Oxidation of benzyl alcohol	ref [111]

Table 1.3. *Supported bimetallic nanoparticles by ALD.*

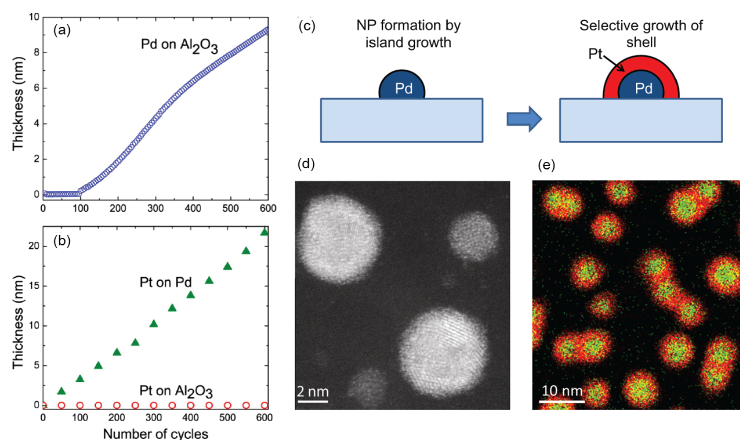

Figure 1.14. *a) Thickness evolution of Pd during ALD using Pd(hfac)$_2$ and a H_2 plasma at a pressure of 1 Pa on Al_2O_3 as obtained from in situ spectroscopic ellipsometry (SE). b) Thickness evolution of Pt during ALD from MeCpPtMe$_3$ and O_2 gas at a pressure of 1 Pa. The data were obtained from* in situ *SE. The Pt was deposited on Pd (green triangles) and Al_2O_3 (red circles) surfaces. The process allows for direct growth on Pd, whereas no growth could be observed on alumina even after 600 cycles. (Adapted with permission from Ref[59] Copyright 2012 American Chemical Society) c) Schematic illustration of the two-step ALD process to deposit core/shell NPs of Pd/Pt. d) HAADF-STEM image and e) EDX mapping of Pd/Pt core/shell NPs (150 cycles Pd; 50 cycles Pt) on an Al_2O_3-covered Si_3N_4 TEM window. (Adapted with permission from Ref[60] Copyright 2015 IOP Publishing Ltd).*

1.3 Goals and Outline of the Thesis

As it is clear from what has been discussed thus far, ALD has emerged as a powerful method for the design and synthesis of catalyst materials. Synthesis of BMNPs is one of the important methods among them, but as evident from the **Table 1.3**, this ALD based approach has to date only been applied for the synthesis of binary noble metal nanoparticles, which is a very limited subset in the class of bimetallic materials. The main goal of this thesis work is to develop a new ALD based methodology for the controlled synthesis of bimetallic alloys containing both noble and non-noble metals and thereby add a new possibility to the ALD based supported catalyst design (**Figure 1.15**), which is accompanied by the development of new ALD processes and some preliminary catalytic experiments.

In short, the goals of this work can be summarized as follows: (i) develop new ALD processes for metal (Pt) and metal oxides (Ga_2O_3, In_2O_3 and Fe_2O_3), which are relevant for catalysis. (ii) Synthesis of bimetallic nanoparticles containing both noble and non-noble metals by combining the respective ALD processes and (iii) study the feasibility of using the developed methods in designing supported metal catalysts. The thesis is article based and most of the results are presented by means of papers that have been published in or will be submitted to peer-reviewed jour-

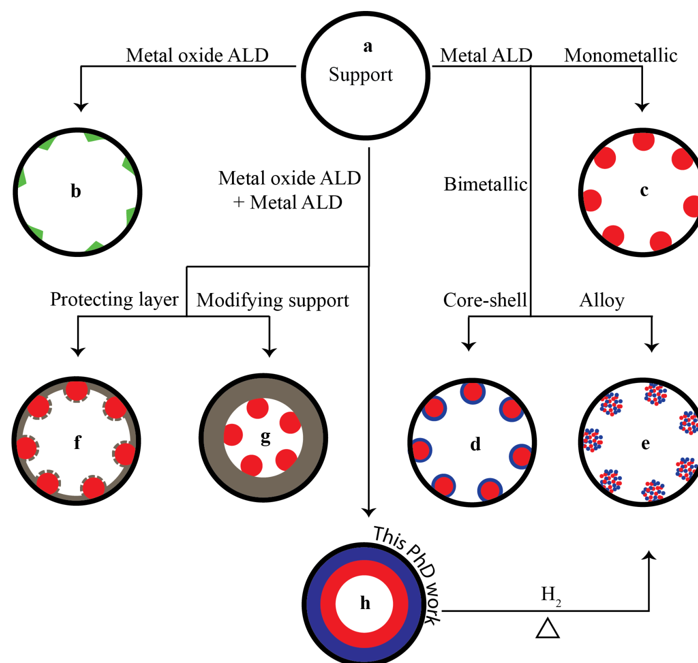

Figure 1.15. *Possibilities of ALD in supported catalyst design - one step forward: a) Porous support, b) Introducing catalytic sites on the pore walls, Introducing catalytic c) monometallic, d) bimetallic core-shell and e) bimetallic alloy nanoparticles of noble metals on the pore walls, f) Stabilizing catalytic nanoparticles with an ALD over-layer, g) Tuning pore size of the support prior to the introduction of catalytic nanoparticles, h) Synthesis of bimetallic alloy nanoparticles containing both noble and non-noble metals (**this work**).*

nals. Moreover, this introduction chapter itself is accepted and will be published as a chapter entitled "ALD for catalysis" in a book: "Nanotechnology in catalysis - Applications in the chemical industry, energy research, and environment protection" by WILEY-VCH publications.

Chapter 2 gives an overview of the experimental aspects related to this work. Chapters 3 focuses on the ALD of metals and metal oxides and their applications in heterogeneous catalysis. An overview of the existing ALD processes Pt and MO_x (M = Ga, In, Fe) are tabulated in the first section of the chapter, followed by a short overview of the newly developed ALD processes. Complete details of the newly developed processes can be found in papers I - IV. As one of the final goals of this thesis work is the deposition of bimetallic material by combining different ALD processes, ALD processes with wide temperature window were targeted. The second section of this chapter explains the importance of metal and metal oxides in catalysis and the role of ALD in preparing supported catalyst materials. The chapter concludes with two case studies where ALD is employed for the synthesis of supported catalysts.

Chapter 4 discusses the importance of bimetallic materials in catalysis and how different ALD processes can be combined to deposit these materials. The chapter starts with a short introduction to bimetallic nanoparticle and their relevance for catalysis. Section 4.2 discusses the synthesis of bimetallic nanoparticles by ALD and the need for a new ALD based synthesis strategy. The chapter ends with a brief discussion on the novel ALD based approach for the synthesis of bimetallic nanoparticles containing both noble and non-noble metals, which were developed during this thesis work. A detailed description of this method and its application towards catalysis is given in paper V and VI.

The conclusions of this thesis and suggestions for future work are presented in the last chapter, Chapter 5.

References

[1] T. Suntola and J. Antson, *U.S. Patent No. 4,058,430* (1977).

[2] M. Ahonen, M. Pessa, and T. Suntola, *Thin Solid Films* **65**(3), 301–307 (1980).

[3] V. Miikkulainen, M. Leskelä, M. Ritala, and R. L. Puurunen, *Journal of Applied Physics* **113**(2), 021301 jan (2013).

[4] R. L. Puurunen, *Journal of Applied Physics* **97**(12), 121301 (2005).

[5] S. M. George, *Chemical reviews* **110**(1), 111–131 (2010).

[6] M. Lindblad, L. Peter, and T. Suntola, *Catalysis Letters* **27**, 323–336 (1994).

[7] A. Kytokivi, J.-P. Jacobs, A. Hakuli, J. Merilainen, and H. H. Brongersma, *Journal of Catalysis* **162**(2), 190–197 (1996).

[8] L. B. Backman, A. Rautiainen, A. O. I. Krause, and M. Lindblad, *Catalysis Today* **43**(12), 11–19 (1998).

[9] S. Haukka, E.-L. Lakomaa, and T. Suntola, *Studies in Surface Science and Catalysis* **120**, 715–750 (1998).

[10] B. J. O'neill, D. H. K. Jackson, J. Lee, C. Canlas, P. C. Stair, C. L. Marshall, J. W. Elam, T. F. Kuech, J. A. Dumesic, and G. W. Huber, *ACS Catalysis* **5**, 1804–1825 (2015).

[11] J. Dendooven, *Atomically-Precise Methods for Synthesis of Solid Catalysts*, RSC Catalysis Series. Royal Society of Chemistry, Cambridge, (2015).

[12] A. B. F. Martinson, J. W. Elam, and M. J. Pellin, *Applied Physics Letters* **94**(12), 123107 (2009).

[13] B. Hoex, J. Schmidt, P. Pohl, M. C. M. van de Sanden, and W. M. M. Kessels, *Journal of Applied Physics* **104**(4), 044903 (2008).

[14] J. A. van Delft, D. Garcia-Alonso, and W. M. M. Kessels, *Semiconductor Science and Technology* **27**(7), 074002 (2012).

[15] Y. Wang, S. Park, J. T. W. Yeow, A. Langner, and F. Muller, *Sensors and Actuators, B: Chemical* **149**(1), 136–142 (2010).

[16] D. J. Comstock, S. T. Christensen, J. W. Elam, M. J. Pellin, and M. C. Hersam, *Advanced Functional Materials* **20**(18), 3099–3105 (2010).

[17] T. Yoshimura, S. Tatsuura, and W. Sotoyama, *Applied Physics Letters* **59**(4), 482–484 (1991).

[18] S. M. George, B. Yoon, and A. a. Dameron, *Accounts of chemical research* **42**(4), 498–508 (2009).

[19] H. Zhou and S. F. Bent, *Journal of Vacuum Science & Technology A* **31**(4), 18 (2013).

[20] P. Sundberg and M. Karppinen, *Beilstein Journal of Nanotechnology* **5**(1), 1104–1136 (2014).

[21] O. Nilsen, K. Klepper, H. Nielsen, and H. Fjellvag, *ECS Transactions* **16**(4), 3–14 (2008).

[22] D. Y. DeSario and F. J. DiSalvo, *Chemistry of Materials* **26**(8), 2750–2757 (2014).

[23] J. S. King, A. Wittstock, J. Biener, S. O. Kucheyev, Y. M. Wang, T. F. Baumann, S. K. Giri, A. V. Hamza, M. Baeumer, and S. F. Bent, *Nano*

Letters **8**(8), 2405–2409 (2008).

[24] C. C. Chao, C.-M. Hsu, Y. Cui, and F. B. Prinz, *ACS Nano* **5**(7), 5692–5696 (2011).

[25] N. Cheng, Y. Shao, J. Liu, and X. Sun, *Nano Energy* **29**, 220–242 (2016).

[26] I. D. Scott, Y. S. Jung, A. S. Cavanagh, Y. Yan, A. C. Dillon, S. M. George, and S. H. Lee, *Nano Letters* **11**(2), 414–418 (2011).

[27] H. C. M. Knoops, M. E. Donders, M. C. M. van de Sanden, P. H. L. Notten, and W. M. M. Kessels, *Journal of Vacuum Science & Technology A* **30**(1), 010801 (2012).

[28] L. Wen, M. Zhou, C. Wang, Y. Mi, and Y. Lei, *Advanced Energy Materials* **6**(23), 1600468 (2016).

[29] C. Guan and J. Wang, *Advanced Science* **3**(10), 1500405 (2016).

[30] M. N. Mullings, C. Hagglund, and S. F. Bent, *Journal of Vacuum Science & Technology A: Vacuum, Surfaces, and Films* **31**(6), 061503 (2013).

[31] J. W. Elam, D. A. Baker, A. J. Hryn, A. B. F. Martinson, M. J. Pellin, and J. T. Hupp, *Journal of Vacuum Science & Technology A: Vacuum, Surfaces, and Films* **26**(2008), 244 (2008).

[32] M. Ritala, M. Leskelä, J. Dekker, C. Mutsaers, P. J. Soininen, and J. Skarp, *Chemical Vapor Deposition* **5**(1), 7–9 (1999).

[33] S. Pulinthanathu Sree, J. Dendooven, J. Jammaer, K. Masschaele, D. Deduytsche, J. D'Haen, C. E. A. Kirschhock, J. A. Martens, and C. Detavernier, *Chemistry of Materials* **24**(14), 2775–2780 (2012).

[34] G. Fang, L. Xu, Y. Cao, and A. Li, *Coordination Chemistry Reviews* **322**, 94–103 (2016).

[35] R. J. Crutchley, *Coordination Chemistry Reviews* **257**(23-24), 3153 (2013).

[36] A. Devi, *Coordination Chemistry Reviews* **257**(23-24), 3332–3384 (2013).

[37] T. Hatanpaa, M. Ritala, and M. Leskela, *Coordination Chemistry Reviews* **257**(23-24), 3297–3322 (2013).

[38] C. H. Bartholomew and R. J. Farrauto, *Fundamentals of Industrial Catalytic Processes*, Electrical Engineering Handbook. (2006).

[39] F. Pinna, *Catalysis Today* **41**, 129–137 (1998).

[40] P. Munnik, P. de Jongh, and K. de Jong, *Chemical Reviews* **115**, 6687–6718 (2015).

[41] C. H. Bartholomew, *Applied Catalysis A: General* **212**, 17–60 (2001).

[42] C. T. Campbell, *Science* **298**(5594), 811–814 (2002).

[43] J. Barbier, *Applied Catalysis* **23**(2), 225–243 (1986).

[44] J. A. Moulijn, A. E. Van Diepen, and F. Kapteijn, *Applied Catalysis A: General* **212**, 3–16 (2001).

[45] E. E. Wolf and F. Alfani, *Catalysis Reviews: Science and Engineering* **24**(3), 329–371 (1982).

[46] P. Biloen, J. N. Helle, H. Verbeek, F. M. Dautzenberg, and W. M. H. Sachtler, *Journal of Catalysis* **63**(1), 112–118 (1980).

[47] D. Trimm, *Catalysis Today* **49**, 3–10 (1999).

[48] J. R. Rostrup-Nielsen and I. Alstrup, *Catalysis Today* **53**, 311–316 (1999).

[49] P. M. Arnal, M. Comotti, and F. Schüth, *Angewandte Chemie - International*

Edition **45**(48), 8224–8227 (2006).

[50] K. Yu, Z. Wu, Q. Zhao, B. Li, and Y. Xie, *Journal of Physical Chemistry C* **112**(7), 2244–2247 (2008).

[51] M. Seipenbusch and A. Binder, *Journal of Physical Chemistry C* **113**(48), 20606–20610 (2009).

[52] S. H. Joo, J. Y. Park, C.-K. Tsung, Y. Yamada, P. Yang, and G. A. Somorjai, *Nat. Mater.* **8**(2), 126–31 (2009).

[53] S. Haukka, E.-L. Lakomaa, and T. Suntola, *Thin Solid Films* **225**, 280–283 (1993).

[54] L. B. Backman, A. Rautiainen, M. Lindblad, and A. O. I. Krause, *Applied Catalysis A: General* **191**, 55–68 (2000).

[55] L. B. Backman, A. Rautiainen, M. Lindblad, O. Jylhä, and A. Krause, *Applied Catalysis A: General* **208**, 223–234 (2001).

[56] H. Feng, J. W. Elam, J. A. Libera, M. J. Pellin, and P. C. Stair, *Journal of Catalysis* **269**(2), 421–431 (2010).

[57] S. P. Sree, J. Dendooven, T. I. Korányi, G. Vanbutsele, K. Houthoofd, D. Deduytsche, C. Detavernier, and J. A. Martens, *Catalysis Science & Technology* **1**(2), 218 – 221 (2011).

[58] E. Verheyen, S. Pulinthanathu Sree, K. Thomas, J. Dendooven, M. De Prins, G. Vanbutsele, E. Breynaert, J. P. Gilson, C. E. Kirschhock, C. Detavernier, and J. A. Martens, *Chemical Communications* **50**(35), 4610–4612 (2014).

[59] M. J. Weber, A. J. M. MacKus, M. A. Verheijen, C. Van Der Marel, and W. M. M. Kessels, *Chemistry of Materials* **24**(15), 2973–2977 (2012).

[60] M. J. Weber, M. A. Verheijen, A. A. Bol, and W. M. M. Kessels, *Nanotechnology* **26**(9), 094002 (2015).

[61] J. Lu, K.-B. Low, Y. Lei, J. A. Libera, A. Nicholls, P. C. Stair, and J. W. Elam, *Nature communications* **5**, 3264 (2014).

[62] J. Lu, B. Fu, M. C. Kung, G. Xiao, J. W. Elam, H. H. Kung, and P. C. Stair, *Science* **335**, 1205–1209 (2012).

[63] H. Feng, J. Lu, P. C. Stair, and J. W. Elam, *Catalysis Letters* **141**(4), 512–517 (2011).

[64] B. J. O'Neill, D. H. K. Jackson, A. J. Crisci, C. A. Farberow, F. Shi, A. C. Alba-Rubio, J. Lu, P. J. Dietrich, X. Gu, C. L. Marshall, P. C. Stair, J. W. Elam, J. T. Miller, F. H. Ribeiro, P. M. Voyles, J. Greeley, M. Mavrikakis, S. L. Scott, T. F. Kuech, and J. A. Dumesic, *Angewandte Chemie - International Edition* **52**(51), 13808–13812 (2013).

[65] E. Baktash, P. Littlewood, R. Schomäcker, A. Thomas, and P. C. Stair, *Applied Catalysis B: Environmental* **179**, 122–127 (2015).

[66] H. Zhang, C. Canlas, A. Jeremy Kropf, J. W. Elam, J. A. Dumesic, and C. L. Marshall, *Journal of Catalysis* **326**, 172–181 (2015).

[67] B. K. Kukli, M. Ritala, T. Sajavaara, J. Keinonen, and M. Leskelä, *Chemical Society reviews* (5), 199–204 (2002).

[68] J. Dendooven, K. Devloo-Casier, M. Ide, K. Grandfield, M. Kurttepeli, K. F. Ludwig, S. Bals, P. Van Der Voort, and C. Detavernier, *Nanoscale* **6**(24), 14991–14998 (2014).

[69] E. Verheyen, L. Joos, K. Van Havenbergh, E. Breynaert, N. Kasian, E. Gobechiya, K. Houthoofd, C. Martineau, M. Hinterstein, F. Taulelle, V. Van Speybroeck, M. Waroquier, S. Bals, G. Van Tendeloo, C. E. A. Kirschhock, and J. A. Martens, *Nature Materials* **11**, 1059–1064 (2012).

[70] S. Deng, S. W. Verbruggen, Z. He, D. J. Cott, P. M. Vereecken, J. A. Martens, S. Bals, S. Lenaerts, and C. Detavernier, *RSC Advances* **4**, 11648 (2014).

[71] S. Deng, M. Kurttepeli, D. J. Cott, S. Bals, and C. Detavernier, *J. Mater. Chem. A* **3**, 2642–2649 (2015).

[72] M. Kurttepeli, S. Deng, S. W. Verbruggen, G. Guzzinati, D. J. Cott, S. Lenaerts, J. Verbeeck, G. Van Tendeloo, C. Detavernier, and S. Bals, *The Journal of Physical Chemistry C* **118**(36), 21031–21037 (2014).

[73] T. M. Suzuki, M. Yamamoto, K. Fukumoto, Y. Akimoto, and K. Yano, *Journal of Catalysis* **251**(2), 249–257 (2007).

[74] J. Dendooven, B. Goris, K. Devloo-Casier, E. Levrau, E. Biermans, M. R. Baklanov, K. F. Ludwig, P. V. D. Voort, S. Bals, and C. Detavernier, *Chemistry of Materials* **24**(11), 1992–1994 (2012).

[75] C. Detavernier, J. Dendooven, S. P. Sree, K. F. Ludwig, and J. A. Martens, *Chemical Society reviews* **40**(11), 5242–5253 (2011).

[76] J. Lee, D. Jackson, T. Li, R. E. Winans, J. Dumesic, T. Kuech, and G. Huber, *Energy & Environmental Science* **7**(5), 1657–1660 (2014).

[77] A. T. Bell, *Science* **299**, 1688–91 (2003).

[78] B. V. Haensel and H. S. Bloch, *Platinum Metals Rev.* **8**(1), 2–8 (1964).

[79] J. Lu, J. W. Elam, and P. C. Stair, *Surface Science Reports* **71**(2), 410–472 (2016).

[80] A. J. M. Mackus, M. J. Weber, N. F. W. Thissen, D. Garcia-Alonso, R. H. J. Vervuurt, S. Assali, A. A. Bol, M. A. Verheijen, and W. M. M. Kessels, *Nanotechnology* **27**(3), 034001 (2016).

[81] A. J. M. Mackus, M. J. Weber, N. F. W. Thissen, D. Garcia-Alonso, R. H. J. Vervuurt, S. Assali, A. A. Bol, M. A. Verheijen, and W. M. M. Kessels, *Nanotechnology* **27**(3), 034001 (2016).

[82] J. Dendooven, R. K. Ramachandran, K. Devloo-Casier, G. Rampelberg, M. Filez, H. Poelman, G. B. Marin, E. Fonda, and C. Detavernier, *Journal of Physical Chemistry C* **117**(40), 20557–20561 (2013).

[83] K. Leus, J. Dendooven, N. Tahir, R. Ramachandran, M. Meledina, S. Turner, G. Van Tendeloo, J. Goeman, J. Van der Eycken, C. Detavernier, and P. Van Der Voort, *Nanomaterials* **6**, 45 (2016).

[84] M. Meledina, S. Turner, M. Filippousi, K. Leus, I. Lobato, J. D. Ranjith K. Ramachandran, C. Detavernier, and G. V. T. Pascal Van Der Voort, *Particle and particle system characterization* (2016).

[85] C. Liu, C.-C. Wang, C.-C. Kei, Y.-C. Hsueh, and T.-P. Perng, *Small* **5**(13), 1535–1538 (2009).

[86] C.-T. Hsieh, Y.-Y. Liu, D.-Y. Tzou, and W.-Y. Chen, *The Journal of Physical Chemistry C* **116**(51), 26735–26743 (2012).

[87] S. Sun, G. Zhang, N. Gauquelin, N. Chen, J. Zhou, S. Yang, W. Chen, X.

Meng, D. Geng, M. N. Banis, R. Li, S. Ye, S. Knights, G. A. Botton, T.-K. Sham, and X. Sun, *Scientific reports* **3**, 1775 (2013).
[88] S. Stambula, N. Gauquelin, M. Bugnet, S. Gorantla, S. Turner, S. Sun, J. Liu, G. Zhang, X. Sun, and G. A. Botton, *Journal of Physical Chemistry C* **118**(8), 3890–3900 (2014).
[89] T. D. Gould, A. M. Lubers, A. R. Corpuz, A. W. Weimer, J. L. Falconer, and J. W. Medlin, *ACS Catalysis* **5**(2), 1344–1352 (2015).
[90] J. W. Elam, A. Zinovev, C. Y. Han, H. H. Wang, U. Welp, J. N. Hryn, and M. J. Pellin, *Thin Solid Films* **515**(4), 1664–1673 (2006).
[91] H. Feng, J. A. Libera, P. C. Stair, J. T. Miller, and J. W. Elam, *ACS Catalysis* **1**(6), 665–673 (2011).
[92] L. Assaud, N. Brazeau, M. K. S. Barr, M. Hanbücken, S. Ntais, E. A. Baranova, and L. Santinacci, *ACS Applied Materials & Interfaces* **7**(44), 24533–24542 (2015).
[93] Y. Lei, J. Lu, X. Luo, T. Wu, P. Du, X. Zhang, Y. Ren, J. Wen, D. J. Miller, J. T. Miller, Y. K. Sun, J. W. Elam, and K. Amine, *Nano Letters* **13**(9), 4182–4189 (2013).
[94] T. Gong, L. Qin, W. Zhang, H. Wan, J. Lu, and H. Feng, *Journal of Physical Chemistry C* **119**(21), 11544–11556 (2015).
[95] E. Rikkinen, A. Santasalo-aarnio, S. Airaksinen, M. Borghei, V. Viitanen, J. Sainio, E. I. Kauppinen, T. Kallio, and a. O. I. Krause, *Journal of Physical Chemistry* **115**, 23067–23073 (2011).
[96] C.-S. Chen, J.-H. Lin, T.-W. Lai, and B.-H. Li, *Journal of Catalysis* **263**(1), 155–166 (2009).
[97] C.-S. Chen, J.-H. Lin, and T.-W. Lai, *Chemical Communications* (40), 4983 (2008).
[98] C. S. Chen, J. H. Lin, J. H. You, and C. R. Chen, *Journal of the American Chemical Society* **128**(50), 15950–15951 (2006).
[99] C. Jiang, Z. Shang, and X. Liang, *ACS Catalysis* **5**(8), 4814–4818 (2015).
[100] T. D. Gould, A. M. Lubers, B. T. Neltner, J. V. Carrier, A. W. Weimer, J. L. Falconer, and J. Will Medlin, *Journal of Catalysis* **303**, 9–15 (2013).
[101] Z. Gao, M. Dong, G. Wang, P. Sheng, Z. Wu, H. Yang, B. Zhang, G. Wang, J. Wang, and Y. Qin, *Angewandte Chemie - International Edition* **54**(31), 9006–9010 (2015).
[102] G. A. T. Eyck, J. J. Senkevich, F. Tang, D. Liu, S. Pimanpang, T. Karaback, G. C. Wang, T. M. Lu, C. Jezewski, and W. A. Lanford, *Chemical Vapor Deposition* **11**(1), 60–66 (2005).
[103] T. Aaltonen, M. Ritala, T. Sajavaara, J. Keinonen, and M. Leskela, *Chemistry of Materials* **15**(17), 1924–1928 (2003).
[104] A. J. M. Mackus, S. A. F. Dielissen, J. J. L. Mulders, and W. M. M. Kessels, *Nanoscale* **4**(15), 4477 (2012).
[105] K. Cao, Q. Zhu, B. Shan, and R. Chen, *Scientific Reports* **5**, 8470 (2015).
[106] S. T. Christensen, H. Feng, J. L. Libera, N. Guo, J. T. Miller, P. C. Stair, and J. W. Elam, *Nano Letters* **10**(8), 3047–3051 (2010).
[107] A.-C. Johansson, R. Yang, K. Haugshøj, J. Larsen, L. Christensen, and E.

Thomsen, *International Journal of Hydrogen Energy* **38**(26), 11406–11414 (2013).

[108] A. C. Johansson, J. V. Larsen, M. A. Verheijen, K. B. Haugshøj, H. F. Clausen, W. M. M. Kessels, L. H. Christensen, and E. V. Thomsen, *Journal of Catalysis* **311**, 481–486 (2014).

[109] X. Jiang, T. M. Gür, F. B. Prinz, and S. F. Bent, *Chemistry of Materials* **22**(10), 3024–3032 (2010).

[110] S. T. Christensen and J. W. Elam, *Chemistry of Materials* **22**(8), 2517–2525 (2010).

[111] H. Wang, C. Wang, H. Yan, H. Yi, and J. Lu, *Journal of Catalysis* **324**, 59–68 (2015).

2
Experimental

This chapter discusses the experimental methods used in this work. Section 2.1 describes the details of the ALD depositions, whereas section 2.2 gives a brief overview of the main characterization techniques applied to examine the deposited ALD coatings.

2.1 Thin film deposition by ALD

2.1.1 Substrates for ALD

Most of the depositions were performed on a Si substrates covered with 100 nm SiO_2 (SiO_2/Si). Prior to ALD, the substrates are cleaned with O_2 plasma exposure inside the ALD chamber. High surface area substrates like nanoporous thin films and powders were also used as per the requirement, for which synthesis procedures are discussed in the respective chapters and the references therein. Prior to ALD, the nanoporous materials are allowed to outgas inside the ALD chamber by keeping them in vacuum at elevated temperature for 1 - 2 hours.

2.1.2 ALD Precursors and reactants

The materials grown during this work include Pt, Fe_2O_3, In_2O_3, Ga_2O_3 and SnO_2. Out of these, the former four were deposited by using new ALD processes developed as a part of this thesis. Pt and Fe_2O_3 were grown using cyclopentadienyl based precursors. For Pt, the well-known (methylcyclopentadienyl)trimethylplatinum [(MeCp)$PtMe_3$] precursor was used together with ozone as reactant. Fe_2O_3 was deposited using tert-butylferrocene [(t-BuCp)FeCp;

TBF] and O_2 plasma. Beta-diketonate precursors, tris(2,2,6,6-tetramethyl-3,5-heptanedionato)indium(III), [In(TMHD)$_3$] and tris(2,2,6,6-tetramethyl-3,5-heptanedionato)gallium (III), [Ga(TMHD)$_3$], were used for depositing indium and gallium oxides, respectively, together with O_2 plasma as reactant. Further details of these ALD processes are presented as papers in Chapter 3. SnO_2 was deposited by using an existing ALD process that uses an amino based precursor, tetrakis(dimethylamino)tin [Sn(N(CH$_3$)$_2$)$_4$; TDMASn] and water as reactant.[1]

2.1.3 ALD Setup

All the depositions in this work were carried out in a home-built ALD setup in the lab in Ghent[2;3] (**Figure 2.1**). The ALD chamber is connected through a gate valve to a turbo pump backed up by a rotary pump and is continuously evacuated to a base pressure in the range 10^{-7} - 10^{-6} mbar. A second gate valve was installed for pre-evacuation of the chamber via a bypass line to the rotary pump. The gate valve between the chamber and the turbo pump can be closed to enable high pressure ($> 10^{-2}$ mbar) operation of the chamber (static exposure mode[4]). Computer controlled valves arrange for either rough pumping of the chamber by the rotary pump through the bypass-line or direct pumping through the gate valve using the turbo pump. The precursors, kept in a stainless steel container, are heated by means of heating wires to ensure evaporation. The delivery lines to the chamber are heated a few degrees above the container temperature to prevent condensation of the precursor. Argon was used as a carrier gas for the precursors. An inductively coupled radio frequency plasma source, in a remote plasma configuration, is used for the generation of plasma and the ozone is produced from a pure O_2 flow with an OzoneLabTM OL100 ozone generator, resulting in an O_3 concentration of ~ 175 μg/ml. Computer-controlled pneumatic valves are used to regulate the vapor flow into the chamber during ALD and the pressure of the precursor (reactant) entering to the chamber can be set by means of needle valves. Samples are placed onto a molybdenum sample holder and introduced into the ALD chamber *via* a loadlock. The loadlock can be pumped from atmospheric pressure to $\sim 10^{-3}$ mbar with a rotary vane pump, before opening the gate valve to the chamber to transfer the sample holder, which allows sample loading without a vacuum break. For ALD on powders, the loadlock is slowly pumped through a needle valve during loading and slowly vented during unloading to prevent loss of the powders caused by a sudden pressure difference. The sample holder is then placed onto a copper block and heated to the desired temperature using resistive heating elements. For real-time x-ray studies (*in situ* XRF) during Pt ALD and for other synchrotron based characterization techniques (XAS and GISAXS), a dedicated mobile ALD setup was used. For detailed information on this mobile ALD setup, the reader is referred to the recent article by Dendooven *et al.*[5]

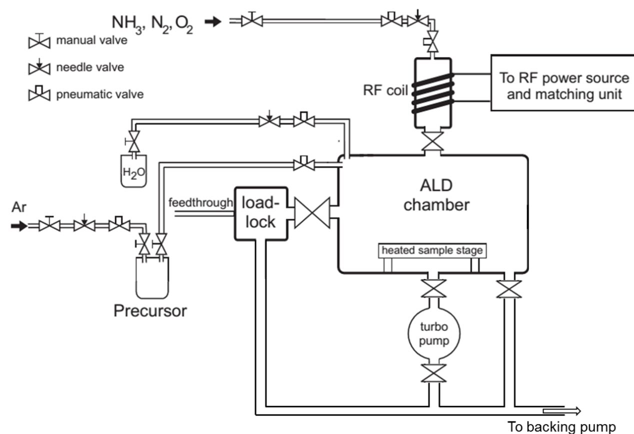

Figure 2.1. *Schematic drawing of the ALD reactor used during this research.*

2.2 Characterization methods

2.2.1 Spectroscopic Ellipsometry (SE)

Spectroscopic ellipsometry (SE) is based on the interaction of a polarized light beam with a surface. It can be used for studying the properties of thin films, including optical constants, thickness, *etc.* The technique of ellipsometry is based on the measurement of changes in the state of polarization of light upon reflection from a surface. For a clean reflecting surface the optical constants of the surface and the reflection coefficients of the system can be calculated from these changes. A thin transparent film on the reflecting surface causes additional changes in the reflected light. By proper modelling of the substrate and film, the thickness and refractive index of the film can be determined. The measurement equipment consists of a light source, a polarizer, a polarization analyzer and a detector (**Figure 2.2**). The SE measurements presented in this work were carried out using a Woollam M-2000U ellipsometer mounted directly on an ALD setup, which allowed the *in situ* monitoring of film thickness during the ALD process.

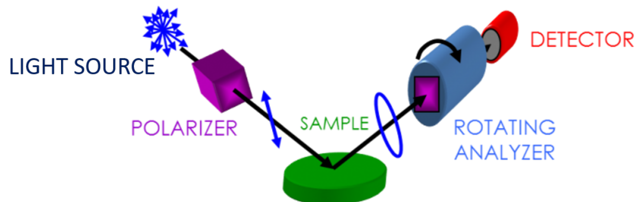

Figure 2.2. *Schematic representation of a basic ellipsometer system.*[6]

2.2.2 Mass Spectrometry (MS)

Mass spectrometry is a powerful analytical technique used to quantify known materials, to identify unknown molecules within a gaseous sample, and to elucidate the molecular structure and chemical properties. This technique basically studies the effect of ionizing energy on molecules. A mass spectrometer generates gas phase ions from the sample under investigation. This molecular ion undergoes fragmentation. Each primary product ion derived from the molecular ion, in turn, undergoes fragmentation, and so on. The ions are separated in the mass spectrometer according to their mass-to-charge ratio, and are detected in proportion to their abundance. A mass spectrum of the molecule is thus produced. It displays the result in the form of a plot of ion abundance versus mass-to-charge ratio, as shown in **Figure 2.3** for methane molecule. Ions provide information concerning the nature and the structure of their precursor molecule. In this work, a HPR-30/HAL 201 RC (Hiden Analytical) Quadrupole mass spectrometer (QMS), using a Faraday cup detector, was directly attached to the ALD chamber to analyse the reaction products formed, *in situ*, during an ALD process cycle.

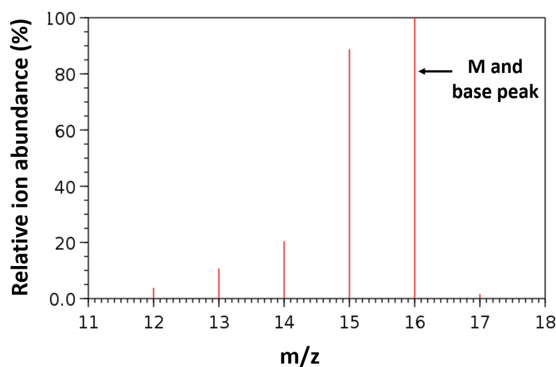

Figure 2.3. *Mass spectrum of methane.*[7]

2.2.3 Scanning Electron Microscopy (SEM) and Energy Dispersive X-ray Spectroscopy (EDX)

Scanning Electron Microscopy (SEM) is used to observe the morphology of a sample at higher magnification, higher resolution and depth of focus compared to an optical microscope. In this technique, an accelerated beam of mono-energetic electrons is focused onto the surface of the sample and it is scanned over a small area. Several signals are generated and appropriate ones are selected depending on the mode of its operation. This signal is amplified and made to form synchronous image on a cathode ray tube. **Figure 2.4** schematically shows the basic principles of SEM. The impinging electrons can also excite deep shells of substrate atoms.

The characteristic X-rays that are emitted can be detected by an EDX detector, enabling the identification of elements in a specific region of the sample. SEM/EDX measurements related to this work were carried out with a FEI Quanta 200F instrument. The high resolution SEM (HRSEM) images on the powder samples were obtained on a Nova NanoSEM450 (FEI) at COK (KU Leuven).

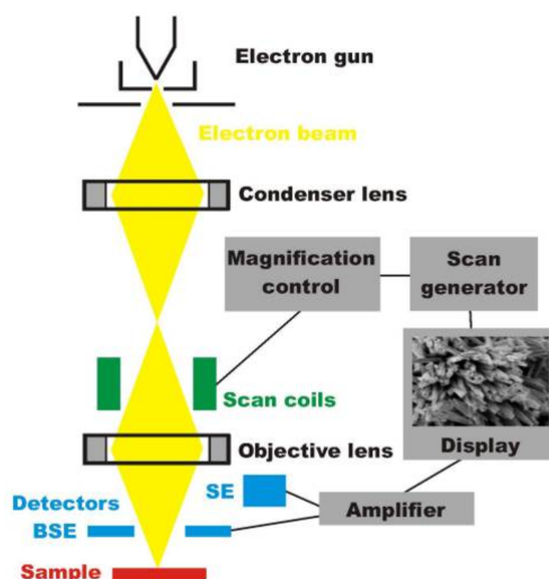

Figure 2.4. *Schematic representation of a SEM.*[8]

2.2.4 Atomic Force Microscopy (AFM)

The ability of the atomic force microscope (AFM) to create three-dimensional micrographs with resolution down to the nanometer scale has made it an essential tool for imaging surfaces. **Figure 2.5** gives a schematic illustration of the operation principle of AFM. By scanning the AFM cantilever over a surface and recording the deflection of the cantilever, the local height is measured. The measured cantilever deflection allows a computer to generate a map or surface topography. Three-dimensional topographical maps of the surface are then constructed by plotting the local sample height versus horizontal probe tip position. Other imaging techniques are also used including measuring the change in amplitude or phase of an oscillating cantilever, using tapping mode. This tapping mode is useful to study the surface morphology of thin films. In this work, the AFM measurements were carried out using a Bruker Dimension Edge system.

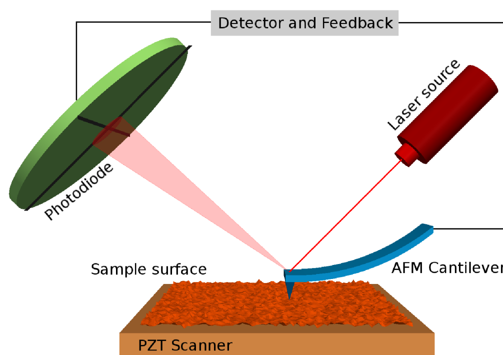

Figure 2.5. *Schematic illustration of the operation principle of AFM.*[9]

2.2.5 X-ray Photoelectron Spectroscopy (XPS)

X-ray photoelectron spectroscopy (XPS) is a nondestructive method for studying the electronic structure of atoms, molecules, and solids. The sample is illuminated with low energetic monochromatic X-rays, which cause the emission of electrons from deep or core shells of atoms in the sample. The difference in energy of an X-ray photon and the photoelectron gives the binding energy of the electrons, which is determined by the element and its chemical state. Although X-rays can penetrate a substrate for several micrometers, inelastic scattering causes energy loss limiting the depth from which photoelectrons can escape from the sample without losing energy, which make XPS a surface sensitive technique. The basic components of an XPS instrument is outlined in **Figure 2.6**, which consists of a source of fixed energy radiation, an electron energy analyzer and an ultra high vacuum (UHV) chamber which enables the emitted photoelectrons to be analysed without interference from gas phase collisions. In this work, all experiments were performed on a Theta Probe system of Thermo Scientific using a monochromatic Al Kα X-ray source.

2.2.6 X-ray Absorption and X-ray Fluorescence Spectroscopy (XAS and XRF)

X-rays are ionizing radiation which has sufficient energy to eject a core electron from an atom. Since each core shell has a distinct binding energy, if one plots X-ray absorption as a function of energy, the spectrum for any atom would resemble the schematics shown in **Figure 2.7**, left, which is known as X-ray absorption spectrum. When the X-ray energy is scanned through the binding energy of a core shell, there is an abrupt increase in absorption cross-section, which is the so-called absorption edge, with each edge representing a different core-electron binding energy. The edges are named according to the principle quantum number of the electron that is excited. X-ray absorption spectroscopy (XAS) refers to the

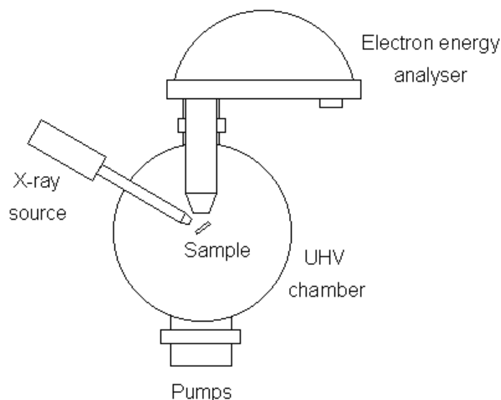

Figure 2.6. *Schematic representation of a basic XPS setup.*[10]

measurement of X-ray absorption in the vicinity of one or more absorbing edges. A closer look to any of the absorption edges (**Figure 2.7**, right) reveals significant structure both in the immediate vicinity of the edge jump and well above the edge. The structure in the vicinity of the edge is referred to as X-ray Absorption Near-Edge Structure (XANES). The oscillations above the edge, which can extend for 1,000 eV or more, are often referred to as Extended X-ray Absorption Fine Structure (EXAFS). By proper analysis of the XAS spectrum, one can obtain both electronic and structural information of the material under investigation. All the XAS experiments related to this thesis were performed at the SAMBA beam line of the 2.75 GeV SOLEIL synchrotron (Saint-Aubin, France) using a top-up electron beam of 430 mA, in collaboration with the Laboratory for Chemical Technology (LCT) at Ghent University. The data were analyzed and interpreted by Dr. Matthias Filez, as a part of his doctoral research.

As a consequence of the ejection of electrons, vacancies are created within the respective shells as illustrated in **Figure 2.8**a. These vacancies allow for electrons in higher shells to fall back to these lower shells, causing emission of fluorescent X-rays, as shown in **Figure 2.8**b. The energy of the emitted X-rays is related to the difference in binding energy of the two shells involved, which is characteristic of the chemical element. Because of the long mean free path of X-rays, the information depth of XRF is much higher than for XPS. From a practical point of view, XRF is fast and non-destructive. In this work, *ex situ* XRF measurements were performed using a Bruker Artax system consisting of Mo X-ray source and an XFlash 5010 silicon drift detector. *In situ* XRF measurements during Pt ALD were performed at the SAMBA beam line of the 2.75 GeV SOLEIL synchrotron (Saint-Aubin, France) using a top-up electron beam of 430 mA and a Canberra 35-elements planar germanium detector.

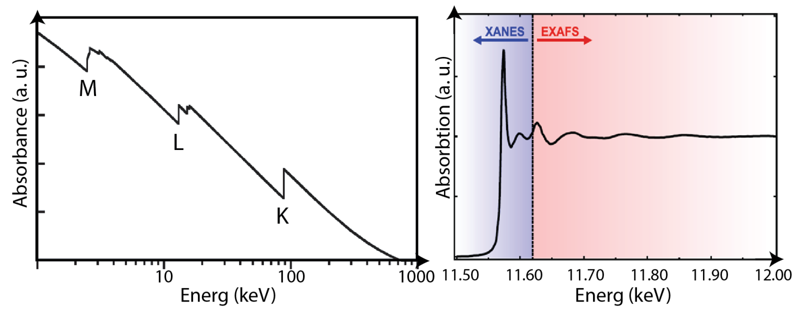

Figure 2.7. *Schematics illustration of (left) a low-resolution X-ray absorption spectrum of Pt. Three major transitions are seen (K, L, and M edges), corresponding to excitation of an electron from n = 1, 2, and 3 shells, respectively and (right) the zoom an absorption edge (Pt L_{III}) showing XANES and EXAFS.* [11]

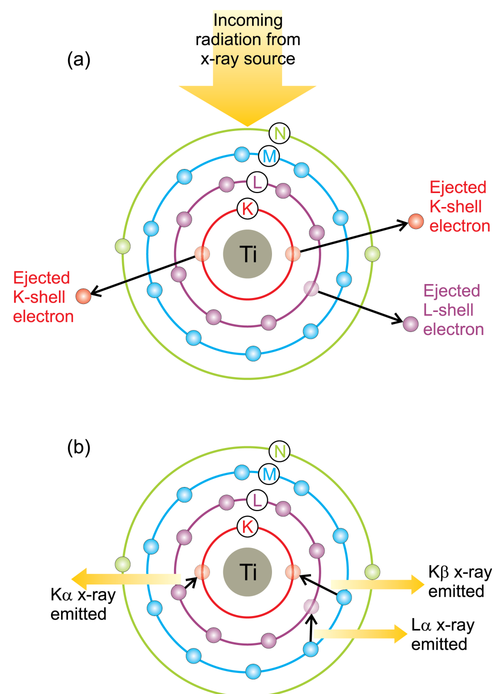

Figure 2.8. *Schematics illustration of X-ray fluorescence.* [12]

2.2.7 X-ray Diffractometry (XRD)

X-ray diffraction (XRD) is the most widely used method for determining the crystallinity of materials, which is based on the constructive interference of X-rays scattering from parallel planes of the sample under investigation. When the angles between X-rays and planes satisfy the Bragg condition $[2dsin\theta = n\lambda]$, where d is the distance between the planes, n is an integer number and λ is the X-ray wavelength), the diffracted X-rays interfere constructively. A diffraction peak will then be recorded at an angle 2θ with respect to the incident beam. All the *ex situ* XRD measurements related to this work were carried out using a Bruker D8 Discover, equipped with a Cu Kα X-ray source and a Vantec linear detector.

Apart from the *ex situ* XRD setup, our research group (CoCooN) has got a dedicated *in situ* XRD setup for monitoring the crystalline changes in the materials while annealing them under different atmospheres (oxidation, reduction and inert), which is schematically represented in **Figure 2.9**. The setup is equipped with stainless steel annealing chamber, which consists of a sample heating block, inlet and outlet for different gases and two Kapton® windows for the transmission of incident and diffracted X-ray beams. The chamber can be evacuated to pressures below 5×10^{-2} mbar by using a rotary vane pump. A linear detector can record a pattern in a 2θ - window of $20°$. The system was originally designed and built by Dr. Werner Knaepen and improved substantially by Dr. Geert Rampelberg.

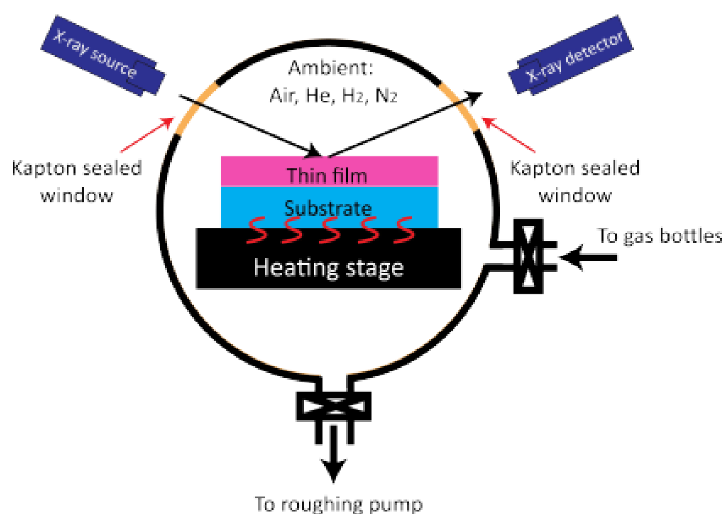

Figure 2.9. *Shematic representation of in situ XRD chamber.*[13]

2.2.8 X-ray Reflectivity (XRR)

XRR is another non-destructive X-ray technique used for the determination of the density, thickness and roughness of thin films. In this technique, a monochromatic X-ray beam is allowed to fall on the sample surface at very low incident angle (typically 0.6 to 6°). The intensity of X-ray beam that is specularly reflected from the sample is then measured as a function of the incident angle. When the incident angle of the X-rays is slightly larger than the critical angle, interference between X-rays reflected from the top surface and from interfaces of different layers beneath will cause an oscillated intensity of the reflected signal. Information such as film thickness, density and roughness can be obtained by fitting a theoretical curve to the measured signal (**Figure 2.10**). The XRR measurements in this work were carried out using a Bruker D8 Discovery system.

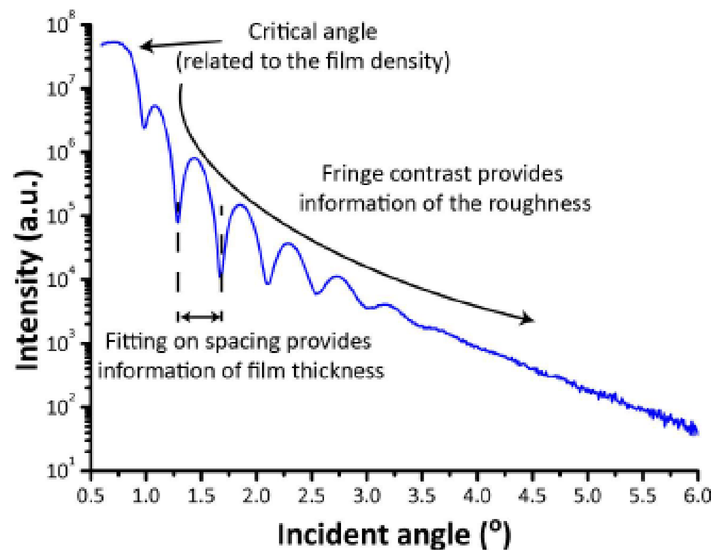

Figure 2.10. *XRR pattern and its interpretation of a 17.9 nm HfO_2 film on a 100 nm SiO_2 substrate.*[13]

2.2.9 Grazing-Incidence Small-Angle X-ray Scattering (GISAXS)

Grazing-incidence small-angle X-ray scattering (GISAXS) is a powerful tool for morphological characterization of nanoscopic objects. In this technique, a monochromatic beam of X-rays is sent to the sample surface at grazing incidence (α_i) [**Figure 2.11**]. Any kind of roughness on the surface or any kind of electronic contrast variation in the subsurface region leads to beam scattering in an

non-specular direction. The scattered intensity is then recorded by a 2D detector, which is located at 1-4 m from the sample, as a function of the out-of-plane angle α_f and an in-plane angle θ_f. A proper analysis of the collected data can provide information about the shape of nanoscopic objects at surfaces, at buried interfaces, or in thin films. All the GISAXS measurements related to this work were performed at the DUBBLE beamline of the ESRF synchrotron facility (Grenoble, France) and the data were analyzed and interpreted by Dr. Jolien Dendooven.

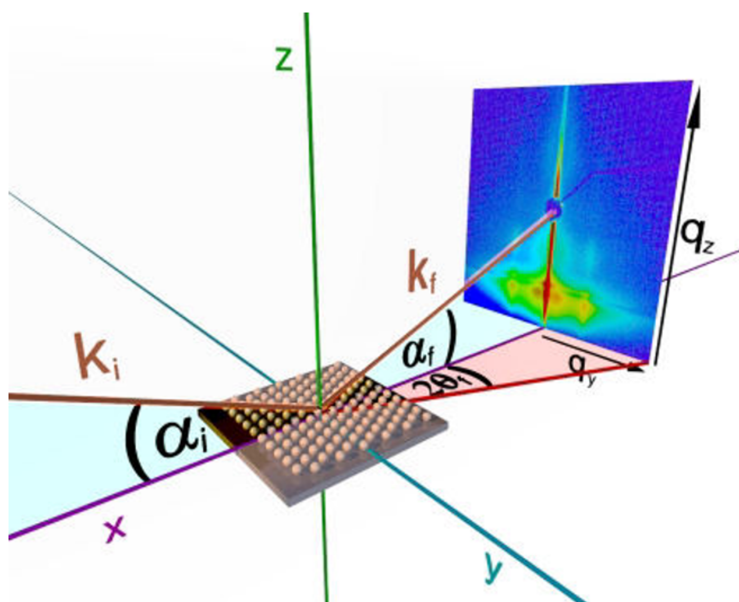

Figure 2.11. *GISAXS geometry.*[14] *Scattering vector q is defined as k_f - k_i, with k_i and k_f the wave vectors of the incident and scattered beams, respectively.*

2.2.10 Transmission Electron Microscopy (TEM)

In Transmission Electron Microscope, an electron beam from an electron gun is transmitted through an ultra-thin section of the microscopic object and the image is magnified by electromagnetic fields. The transmission of the electron beam is highly dependent on the properties of the material being examined. When a tiny convergent electron beam is scanned over a defined area of the sample, it is called as scanning TEM (STEM). The generated signals are recorded and used to build up an image. Depending on the configuration of the detector used for collecting the signals (**Figure 2.12**), different types of images such as bright field STEM (BF-STEM), annular dark field (ADF) STEM (ADF-STEM) and high angle ADF-STEM (HAADF-STEM) are obtained. A BF-STEM is obtained by collecting the direct beam from the sample, whereas the ADF and HAADF detectors are discs with a hole in their centre, which collects scattered electrons for image formation.

Since the diameter is large, HAADF detector collects only incoherently scattered electrons (electrons scattered to higher angles) and thereby, HAADF-STEM images show little or no diffraction effects and are highly sensitive to variations in the atomic number of atoms in the sample. In this work, the mesoporous SiO_2 sample was characterized using a JEOL JEM-2200FS Cs-corrected microscope operated at 200 kV, and equipped with a Schottky-type field-emission gun and EDX JEOL JED-2300D, at the Department of Materials Science and Engineering, Ghent University.

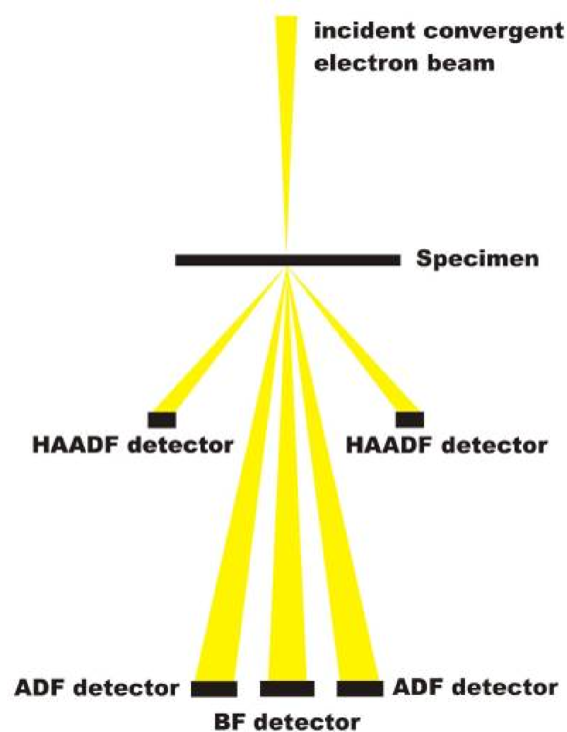

Figure 2.12. *Schematic outline of the arrangement of the various STEM detectors.*[15]

References

[1] M. N. Mullings, C. Hagglund, and S. F. Bent, *Journal of Vacuum Science & Technology A: Vacuum, Surfaces, and Films* **31**(6), 061503 (2013).

[2] Q. Xie, Y.-L. Jiang, C. Detavernier, D. Deduytsche, R. L. Van Meirhaeghe, G.-P. Ru, B.-Z. Li, and X.-P. Qu, *Journal of Applied Physics* **102**(8), 083521 (2007).

[3] J. Musschoot, Q. Xie, D. Deduytsche, S. Van den Berghe, R. Van Meirhaeghe, and C. Detavernier, *Microelectronic Engineering* **86**(1), 72–77 (2009).

[4] J. Dendooven, R. K. Ramachandran, K. Devloo-Casier, G. Rampelberg, M. Filez, H. Poelman, G. B. Marin, E. Fonda, and C. Detavernier, *Journal of Physical Chemistry C* **117**(40), 20557–20561 (2013).

[5] J. Dendooven, E. Solano, M. M. Minjauw, K. V. D. Kerckhove, A. Coati, E. Fonda, G. Portale, Y. Garreau, and C. Detavernier, *Review of Scientific Instruments* **87**, 113905 (2016).

[6] *https://www.jawoollam.com/resources/ellipsometry-tutorial/ellipsometry-measurements* .

[7] *http://web.chem.ucla.edu/˜harding/IGOC/M/mass_spectrum.html* .

[8] *http://www.microscopy.ethz.ch/sem.htm* .

[9] *http://www.iue.tuwien.ac.at/phd/filipovic/node36.html* .

[10] *http://www.chem.qmul.ac.uk/surfaces/scc/scat5_3.htm* .

[11] R. M. V. D. Veen, *Ultrafast X-ray and Optical Spectroscopy of Binuclear Molecular Complexes, PhD Thesis, University of Illinois* (2010).

[12] J. Dendooven, *Modeling and In Situ Characterization of the Conformality of Atomic Layer Deposition in High Aspect Ratio Structures and Nanoporous Materials, PhD Thesis, Ghent University* (2012).

[13] S. Deng, *Templated synthesis of porous materials via atomic layer deposition, PhD Thesis, Ghent University* (2015).

[14] *http://www.gisaxs.de/theory.html* .

[15] *http://www.microscopy.ethz.ch/STEM.htm* .

3

Process development for the ALD of Pt and MO_x (M = Ga, In and Fe)

This chapter gives an overview of the new ALD processes for Pt metal and different metal oxides, developed during the period of this thesis work. Since, the deposition of bimetallic materials by combing different ALD processes has been one of the final goals of this research, an ALD process with wide temperature window was intended. Each of these new processes are now published in peer reviewed journals and are discussed at the end of this chapter as papers I - IV. In section 3.1 and 3.2, an overview of the existing ALD processes for Pt and MO_x (M = Ga, In and Fe), respectively, are discussed together with their catalytic importance. Finally, in section 3.3, catalytic results obtained by using different catalysts prepared by the developed ALD processes are discussed.

3.1 Importance of Pt and Pt ALD in catalysis

Importance of Pt

The catalytic activity of noble metals, especially Pt, is widely exploited in a variety of chemical processes. Industrial catalysts containing about 1 nm sized Pt-particles on chlorinated alumina were already introduced in the 1960s [1]. Hydrocarbon conversion is one of the most studied catalytic reactions using Pt. [2] In fact, Pt is the most extensively studied noble-metal based catalyst for the nonoxidative dehydrogenation of light olefins. It has been studied as a catalyst for the reduction of nitric oxide from exhaust gases of diesel and gasoline engines. [3] Pt is used as three-way

catalyst in automobile catalytic converters together with palladium and rhodium[4] and in fuel cell technology for production of carbon monoxide free hydrogen.[5] Platinum and its alloys with foreign metals have been studied as electrocatalysts for low temperature fuel cells.[6;7] Noble metal catalysts are quite often prepared by different liquid phase techniques, but gas phase methods can be used as well.[8]

Importance of Pt ALD

The control over the nanoparticle size and shape is of fundamental importance for catalysis, where ALD has already shown its immense potential.[9–11] The applicability of ALD in the synthesis of supported metal catalysts is ascribed to the successful development of ALD processes for the growth of noble metals that started in 2003.[12;13] Pt ALD is one of the most extensively investigated metal ALD processes.[13–20] The islands type growth behaviour during the initial cycles of Pt ALD has been exploited by several research groups for the fabrication of different catalytic nanoparticles, as described in chapter 1, section 1.2.2.2. In this work, a case study is carried out on the ALD based synthesis of a Pt based bifunctional catalyst on a ZSM-5 zeolite and its catalytic properties as described in section 3.3.1.

Table 3.1 gives an overview of the existing Pt-ALD processes. Pt-ALD is usually performed using (methylcyclopentadienyl)trimethylplatinum ($MeCpPtMe_3$) as the Pt source and molecular oxygen,[13] ozone,[16;17] O_2 plasma[15] or N_2/NH_3 plasma[18] as reactant and uses a temperature greater than 250 °C. A low temperature process for depositing metallic Pt would be beneficial for applications that uses temperature sensitive materials. Even though there exists some low temperature processes,[14;18] they some times lead to the deposition of oxidized platinum layers[21] and require additional reduction step to form Pt.[19–22] During this thesis work, a new ALD process has been developed using ($MeCpPtMe_3$) and ozone as reactant, which enables the deposition of metallic Pt in a broad temperature window starting from 100 to 300 °C (**Figure 3.1**). The details of this novel ALD processes are described in paper I.

Precursor	Reactant	Temperature window (°C)	Growth rate (Å/cycle)	Remarks/References
$(MeCp)PtMe_3$	O_2	300	0.45	ref[13;23–26]
$Pt(acac)_2$	O_3	120 - 140	0.30 - 0.55	PtO_x was obtained between 120 - 130 °C[14]
$(MeCp)PtMe_3$	O_2 plasma	100 - 300	0.47	PtO_x was obtained for long plasma exposures[20;21]
$(MeCp)PtMe_3$	O_2 plasma	150 - 300	0.45	ref[18]
$(MeCp)PtMe_3$	N_2 plasma	250 - 300	0.30	ref[18]
$(MeCp)PtMe_3$	NH_3 plasma	250 - 300	0.40	ref[18]
$(MeCp)PtMe_3$	O_3	100 - 300	0.45	This work[16]

Table 3.1. *Overview of existing ALD processes for platinum.*

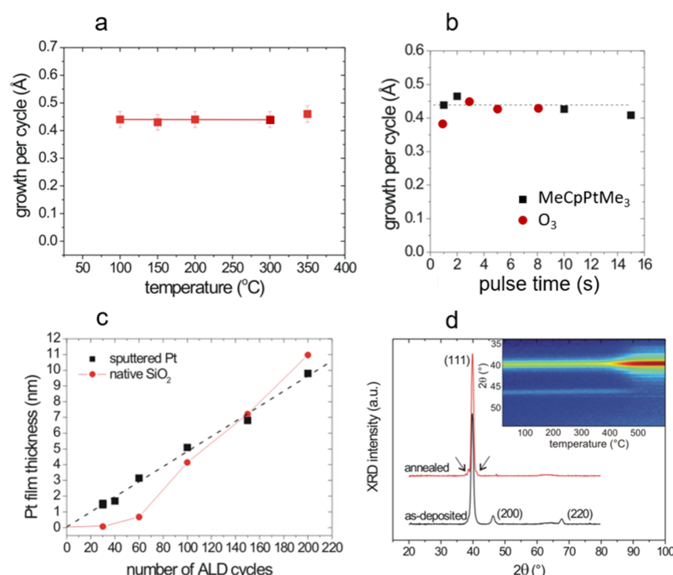

Figure 3.1. Overview of the Pt ALD process developed during this thesis work. a) temperature window, b) saturation, c) linearity and d) XRD of the as-deposited and annealed Pt film. Detailed description of the process is given in paper I

3.2 Importance of Metal oxides and Metal oxide ALD in catalysis

Importance of MO_x (M = Ga, In and Fe)

Metal oxides play an important role in heterogeneous catalysis, either as support for active materials or as an active component itself. Due to their unique acid-base and redox properties, metal oxides have been widely used in a broad range of catalytic reactions. Dehydrogenation of hydrocarbons is one of the important classes of heterogeneous catalysis using gallium, indium and iron oxides. Ga_2O_3 has been used as a dehydrogenation catalysts in both bulk and supported form. For example Ga_2O_3 supported on ZSM-5 and silica has been used for the dehydrogenation of propane.[27–30] Being adjacent members in the periodic table, indium and gallium share many catalytic properties. For example, both of them display a similar activity in the reduction of NO_x.[31] The propane dehydrogenation reaction on Ga- and In-loaded ZSM-5 is found to have similar activity and selectivity values.[32] Similarly, supported iron oxide is active in many catalytic reactions such as dehydrogenation of ethylbenzene and 1-butene.[33;34] Iron oxide mixed with alumina has shown excellent activity in propane dehydrogenation.[35] Active propane dehydrogenation catalysts can also be obtained by incorporating Fe ions in the framework

of ZSM-5 zeolites, where the catalytic activity is ascribed to the redox reaction of Fe ions (Fe^{2+} and Fe^{3+}).[36] Also, iron containing zeolite catalysts are found to be very effective in the decomposition of N_2O.[37]

Importance of Metal oxide ALD

As discussed in the introductory chapter, several researchers have explored the unique characteristics of ALD in different aspects of heterogeneous catalysis. This includes the creation of catalytic sites, tuning the substrate morphology, photocatalysis and for depositing protective over-layers on other catalytic materials. In this part, we mainly focused on introducing acidic catalytic centers in to zeolite materials. This can be obtained by applying one or a few ALD oxide cycles to the support. For example, Backman *et al.* introduced catalytically active Co species into mesoporous silica[38;39] and alumina[40] powder for the hydroformylation of ethene and the hydrogenation of toluene. Five ALD cycles of CoO_x species were carried out using Cobalt(III)acetylacetonate [Co(acac)$_3$] as precursor, after which the CoO_x species were partially reduced to Co in flowing H_2 at 500 - 600 °C. The ALD synthesized Co catalysts showed improved activities compared to catalysts prepared by impregnation from $Co(NO_3)_2$, due to the higher dispersion* of the active species. Stair *et al.* reported ALD synthesized VO_x catalysts on anodic aluminum oxide[41], which showed specific activities between 2 and 7.5 times higher than catalysts of similar loading prepared by incipient wetness impregnation (I-WI). This reflects the higher dispersion of the VO_x species introduced by ALD compared to IWI.

In 2011, in collaboration with the Centre for Surface Chemistry and Catalysis (COK) of the University of Leuven, our group demonstrated that the Al-ALD process using TMA and H_2O is suited for the incorporation of AlO_x species in a zeolite framework to increase the acidity and thereby enhance the catalytic activity of mesoporous zeolites and ordered micro/mesoporous zeotile-4 material[42]. More recently, this method was successfully extended for introducing catalytically active aluminum species on a purely siliceous zeolite (-COK-14), and thereby making it catalytically active. A detailed description of this approach can be found in the introductory chapter section 1.2.2.1 and in reference.[43] A similar approach is employed in this work for the incorporation of Ga species in to the -COK-14 zeolite material. Details of this experiment is given in section 3.3.2.

The Ga_2O_3 ALD was performed with the newly developed process using a β-diketonate precursor, Ga(TMHD)$_3$, as Ga source and O_2 plasma as reactant. The exceptional stability and low cost make this precursor highly interesting. A constant growth per cycle value of 0.1 Å/cycle was obtained within a temperature

*In ALD, dispersion refers to the uniform distribution of particles all over the available surface. On the other hand, in heterogeneous catalysis dispersion is the fraction of atoms exposed, *i.e.* the ratio of surface atoms versus the total number of atoms for a given particle (size). Since this is directly related to the size of the particles and knowing the fact that ALD is well capable of controlling the size of the particles deposited, one could say that well-dispersed catalytic nanoparticles can be accomplished by ALD.

window ranging from 100 to 400 °C (**Figure 3.2**). This broad temperature window could be of interest for doping applications, where the deposition temperatures for different ALD processes have to overlap. As-deposited films were amorphous, which could be crystallized into a monoclinic β - Ga_2O_3 crystal structure by a post deposition annealing in He. The refractive index and optical band gap of the material were determined to be 1.84 and 4.95 eV, which are in agreement with the values reported in literature.[44–46;46;47] A similar kind of precursor, $In(TMHD)_3$, was used for the ALD of In_2O_3 together with O_2 plasma plasma, which resulted in the deposition of crystalline In_2O_3 films with a GPC value of 0.14 Å/cycle over a broad temperature window of 100 to 400 °C (**Figure 3.3**). The optical transparency of the films was excellent with an average transmission of about 94.0% in the wavelength range 380 - 1000 nm. The refractive indices of the films were in the range of 2.01 to 2.05 at 632.8 nm, which is in line with previously reported refractive indices for In_2O_3 films.[48;49] The resistivity of the films deposited at and above 300 °C was in the range of 2.5 $m\Omega \cdot \mathrm{cm}$, which corresponds to most of the reported literature values,[49–52] but higher than the value of 0.35 and 0.27 $m\Omega \cdot \mathrm{cm}$ reported by Libera *et al.*[53] and Macco *et al.*,[54] respectively. Further details of these new ALD processes are discussed at the end of this chapter as paper II and III, whereas **Table 3.2** and **3.3** give an overview of the existing ALD processes for gallium and indium oxides respectively.

Precursor	Reactant	Temperature window (°C)	Growth rate (Å/cycle)	Remarks/References
$Ga(acac)_3$	H_2O or O_3	350 - 370	0.33 or 0.28	ref[55]
$Ga_2(NMe_2)_6$	H_2O	170 - 250	1.0	ref[56]
$[(CH_3)_2GaNH_2]_3$	O_2 plasma	200	-	ref[56–58]
$Me_2GaOiPr$	H_2O	280 - 300	0.30	ref[59]
$Ga(OiPr)_3$	H_2O	150 - 250	2.5	ref[60]
TMGa	O_3	250 - 450	0.40 - 0.50	ref[61]
TMGa	O_2 plasma	100 - 400	0.53	ref[62]
$Ga(TMHD)_3$	O_2 plasma	100 - 400	0.10	This work[63]

Table 3.2. *Overview of existing ALD processes for gallium oxide.*

Precursor	Reactant	Temperature window (°C)	Growth rate (Å/cycle)	Remarks/References
$InCl_3$	H_2O	400 - 450	0.27	ref[50]
In(Cp)	O_3	300 - 450	1.3 - 2.0	ref[64]
$In(acac)_3$	H_2O	165 - 200	0.20	ref[51]
$In(acac)_3$	O_3	165 - 225	0.12	ref[51]
In(Cp)	O_2 + H_2O	100 - 250	1.0 - 1.6	ref[53]
TMIn	H_2O	200 - 251	0.39	ref[52]
$[In[(iPr)_2CNR_2]_3]$	H_2O	230 - 300	0.45	ref[65]
TMIn	O_3	100 - 200	0.46	ref[66]
$In(TMHD)_3$	O_2 plasma	100 - 400	0.14	This work[67]

Table 3.3. *Overview of existing ALD processes for indium oxide.*

Even though these two ALD processes exhibit very low GPC, this could be of interest for doping applications, where an atomic level control of dopant is required. For example, transparent conducting oxides (TCOs) such as Al doped ZnO (AZO),[68–71] Ga doped ZnO (GZO),[70;72–75] In doped ZnO (IZO),[76–78] and In and Ga doped ZnO (IGZO)[79–82] have recently attracted considerable attention as an alternative for the commonly used ITO films. Doping of ZnO with these group III elements can substantially improve its electrical properties,[82;83] which can be tuned by controlling the dopant concentration. As an example, Chalker *et al.*[72] observed that the sheet resistance of GZO decrease with increasing concentration of Ga and attain a minimum value at a Ga at% of 0.5 - 1. Above this value, the sheet resistance rise monotonically and becomes more resistive than the undoped ZnO. A maximum carrier concentration of $5 \times 10^{20} cm^{-3}$ with a carrier mobility of approximately 7 cm^2/Vs was found at 1 at% gallium doping. **Table 3.4** summarizes the properties of IZO and GZO films prepared by different ALD processes.

Dopant	Optimum concentration (at%)	Thickness (nm)	Resistivity ($\Omega \cdot$ cm)	Transmittance (%)	ALD process
Ga	3	85	3.3×10^{-4}	-	HDMAGa/H_2O [74]
Ga	5	35	3.5×10^{-3}	80	GTIP/H_2O [73]
Ga	2.7	35	1.49×10^{-3}	85	TMGa/H_2O [75]
In	15.4	-	6.15×10^{-2}	-	DMLDMIn/H_2O [77]

Table 3.4. *Properties of GZO and IZO prepared by ALD*

Fe_2O_3 ALD is generally performed at very high temperatures (>350 °C) and uses ferrocene as precursor. In paper IV a new ALD process for the deposition of Fe_2O_3 using t-butyl ferrocene (TBF) and O_2 plasma is discussed (**Figure 3.4**). This novel process enables the deposition of Fe_2O_3 in a low and broad temperature range (150 - 350 °C), compared to the existing ALD processes (**Table 3.5**). Recently, a number of new iron oxide ALD processes have been reported,[84–86] among which one using an amidinate precursor, FeAMD, and water as counter reactant.[85] This process could be of interest for the conformal deposition of iron oxide on sensitive materials which cannot withstand harsh conditions such as O_2 plasma or ozone.

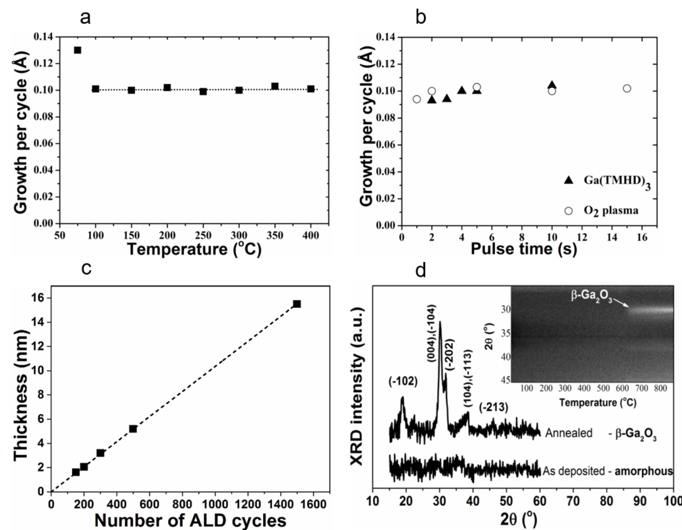

Figure 3.2. *Overview of the gallium oxide ALD process developed during this thesis work. a) temperature window, b) saturation c) linearity and d) XRD of the as-deposited and annealed Ga_2O_3 film. Detailed description of the process is given in paper II*

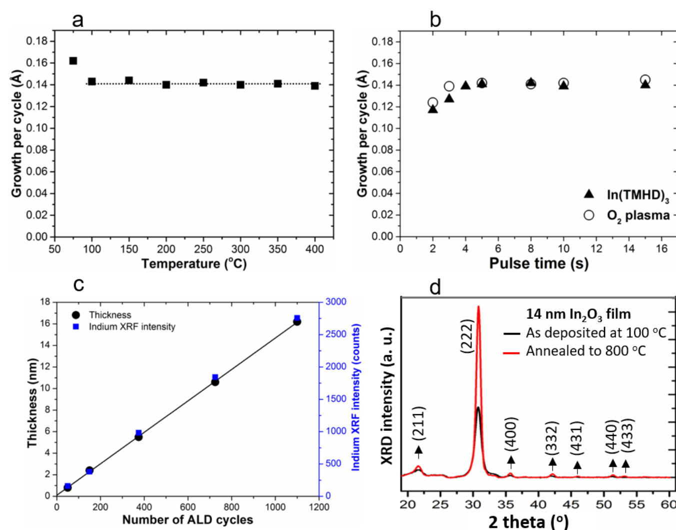

Figure 3.3. *Overview of the indium oxide ALD process developed during this thesis work. a) temperature window, b) saturation c) linearity and d) XRD of the as-deposited and annealed In_2O_3 film. Detailed description of the process is given in paper III*

Precursor	Reactant	Temperature window (°C)	Growth rate (Å/cycle)	Remarks/References
$Fe(thd)_3$	O_3	160 - 210	0.13	ref[87]
$Fe_2(OtBu)_6$	H_2O	130 - 180	0.26	ref[88;89]
$(Me_2CP)_2Fe$	O_3 or H_2O_2	120	0.60	H_2O_2 resulted in less oxidized Fe_3O_4 [90]
$Fe(Cp)_2$	O_2	350 - 500	1.4	ref[91]
$Fe(Cp)_2$	O_3	300 - 500	0.21 - 0.97	ref[92]
$Fe(Cp)_2$	O_3	200 - 350	1.4	ref[93]
$Fe(hfa)_2TMEDA$	O_3	250 - 350	0.20	ref[94]
TBF	O_2 plasma	150 - 350	0.20 - 1.2	This work[95]
DMAMFc	O_3	230	.25	ref[84]
FeAMD	H_2O	130 - 200	0.55	ref[85]
$Fe(btmsa)_2$	H_2O_2	150 - 175	0.32	ref[86]

Table 3.5. *Overview of existing ALD processes for iron oxide.*

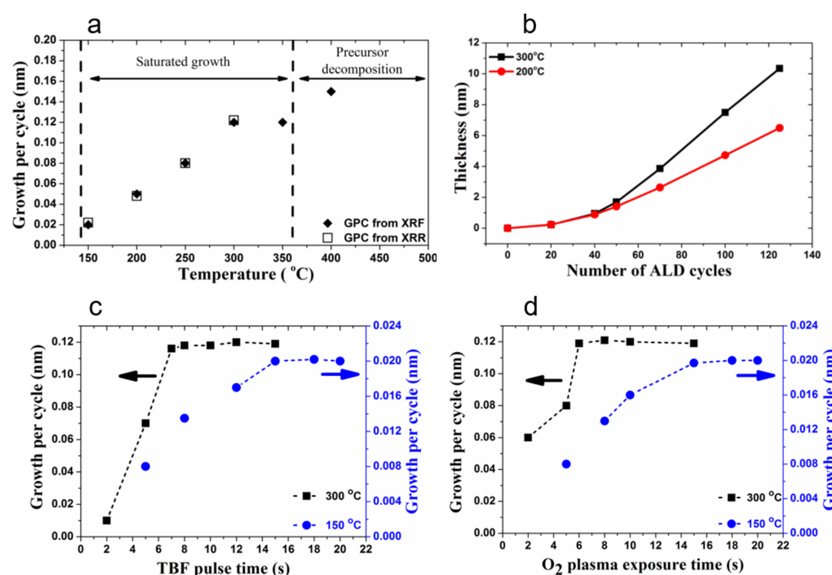

Figure 3.4. *Overview of the iron oxide ALD process developed during this thesis work. a) temperature window, b) linearity and c & d) saturation. Detailed description of the process is given in paper IV*

3.3 Catalytic applications

3.3.1 Case study I: Bifunctional hydroconversion catalyst *via* atomic layer deposition of platinum

Hydro conversion of hydrocarbons is a catalytic process in which a long n-alkane is converted into isoalkanes of the same (hydroisomerization) or reduced molecular weight (hydrocracking). The catalyst used in this process is a bifunctional one. It is composed of a metallic part, usually platinum or palladium, to catalyze (de)hydrogenation reactions, and an acid part, generated by zeolites like mordenite and ZSM-5, to catalyze isomerization and cracking reactions. Conversion of n-decane using Pt loaded ZSM-5 catalyst (Pt/ZSM-5) is one of the most studied hydroconversion processes. Conventionally, Pt is introduced in to ZSM-5 by using incipient wetness impregnation. In this work, Pt-ALD is employed for the introduction of Pt in to ZSM-5 and the resulting catalysts were tested for n-decane hydroconversion.

ZSM-5 powder was provided by the COK group of the University of Leuven. Pt ALD was carried out in a home built cold wall ALD chamber, using the newly developed ozone-based Pt ALD process (Paper I). The powder sample was loaded in a molybdenum sample cup, which was then transferred into the ALD reactor through the load-lock and placed on a heated block. The sample was then heated to 200 °C and allowed to outgas and thermally equilibrate for at least 1 h under vacuum. A static exposure mode was applied during both ALD half-cycles [16]. The pulse time of the $MeCpPtMe_3$ precursor was 10 s, after which the valves to the pumping system were kept closed for another 20 s, resulting in a total exposure time of 30 s. The same pulse time and exposure time were used for the O_3 also. During the precursor and reactant exposures, the pressure in the chamber increased to *ca.* 0.5 mbar and 1 mbar, respectively.

Two different sets of catalysts were synthesized by introducing Pt in to parent ZSM-5 (ZSM-5-P) or desilicated ZSM-5 (ZSM-5-D) by using ALD and incipient wetness impregnation. The resulting catalysts were labelled as Pt/ZSM-P-ALD, Pt/ZSM-P-IWI and Pt/ZSM-D-ALD, Pt/ZSM-D-IWI, respectively. High resolution scanning electron microscopy (HRSEM) measurements revealed highly dispersed Pt particles with very small particle size for the ALD treated samples (**Figure 3.5**(b)) compared to the incipient wetness impregnated samples (**Figure 3.5**(a)). The desilicated ZSM-5-D zeolite had smaller Pt particles, but were less prominent on the surface suggesting that Pt is occluded inside the zeolite (**Figure 3.5**(c)). The presence of the Pt particles inside the ALD treated desilicated ZSM-5-D zeolite crystals was confirmed with TEM measurements (**Figure 3.6**).

The catalytic activity of the prepared catalysts was tested for the n-decane hydroconversion reaction. In the case of parent ZSM-5-P, the ALD treated sample showed a catalytic activity and selectivity comparable to or slightly better than the incipient wetness impregnated sample (**Figure 3.7**). On the other hand, in the case of desilicated (mesoporous) ZSM-5-D, the ALD treated sample exhibited a superior activity compared to the incipient wet impregnated sample, while

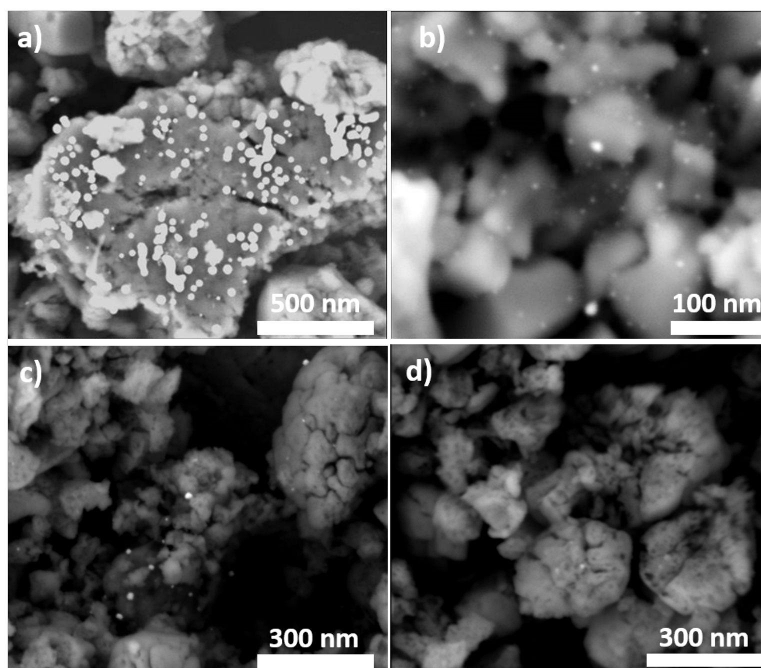

Figure 3.5. HR SEM images revealing the dispersion of platinum over a) Pt/ZSM-P-IWI, b) Pt/ZSM-P-ALD, c) Pt/ZSM-D-IWI and d) Pt/ZSM-D-ALD

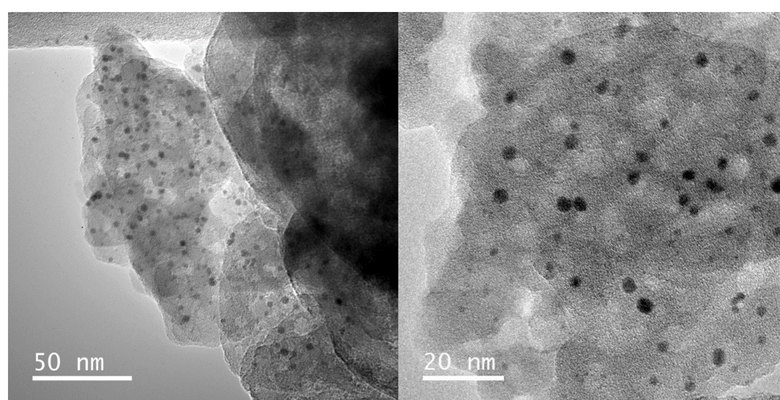

Figure 3.6. TEM images of Pt/ZSM-D-ALD revealing the dispersion of platinum nanoparticles (2-4 nm) inside (mostly) the mesopores

retaining its selectivity (**Figure 3.8**). This superior activity could be ascribed to the well dispersed Pt nanoparticles inside the mesopores (**Figure 3.6**). Hence it is proven by this study that bifunctional catalyst for hydroconversion reactions could

be achieved *via* Pt ALD. This could be advantageous over classical wetness impregnation as ALD allows better tuning of particle size and positioning, which is interesting in the area of heterogenous catalytic processes like alkane hydroconversion.[96]

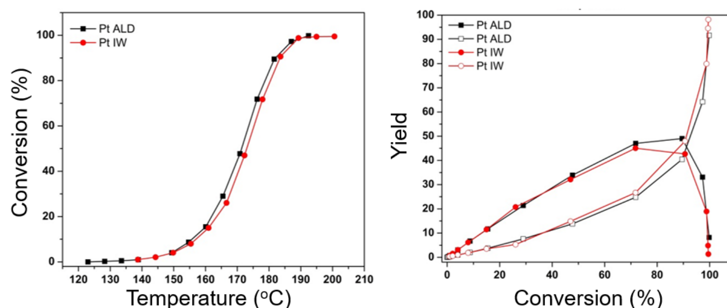

Figure 3.7. *(Left) n-decane conversion against reaction temperature on parent ZSM-5, Pt loaded via ALD and incipient wetness. (Right) Isomerization yield (closed symbols) and cracking yield (open symbols) against n-decane conversion on parent ZSM-5, Pt loaded via ALD and incipient wetness.*

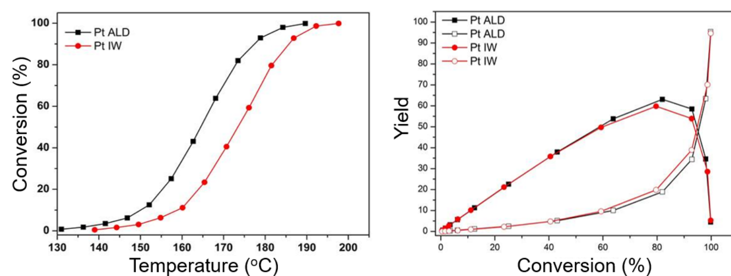

Figure 3.8. *(Left) n-decane conversion against reaction temperature on desilicated ZSM-5, Pt loaded via ALD and incipient wetness. (Right) Isomerization yield (closed symbols) and cracking yield (open symbols) against n-decane conversion on mesoporous ZSM-5, Pt loaded via ALD and incipient wetness.*

3.3.2 Case study II: Introduction of acid sites in an all-silica -COK-14 zeolite by Ga-ALD and its catalytic activation.

-COK-14 is a purely siliceous zeolite material with a 10R (10-membered rings of tetrahedra) and 12R (12-membered rings of tetrahedra) intersecting 2D channel system.[97] The presence of hydrophilic 12R channel and the hydrophobic 10R

channel system is expected to make -COK-14 highly useful in catalytic conversion reactions, which include molecules with different polarity. It has got a plate like morphology having sizes more than 5 μm and thickness around 100 - 200 nm. Micropores of -COK-14 run parallel to the flat surface, whereby the pore mouths are accessible mainly at the rim of the plates. Recently, in collaboration with COK, our group successfully demonstrated the introduction of catalytically active aluminum species on this purely siliceous -COK-14, and thereby making it catalytically active.[43] Here, we demonstrate a similar approach for introducing acidic gallium species in to -COK-14. The catalytic activity and selectivity of the resulting material were investigated for the hydroconversion of n-decane. The results are compared to those of Al-ALD treated COK-14.

The COK-14 sample was provided by COK, which was synthesized according to the procedure reported elsewhere.[97] Ga-ALD was carried out in a home built cold wall ALD chamber using the newly developed Ga-ALD processes (Paper II). For each deposition, 300 mg of powder was loaded in the ALD reactor and kept at 200 °C under vacuum for 2 h. $Ga(TMHD)_3$ vapour and O_2 plasma were alternately introduced to the ALD chamber at pressures of *ca.* 1 Pa. Twenty cycles of ALD were performed, each cycle comprising exposure to $Ga(TMHD)_3$ for 30 s, evacuation under vacuum, and exposure to O_2 plasma for 20 s followed by evacuation. Successful deposition of Ga was confirmed by X-ray fluorescence (XRF) measurements. For the introduction of Al, trimethylaluminum (TMA) vapour and H_2O vapour were alternately introduced to the ALD chamber at pressures of *ca.* 0.5 Pa. 5 cycles of ALD were performed, each cycle comprising exposure to TMA for 30s, evacuation under vacuum, and exposure to water vapour for 30 s followed by evacuation.

The samples were then converted to bifunctional catalysts by impregnation with $Pt(NH_3)_4Cl_2$ solution such that the Pt content in the final catalyst would be 0.5 wt%, followed by calcination and reduction. The resulting catalysts were labelled as Pt/COK-14 (-COK-14 impregnated with Pt), Pt/COK-14-Ga (Ga-ALD treated -COK-14 impregnated with Pt) and Pt/COK-14-Al (Al-ALD treated -COK-14 impregnated with Pt) and were tested for n-decane hydroconversion reaction.

The surface analysis after catalysis using HRSEM imaging revealed a striking difference between the distribution of Pt nanoparticles on Pt/COK-14-Al and Pt/COK-14-Ga. In the case of Pt/COK-14-Al (**Figure 3.9**), a uniform distribution of ~6 nm Pt nanoparticles was observed all over the external surface of the zeolite. On the other hand, on the Pt/COK-14-Ga sample (**Figure 3.10**) the Pt nanoparticles were distributed along the rims of the zeolite (mainly located near the pore mouths) with slightly higher particle size of ~8 nm and almost no Pt particles were found on the flat surface of this sample.

Figure 3.11 (left) shows the conversion of n-decane plotted against reaction temperature. The conversion using a parent purely siliceous Pt/COK-14 without any acidic sites is included in the figure for comparison, which shows no catalytic activity. This is expected, because a Brønsted acid site is mandatory for the hydroconversion to occur by catalyzing the isomerization reaction. On the other hand, the bifunctional Pt/COK-14-Ga and Pt/COK-14-Al having Brønsted

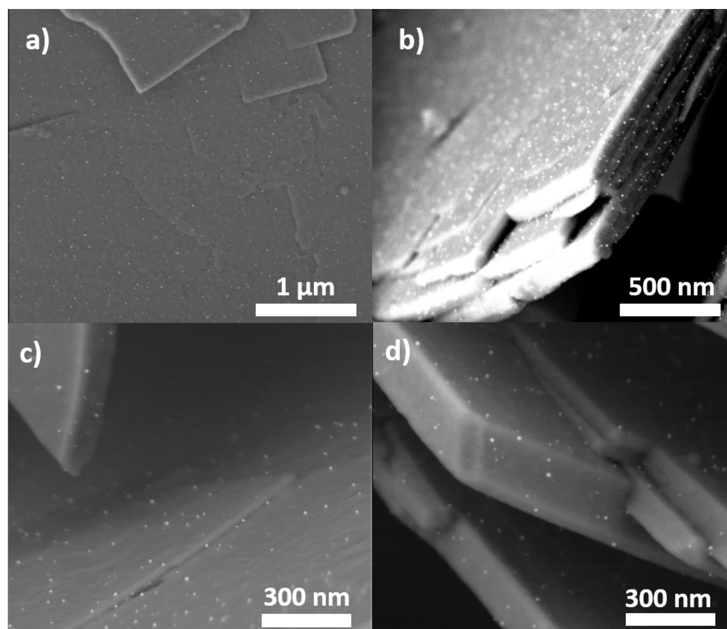

Figure 3.9. *HR SEM images revealing the dispersion of platinum over Al-ALD modified -COK-14.*

acid sites were active and reached full conversion of n-decane at a reaction temperature of 310 °C. The activity of Pt/COK-14-Ga catalyst was slightly lower compared to Pt/COK-14-Al catalyst. But, in contrast to the low conversion activity, the Pt/COK-14-Ga catalyst exhibited a remarkably higher selectivity towards hydroisomerisation (**Figure 3.11** (right)). These preliminary experiments further demonstrate the capability of ALD in functionalizing pure silica materials to produce superior catalysts. Further investigations are required to understand the catalytic chemistry involved in this process.

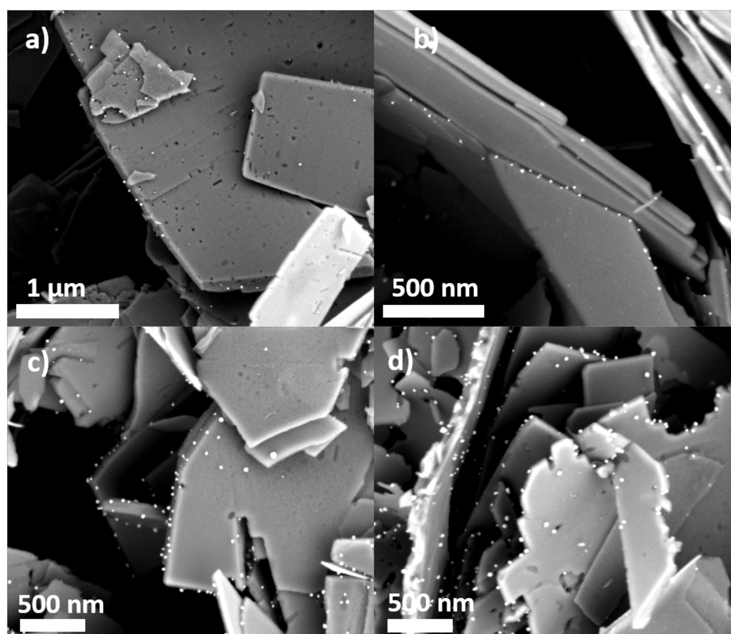

Figure 3.10. *HR SEM images revealing the dispersion of platinum over Ga-ALD modified -COK-14.*

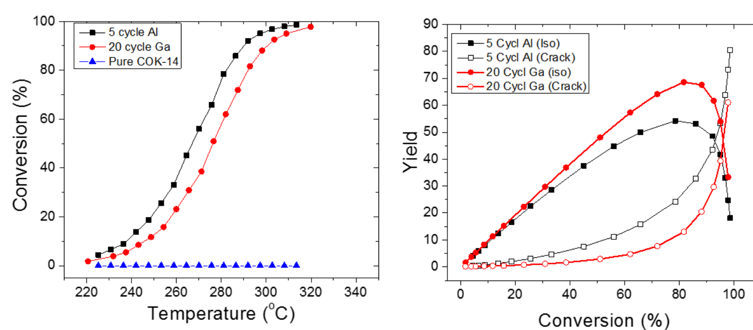

Figure 3.11. *(Left) n-decane conversion over Pt-loaded all-silica -COK-14 (triangle), Pt-loaded Al-ALD modified -COK-14 (square) and Pt-loaded Ga-ALD modified -COK-14 (circle). (Right) Isomerization yield (solid) and cracking yield (open) against n-decane conversion over Pt-loaded Al-ALD modified -COK-14 (square) and Pt-loaded Ga-ALD modified -COK-14 (circle).*

References

[1] B. V. Haensel and H. S. Bloch, *Platinum Metals Rev.* **8**(1), 2–8 (1964).
[2] D. R. Kennedy, G. Webb, S. D. Jackson, and D. Lennon, *Applied Catalysis A: General* **259**(1), 109–120 (2004).
[3] M. D. Amiridis, C. Mihut, M. Maciejewski, and A. Baiker, *Topics in Catalysis* **28**, 141 (2004).
[4] M. Shelef and R. W. McCabe, *Catalysis Today* **62**(1), 35–50 (2000).
[5] D. K. Liguras, D. I. Kondarides, and X. E. Verykios, *Applied Catalysis B: Environmental* **43**(4), 345–354 (2003).
[6] P. K. Shen and Z. Tian, *Electrochimica Acta* **49**(19), 3107–3111 (2004).
[7] Y. Sung, J. Hwang, and J. S. Chung, *International Journal of Hydrogen Energy* **36**(6), 4007–4014 (2011).
[8] P. Serp, P. Kalck, and R. Feurer, *Chemical Reviews* **102**(9), 3085–3128 (2002).
[9] J. Dendooven, *Atomically-Precise Methods for Synthesis of Solid Catalysts*, RSC Catalysis Series. Royal Society of Chemistry, Cambridge, (2015).
[10] J. Lu, J. W. Elam, and P. C. Stair, *Surface Science Reports* **71**(2), 410–472 (2016).
[11] A. J. M. Mackus, M. J. Weber, N. F. W. Thissen, D. Garcia-Alonso, R. H. J. Vervuurt, S. Assali, A. A. Bol, M. A. Verheijen, and W. M. M. Kessels, *Nanotechnology* **27**(3), 034001 (2016).
[12] T. Aaltonen, P. Alén, M. Ritala, and M. Leskelä, *Chemical Vapor Deposition* **9**(1), 45–49 (2003).
[13] T. Aaltonen, M. Ritala, T. Sajavaara, J. Keinonen, and M. Leskela, *Chemistry of Materials* **15**(17), 1924–1928 (2003).
[14] J. Hämäläinen, F. Munnik, M. Ritala, and M. Leskelä, *Chemistry of Materials* **20**(21), 6840–6846 (2008).
[15] L. Baker, A. S. Cavanagh, D. Seghete, S. M. George, A. J. M. Mackus, W. M. M. Kessels, Z. Y. Liu, and F. T. Wagner, *Journal of Applied Physics* **109**(8) (2011).
[16] J. Dendooven, R. K. Ramachandran, K. Devloo-Casier, G. Rampelberg, M. Filez, H. Poelman, G. B. Marin, E. Fonda, and C. Detavernier, *Journal of Physical Chemistry C* **117**(40), 20557–20561 (2013).
[17] H.-B.-R. Lee, K. L. Pickrahn, and S. F. Bent, *The Journal of Physical Chemistry C* **118**(23), 12325–12332 (2014).
[18] D. Longrie, K. Devloo-Casier, D. Deduytsche, S. Van den Berghe, K. Driesen, and C. Detavernier, *ECS Journal of Solid State Science and Technology* **1**(6), Q123–Q129 (2012).
[19] R. H. E. C. Bosch, F. L. Bloksma, J. M. M. Huijs, M. A. Verheijen, and W. M. M. Kessels, *The Journal of Physical Chemistry C* **120**(1), 750–755 (2016).
[20] I. J. M. Erkens, M. A. Verheijen, H. C. M. Knoops, T. F. Landaluce, F. Roozeboom, and W. M. M. Kessels, *Chemical Vapor Deposition* **20**(7-9), 258–268 (2014).

[21] H. C. M. Knoops, A. J. M. Mackus, M. E. Donders, M. C. M. van de Sanden, P. H. L. Notten, and W. M. M. Kessels, *Electrochemical and Solid-State Letters* **12**(7), G34 (2009).

[22] A. J. M. Mackus, D. Garcia-Alonso, H. C. M. Knoops, A. A. Bol, and W. M. M. Kessels, *Chemistry of Materials* **25**(9), 1769–1774 (2013).

[23] T. Aaltonen, A. Rahtu, M. Ritala, and M. Leskela, *Electrochemical and Solid-State Letters* **6**(9), C130 (2003).

[24] W. M. M. Kessels, H. C. M. Knoops, S. A. F. Dielissen, A. J. M. Mackus, and M. C. M. van de Sanden, *Applied Physics Letters* **95**(1), 013114 (2009).

[25] I. J. M. Erkens, A. J. M. Mackus, H. C. M. Knoops, P. Smits, T. H. M. van de Ven, F. Roozeboom, and W. M. M. Kessels, *ECS Journal of Solid State Science and Technology* **1**(6), P255–P262 (2012).

[26] A. J. M. Mackus, N. Leick, L. Baker, and W. M. M. Kessels, *Chemistry of Materials* **24**(10), 1752–1761 (2012).

[27] L. Rodríguez, D. Romero, D. Rodríguez, J. Sánchez, F. Domínguez, and G. Arteaga, *Applied Catalysis A: General* **373**, 66–70 (2010).

[28] I. Takahara, M. Saito, M. Inaba, and K. Murata, *Catal. Lett.* **96**, 29–32 (2004).

[29] B. Xu, B. Zheng, W. Hua, Y. Yue, and Z. Gao, *Journal of Catalysis* **239**(2), 470–477 (2006).

[30] M. Chen, J. Xu, F. Z. Su, Y. M. Liu, Y. Cao, H. Y. He, and K. N. Fan, *Journal of Catalysis* **256**(2), 293–300 (2008).

[31] J. A. Perdigon-Melon, A. Gervasini, and A. Auroux, *Journal of Catalysis* **234**, 421–430 (2005).

[32] J. Halász, Z. Kónya, Á. Fudala, A. Béres, and I. Kiricsi, *Catalysis Today* **31**, 293–304 (1996).

[33] L. Boot, *Journal of Catalysis* **163**(1), 195–203 (1996).

[34] C. Wang, J. Shi, X. Cui, J. Zhang, C. Zhang, L. Wang, and B. Lv, *Journal of Catalysis* **345**, 104–112 (2017).

[35] S. Tan, B. Hu, W.-G. Kim, S. H. Pang, J. S. Moore, Y. Liu, R. S. Dixit, J. G. Pendergast, D. S. Sholl, S. Nair, and C. W. Jones, *ACS Catalysis* **6**, 5673–5683 (2016).

[36] J. H. Yun and R. F. Lobo, *Journal of Catalysis* **312**, 263–270 (2014).

[37] P. Xie, Y. Luo, Z. Ma, C. Huang, C. Miao, Y. Yue, W. Hua, and Z. Gao, *Journal of Catalysis* **330**, 311–322 (2015).

[38] L. B. Backman, A. Rautiainen, A. O. I. Krause, and M. Lindblad, *Catalysis Today* **43**(12), 11–19 (1998).

[39] L. B. Backman, A. Rautiainen, M. Lindblad, O. Jylhä, and A. Krause, *Applied Catalysis A: General* **208**, 223–234 (2001).

[40] L. B. Backman, A. Rautiainen, M. Lindblad, and A. O. I. Krause, *Applied Catalysis A: General* **191**, 55–68 (2000).

[41] H. Feng, J. W. Elam, J. A. Libera, M. J. Pellin, and P. C. Stair, *Journal of Catalysis* **269**(2), 421–431 (2010).

[42] S. P. Sree, J. Dendooven, T. I. Korányi, G. Vanbutsele, K. Houthoofd, D. Deduytsche, C. Detavernier, and J. A. Martens, *Catalysis Science & Technology*

1(2), 218 – 221 (2011).

[43] E. Verheyen, S. Pulinthanathu Sree, K. Thomas, J. Dendooven, M. De Prins, G. Vanbutsele, E. Breynaert, J. P. Gilson, C. E. Kirschhock, C. Detavernier, and J. A. Martens, *Chemical Communications* **50**(35), 4610–4612 (2014).

[44] M. Passlack, N. E. J. Hunt, E. F. Schubert, G. J. Zydzik, M. Hong, J. P. Mannaerts, R. L. Opila, and R. J. Fischer, *Applied Physics Letters* **64**(20), 2715 (1994).

[45] A. Ortiz, J. C. Alonso, E. Andrade, and C. Urbiola, *Journal of The Electrochemical Society* **148**(2), F26–F29 (2001).

[46] F. K. Shan, G. X. Liu, W. J. Lee, G. H. Lee, I. S. Kim, and B. C. Shin, *Journal of Applied Physics* **98**(2), 023504 (2005).

[47] K. Takakura, D. Koga, H. Ohyama, J. Rafi, Y. Kayamoto, M. Shibuya, H. Yamamoto, and J. Vanhellemont, *Physica B: Condensed Matter* **404**(23-24), 4854–4857 dec (2009).

[48] F. O. Adurodija, L. Semple, and R. Brüning, *Thin Solid Films* **492**, 153–157 (2005).

[49] K. Chopra, S. Major, and D. Pandya, *Thin Solid Films* **102**, 1–46 (1983).

[50] T. Asikainen, M. Ritala, and M. Leskeei, *J. Electrochem. Soc.* **141**(11), 3210–3213 (1994).

[51] O. Nilsen, R. Balasundaraprabhu, E. Monakhov, N. Muthukumarasamy, H. Fjellvåg, and B. Svensson, *Thin Solid Films* **517**, 6320–6322 (2009).

[52] D.-J. Lee, J.-Y. Kwon, J. I. Lee, and K.-B. Kim, *The Journal of Physical Chemistry C* **115**, 15384–15389 (2011).

[53] J. A. Libera, J. N. Hryn, and J. W. Elam, *Chemistry of Materials* **23**(8), 2150–2158 (2011).

[54] B. Macco, Y. Wu, D. Vanhemel, and W. M. M. Kessels, *physica status solidi (RRL) - Rapid Research Letters* **8**(12), 987–990 dec (2014).

[55] M. Nieminen, L. Niinisto, and E. Rauhala, *Journal of Materials Chemistry* **6**(1), 27–31 (1996).

[56] C. L. Dezelah, J. Niinisto, K. Arstila, L. Niinisto, and C. H. Winter, *Chemistry of Materials* **18**, 471–475 (2006).

[57] N.-J. Seong, S.-G. Yoon, and W.-J. Lee, *Applied Physics Letters* **87**(8), 082909 (2005).

[58] F. K. Shan, G. X. Liu, W. J. Lee, G. H. Lee, I. S. Kim, and B. C. Shin, *Integrated Ferroelectrics* **80**(1), 197–206 (2006).

[59] H. Lee, K. Kim, J.-J. Woo, D.-J. Jun, Y. Park, Y. Kim, H. W. Lee, Y. J. Cho, and H. M. Cho, *Chemical Vapor Deposition* **17**(7-9), 191–197 (2011).

[60] D. W. Choi, K.-B. Chung, and J.-S. Park, *Thin Solid Films* **546**, 31–34 (2013).

[61] D. J. Comstock and J. W. Elam, *Chemistry of Materials* **24**, 4011–4018 (2012).

[62] I. Donmez, C. Ozgit-Akgun, and N. Biyikli, *Journal of Vacuum Science & Technology A* **31**(1), 01A110 (2013).

[63] R. K. Ramachandran, J. Dendooven, J. Botterman, S. P. Sree, D. Poelman, J. A. Martens, H. Poelman, and C. Detavernier, *Journal of Materials Chemistry A* **2**, 19232–19238 (2014).

[64] J. W. Elam, A. B. F. Martinson, M. J. Pellin, and J. T. Hupp, *Chemistry of Materials* **18**, 3571–3578 (2006).

[65] M. Gebhard, M. Hellwig, H. Parala, K. Xu, M. Winter, and A. Devi, *Dalton Trans.* **43**(3), 937–940 (2014).

[66] A. U. Mane, A. J. Allen, R. K. Kanjolia, and J. W. Elam, *The Journal of Physical Chemistry C* **120**(18), 9874–9883 (2016).

[67] R. K. Ramachandran, J. Dendooven, H. Poelman, and C. Detavernier, *The Journal of Physical Chemistry C* **119**(21), 11786–11791 (2015).

[68] D. Garcia-Alonso, S. E. Potts, C. a. a. van Helvoirt, M. a. Verheijen, and W. M. M. Kessels, *J. Mater. Chem. C* **3**(13), 3095–3107 (2015).

[69] X. Qian, Y. Cao, B. Guo, H. Zhai, and A. Li, *Chemical Vapor Deposition* **19**(4-6), 180–185 (2013).

[70] M.-C. Jun, S.-U. Park, and J.-H. Koh, *Nanoscale Research Letters* **7**(1), 639 (2012).

[71] M. T. Hosseinnejad, M. Ghoranneviss, M. R. Hantehzadeh, and E. Darabi, *Journal of Inorganic and Organometallic Polymers and Materials* **27**(1), 61–72 (2017).

[72] P. R. Chalker, P. A. Marshall, S. Romani, J. W. Roberts, S. J. C. Irvine, D. A. Lamb, A. J. Clayton, and P. A. Williams, *Journal of Vacuum Science & Technology A: Vacuum, Surfaces, and Films* **31**(1), 01A120 (2013).

[73] W. J. Maeng and J.-S. Park, *Journal of Electroceramics* **31**(3-4), 338–344 (2013).

[74] Z. Szabo, Z. Baji, P. Basa, Z. Czigany, I. Barsony, H.-Y. Wang, and J. Volk, *Applied Surface Science* **379**, 304–308 aug (2016).

[75] T. Nam, C. W. Lee, H. J. Kim, and H. Kim, *Applied Surface Science* **295**, 260–265 (2014).

[76] G. Machado, D. Guerra, D. Leinen, J. Ramos-Barrado, R. Marotti, and E. Dalchiele, *Thin Solid Films* **490**(2), 124–131 (2005).

[77] D. Kim, T. Nam, J. Park, J. Gatineau, and H. Kim, *Thin Solid Films* **587**, 83–87 (2015).

[78] X. Liang, Y. Ren, S. Bai, N. Zhang, X. Dai, X. Wang, H. He, C. Jin, Z. Ye, Q. Chen, L. Chen, J. Wang, and Y. Jin, *Chemistry of Materials* **26**(17), 5169–5178 (2014).

[79] C.-M. Hsu, W.-C. Tzou, C.-F. Yang, and Y.-J. Liou, *Materials* **8**(5), 2769–2781 (2015).

[80] C.-C. Lo and T.-E. Hsieh, *Ceramics International* **38**(5), 3977–3983 (2012).

[81] J.-Y. Huh, S.-B. Seo, H.-S. Park, J.-H. Jeon, H.-H. Choe, K.-W. Lee, J.-H. Seo, M.-K. Ryu, S.-H. Ko Park, and C.-S. Hwang, *Current Applied Physics* **11**(5), S49–S53 (2011).

[82] Y. Liu, Y. Li, and H. Zeng, *Journal of Nanomaterials* **2013**, 1–9 (2013).

[83] T. Tynell and M. Karppinen, *Semiconductor Science and Technology* **29**(4), 043001 (2014).

[84] L. Steier, J. Luo, M. Schreier, M. T. Mayer, T. Sajavaara, and M. Grätzel, *ACS Nano* **9**(12), 11775–11783 (2015).

[85] J. R. Avila, D. W. Kim, M. Rimoldi, O. K. Farha, and J. T. Hupp, *ACS*

Applied Materials & Interfaces **7**(30), 16138–16142 (2015).
[86] S. Selvaraj, H. Moon, J.-Y. Yun, and D.-H. Kim, *Korean Journal of Chemical Engineering* **33**(12), 3516–3522 (2016).
[87] M. Lie, H. Fjellvåg, and A. Kjekshus, *Thin Solid Films* **488**(1-2), 74–81 (2005).
[88] K. Nielsch, J. Bachmann, M. Daub, J. Jing, M. Knez, U. Gosele, S. Barth, S. Mathur, J. Escrig, and D. Altbir, *ECS Transactions* **11**(7), 139–148 (2007).
[89] J. Bachmann, J. Jing, M. Knez, S. Barth, H. Shen, S. Mathur, U. Gösele, and K. Nielsch, *Journal of the American Chemical Society* **129**(31), 9554–5 (2007).
[90] S. C. Riha, J. M. Racowski, M. P. Lanci, J. A. Klug, A. S. Hock, and A. B. F. Martinson, *Langmuir* **29**(10), 3439–45 (2013).
[91] M. Rooth, A. Johansson, K. Kukli, J. Aarik, M. Boman, and A. Hårsta, *Chemical Vapor Deposition* **14**(3-4), 67–70 (2008).
[92] A. Tamm, M. C. Dimri, J. Kozlova, A. Aidla, T. Tätte, T. Arroval, U. Mäeorg, H. Mändar, R. Stern, and K. Kukli, *Journal of Crystal Growth* **343**(1), 21–27 (2012).
[93] A. B. F. Martinson, M. J. DeVries, J. A. Libera, S. T. Christensen, J. T. Hupp, M. J. Pellin, and J. W. Elam, *The Journal of Physical Chemistry C* **115**(10), 4333–4339 (2011).
[94] J. E. Bratvold, G. Carraro, D. Barreca, and O. Nilsen, *Applied Surface Science* **347**, 861–867 (2015).
[95] R. K. Ramachandran, J. Dendooven, and C. Detavernier, *Journal of Materials Chemistry A* **2**(27), 10662 (2014).
[96] J. Zecevic, G. Vanbutsele, K. P. de Jong, and J. A. Martens, *Nature* **528**(7581), 245–248 (2015).
[97] E. Verheyen, L. Joos, K. Van Havenbergh, E. Breynaert, N. Kasian, E. Gobechiya, K. Houthoofd, C. Martineau, M. Hinterstein, F. Taulelle, V. Van Speybroeck, M. Waroquier, S. Bals, G. Van Tendeloo, C. E. A. Kirschhock, and J. A. Martens, *Nature Materials* **11**, 1059–1064 (2012).

Paper I
Low Temperature Atomic Layer Deposition of Platinum using (methylcyclopentadienyl)Trimethylplatinum and Ozone *

Abstract

Thermal atomic layer deposition (ALD) of platinum is usually achieved using molecular oxygen as reactant gas and deposition temperatures in the range 250 °C - 300 °C. In this work, crystalline thin films of metallic Pt have been grown by ALD at temperatures as low as 100 °C using (methylcyclopentadienyl)trimethylplatinum ($MeCpPtMe_3$) as Pt precursor and ozone as reactant gas. The novel process is characterized by a constant growth rate of 0.45 Å per cycle within the 250 °C - 300 °C temperature window. The Pt films are uniform with low impurity levels and close-to-bulk resistivities, even at the lowest deposition temperature. We show that the initial growth on SiO_2 surfaces is nucleation controlled and island-like, and demonstrate the good conformality of the low-temperature ALD process by Pt deposition on anodic alumina nanopores and mesoporous silica thin films.

*Published as: #Dendooven, J.; #Ramachandran, R. K.; Devloo-Casier, K.; Rampelberg, G.; Filez, M.; Poelman, H.; Marin, G. B.; Fonda, E.; Detavernier, C., *J. Phys. Chem. C*, 2013, 117, 20557-20561. (#Equally contributed: JD designed the experiments and wrote the manuscript. RKR performed all the experiments and helped in the manuscript preparation)

Introduction

Owing to the self-limiting nature of the surface reactions, atomic layer deposition (ALD) enables the controlled deposition of ultra-small amounts of platinum on complex 3D morphologies. This can be either as a thin conformal layer or, if growth is inhibited during nucleation, as dispersed nanoparticles.[1–3] Given the excellent electric and catalytic properties of Pt, but also its high cost, ALD of Pt has therefore attracted considerable attention for applications in nanoelectronics, electrochemistry, catalysis and sensing.[4–9]

The most commonly applied ALD process for Pt uses (methylcyclopentadienyl)trimethylplatinum ($MeCpPtMe_3$) and O_2 as precursors.[10] The reaction mechanism of this process has intensively been researched in recent literature and relies on combustion-like reactions that occur during both ALD half-cycles.[11–15] During the reactant pulse, O_2 is dissociatively chemisorbed on the Pt surface inducing combustion of the remaining ligands of the adsorbed $MeCpPtMe_3$ molecules and the formation of a layer of adsorbed O atoms on the surface. These O atoms then react with some of the precursor ligands during the subsequent $MeCpPtMe_3$ pulse. The optimum deposition temperature for this process is 300 °C.[10;15] Higher temperatures cause thermal decomposition of the $MeCpPtMe_3$ precursor, and for temperatures below 250 °C very low growth rates are observed. Therefore, this process cannot be applied on heat-sensitive substrates.

By using $Pt(acetylacetonato)_2$ and O_3 as precursors, metallic Pt thin films can be obtained at140 °C.[16] At 120 and 130 °C, this process results in amorphous platinum oxide thin films. Alternatively, the $MeCpPtMe_3$ precursor can be combined with an O_2 plasma to grow Pt thin films at temperatures below 300 °C. Using the O_2 plasma based process, Longrie *et al.* obtained high purity Pt films in a broad temperature window from 150 to 300 °C.[14] However, other work showed that the strong oxidizing power of the plasma can lead to oxidized platinum layers at temperatures below 300 °C.[17;18] Therefore, Knoops et al. included a third reaction step in the ALD cycle to obtain high purity Pt films at 100 °C: following the O_2 plasma step, reduction of the oxidized platinum was achieved by exposure to H_2 gas.[17]

Longrie *et al.* also reported ALD of Pt using the $MeCpPtMe_3$ precursor and a N_2 or NH_3 plasma as reactant.[14] Compared to the better known O_2 plasma process, these processes are characterized by a faster nucleation on SiO_2 substrates, resulting in very smooth Pt films. However, their temperature windows are more narrow and extend only from 250 to 300 °C for both reactants.

In this work, we studied the growth kinetics, crystalline structure, resistivity and purity of Pt thin films grown using O_3 as reactant gas in combination with the $MeCpPtMe_3$ precursor. It is shown that, despite the oxidizing power of O_3, pure Pt thin films can be obtained even at a deposition temperature of 100 °C, making this process highly attractive for Pt deposition on thermally fragile substrates. Additionally, the conformality of the $MeCpPtMe_3/O_3$ process and its nucleation behavior on a SiO_2 surface are discussed.

Experimental methods

All the depositions were performed in an experimental cold-wall ALD chamber connected through a gate valve to a turbo pump backed up by a rotary pump. A second gate valve was installed for pre-evacuation of the chamber *via* a bypass line to the rotary pump. The solid $MeCpPtMe_3$ precursor (99% Strem Chemicals), kept in a stainless steel container, was heated above its melting point (30 °C), and the delivery line to the chamber was heated to 60 °C. Argon was used as a carrier gas for the Pt precursor. O_3 was produced from a pure O_2 flow with an OzoneLabTM OL100 ozone generator, resulting in an O_3 concentration of 175 μg/ml. During both ALD half-cycles a static exposure mode was applied, meaning that the valves to the pumping system were closed while exposing the sample to the precursor or the reactant gas. Unless stated otherwise, the pulse time of the $MeCpPtMe_3$ precursor was 10 s, after which the valves to the pumping system were kept closed for another 5 s, resulting in a total exposure time of 15 s. For O_3, the pulse time was 5 s and the total exposure time 8 s. During the precursor and reactant exposures, the pressure in the chamber increased to ca. 5×10^{-1} mbar and 1 mbar, respectively. In between two exposures, first the valve to the rotary pump was opened for 5 s and then the valve to the turbo pump was opened for another 45 - 50 s. In this way, the chamber was pumped down to a pressure of *ca.* 2×10^{-5} mbar. No purge gas was used.

Film thicknesses were determined from x-ray reflectivity (XRR) and X-ray fluorescence (XRF) measurements. XRF was performed using a Bruker Artax system comprising a Mo X-ray source and an XFlash 5010 silicon drift detector. XRR and X-ray diffraction (XRD) were carried out using a Bruker D8 system with Cu Kα radiation. In situ XRD measurements were acquired during annealing of the films in a homebuilt heating chamber mounted on the diffractometer.[19;20] A linear Vantec detector with a range of 20° in 2θ was used to collect the diffracted x-rays at 3 s time intervals. The chemical composition of the deposited films was determined by x-ray photoelectron spectroscopy (XPS) using a Thermo VG Scientific ESCALAB 220i-XL with a monochromatic Al Kα X-ray source. Scanning electron microscopy (SEM) analysis was done on a FEI Quanta 200F instrument; atomic force microscopy (AFM) on a Bruker Dimension Edge system. In situ XRF measurements during ALD of Pt were performed on the SAMBA beamline at SOLEIL Synchrotron, France (proposal number 20120293).[21;22] The fluorescent radiation from the sample was captured with a Canberra 35-elements planar germanium detector.

Results and Discussion

The temperature window of the ALD process was investigated on Pt seed layers grown by sputter deposition to avoid nucleation problems. The substrates were placed on a heated sample stage and the deposition temperature was varied from 60 to 350 °C. After the deposition of 60 ALD cycles, the thickness increase of

the Pt layer was determined by XRR. A constant growth rate of 0.45 Å per cycle was obtained within a broad temperature window ranging from 100 to 300 °C (Figure 1). Nothing was deposited at 60 °C. At 350 °C, thermal decomposition of the $MeCpPtMe_3$ precursor likely contributed to the growth resulting in a slightly higher growth rate.[10] **Figure 1** also shows the temperature dependence of the growth rate for the well-known $MeCpPtMe_3/O_2$ process. Erkens *et al.* correlated the low growth rates below 250 °C to a lower combustion rate of the precursor ligands during the O_2 pulse.[15] The present data suggest that O_3 allows for more efficient removal of the precursor ligands without oxidizing the deposited Pt layer.

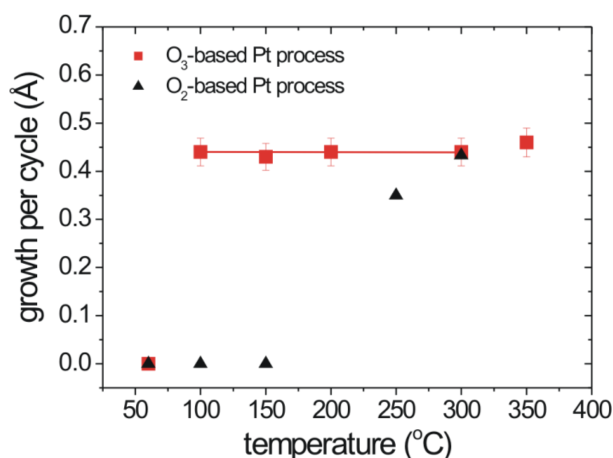

Figure 1. *ALD temperature windows of the O_3 - based and the well-known O_2 - based Pt processes. The O_3 - based process has a very broad temperature window ranging from 100 to 300 °C. The line serves as guide to the eye.*

Saturation of the ALD half-cycles was studied on sputtered Pt substrates at a deposition temperature of 150 °C. First, the pulse time of the $MeCpPtMe_3$ precursor (followed by an additional 5 s static exposure) was varied. The experiments showed that a pulse time of 1 s, resulting in a pressure of 2×10^{-1} mbar in the chamber, was sufficient to reach saturated growth (**Figure 2**a). Similar experiments were then performed for the O_3 step in the ALD process indicating that saturation of the growth per cycle was achieved at an O_3 pulse time of 3 s (followed by an additional 3 s static exposure) (**Figure 2**b).

Next, the effect of the pump time following the O_3 step on the Pt growth rate was examined (**Figure 2**c). Increasing the pump time to several minutes resulted in a significantly lower growth per cycle, a behavior that can be explained based on the reaction mechanism of the Pt ALD process. Similar to the O_2-based and O_2 plasma-based processes, a layer of adsorbed O atoms is expected to be formed on the Pt surface during the O_3 exposure step. These O atoms are needed in the subsequent precursor pulse to react with the $MeCpPtMe_3$ precursor molecules. When using long pump times, however, a fraction of the O atoms may desorb

leading to a lower Pt growth per cycle. This effect was also observed for the NH_3 and N_2 plasma-enhanced ALD processes where unstable platinum nitride intermediates are likely formed on the surface during the plasma pulse.[14]

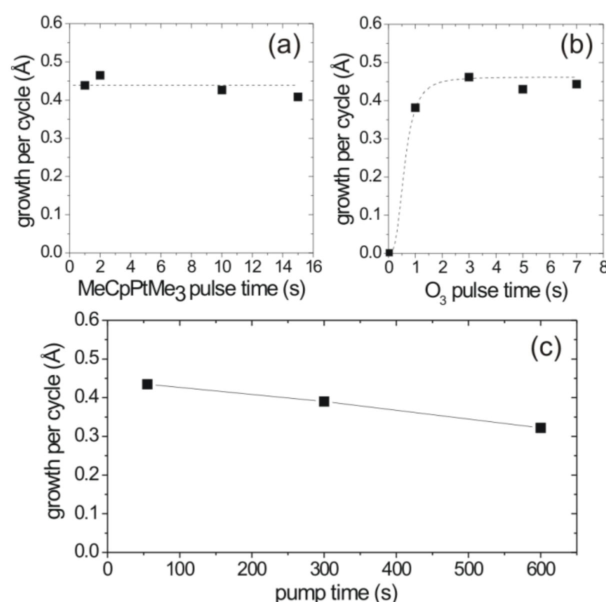

Figure 2. ALD characteristics for the $MeCpPtMe_3/O_3$ process at 150 °C on sputtered Pt substrates. The dashed lines serve as guides to the eye. (a) Growth per cycle against the $MeCpPtMe_3$ pulse time with a fixed total exposure time for O_3 of 8 s. (b) Growth per cycle against the O_3 pulse time with a fixed total exposure time for $MeCpPtMe_3$ of 15 s. (c) Growth per cycle for various pump times used after the O_3 step.

Linearity of the ALD process at 150 °C was verified on sputtered Pt and on native SiO_2/Si substrates. The thickness of the deposited Pt films was extracted from XRF measurements. On the Pt surface, the film thickness increased linearly with the number of ALD cycles without nucleation delay (**Figure 3**a). On the native SiO_2 surface, the growth rate was initially much lower than on the Pt surface, but increased then to a higher value. This behavior is often indicative of island growth,[23] a growth mode which was also observed for the thermal and plasma-enhanced O_2-based Pt ALD processes on metal oxide surfaces.[24–26] SEM images confirmed the presence of island-like Pt structures on the native SiO_2 surface (**Figure 3**b). After 200 ALD cycles, the Pt layer deposited on the Si substrate appeared to be continuous in SEM and had a RMS roughness of less than 1 nm according to AFM measurements.

The uniformity of the Pt layers was excellent, with a typical deviation in thickness of less than 2% across a two-inch area.

XPS measurements were performed on Pt layers deposited at 100, 150 and 300 °C using 200 ALD cycles on a native SiO_2/Si substrate. The C and O levels

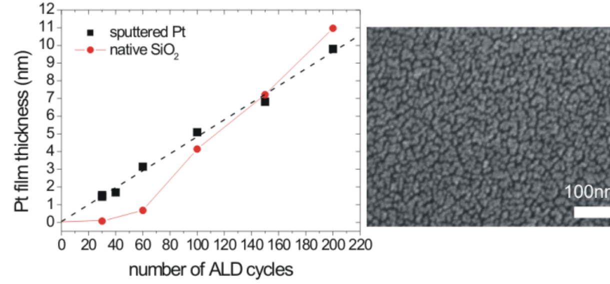

Figure 3. *ALD characteristics for the $MeCpPtMe_3/O_3$ process at 150 °C on sputtered Pt and native SiO_2/Si substrates. (a) Thickness of the deposited Pt films against the number of ALD cycles. The dashed line is a linear fit to the black square data points. (b) SEM image of a Pt layer deposited on a native SiO_2/Si substrate using 100 ALD cycles.*

were below 5 at.% in all three Pt layers and the $Pt4f_{7/2}$ peak position was 71.0 eV, indicative of metallic Pt.[27] The deposition of metallic Pt at 100 °C is in contrast with the earlier reported O_3-based process using the Pt(acetylacetonato)$_2$ precursor, which resulted in PtO_x below 140 °C.[16] A possible reason for this different outcome at low temperatures could be the difference in reactor design, involving the use of higher process pressures in reference 16 compared to our work.

The purity and metallic nature of the films was further confirmed by four point probe resistivity measurements. **Table 1** lists the resistivity values measured on 15.5 nm thick Pt layers deposited on native SiO_2/Si at different temperatures. With increasing deposition temperature, less ALD cycles were needed to obtain a Pt thickness of *ca.* 15.5 nm, most likely because of a shorter incubation period at the start of the ALD process on the native SiO_2 surface. The resistivity decreased slightly with increasing deposition temperature. The resistivity also decreased with increasing film thickness; a value of 11.9 $\mu\Omega \cdot \mathrm{cm}$ (as compared to 10.8 $\mu\Omega \cdot \mathrm{cm}$ for bulk Pt) was measured on a 24 nm thick Pt layer grown at 150 °C.

Temperature (°C)	**ALD cycles**	**Thickness (nm)**	**RMS roughness (nm)**	**Resistivity ($\mu\Omega \cdot \mathrm{cm}$)**
100	300	15.8	0.3 (± 0.02)	21.2 (± 0.5)
150	250	15.5	0.3 (± 0.02)	19.3 (± 0.5)
300	200	15.3	0.9 (± 0.02)	18.9 (± 0.3)
150	400	24.0	0.3 (± 0.02)	11.9 (± 0.2)

Table 1. *Thickness, RMS roughness and resistivity of Pt ALD films grown on native SiO_2/Si substrates at different temperatures.*

The crystalline structure of the deposited Pt films was examined by XRD. Independent of the deposition temperature, the XRD pattern revealed (111) preferentially oriented Pt (Figure 4). Additionally, the effect of annealing was studied by *in situ* XRD measurements.[19;20] A 11.2 nm thick Pt film grown on native SiO_2/Si at

150 °C was annealed in He to 600 °C at a heating rate of 1 °C/s. The inset of Figure 4 shows the evolution of the XRD pattern during this thermal treatment. The small diffraction peaks [(200) and (220)] disappeared at 450 °C, while the (111) peak intensified. Moreover, additional peaks appeared symmetrically around the (111) diffraction peak. These peaks are the result of constructive interference of x-rays reflected from the surface of the Pt film and the interface with the Si substrate. Because a smooth surface is required to obtain interference fringes, the presence of these peaks suggests that the annealing induced the formation of large, much wider than thick, smooth grains.[28]

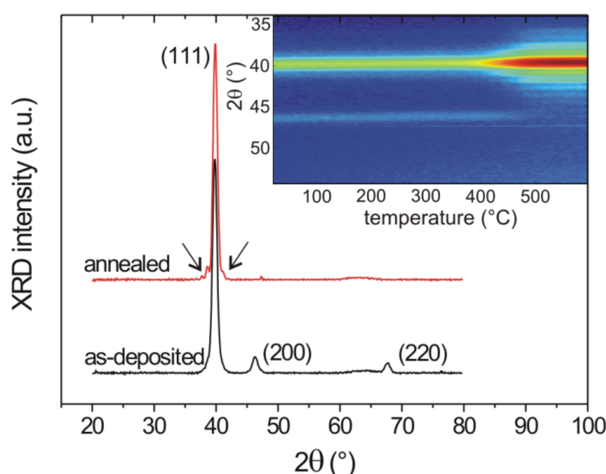

Figure 4. *XRD spectra of a Pt ALD layer grown on Si at 150 °C and of the same Pt layer after annealing in He to 600 °C at a rate of 1 °C/s. The spectra were shifted for clarity. The inset shows the evolution of the XRD pattern (logarithmic scale) during this thermal treatment.*

The conformality of the O_3-based Pt ALD process was verified by deposition on a porous anodic alumina film on Si.[29] The array of straight alumina pores with an average diameter of 23 nm was subjected to 250 ALD cycles at 150 °C using exposure times of 25 s for the $MeCpPtMe_3$ precursor and 20 s for O_3. **Figure 5**a shows a cross-sectional SEM image of the coated pore structure. Pt was clearly deposited inside the nanopores down to a depth of *ca.* 0.8μm, corresponding to a coated aspect ratio of ~ 35. The depth profile of the Pt coating was quantified using EDX line scans and is shown in **Figure 5**b. Conformal coating of larger aspect ratios should be possible by optimizing the deposition parameters.

In view of catalytic applications where the support material often contains smaller mesopores (< 10 nm), the conformality of the O_3-based Pt process was also verified in a mesoporous silica thin film with only 4 nm wide pores.[30] Ellipsometric porosimetry measurements showed that the silica film had a thickness of 161 nm, a porosity of 70% and a surface area of *ca.* 30 cm^2 per cm^2 of

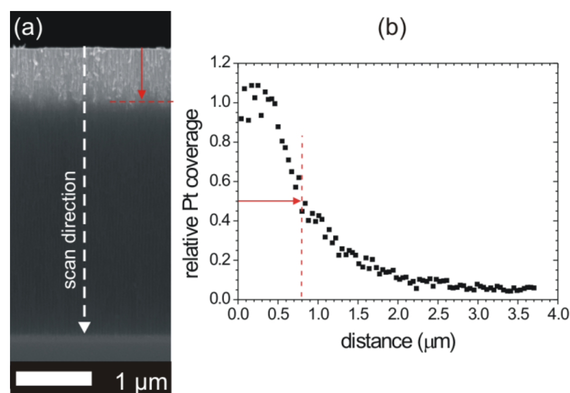

Figure 5. *(a) Cross-sectional SEM image of 23 nm wide anodic alumina nanopores coated with Pt. (b) Relative Pt coverage profile as obtained from EDX measurements. The Pt profile has been normalized to the average Pt coverage measured in the top part of the nanopores. The scan direction is indicated in (a).*

film.[31;32] Because cross-sectional studies were found to be difficult on this type of porous films, the conformality was investigated by means of *in situ* XRF measurements.[21;22] The mesoporous film was coated with Pt in an experimental ALD chamber positioned in the path of the X-ray beam at the SAMBA beamline of the SOLEIL synchrotron radiation facility, allowing for *in situ* determination of an XRF growth curve. The result is shown in **Figure 6** together with the growth curve measured on a planar Si substrate. Considerably more Pt was deposited in the mesoporous film, which is indicative of growth on the interior surface of the very small silica pores.[22]

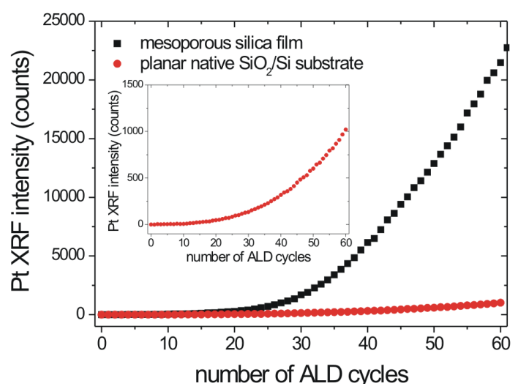

Figure 6. *XRF growth curves for Pt ALD at 150 °C in a mesoporous silica thin film and on a planar Si substrate. The inset shows the XRF growth curve for the planar substrate in more detail.*

Conclusion

$MeCpPtMe_3$ vapor was used in combination with O_3 to grow Pt thin films by ALD. A broad temperature window ranging from 100 to 300 °C was obtained for this novel process. For saturated pulse times, the growth per cycle was constant and equal to 0.45 Å within this temperature range. XRD and XPS measurements revealed that the $MeCpPtMe_3/O_3$ process yielded crystalline (strongly (111) oriented) Pt films that were metallic and pure. A close-to-bulk resistivity of 11.9 $\mu\Omega \cdot \mathrm{cm}$ was obtained for a 24 nm thick layer deposited on Si at 150 °C. The conformality of the process was proven to be excellent. We conclude that the low temperature $MeCpPtMe_3/O_3$ ALD process is very attractive for applications that require the controlled deposition of Pt on heat-sensitive substrates, including polymeric surfaces.

Acknowledgments

This research was supported by the European Research Council (Starting Grant No. 239865), by the Flemish Research Foundation FWO (Project G.0209.11), by the Special Research Fund BOF of Ghent University and by the Flemish Government through long term structural funding (Methusalem). For the XRF measurements, the authors received funding from the European Community's Trans National Access Program CALIPSO. The authors acknowledge A. Romo-Negreira and P. M. Vereecken (IMEC) for providing porous alumina substrates, S. P. Sree (Centre for Surface Chemistry and Catalysis, KULeuven) for preparing mesoporous silica films and M. Ritala (University of Helsinki) for interesting discussions. We are also grateful to the SOLEIL staff for smoothly running the facility.

References

[1] J. S. King, A. Wittstock, J. Biener, S. O. Kucheyev, Y. M. Wang, T. F. Baumann, S. K. Giri, A. V. Hamza, M. Baeumer, and S. F. Bent, *Nano Letters* **8**(8), 2405–2409 (2008).

[2] S. T. Christensen, J. W. Elam, F. A. Rabuffetti, Q. Ma, S. J. Weigand, B. Lee, S. Seifert, P. C. Stair, K. R. Poeppelmeier, M. C. Hersam, and M. J. Bedzyk, *Small* **5**(6), 750–757 (2009).

[3] C. Liu, C.-C. Wang, C.-C. Kei, Y.-C. Hsueh, and T.-P. Perng, *Small* **5**(13), 1535–1538 (2009).

[4] X. Jiang, H. Huang, F. B. Prinz, and S. F. Bent, *Chemical Materials* **20**(10), 3897–3905 (2008).

[5] R. R. Hoover and Y. V. Tolmachev, *Journal of The Electrochemical Society* **156**, A37 (2009).

[6] I. J. Hsu, D. A. Hansgen, B. E. McCandless, B. G. Willis, and J. G. Chen, *The Journal of Physical Chemistry C* **115**(9), 3709–3715 (2011).

[7] J. A. Enterkin, W. Setthapun, J. W. Elam, S. T. Christensen, F. A. Rabuffetti, L. D. Marks, P. C. Stair, K. R. Poeppelmeier, and C. L. Marshall, *ACS Catalysis* **1**(6), 629–635 (2011).

[8] Y.-H. Lin, Y.-C. Hsueh, P.-S. Lee, C.-C. Wang, J. M. Wu, T.-P. Perng, and H. C. Shih, *Journal of Materials Chemistry* **21**(28), 10552 (2011).

[9] S. Yoneoka, J. Lee, M. Liger, G. Yama, T. Kodama, M. Gunji, J. Provine, R. T. Howe, K. E. Goodson, and T. W. Kenny, *Nano letters* **12**(2), 683–6 (2012).

[10] T. Aaltonen, M. Ritala, T. Sajavaara, J. Keinonen, and M. Leskela, *Chemistry of Materials* **15**(17), 1924–1928 (2003).

[11] T. Aaltonen, A. Rahtu, M. Ritala, and M. Leskela, *Electrochemical and Solid-State Letters* **6**(9), C130 (2003).

[12] W. M. M. Kessels, H. C. M. Knoops, S. A. F. Dielissen, A. J. M. Mackus, and M. C. M. van de Sanden, *Applied Physics Letters* **95**(1), 013114 (2009).

[13] A. J. M. Mackus, N. Leick, L. Baker, and W. M. M. Kessels, *Chemistry of Materials* **24**(10), 1752–1761 (2012).

[14] D. Longrie, K. Devloo-Casier, D. Deduytsche, S. Van den Berghe, K. Driesen, and C. Detavernier, *ECS Journal of Solid State Science and Technology* **1**(6), Q123–Q129 (2012).

[15] I. J. M. Erkens, A. J. M. Mackus, H. C. M. Knoops, P. Smits, T. H. M. van de Ven, F. Roozeboom, and W. M. M. Kessels, *ECS Journal of Solid State Science and Technology* **1**(6), P255–P262 (2012).

[16] J. Hämäläinen, F. Munnik, M. Ritala, and M. Leskelä, *Chemistry of Materials* **20**(21), 6840–6846 (2008).

[17] H. C. M. Knoops, A. J. M. Mackus, M. E. Donders, M. C. M. van de Sanden, P. H. L. Notten, and W. M. M. Kessels, *Electrochemical and Solid-State Letters* **12**(7), G34 (2009).

[18] F. T. Erkens, Landaluce, A. Mackus, H. Knoops, M. Verheijen, H. Brongersma, F. Roozeboom, and E. Kessels, *Presented at the AVS Topical*

Conference on ALD, Dresden, Germany, June 17-20 (2012).

[19] W. Knaepen, C. Detavernier, R. Van Meirhaeghe, J. Jordan Sweet, and C. Lavoie, *Thin Solid Films* **516**(15), 4946–4952 (2008).

[20] W. Knaepen, S. Gaudet, C. Detavernier, R. L. Van Meirhaeghe, J. J. Sweet, and C. Lavoie, *Journal of Applied Physics* **105**(8), 083532 (2009).

[21] V. Briois, E. Fonda, S. Belin, L. Barthe, C. La Fontaine, F. Langlois, M. Ribbens, and F. Villain, *SAMBA: The 4-40 keV X-ray absorption spectroscopy beamline at SOLEIL* **2010**, 41–47 (2011).

[22] J. Dendooven, S. P. Sree, K. D. Keyser, D. Deduytsche, J. A. Martens, K. F. Ludwig, and C. Detavernier, *The Journal of Physical Chemistry C* **115**(14), 6605–6610 (2011).

[23] R. L. Puurunen and W. Vandervorst, *Journal of Applied Physics* **96**(12), 7686–7695 dec (2004).

[24] S. T. Christensen, J. W. Elam, B. Lee, Z. Feng, M. J. Bedzyk, and M. C. Hersam, *Chemistry of Materials* **21**(3), 516–521 (2009).

[25] L. Baker, A. S. Cavanagh, D. Seghete, S. M. George, A. J. M. Mackus, W. M. M. Kessels, Z. Y. Liu, and F. T. Wagner, *Journal of Applied Physics* **109**(8) (2011).

[26] H.-b.-r. Lee and S. F. Bent, *Chemistry of Materials* **24**, 279286 (2012).

[27] *NIST X-ray Photoelectron Spectroscopy Database, Version 4.1 (National Institute of Standards and Technology, Gaithersburg, 2012)* .

[28] J. Musschoot, Q. Xie, D. Deduytsche, K. De Keyser, D. Longrie, J. Haemers, S. Van den Berghe, R. Van Meirhaeghe, J. D'Haen, and C. Detavernier, *Microelectronic Engineering* **87**(10), 1879–1883 (2010).

[29] J. M. Vico, F. Jansen, K. Maex, G. Groeseneken, and P. M. Vereecken, *ECS Transactions* **3**(21), 85–93 (2007).

[30] S. P. Sree, J. Dendooven, D. Smeets, D. Deduytsche, A. Aerts, K. Vanstreels, M. R. Baklanov, J. W. Seo, K. Temst, A. Vantomme, C. Detavernier, and J. A. Martens, *Journal of Materials Chemistry* **21**(21), 7692 (2011).

[31] M. R. Baklanov, K. P. Mogilnikov, V. G. Polovinkin, and F. N. Dultsev, *J. Vac. Sci. Technol. B* **18**(3), 1385 (2000).

[32] J. Dendooven, K. Devloo-Casier, E. Levrau, R. Van Hove, S. Pulinthanathu Sree, M. R. Baklanov, J. A. Martens, and C. Detavernier, *Langmuir* **28**(8), 3852–3859 (2012).

Paper II
Plasma enhanced atomic layer deposition of Ga_2O_3 thin films *

Abstract

Amorphous Ga_2O_3 thin films have been grown on SiO_2/Si substrates by atomic layer deposition (ALD) using tris (2,2,6,6-tetramethyl-3,5-heptanedionato)gallium(III) [Ga(TMHD)$_3$] as a gallium source and O_2 plasma as reactant. A constant growth rate of 0.1 Å/cycle was obtained in a broad temperature range starting from 100 to 400 °C. X-ray photoelectron spectroscopy (XPS) analysis revealed stoichiometric Ga_2O_3 thin films with no detectable carbon contamination. A double beam - double monochromator spectrophotometer was used to measure the transmittance of Ga_2O_3 thin films deposited on a quartz substrate and analysis of the adsorption edge yielded a band gap energy of 4.95 eV. The refractive index of the Ga_2O_3 films was determined from spectroscopic ellipsometry measurements and found to be 1.84 at a wavelength of 632.8 nm. Atomic force microscopic (AFM) analysis showed surface roughness values of 0.15 and 0.51 nm for films deposited at 200 and 400 °C, respectively. Finally, all the films could be crystallized into a monoclinic β - Ga_2O_3 crystal structure by a post deposition annealing in He as indicated by X-ray diffraction (XRD) measurements.

*Published as: Ramachandran, R. K.; Dendooven, J.; Botterman, J.; Sree, S. P.; Poelman, D.; Martens, J. A.; Poelman, H.; Detavernier, C., *J. Mater. Chem. A*, 2014, 2, 19232-19238.

Introduction

Gallium oxide exists in several crystalline forms, of which the monoclinic (β - Ga_2O_3) phase has attracted much attention in recent years. Its very high thermal and chemical stability, along with the temperature dependent conducting behavior[1] makes it an important material in gas sensing applications. For example, at high temperatures (800 -1000 °C) the films can be used as oxygen sensors[2–6] while at lower temperatures (< 700 °C) they are suitable for sensing reducing gases.[7–9] With a wide band gap of 4.9 eV, Ga_2O_3 exhibits conductive and photoluminescent[10–12] properties, rendering it a promising candidate for applications such as transparent conducting material[13–16] in next generation optoelectronic devices and deep-UV photodetectors.[17;18] The value of the refractive index close to the square root of the refractive index of GaAs allows it to be used as an efficient single-layer antireflection coating for GaAs.[19–21] Ga_2O_3 has also been used in catalytic[22;23] and photocatalytic[24] applications. Moreover gallium doped zinc oxide (Ga: ZnO) has become one of the most important candidates for TCO applications.[25;26]

Currently, there are several methods employed for gallium oxide thin film deposition including sol-gel synthesis,[4;22;24;27] spray pyrolysis,[10;28] electron beam evaporation,[20;21;29] pulsed laser deposition,[12–15;30;31] sputter deposition,[2;3;5–9;32] molecular beam epitaxy (MBE),[16;17] chemical vapour deposition (CVD)[33–37] and atomic layer deposition (ALD).[38–49] Among them, ALD is one of the most promising, allowing one to obtain highly conformal materials with excellent thickness uniformity and composition control. There have been many efforts to obtain conformal ALD - Ga_2O_3 films using various precursors. The first successful ALD process for Ga_2O_3 was demonstrated by Nieminen et al.[38] employing $Ga(acac)_3$ and either water or ozone, but relatively high deposition temperatures (> 370 °C) were required and an acceptable composition was only obtained with ozone. Among the processes that use amine-based precursors, the $Ga_2(NMe_2)_6$ and water process[40] has a narrow temperature window (170 - 250 °C), while the process that uses $[(CH_3)_2GaNH_2]_3$ and O_2 plasma[39–41;49] is limited to a working temperature of 200 °C. Similarly, isopropoxide precursors are also limited by a narrow temperature window (280 - 300 °C[43] and 150 - 250 °C[46]). Trimethyl gallium (TMGa) was recently introduced as a promising precursor for ALD of Ga_2O_3 in combination with ozone[44] or O_2 plasma.[47] Especially the plasma-activated process exhibits a wide temperature window, enabling the deposition of Ga_2O_3 films with a growth rate of 0.53 Å/cycle at temperatures as low as 100 °C.[47]

In this work, we use a beta-diketonate precursor, tris (2,2,6,6-tetramethyl-3,5-heptanedionato)gallium(III), $[Ga(TMHD)_3]$ as a gallium source and O_2 plasma as reactant. This process exhibits a broad temperature window (100 to 400 °C) similar to the TMGa and O_2 plasma process. Even though the growth rate of the novel process is lower (0.1 Å/cycle), this could be beneficial for doping applications where the concentration of the dopant has to be precisely controlled.[25;26] Additional advantages are its low cost, non-toxicity, and ease of handling. Moreover, it is worth mentioning that the beta-diketonate precursor has an enhanced volatility and thermal stability compared to the acetylacetone parent derivative induced

by the replacement of the methylsubstituents on the acac ligands with tert-butyl groups.[50;51] As oxygen source, we tested H_2O, O_3 and O_2 plasma and found that only O_2 plasma resulted in successful deposition of gallium oxide. Hardly any growth was observed by performing 200 ALD cycles using H_2O or O_3 as reactant at a deposition temperature of 300 °C. On the other hand, the introduction of plasma during the ALD process enabled the deposition of high quality thin films at low temperatures.

Experimental methods

All the depositions were performed on Si substrates covered with 100 nm thermally grown SiO_2 (SiO_2/Si) in a home-built pump type ALD reactor[52;53] with an operating base pressure of below 5×10^{-6} mbar. The chamber wall was heated to 150 °C. The solid Ga(TMHD)$_3$ precursor (99%, Strem Chemicals), kept in a stainless steel container, was heated to 135 °C, and the delivery line to the chamber was heated to 138 °C. For the remote plasma process the O_2 gas flowed through the plasma source at a pressure of 0.03 mbar and the RF plasma power was set at 300 W. The precursor was injected through a quarter inch stainless steel tube located at the top of the ALD chamber. Unless stated otherwise, the pulse times were 5 s for both the Ga(TMHD)$_3$ precursor and O_2 plasma. No purge gas was used in the deposition cycle.

The thickness of the growing Ga_2O_3 films was monitored *in situ* using spectroscopic ellipsometry (SE, J. A. Woollam M-2000). A Cauchy model was applied for fitting the ellipsometric data to obtain the film thickness and optical properties. The determination of film thickness by *in situ* SE was complemented by *ex situ* X-ray reflectivity (XRR) measurements. XRR was carried out using a Bruker D8 Discover system with Cu Kα radiation. X-ray fluorescence (XRF) measurements were performed using a Mo X-ray source (at an angle of 45° with sample surface) and a silicon drift detector placed at an angle of 52° with the sample surface. The fluorescence signal was integrated over a period of 100 s. The chemical composition of the deposited films was determined by X-ray photoelectron spectroscopy (XPS) using a Thermo VG Scientific ESCALAB 220i-XL with a monochromatic Al Kα X-ray source. The reported Binding Energy values (BE) were corrected for charging effects by assigning a BE of 284.6 eV to the C1s signal. The film crystallinity was investigated by X-ray diffraction (Bruker D8 Discover, Cu Kα radiation). The surface roughness of the films was determined by atomic force microscopy (AFM) on a Bruker Dimension Edge system operating in tapping mode in air. The Root Mean Square (RMS) roughness values were calculated on 5 μm x 5 μm micrographs. To measure the transmittance, a 10 nm thick Ga_2O_3 film was deposited on a quartz substrate. The optical transmittance at normal incidence was measured with a double beam double monochromator UV-VIS-NIR spectrophotometer (Cary 500, Varian, USA) in the UV-visible range (200 - 600 nm).

The ALD process was characterized by *in situ* quadrupole mass spectrometry (QMS, Hiden Analytical) using the spectrometer in Multiple Ion Detection (MID)

mode with the Faraday detector (source voltage 70 V).

Finally, post-annealing of the deposited films in He was performed in a home-built heating chamber mounted on a Bruker D8 diffractometer[54;55] to enable *in situ* XRD characterization. A linear detector was used to collect the diffracted X-rays at 2 s time intervals.

Results and Discussion

Characteristics of the Gallium Oxide ALD process

The temperature window of the ALD process was investigated on Si substrates covered with 100 nm thermally grown SiO_2. Depositions were carried out over a wide temperature range from 75 to 400 °C. **Figure 1** shows the variation in growth per cycle (GPC) with the temperature of the substrate. A constant growth rate of 0.1 Å per cycle was obtained within a temperature window ranging from 100 to 400 °C. This broad temperature window could be of interest for doping applications, where the deposition temperatures for different ALD processes have to overlap.[25;26] A higher growth rate was observed below 100 °C, probably due to condensation of the precursor onto the substrate or the incomplete removal of the reaction by-products at low temperatures causing some organic residues from the precursor ligands to become incorporated into the film. The temperature stability of the $Ga(TMHD)_3$ precursor at higher temperature was also tested. For this, a SiO_2/Si substrate and an ALD grown Ga_2O_3 film were placed on the sample holder at 400 °C. Then the precursor alone was pulsed into the reactor without O_2 plasma half cycle. No thickness increase was found even after 300 precursor pulses, confirming that no decomposition of the precursor occurred at 400 °C.

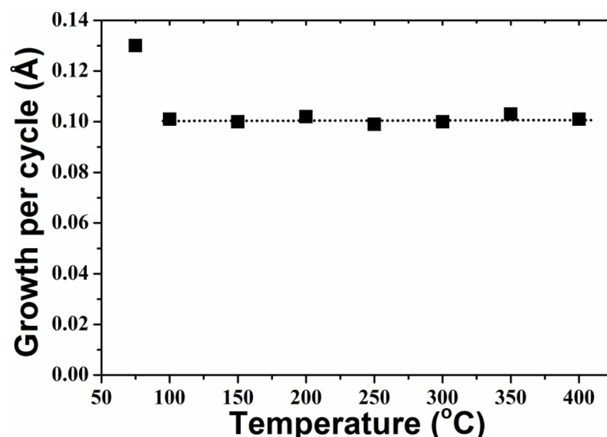

Figure 1. *Growth rate as a function of deposition temperature. The dotted line serves as a guide to the eye.*

Saturation of the ALD half-cycles was studied on SiO_2/Si substrates at a deposition temperature of 200 °C. **Figure 2** shows the saturation curves for the $Ga(TMHD)_3$ precursor (triangles) and O_2 plasma (circles) half cycles respectively. First, the pulse time of the $Ga(TMHD)_3$ precursor was varied while keeping a constant O_2 plasma exposure of 5s. The experiments showed that a pulse time of 4s, at a pressure of 3×10^{-3} mbar in the chamber, was sufficient to reach saturated growth. Similar experiments were then performed for the O_2 plasma step and the saturation of the growth per cycle was achieved at an O_2 plasma pulse time of 2 s.

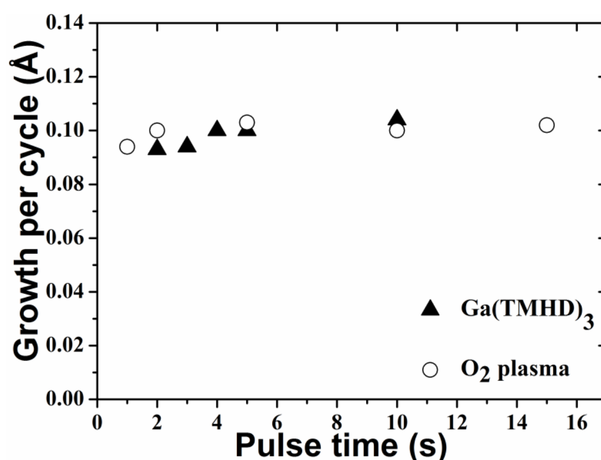

Figure 2. *Growth per cycle against the $Ga(TMHD)_3$ pulse time (triangles), using a fixed O_2 plasma exposure of 5 s and growth per cycle against the O_2 plasma exposure time (circles), using a fixed $Ga(TMHD)_3$ pulse time of 5s at 200 °C.*

To get more insights into the mechanisms of this novel process, *in situ* QMS was used to analyze the reaction products formed during both ALD half cycles. The surface reaction kinetics of adsorbed metal β-diketonate precursors with O radicals has been studied extensively by T.T. Van and J.P. Chang.[51;56] According to the mechanism described in their work, the incoming $Ga(TMHD)_3$ molecules are expected to adsorb non-dissociatively on the surface during the precursor pulse. In the subsequent O_2 plasma pulse, O radicals will react with the organic β-diketonate ligands, likely leading to the formation of non-volatile metal oxide and volatile CO and CO_2. This type of ligand combustion mechanism is common in plasma enhanced ALD processes using any kind of organometallic precursors.[57–60] To analyze the formation of reaction products during the $Ga(TMHD)_3/O_2$ plasma process a series of QMS measurements in MID mode were performed. In the same scan 5 precursor pulses (A) were monitored, followed by 3 full ALD cycles (*i.e.* precursor and reactant pulse (AB)) and nally 5 reactant pulses (B). The sequence monitored is thus: AAAAA ABABAB BBBBB. During the successive precursor pulses (A) and successive reactant pulses (B), no reactions occur, so a clean precursor (A) or reactant (B) signal is obtained for the dierent mass-to-charge ratios

that are being monitored. By comparing these reference signals with the precursor and reactant signal during the ALD cycles (AB), the formation of reaction products can be interpreted. A series of relevant mass-to-charge ratios was followed during the scan, however, the only reaction products that could be detected were CO (m/z = 28) and CO_2 (m/z = 44). The QMS data recorded during the fifth precursor pulse (A), the three complete ALD cycles (ABABAB) and the next two O_2 plasma (B) pulses are shown in the **Figure 3**. It can be seen that similar QMS signals are obtained during both the pure precursor pulse (A) and the precursor pulse in the ALD cycle (AB), which indicates that no gaseous reaction products can be detected during the precursor half cycle and that the precursor molecules indeed adsorb non-dissociatively on the surface. After pumping out the reaction products, oxygen plasma was introduced and the partial pressure of both CO_2 and CO increased. As oxygen plasma continued to be dosed, both reaction product signals decreased, meaning that the reaction approached completion. The sharp spike in the MID signal was not observed during the pure O_2 plasma (B) pulse, indicating that the detected formation of CO_2 and CO during the O_2 plasma (B) pulse of the ALD cycle (AB) can be attributed the reaction of O radicals with the adsorbed precursor molecules. The results obtained from our experiment are therefore consistent with the observations in the above mentioned references.[51;56]

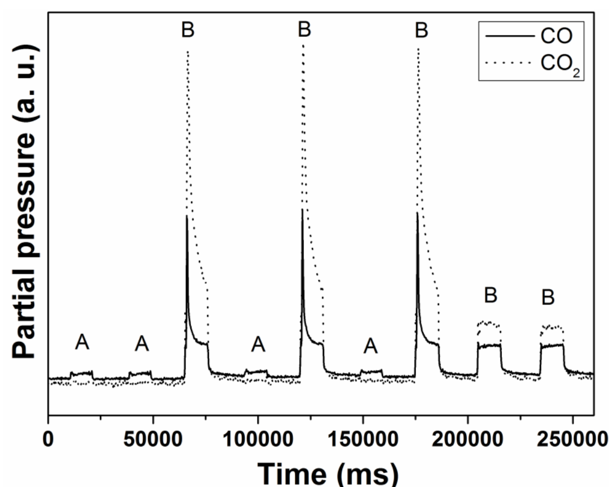

Figure 3. *In situ mass spectrometry results for CO (m/z = 28) and CO_2 (m/z = 44) during different precursor (A) and reactant (B) pulses.*

Linearity of the ALD process at 200 °C was verified on SiO_2/Si substrates. Figure 4 shows that the film thickness depends linearly on the number of reaction cycles without any nucleation delay, that is, the growth rate remains constant throughout the process.

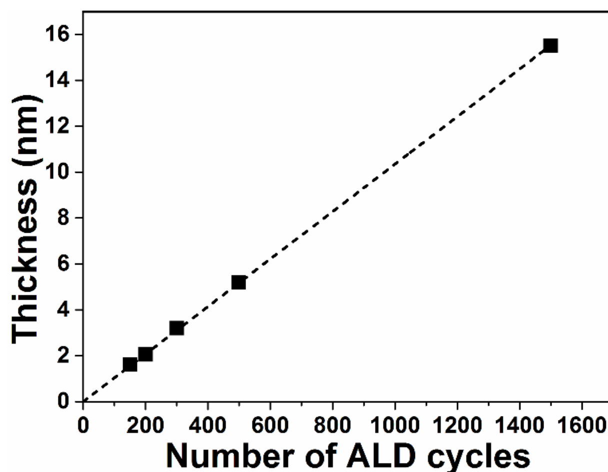

Figure 4. *Thickness of the Ga_2O_3 films deposited at 200 °C on SiO_2/Si substrates against the number of ALD cycles.*

Properties of the Gallium Oxide Films

Gallium oxide films were deposited on 100 nm SiO_2/ Si substrates using the conditions described in the experimental section. All the deposited films were continuous and the thickness uniformity was excellent, with a typical deviation in thickness of less than 2% across a two-inch area. Phase identification of *ca.* 30 nm thick films was performed using XRD measurements. All the films were found to be amorphous in the as-deposited state irrespective of their deposition temperature. Upon annealing under He atmosphere, polycrystalline β - Ga_2O_3 films with a monoclinic crystal structure were obtained. **Figure 5** shows the XRD patterns for the as-deposited film at 200 °C and for the same film annealed in He to 900 °C at a heating rate of 0.2 °C/s. The inset of **Figure 5** shows the evolution of the XRD pattern during this thermal treatment. Crystallization of the film started at 630 °C, as revealed by the intensification of the peak corresponding to β - Ga_2O_3 [(004), (-104)].

Chemical composition and bonding states of the deposited Ga_2O_3 thin films were studied by XPS. **Figure 6** (a) shows the survey spectra collected for the film deposited on the SiO_2/Si substrate at 200 °C before and after sputtering in the XPS chamber. The spectra show relevant photoelectron peaks for gallium (Ga $2p_{1/2}$, Ga $2p_{3/2}$, Ga 3s, Ga 3p, and Ga 3d) and oxygen (O 1s, O 2s), together with the Auger lines from gallium (GaLMM) and oxygen (OKVV, OKLL).[33;35;43;61] The spectrum before sputtering showed surface contamination by carbon, but after the sputtering process, the carbon peak was not observed. The binding energies of the Ga $2p_{1/2}$ (1118.5 eV), Ga $2p_{3/2}$ (1145.5 eV) [**Figure 6**(b)] and O 1s (531.5 eV) photoelectron peaks obtained from a high-resolution spectrum indicate that the gallium is in the 3^+ oxidation state (Ga^{3+}). The Ga/O ratio (0.64) was found

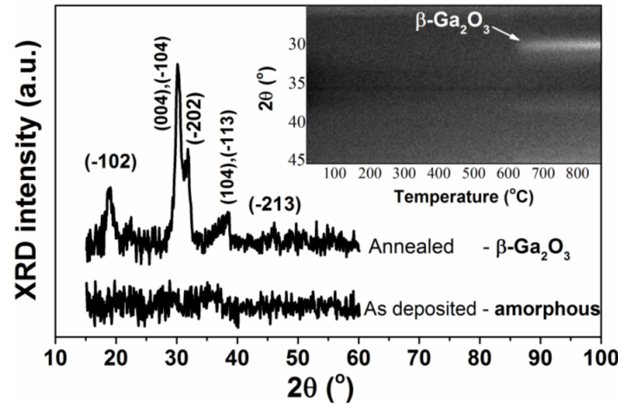

Figure 5. *XRD patterns of a 30 nm thick Ga_2O_3 film deposited at 200 °C on a SiO_2/Si substrate and of the same film after annealing in He to 900 °C at a heating rate of 0.2 °C/s. The inset shows the evolution of the XRD pattern during this thermal treatment.*

to be in agreement with the stoichiometry expected for Ga_2O_3. Comparing these observations with those reported in literature,[33;35;37;38;43;45;61;62] it can be concluded that the deposited films are Ga_2O_3.

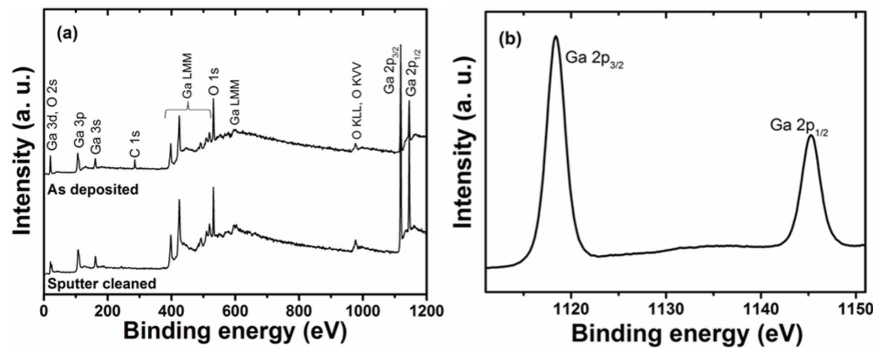

Figure 6. *XPS spectra of a Ga_2O_3 film deposited at 200 °C. (a) Survey spectra and (b) high-resolution measurement of the Ga 2p peaks.*

The optical properties of the as-deposited Ga_2O_3 films were determined using spectroscopic ellipsometry and optical transmittance measurements. The inset of **Figure 7** shows the transmittance of a 10 nm thick (determined with XRR) Ga_2O_3 film deposited on a quartz substrate at 200 °C divided by the transmittance of the bare quartz substrate. The film shows a nearly 100% optical transmission in the visible region, which is an important property for applications of Ga_2O_3 as TCO material or as antireflection coating. To determine the band gap (Eg) of the material, the absorption coefficient α was calculated form the transmittance, T, and

the film thickness, d, as ln(T)/d. In **Figure 7**, $[\alpha(h\nu)]^2$ is plotted against the photon energy hν. Because β - Ga_2O_3 is a direct band gap material, the value of the optical band gap can be determined from this plot by interpolation of the linear fit to the absorption edge to zero.[49;63] As shown in **Figure 7**, this analysis yielded a value of 4.95 eV, in agreement with reported values in literature.[49;64]

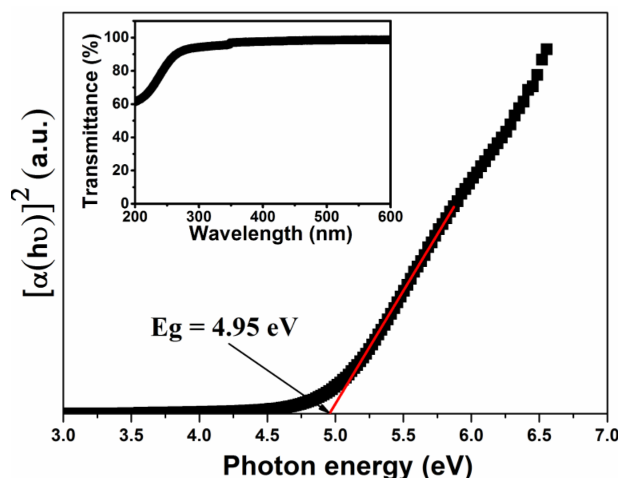

Figure 7. *$[\alpha(h\nu)]^2$ versus photon energy plot for a 10 nm β - Ga_2O_3 film deposited on a quartz substrate at 200 °C. The band gap energy is determined from the linear fit (red line) to the absorption edge as indicated. The inset of the figure shows the transmittance spectrum of the same film divided by the transmittance of the bare quartz substrate.*

In spectroscopic ellipsometry, the change in polarization of light upon reflection from a sample is described by an amplitude ratio, Ψ, and a phase difference, Δ, and is measured for a range of photon wavelengths (245 - 1200 nm). **Figure 8** shows the Ψ (red line) and Δ (blue line) values measured for a 10.5 nm thick (determined with XRR) Ga_2O_3 film deposited on a SiO_2 substrate at 200 °C. From this data, the refractive index of the Ga_2O_3 film can be deduced through a fitting-based analysis. Because of the excellent transparency of the Ga_2O_3 film in the considered wavelength range, as revealed by the transmittance measurements, it is valid to use a Cauchy relation to model the refractive index of the Ga_2O_3 film: $n(\lambda) = A + B/\lambda^2 + C/\lambda^4$. As can be seen in **Figure 8**, an excellent fit (dashed black lines) is obtained for values of 1.805, 0.013 and 0.000442 for A, B and C respectively. The variation of refractive index (n) with the wavelength as obtained from the analysis is shown in the inset of **Figure 8**. Independent of the deposition temperature, this fitting procedure yielded a refractive index value (n) of 1.84 at a wavelength of 632.8 nm, in agreement with literature values reported for Ga_2O_3 films prepared by other methods.[20;28;49]

The morphology of the films was studied using AFM (**Figure 9**). The films grown at low temperature (200 °C) were found to be very smooth (rms roughness

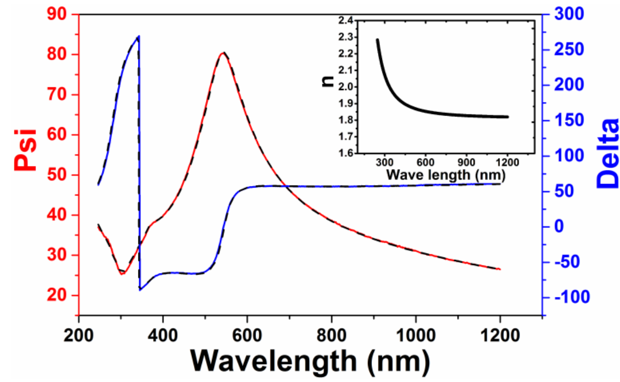

Figure 8. *Ellipsometry signals Ψ (red line) and Δ (blue line) for a 10.5 nm Ga_2O_3 film deposited on a SiO_2 substrate at 200 °C. The dashed lines are the and curves generated by the Cauchy model. The inset shows the variation of refractive index (n) with the wavelength.*

∼ 1 - 2 Å), with a roughness that slightly increased during crystallization anneal (up to ∼ 3 Å). Films grown at a higher temperature (400 °C) were slightly rougher as-deposited (rms roughness ∼ 5 - 6 Å), but the roughness did not increase after crystallization. The rms roughness values obtained from the AFM analysis were in good agreement with the roughness estimated from XRR measurements. XRR analysis also revealed a roughness of ∼ 3 - 4 Å for the Si or SiO_2 substrate after the deposition of Ga_2O_3, suggesting a smooth film/substrate interface.

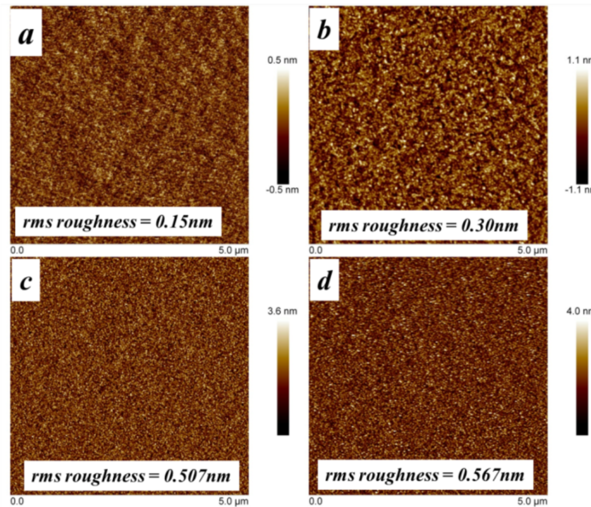

Figure 9. *Atomic force micrographs of 30 nm thick Ga_2O_3 films deposited at 200 °C (a) before and (b) after crystallization, and at 400 °C (c) before and (d) after crystallization.*

Finally, in view of applications where Ga_2O_3 thin films are needed on complex 3D substrates, e.g. large area nanostructured substrates for sensing or catalytic applications, the conformal nature of the novel PE-ALD process was verified. Ga_2O_3 was deposited in a mesoporous silica thin film with only 6 nm wide pores. Mesoporous films with fully accessible porosity was synthesized on Si supports using a reported procedure.[65] Ellipsometric porosimetry measurements showed that the silica film had a thickness of 150 nm, a porosity of 55% and a surface area of ca. 25 cm^2 per square centimeter of film. Because cross-sectional electron microscopy studies were found to be difficult for this type of porous films, the conformality was investigated by means of XRF.[57;66–69] The mesoporous film together with a planar SiO_2/Si reference was loaded into the deposition chamber and was heated to 200 °C. A long pulse time of 20 s was used for the Ga(TMHD)$_3$ to ensure the conformal coating into the pores. The O_2 plasma exposure time was 15 s. A series of depositions were performed by varying the number of ALD cycles. After the deposition the amount material deposited was determined by XRF measurements. The integrated area under the Ga Kα peak was then plotted against the number of ALD cycles (**Figure 10**). Considerably more Ga_2O_3 was deposited in the mesoporous film during the first 200 ALD cycles, confirming conformal growth on the interior surface of the very small silica pores. From 250 ALD cycles, linear growth at a rate which is more similar to the growth on the planar reference is observed. This indicates that the small mesopores became inaccessible for the Ga(TMHD)$_3$ precursor and that growth continued on top of the coated mesoporous film.

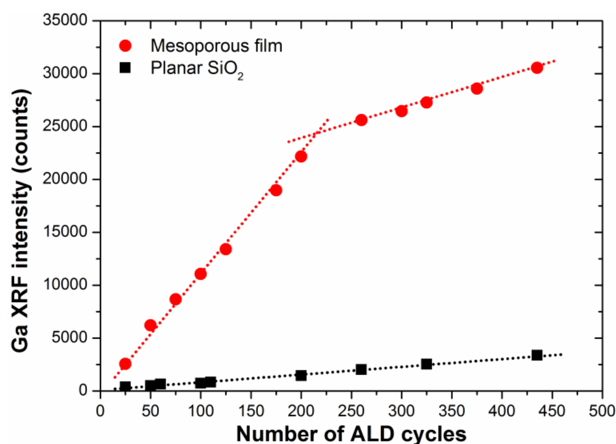

Figure 10. *XRF growth curves for Ga_2O_3 ALD at 200 °C in a mesoporous silica thin film and on a planar SiO_2 substrate.*

Conclusion

We have demonstrated a new process for the ALD of Ga_2O_3 thin films using tris (2,2,6,6-tetramethyl-3,5-heptanedionato) gallium(III) [Ga(TMHD)$_3$] as a gallium source and O_2 plasma as reactant. A constant growth rate of 0.1 Å/cycle was obtained in a broad temperature range starting from 100 to 400 °C. XPS studies confirmed the presence of Ga_2O_3. As-deposited films were found to be amorphous, while annealing in He resulted in the formation of β - Ga_2O_3 with monoclinic crystal structure. The refractive index and optical band gap of the material were determined to be 1.84 and 4.95 eV, respectively. Surface morphology studies of the films showed fairly smooth films (RMS roughness of 0.15 to 0.51 nm) with a slight increase in roughness upon annealing. Finally, Ga_2O_3 was deposited conformally in sub-10 nm silica mesopores, making this process attractive for the design of novel sensing and catalytic nanostructured surfaces.

Acknowledgments

This research was supported by the European Research Council (Starting Grant No. 239865), by the Flemish Research Foundation (FWO), the 'Long Term Structural Methusalem Funding by the Flemish Government' and by the Special Research Fund BOF of Ghent University (GOA 01G01513).

References

[1] M. Fleischer and H. Meixner, *Journal of Applied Physics* **74**(1), 300 (1993).
[2] M. Fleischer and H. Meixner, *Sensors and Actuators B* **5**, 115–119 (1991).
[3] M. Ogita, *Applied surface science* **142**, 188–191 (1999).
[4] Y. Li, A. Trinchi, W. Wlodarski, K. Galatsis, and K. Kalantar-Zadeh, *Sensors and Actuators B* **93**(1-3), 431–434 (2003).
[5] M. Ogita, S. Yuasa, K. Kobayashi, Y. Yamada, Y. Nakanishi, and Y. Hatanaka, *Applied Surface Science* **212-213**, 397–401 (2003).
[6] C. Baban, Y. Toyoda, and M. Ogita, *Thin Solid Films* **484**(1-2), 369–373 (2005).
[7] M. Fleischer, J. Giber, and H. Meixner, *Applied Physics A* **54**, 560–566 (1992).
[8] O.-A. Ring and D. Mllnchen, *Sensors and Actuators B* **34**, 378–382 (1996).
[9] M. Fleischer, S. Kornely, T. Weh, J. Frank, and H. Meixner, *Sensors and Actuators B* **69**(1), 205–210 (2000).
[10] J. Hao and M. Cocivera, *Journal of Physics D* **35**, 433–438 (2002).
[11] E. Nogales, J. A. Garcia, B. Mendez, and J. Piqueras, *Journal of Applied Physics* **101**(3), 033517 (2007).
[12] P. Wellenius, A. Suresh, and J. F. Muth, *Applied Physics Letters* **92**(2), 021111 (2008).
[13] M. Orita, H. Ohta, M. Hirano, and H. Hosono, *Applied Physics Letters* **77**(25), 4166–4168 (2000).
[14] M. Orita, H. Hiramatsu, H. Ohta, M. Hirano, and H. Hosono, *Thin Solid Films* **411**(1), 134–139 (2002).
[15] K. Matsuzaki, H. Yanagi, T. Kamiya, H. Hiramatsu, K. Nomura, M. Hirano, and H. Hosono, *Applied Physics Letters* **88**(9), 092106 (2006).
[16] E. G. Villora, K. Shimamura, K. Kitamura, and K. Aoki, *Applied Physics Letters* **88**(3), 031105 (2006).
[17] T. Oshima, T. Okuno, and S. Fujita, *Japanese Journal of Applied Physics* **46**(11), 7217–7220 (2007).
[18] S. Kumar and R. Singh, *physica status solidi (RRL)* **7**(10), 781–792 (2013).
[19] M. Taniguchi, T. Murakawa, and Y. Kajitani, *Applied surface science* **56-58**, 827–831 (1992).
[20] M. Passlack, N. E. J. Hunt, E. F. Schubert, G. J. Zydzik, M. Hong, J. P. Mannaerts, R. L. Opila, and R. J. Fischer, *Applied Physics Letters* **64**(20), 2715 (1994).
[21] N. C. Oldham, C. J. Hill, C. M. Garland, and T. C. McGill, *Journal of Vacuum Science & Technology A* **20**(3), 809–813 (2002).
[22] M. Haneda, Y. Kintaichi, T. Mizushima, N. Kakuta, and H. Hideaki, *Applied Catalysis B* **31**, 81–92 (2001).
[23] K.-J. Chao and P.-H. Liu, *Catalysis Surveys from Asia* **9**(1), 11–15 (2005).
[24] Y. Hou, L. Wu, X. Wang, Z. Ding, Z. Li, and X. Fu, *Journal of Catalysis* **250**(1), 12–18 (2007).
[25] W. J. Maeng and J.-S. Park, *Journal of Electroceramics* **31**(3-4), 338–344

(2013).

[26] P. R. Chalker, P. A. Marshall, S. Romani, J. W. Roberts, S. J. C. Irvine, D. A. Lamb, A. J. Clayton, and P. A. Williams, *Journal of Vacuum Science & Technology A: Vacuum, Surfaces, and Films* **31**(1), 01A120 (2013).

[27] T. Minami, T. Shirai, T. Nakatani, and T. Miyata, *Japanese Journal of Applied Physics* **39**, L524–L526 (2000).

[28] A. Ortiz, J. C. Alonso, E. Andrade, and C. Urbiola, *Journal of The Electrochemical Society* **148**(2), F26–F29 (2001).

[29] S. Pal, S. K. Ray, B. R. Chakraborty, S. K. Lahiri, and D. N. Bose, *Journal of Applied Physics* **90**(8), 4103–4107 (2001).

[30] K. Matsuzaki, H. Hiramatsu, K. Nomura, H. Yanagi, T. Kamiya, M. Hirano, and H. Hosono, *Thin Solid Films* **496**(1), 37–41 (2006).

[31] L. Nagarajan, R. A. De Souza, D. Samuelis, I. Valov, A. Börger, J. Janek, K.-D. Becker, P. C. Schmidt, and M. Martin, *Nature materials* **7**(5), 391–398 (2008).

[32] S. S. Kumar, E. Rubio, M. Noor-A-Alam, G. Martinez, S. Manandhar, V. Shutthanandan, S. Thevuthasan, and C. Ramana, *The Journal of Physical Chemistry C* **117**(8), 4194–4200 (2013).

[33] G. Battiston, R. Gerbasi, M. Porchia, R. Bertoncello, and F. Caccavale, *Thin Solid Films* **279**(1-2), 115–118 (1996).

[34] S. Bott, L. Miine, S. Suh, J. Liu, W. Chu, and D. Hoffman, *Journal of Materials Chemistry* **9**(4), 929–935 (1999).

[35] M. Valet and D. M. Hoffman, *Chemistry of Materials* **13**(6), 2135–2143 (2001).

[36] H. W. Kim and N. H. Kim, *Applied Surface Science* **230**(1-4), 301–306 (2004).

[37] S. Basharat, C. J. Carmalt, R. Binions, R. Palgrave, and I. P. Parkin, *Dalton transactions* **9226**(5), 591–595 (2008).

[38] M. Nieminen, L. Niinisto, and E. Rauhala, *Journal of Materials Chemistry* **6**(1), 27–31 (1996).

[39] N.-J. Seong, S.-G. Yoon, and W.-J. Lee, *Applied Physics Letters* **87**(8), 082909 (2005).

[40] C. L. Dezelah, J. Niinisto, K. Arstila, L. Niinisto, and C. H. Winter, *Chemistry of Materials* **18**, 471–475 (2006).

[41] F. K. Shan, G. X. Liu, W. J. Lee, G. H. Lee, I. S. Kim, and B. C. Shin, *Integrated Ferroelectrics* **80**(1), 197–206 (2006).

[42] G. X. Liu, F. K. Shan, J. J. Park, W. J. Lee, G. H. Lee, I. S. Kim, B. C. Shin, and S. G. Yoon, *Journal of Electroceramics* **17**, 145–149 (2006).

[43] H. Lee, K. Kim, J.-J. Woo, D.-J. Jun, Y. Park, Y. Kim, H. W. Lee, Y. J. Cho, and H. M. Cho, *Chemical Vapor Deposition* **17**(7-9), 191–197 (2011).

[44] D. J. Comstock and J. W. Elam, *Chemistry of Materials* **24**, 4011–4018 (2012).

[45] A. K. Chandiran, N. Tetreault, R. Humphry-Baker, F. Kessler, E. Baranoff, C. Yi, M. K. Nazeeruddin, and M. Grätzel, *Nano letters* **12**(8), 3941–3947 (2012).

[46] D. W. Choi, K.-B. Chung, and J.-S. Park, *Thin Solid Films* **546**, 31–34 (2013).

[47] I. Donmez, C. Ozgit-Akgun, and N. Biyikli, *Journal of Vacuum Science & Technology A* **31**(1), 01A110 (2013).

[48] H. Altuntas, I. Donmez, C. Ozgit-Akgun, and N. Biyikli, *Journal of Vacuum Science & Technology A* **32**(4), 041504 (2014).

[49] F. K. Shan, G. X. Liu, W. J. Lee, G. H. Lee, I. S. Kim, and B. C. Shin, *Journal of Applied Physics* **98**(2), 023504 (2005).

[50] B. D. Fahlman and A. R. Barron, *ADVANCED MATERIALS FOR OPTICS AND ELECTRONICS* **10**, 223–232 (2000).

[51] T. T. Van and J. P. Chang, *Applied Surface Science* **246**(1-3), 250–261 jun (2005).

[52] Q. Xie, Y.-L. Jiang, C. Detavernier, D. Deduytsche, R. L. Van Meirhaeghe, G.-P. Ru, B.-Z. Li, and X.-P. Qu, *Journal of Applied Physics* **102**(8), 083521 (2007).

[53] J. Musschoot, Q. Xie, D. Deduytsche, K. De Keyser, D. Longrie, J. Haemers, S. Van den Berghe, R. Van Meirhaeghe, J. D'Haen, and C. Detavernier, *Microelectronic Engineering* **87**(10), 1879–1883 (2010).

[54] W. Knaepen, C. Detavernier, R. Van Meirhaeghe, J. Jordan Sweet, and C. Lavoie, *Thin Solid Films* **516**(15), 4946–4952 (2008).

[55] W. Knaepen, S. Gaudet, C. Detavernier, R. L. Van Meirhaeghe, J. J. Sweet, and C. Lavoie, *Journal of Applied Physics* **105**(8), 083532 (2009).

[56] T. T. Van and J. P. Chang, *Surface Science* **596**(1-3), 1–11 (2005).

[57] R. K. Ramachandran, J. Dendooven, and C. Detavernier, *Journal of Materials Chemistry A* **2**(27), 10662 (2014).

[58] D. Longrie, K. Devloo-Casier, D. Deduytsche, S. Van den Berghe, K. Driesen, and C. Detavernier, *ECS Journal of Solid State Science and Technology* **1**(6), Q123–Q129 (2012).

[59] I. J. M. Erkens, A. J. M. Mackus, H. C. M. Knoops, P. Smits, T. H. M. van de Ven, F. Roozeboom, and W. M. M. Kessels, *ECS Journal of Solid State Science and Technology* **1**(6), P255–P262 (2012).

[60] S. M. George, *Chem. Rev* **110**, 111–131 (2010).

[61] D. H. Kim, S. H. Yoo, T.-M. Chung, K.-s. An, H.-S. Yoo, and Y. Kim, *Bull. Korean Chem. Soc* **23**(2), 225–228 (2002).

[62] R. Carli and C. Bianchi, *Applied surface science* **74**, 99–102 (1994).

[63] K. Prabakar, S. Venkatachalam, Y. Jeyachandran, S. Narayandass, and D. Mangalaraj, *Materials Science and Engineering: B* **107**(1), 99–105 (2004).

[64] K. Takakura, D. Koga, H. Ohyama, J. Rafi, Y. Kayamoto, M. Shibuya, H. Yamamoto, and J. Vanhellemont, *Physica B: Condensed Matter* **404**(23-24), 4854–4857 dec (2009).

[65] S. P. Sree, J. Dendooven, D. Smeets, D. Deduytsche, A. Aerts, K. Vanstreels, M. R. Baklanov, J. W. Seo, K. Temst, A. Vantomme, C. Detavernier, and J. A. Martens, *Journal of Materials Chemistry* **21**(21), 7692 (2011).

[66] C. Detavernier, J. Dendooven, S. P. Sree, K. F. Ludwig, and J. A. Martens, *Chemical Society reviews* **40**(11), 5242–5253 (2011).

[67] J. Dendooven, S. P. Sree, K. D. Keyser, D. Deduytsche, J. A. Martens, K. F.

Ludwig, and C. Detavernier, *The Journal of Physical Chemistry C* **115**(14), 6605–6610 (2011).

[68] J. Dendooven, R. K. Ramachandran, K. Devloo-Casier, G. Rampelberg, M. Filez, H. Poelman, G. B. Marin, E. Fonda, and C. Detavernier, *Journal of Physical Chemistry C* **117**(40), 20557–20561 (2013).

[69] J. Dendooven, B. Goris, K. Devloo-Casier, E. Levrau, E. Biermans, M. R. Baklanov, K. F. Ludwig, P. V. D. Voort, S. Bals, and C. Detavernier, *Chemistry of Materials* **24**(11), 1992–1994 (2012).

Paper III
Low temperature atomic layer deposition of crystalline In_2O_3 films *

Abstract

Crystalline In_2O_3 thin films were deposited by atomic layer deposition (ALD) using tris(2,2,6,6-tetramethyl-3,5-heptanedionato) indium(III), [In(TMHD)$_3$] as an indium source and O_2 plasma. Resulting growth rates were studied as a function of precursor pulse, reactant pulse, deposition temperature, and number of ALD cycles. The film growth rate was found to be 0.14 Å/cycle within the wide ALD temperature window of 100 - 400 °C. X-ray photoelectron spectroscopic (XPS) and X-ray diffraction (XRD) analysis revealed stoichiometric In_2O_3 thin films with polycrystalline cubic structure, even at 100 °C. All the as-deposited films were smooth, with RMS roughness values between 0.39 to 0.47 nm, as shown by atomic force microscopic (AFM) analysis. The optical properties and electrical resistivities of the films were determined by spectroscopic ellipsometry (SE) and four-point probe measurements. The highly transparent (*ca.* 94% in the visible region) films had a refractive index of 2.01 - 2.05 and a resistivity of 2.5 - 3 $m\Omega \cdot \mathrm{cm}$.

*Published as: Ramachandran, R. K.; Dendooven, J.; Poelman, H.; Detavernier, C., *J. Phys. Chem. C*, 2015, 119, 11786-11791.

Introduction

Indium oxide (In_2O_3), an n-type semiconducting binary oxide with a wide band gap (3.5 - 3.7 eV), has attracted much interest for microelectronic and optoelectronic applications due to its high electrical conductivity and good optical transparency. For example, it can be used as a transparent electrical contact in organic light emitting diodes (OLED)[1;2] liquid crystal displays,[3] and solar cells.[4] It can also be used in toxic gas detectors,[5–7] catalysis[8;9] and as a dopant for making In-doped ZnO (IZO).[10–12] In addition, Sn-doped indium oxide is one of the most industrially important transparent conducting oxides.[3;13;14]

Different methods, such as spin coating,[5;15] spray pyrolysis,[7] molecular beam epitaxy (MBE),[6] pulsed laser deposition,[16] chemical vapor deposition (CVD)[2;17;18] and atomic layer deposition (ALD)[4;13;19–23] have been employed for the deposition of indium oxide thin films. ALD is a most powerful method for depositing highly uniform and conformal layers, which is an important requirement for coating nanostructured surfaces. The first successful ALD of In_2O_3 was demonstrated by Asikainen *et al.*[19] by using $InCl_3$ as the indium source and H_2O as the oxygen source. A growth per cycle (GPC) value of 0.27 Å/cycle was obtained at relatively high growth temperatures of 400 - 450 °C. The conformal coating of porous substrates was reported to be hindered due to etching of the deposited In_2O_3 layer by $InCl_3$. An ALD process that uses the nonhalogenated precursor cycopentadienyl indium (InCp) together with ozone as a reactant, developed by Elam *et al.*[20] resulted in a GPC value of 1.3 - 2.0 Å/cycle. They found that the catalyzed decomposition of O_3 by In_2O_3 limits the conformality of the In_2O_3 films in high aspect ratio pores and causes thickness nonuniformities in the films. The lowest deposition temperature for this process was determined to be 200 °C. In a later publication, lower deposition temperatures (100 - 250 °C) were achieved with the same precursor, but using a combination of oxygen and water as reactant,[23] with a GPC of 1.0 - 1.6 Å/cycle. The processes using indium(III)acetylacetonate and either H_2O (165 - 200 °C) or O_3 (165 - 225 °C) as reactant, demonstrated by Nilsen *et al.*,[21] showed GPC values of 0.20 and 0.12 /cycle, respectively. Recently, an ALD process that utilizes trimethyl indium (TMIn) and water has been reported[22] in a temperature window of 200 - 251 °C, with a GPC value of 0.39 Å/cycle. An extremely large Langmuir exposure of water was required to achieve self-limiting growth.

In this work, we demonstrate an ALD process for depositing crystalline In_2O_3 films at a temperature as low as 100 °C. Recently, the authors reported on an ALD process for Ga2O3[24] using tris(2,2,6,6-tetramethyl-3,5-heptanedionato) gallium(III), [Ga(TMHD)$_3$] and O_2 plasma. In this work, we use a similar low cost, low toxic, and stable β-diketonate precursor, tris(2,2,6,6-tetramethyl-3,5-heptanedionato) indium(III), [In(TMHD)$_3$], as an indium source and O_2 plasma as reactant for the deposition of In_2O_3. ALD of In_2O_3 using [In(TMHD)$_3$] has been attempted before in combination with either H_2O or H_2O_2, but no film formation could be detected.[20] Here, we demonstrate a successful deposition of crystalline In_2O_3 thin films by using [In(TMHD)$_3$] in combination with O_2 plasma. The pro-

cess exhibits a growth rate of 0.14 Å/cycle over a broad temperature range from 100 to 400 °C. This could be of great interest for doping applications, where the deposition temperatures for different ALD processes have to be compatible. To the best of our knowledge, this is the first ALD process that could yield a crystalline In_2O_3 film at temperatures as low as 100 °C.

Experimental methods

A homemade temperature-controllable ALD chamber[25;26] was pumped by a turbomolecular pump to a base pressure in the range of 5×10^{-6} mbar. The chamber wall was heated to 150 °C. All the depositions were performed on Si substrates covered with 100 nm thermally grown SiO_2 (SiO_2/Si). Substrates were loaded into the vacuum chamber through a loadlock and were heated using a resistive heating plate providing temperatures up to around 450 °C. The bubbler containing the solid $In(TMHD)_3$ precursor (99%, Strem Chemicals) was heated at 130 °C to develop adequate vapor pressure, while the delivery lines were heated to 135 °C to prevent condensation of the precursor. Ar gas with 99.999% purity was used as carrier gas for the precursor. For the remote plasma process, O_2 gas flowed through the plasma source at a pressure of 0.01 mbar, and the RF plasma power was set at 300 W. A typical ALD cycle lasted 20 s (5 s pulse time for both the precursor and the reactant and 5 s evacuation time after each pulse). During the growth process, in situ quadrupole mass spectrometry (QMS, Hiden Analytical) measurements were performed to analyze the reaction products. The thickness of the growing In_2O_3 films was monitored by *in situ* spectroscopic ellipsometry (SE, J. A. Woollam M - 2000). A Cauchy model was applied for fitting the ellipsometric data to obtain the film thickness and optical properties.

After deposition, the film thickness was routinely measured by X-ray reflectivity (XRR) using a Bruker D8 Discover system with Cu Kα radiation. X-ray fluorescence (XRF) measurements were performed using a Mo X-ray source (at an angle of 45° with sample surface) and a silicon drift detector placed at an angle of 52° with the sample surface. The fluorescence signal was integrated over a period of 100 s. The chemical composition of the deposited films was determined by X-ray photoelectron spectroscopy (XPS) using a Thermo VG Scientific ESCALAB 220i-XL with a monochromatic Al Kα X-ray source. The reported binding energy (BE) values were corrected for charging effects by assigning a BE of 284.6 eV to the C 1s signal. The film crystallinity was investigated by X-ray diffraction (Bruker D8 Discover, Cu Kα radiation). The surface roughness of the films was determined by atomic force microscopy (AFM) on a Bruker Dimension Edge system operating in tapping mode in air. The Root Mean Square (RMS) roughness values were calculated on 5 μm x 5 μm micrographs. To measure the transmittance, a 10 nm thick In_2O_3 film was deposited on a quartz substrate and the optical absorption spectra were acquired by using the spectroscopic ellipsometer operated in transmission mode.

Results and Discussion

Characteristics of the Indium Oxide ALD process

The deposition temperature and pulsing times of In(TMHD)$_3$ and O_2 plasma were varied in order to study the characteristics of the novel In_2O_3 ALD process. Depositions were carried out over a wide temperature range from 75 to 400 °C. **Figure 1** shows the variation in growth per cycle (GPC) with the temperature of the substrate. A constant growth rate of 0.14 Å/cycle was obtained within a temperature window ranging from 100 to 400 °C. A higher growth rate was observed below 100 °C, probably due to condensation of the precursor onto the substrate or incomplete removal of the reaction byproducts at low temperatures causing some organic residues from the precursor ligands to become incorporated into the film. No deposition was detected when only precursor was pulsed into the reactor without O_2 plasma half cycle, even at the highest deposition temperature. This indicates that the In(TMHD)$_3$ precursor is stable to thermal decomposition up to 400 °C. **Figure 2** shows the effect of the precursor pulse times on the film growth rate. As the In(TMHD)$_3$ pulse time (triangles) is increased, the growth rate slightly increases and saturates at 0.14 Å/cycle with pulse times longer than 3 s. Saturation is also observed for O_2 plasma pulse times longer than 2 s

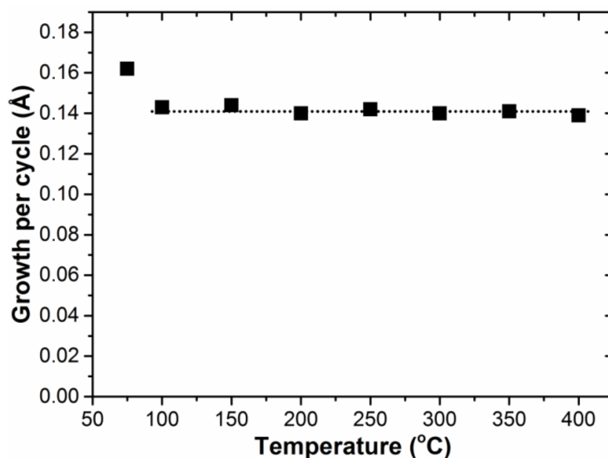

Figure 1. *Growth rate as a function of deposition temperature. The dotted line serves as a guide to the eye.*

Insights in the surface reaction mechanism of the ALD process were obtained by performing *in situ* QMS experiments (Multiple Ion Detection mode) during each ALD half cycle (see Supporting Information). The experimental results revealed the formation of CO_2 and CO during the O_2 plasma pulse, whereas no gaseous reaction products were detected during the precursor half cycle. This observation is consistent with our previous findings for the ALD growth of gallium

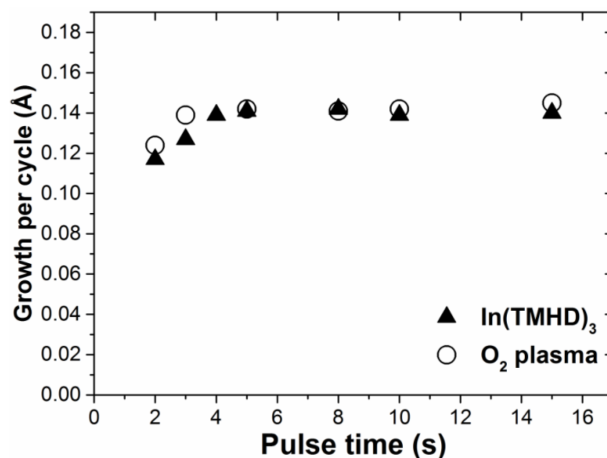

Figure 2. *Growth per cycle against the In(TMHD)$_3$ pulse time (triangles), using a fixed O_2 plasma exposure of 5 s and growth per cycle against the O_2 plasma exposure time (circles), using a fixed In(TMHD)$_3$ pulse time of 5s at 150 °C.*

oxide thin films using a similar precursor, Ga(TMHD)$_3$ and O_2 plasma.[24] The QMS results suggest the nondissociative adsorption of the precursor during the first half cycle, followed by combustion of the ligands by the O radicals in the second half cycle. This type of surface reaction mechanism is generally expected when a metal β- diketonate precursor reacts with O radicals.[27;28]

Figure 3 shows the In_2O_3 film thickness (left Y-axis, circles) as a function of the number of ALD cycles over the range of 50 to 1100 cycles. The depositions were carried out on SiO_2/Si substrates at 150 °C. The linear dependence of film thickness on cycle number indicates sustained layer-by-layer growth characteristic of ALD. The linearity of the process was also verified by XRF measurements. The amount of deposited material is proportional to the integrated area under the L fluorescence peak, plotted in **Figure 3** against the number of ALD cycles. It is clear that the amount of In_2O_3 deposited (right Y-axis, squares) increases linearly with the number of ALD cycles.

XRF was also used for studying the conformality[24;29–32] of the In_2O_3 ALD process in nanostructured materials. In_2O_3 was deposited in a mesoporous silica thin film with 6 nm wide pores. The mesoporous film with fully accessible porosity was synthesized on Si supports using a reported procedure.[33] Ellipsometric porosimetry measurements showed that the silica film had a thickness of 150 nm, a porosity of 61% and a surface area of about 24 cm^2 per square centimeter of support. The mesoporous film together with a planar SiO_2/Si reference was loaded into the deposition chamber and was heated to 150 °C. A long pulse time of 20 s was used for the In(TMHD)$_3$ to ensure the conformal adsorption into the pores. The O_2 plasma exposure time was 15 s. A series of depositions were performed by varying the number of ALD cycles. After the deposition the amount

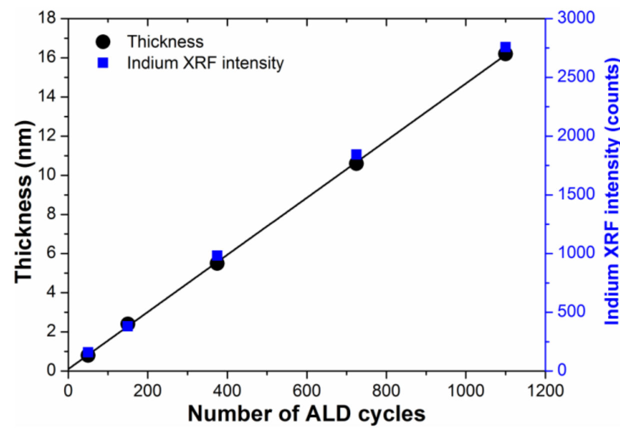

Figure 3. *Thickness (left Y-axis, circles) and In Lα XRF intensity counts (right Y-axis) of the In_2O_3 films deposited at 150 °C on SiO_2/ Si substrates against the number of ALD cycles.*

of deposited material was determined by XRF (**Figure 4**). A considerably higher amount of In_2O_3 was deposited in the mesoporous film compared to the SiO_2/Si reference substrate during the first 150 ALD cycles, confirming growth of In_2O_3 on the interior surface of the very small silica pores. From 200 ALD cycles on, linear growth at a rate, which is more similar to the growth on the planar reference, is observed. This indicates that the small mesopores became inaccessible for the

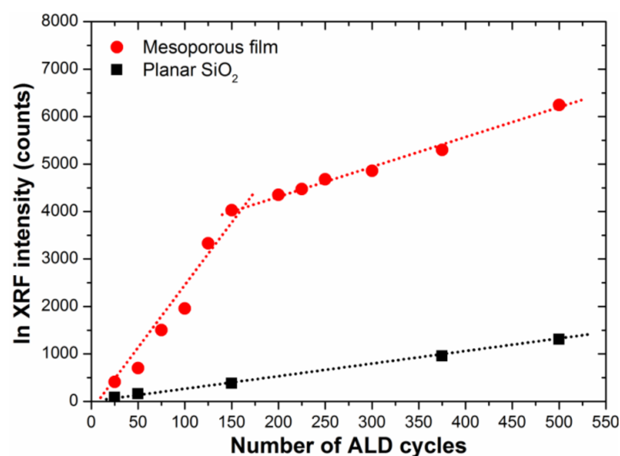

Figure 4. *XRF growth curves for In_2O_3 ALD at 150 °C in a mesoporous silica thin film and on a planar SiO_2 substrate.*

$In(TMHD)_3$ precursor and that growth continued on top of the coated mesoporous film. The conformal nature of In_2O_3 deposition makes this novel process applicable on complex 3D substrates needed for different applications such as large area

nanostructured substrates for sensing or catalytic applications.

Properties of the Indium Oxide Films

All the characterizations were performed on the films deposited on SiO_2/Si substrates. These films were very uniform and exhibited a thickness standard deviation of less than 2%.

XPS measurements were performed on In_2O_3 layers of *ca.* 15 nm deposited at 100, 150, 300, and 400 °C. According to the survey spectra of the XPS analysis, the film surface consisted of oxygen, indium, and small amounts of carbon irrespective of the deposition temperature. The C 1s signal consisted mainly of C-C bonds, typical of surface contamination, which was easily removed by brief sputtering. For the chemical identification of surface species, high resolution spectra of the O 1s and In 3d regions were recorded. The binding energy of O 1s was at 530.4 eV and the binding energy of In $3d_{5/2}$ (444.5 eV) and In $3d_{3/2}$ (452.1 eV; **Figure 5**) were in good agreement with the tabulated values for In_2O_3.[8;9;34;35] Moreover, the In/O ratio (0.65) was found to be in good agreement with the stoichiometry expected for In_2O_3.

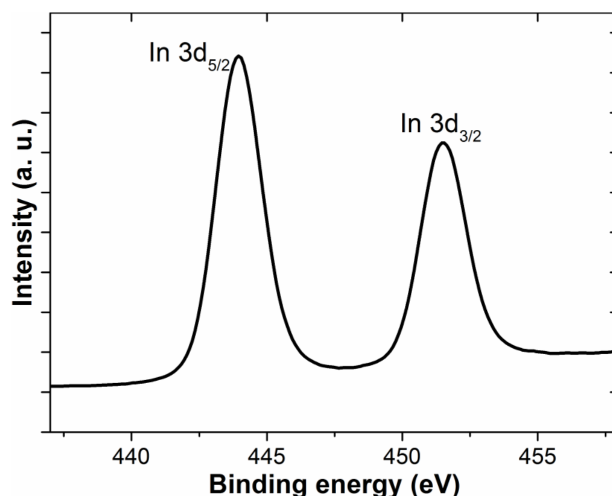

Figure 5. *XPS spectrum of In 3d from the surface of In_2O_3 films deposited (16 nm) on the SiO_2/Si substrate at 150 °C.*

The crystallinity of the In_2O_3 ALD films was investigated using XRD. 2θ scans from 20° to 60° were performed on about 15 nm thick In_2O_3 films deposited on SiO_2/Si substrates at different temperatures. Independent of the deposition temperature, the XRD pattern revealed a polycrystalline, cubic In_2O_3 phase with (222) preferential orientation.[16;20;21;36] The crystallinity of the films increased with increasing deposition temperature. **Figure 6** shows the XRD spectra for the films deposited at 300 (a), 150 (b), and 100 °C (c), respectively. The black line shows

the spectrum of the as-deposited film, and the red line shows the spectrum of the same film annealed in He to 800 °C at a heating rate of 0.5 °C/s. The crystallinity of the films deposited at and below 150 °C increased by annealing the films in an inert atmosphere, whereas the crystallinity remained more or less the same for the films deposited at higher temperatures. It is important to note that this is the first ALD method that is capable of depositing crystalline In_2O_3 films at a temperature as low as 100 °C.

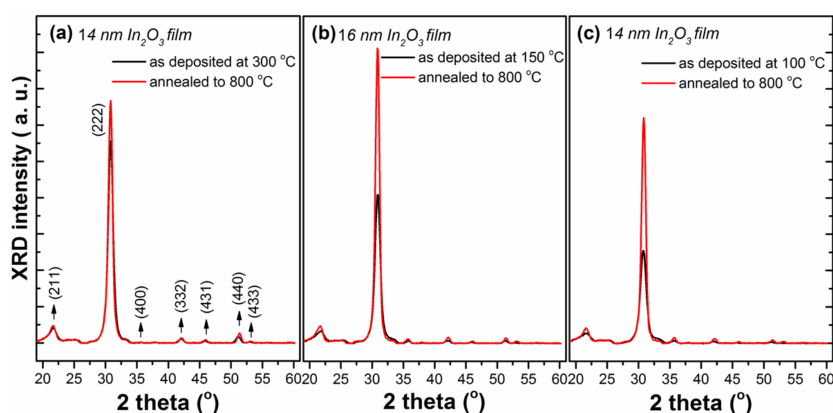

Figure 6. *XRD spectra of In_2O_3 films deposited at 300 (a), 150 (b), and 100 °C (c), respectively. The black line shows the spectrum of an as- deposited film and the red line shows the spectrum of the same film annealed in He to 800 °C at a heating rate of 0.5 °C/s.*

The resistivity of the In_2O_3 films was determined by four-point probe resistivity measurements. **Table 1** lists the resistivity values measured on approximately 15 nm thick In_2O_3 layers deposited on SiO_2/Si at different temperatures. The films show a decrease in resistivity value with increasing deposition temperature. The resistivity of the films deposited at 300 and 400 °C were 2.5 and 2.6 $m\Omega \cdot \mathrm{cm}$, respectively, and these remained the same after annealing to 800 °C in He. These values correspond to the reported resistivity values for In_2O_3 films.[19;21;22;37] The as-deposited films at 100 and 150 °C showed a resistivity value of 18 and 17 $m\Omega \cdot \mathrm{cm}$, which reduced to 2.8 and 3 $m\Omega \cdot \mathrm{cm}$, respectively, after annealing to 800 °C in He. The effect of the deposition temperature on the surface morphology of the In_2O_3 films was analyzed by AFM (see Supporting Information). The root-mean-square values for approximately 15 nm In_2O_3 films deposited at 100, 150, 300, and 400 °C (**Table 1**) revealed relatively smooth surfaces independent of the deposition temperature.

The optical properties of the as-deposited In_2O_3 films were determined by model-based analysis of spectroscopic ellipsometry measurements. The refractive index was modeled by the Cauchy function, while the film thickness was fixed to the value obtained by XRR measurements. Excellent fits to the measurements were obtained and refractive indices in the order of 2.01 to 2.05 were extracted at 632.8 nm. These values are in line with previously reported refractive indices for

Temperature (°C)	Thickness (nm)	RMS roughness (nm) -as deposited	RMS roughness (nm) -annealed	Resistivity ($m\Omega \cdot \mathrm{cm}$) -as deposited	Resistivity ($m\Omega \cdot \mathrm{cm}$) -annealed
100	14	0.46 (± 0.02)	0.47 (± 0.02)	18 (± 2)	2.8 (± 0.2)
150	16	0.41 (± 0.02)	0.42 (± 0.02)	17 (± 1)	3 (± 0.2)
300	14	0.39 (± 0.02)	0.40 (± 0.02)	2.5 (± 0.2)	2.5 (± 0.2)
400	14.5	0.46 (± 0.02)	0.46 (± 0.02)	2.6 (± 0.2)	2.5 (± 0.2)

Table 1. *Thickness, RMS Roughness, and Resistivity of In_2O_3 ALD Films Grown on SiO_2/Si Substrates at Different Temperatures.*

In_2O_3 films,[16;37] and no differences could be observed between the films grown at different temperatures. The inset of **Figure 7** shows the optical transmission spectrum of a 10 nm thick In_2O_3 film deposited on quartz referenced to the spectrum of the uncoated quartz substrate. The average transmission of the In_2O_3 film in the wavelength range 380 - 1000 nm was 94.0% and is comparable to the values reported in literature.[17;19–21] To determine the band gap (Eg) of the material, the absorption coefficient α was calculated from the transmittance, T, and the film thickness, d,as ln(T)/d. The value of $[\alpha(h\nu)]^2$ was then plotted against the photon energy hν and the intercept on the x-axis gives the value of the direct band gap. As shown in **Figure 7**, this analysis yielded a value of 3.6 eV, in agreement with reported values in literature.[17;37]

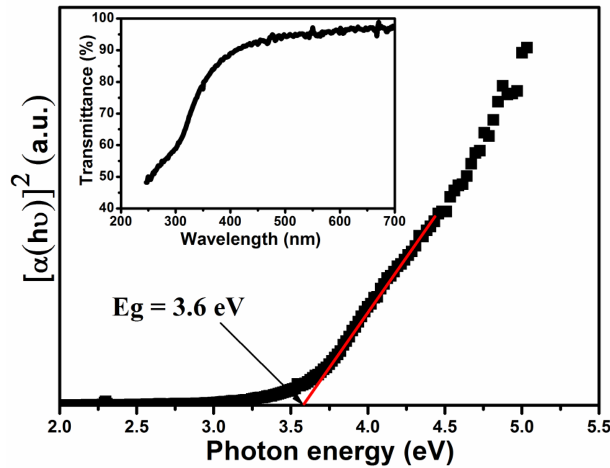

Figure 7. *$[\alpha(h\nu)]^2$ versus photon energy plot for a 10 nm In_2O_3 film deposited on a quartz substrate at 250 °C. The band gap energy is determined from the linear fit (red line) to the absorption edge as indicated. The inset of the figure shows the transmittance spectrum of the same film divided by the transmittance of the bare quartz substrate.*

Conclusion

Polycrystalline cubic In_2O_3 thin films were grown by using tris(2,2,6,6-tetramethyl-3,5-heptanedionato) indium(III), [In(TMHD)$_3$] as an indium source and O_2 plasma as reactant. A wide ALD temperature window was observed from 100 to 400 °C with a constant growth rate of 0.14 Å/cycle. The optical transparency of the films was excellent with an average transmission of about 94.0% in the wavelength range 380 - 1000 nm. The refractive indices of the films were 2.01 - 2.05, independent of the deposition temperature. An optical band gap of 3.6 eV was extracted from optical transmission measurements. The XPS and AFM analysis confirmed the presence of stoichiometric In_2O_3 films with fairly smooth surfaces (RMS roughness of 0.39 - 0.47 nm). The resistivity of films deposited at higher temperatures (300 °C) and all postdeposition annealed films were found to be in the order of 2.5 - 3 $m\Omega \cdot \mathrm{cm}$. The process was shown to be suitable for coating high aspect ratio mesoporous films relevant to solar cell and catalytic applications.

Acknowledgments

This research was supported by the Flemish Research Foundation (FWO) and by the Special Research Fund BOF of Ghent University (GOA 01G01513). J.D. is a postdoctoral fellow of the FWO. The authors acknowledge S. P. Sree (Centre for Surface Chemistry and Catalysis, KU Leuven) for preparing mesoporous silica.

References

[1] C. C. Wu, C. I. Wu, J. C. Sturm, and a. Kahn, *Applied Physics Letters* **70**, 1348 (1997).

[2] J. Ni, H. Yan, A. Wang, Y. Yang, C. L. Stern, A. W. Metz, S. Jin, L. Wang, T. J. Marks, J. R. Ireland, and C. R. Kannewurf, *Journal of the American Chemical Society* **127**(5), 5613–5624 (2005).

[3] U. Betz, M. Kharrazi Olsson, J. Marthy, M. F. Escolá, and F. Atamny, *Surface and Coatings Technology* **200**, 5751–5759 (2006).

[4] B. Macco, Y. Wu, D. Vanhemel, and W. M. M. Kessels, *physica status solidi (RRL)* **8**(12), 987–990 (2014).

[5] W.-Y. Chung, G. Sakai, K. Shimanoe, N. Miura, D.-D. Lee, and N. Yamazoe, *Sensors and Actuators B* **65**, 312–315 (2000).

[6] R. Winter, K. Scharnagl, A. Fuchs, T. Doll, and I. Eisele, *Sensors and Actuators B* **66**, 85–87 (2000).

[7] G. Korotcenkov, V. Brinzari, A. Cerneavschi, M. Ivanov, V. Golovanov, A. Cornet, J. Morante, A. Cabot, and J. Arbiol, *Thin Solid Films* **460**, 315–323 (2004).

[8] J. A. Perdigon-Melon, A. Gervasini, and A. Auroux, *Journal of Catalysis* **234**, 421–430 (2005).

[9] J. Li, J. Hao, X. Cui, and L. Fu, *Catalysis Letters* **103**, 75–82 (2005).

[10] D. H. Kim, N. G. Cho, H. G. Kim, and W.-Y. Choi, *Journal of The Electrochemical Society* **154**(11), H939 – H943 (2007).

[11] S. Ilican, Y. Caglar, M. Caglar, and B. Demirci, *Journal of Optoelectronics and Advanced Materials* **10**(10), 2592–2598 (2008).

[12] H. J. Lee, J. H. Hwang, K. B. Choi, S. G. Jung, K. N. Kim, Y. S. Shim, C. H. Park, Y. W. Park, and B. K. Ju, *ACS Applied Materials and Interfaces* **5**(21), 10397–10403 (2013).

[13] J. Elam, D. Baker, A. Martinson, M. Pellin, and J. Hupp, *Journal of Physical Chemistry C* **112**, 1938–1945 (2008).

[14] M. Fang, A. Aristov, K. V. Rao, A. V. Kabashin, and L. Belova, *RSC Advances* **3**(42), 19501 (2013).

[15] S.-Y. Han, G. S. Herman, and C.-H. Chang, *Journal of the American Chemical Society* **133**(14), 5166–5169 (2011).

[16] F. O. Adurodija, L. Semple, and R. Brüning, *Thin Solid Films* **492**, 153–157 (2005).

[17] M. Girtan and G. Folcher, *Surface and Coatings Technology* **172**(03), 242–250 (2003).

[18] N. H. Kim, J. H. Myung, H. W. Kim, and C. Lee, *Physica Status Solidi (a)* **202**(1), 108–112 (2005).

[19] T. Asikainen, M. Ritala, and M. Leskeei, *J. Electrochem. Soc.* **141**(11), 3210–3213 (1994).

[20] J. W. Elam, A. B. F. Martinson, M. J. Pellin, and J. T. Hupp, *Chemistry of Materials* **18**, 3571–3578 (2006).

[21] O. Nilsen, R. Balasundaraprabhu, E. Monakhov, N. Muthukumarasamy, H.

Fjellvåg, and B. Svensson, *Thin Solid Films* **517**, 6320–6322 (2009).

[22] D.-J. Lee, J.-Y. Kwon, J. I. Lee, and K.-B. Kim, *The Journal of Physical Chemistry C* **115**, 15384–15389 (2011).

[23] J. A. Libera, J. N. Hryn, and J. W. Elam, *Chemistry of Materials* **23**(8), 2150–2158 (2011).

[24] R. K. Ramachandran, J. Dendooven, J. Botterman, S. P. Sree, D. Poelman, J. A. Martens, H. Poelman, and C. Detavernier, *Journal of Materials Chemistry A* **2**, 19232–19238 (2014).

[25] Q. Xie, Y.-L. Jiang, C. Detavernier, D. Deduytsche, R. L. Van Meirhaeghe, G.-P. Ru, B.-Z. Li, and X.-P. Qu, *Journal of Applied Physics* **102**(8), 083521 (2007).

[26] J. Musschoot, Q. Xie, D. Deduytsche, K. De Keyser, D. Longrie, J. Haemers, S. Van den Berghe, R. Van Meirhaeghe, J. D'Haen, and C. Detavernier, *Microelectronic Engineering* **87**(10), 1879–1883 (2010).

[27] T. T. Van and J. P. Chang, *Applied Surface Science* **246**(1-3), 250–261 jun (2005).

[28] T. T. Van and J. P. Chang, *Surface Science* **596**(1-3), 1–11 (2005).

[29] J. Dendooven, S. P. Sree, K. D. Keyser, D. Deduytsche, J. A. Martens, K. F. Ludwig, and C. Detavernier, *The Journal of Physical Chemistry C* **115**(14), 6605–6610 (2011).

[30] C. Detavernier, J. Dendooven, S. P. Sree, K. F. Ludwig, and J. A. Martens, *Chemical Society reviews* **40**(11), 5242–5253 (2011).

[31] J. Dendooven, R. K. Ramachandran, K. Devloo-Casier, G. Rampelberg, M. Filez, H. Poelman, G. B. Marin, E. Fonda, and C. Detavernier, *Journal of Physical Chemistry C* **117**(40), 20557–20561 (2013).

[32] R. K. Ramachandran, J. Dendooven, and C. Detavernier, *Journal of Materials Chemistry A* **2**(27), 10662 (2014).

[33] S. P. Sree, J. Dendooven, D. Smeets, D. Deduytsche, A. Aerts, K. Vanstreels, M. R. Baklanov, J. W. Seo, K. Temst, A. Vantomme, C. Detavernier, and J. A. Martens, *Journal of Materials Chemistry* **21**(21), 7692 (2011).

[34] S. Poznyak, an Golubev, and A. Kulak, *Surface science* **456**, 396–401 (2000).

[35] D. A. Magdas, D. Maestre, A. Cremades, L. Gregoratti, and J. Piqueras, *Superlattices and Microstructures* **45**(4-5), 429–434 (2009).

[36] S. K. Chong, S. Nur, A. Azizan, K. W. Chan, H.-Q. Nguyen, W. S. Chiu, Z. Aspanut, C. F. Dee, and S. A. Rahman, *Nanoscale Research Letters* **8**, 428 (2013).

[37] K. Chopra, S. Major, and D. Pandya, *Thin Solid Films* **102**, 1–46 (1983).

Paper III - supplementary information

Low temperature atomic layer deposition of crystalline In_2O_3 films *

In situ mass spectrometry

The reaction products during each ALD half cycle were followed by using *in situ* QMS measurements, which could give an insight into the surface reaction mechanism of the process. To analyze the formation of reaction products during the process a series of QMS measurements in MID mode were performed (**Figure S1**). In the same scan 5 precursor pulses (A) were monitored, followed by 3 full ALD cycles (i.e. precursor and reactant pulse (AB)) and nally 5 reactant pulses (B). The sequence monitored is thus: AAAAA ABABAB BBBBB. During the successive precursor pulses (A) and successive reactant pulses (B), no reactions occur, so a clean precursor (A) or reactant (B) signal is obtained for the dierent mass-to-charge ratios that are being monitored. By comparing these reference signals with the precursor and reactant signal during the ALD cycles (AB), the formation of reaction products can be interpreted. A series of relevant mass-to-charge ratios was followed during the scan, however, the only reaction products that could be detected were CO (m/z = 28) and CO_2 (m/z = 44). The QMS data recorded during the fifth precursor pulse (A), the three complete ALD cycles (ABABAB) and the next two O_2 plasma (B) pulses are shown in the **Figure S1**. It can be seen that similar QMS signals are obtained during both the pure precursor pulse (A) and the precursor pulse in the ALD cycle (AB), which indicates that no gaseous reaction products can be detected during the precursor half cycle, suggesting that the precursor molecules adsorb non-dissociatively on the surface. After pumping out the reaction products, oxygen plasma was introduced and the partial pressure of both CO_2 and CO increased. As oxygen plasma was continuously dosed, both reaction product signals decreased, indicating that the reaction approached completion. The sharp spike in the MID signal was not observed during the pure O_2 plasma (B) pulse, indicating that the detected formation of CO_2 during the O_2

*Published as: Ramachandran, R. K.; Dendooven, J.; Poelman, H.; Detavernier, C., *J. Phys. Chem. C*, 2015, 119, 11786-11791.

plasma (B) pulse of the ALD cycle (AB) can be attributed the reaction of O radicals with the adsorbed precursor molecules. The relative amount of CO, determined by calculating the area under the peaks, was found to be around 30%. Since this value is higher than the theoretical abundance of CO ($\sim$13%) as CO_2 cracking product, it can be concluded that a part of CO detected is formed as reaction product. The results obtained here correspond well to the reaction mechanism observed during the ALD process for gallium oxide thin films using a similar precursor, $Ga(TMHD)_3$ and O_2 plasma.[1] and with earlier works on the reaction between metal β- diketonate precursor and O radicals.[2;3]

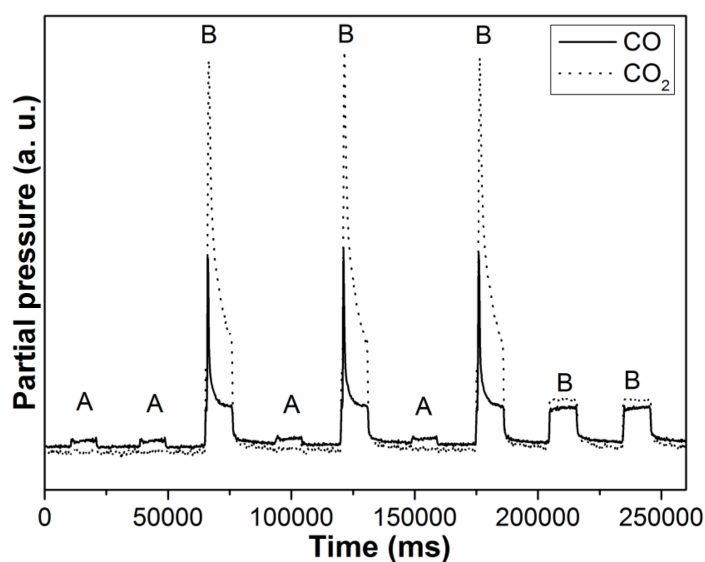

Figure S1. *In-situ mass spectrometry results for CO (m/z = 28) and CO_2 (m/z = 44) during different precursor (A) and reactant (B) pulses.*

Atomic force microscopy

The effect of deposition temperature on the surface morphology of In_2O_3 films was analyzed by AFM. Figure S2 (a), (b), (c) and (d) display AFM images of *ca.* 15 nm In_2O_3 films deposited at 100, 150, 300, 400 °C, demonstrating smooth surfaces independent of the deposition temperature. The root mean square values of the films were in the range 0.39 to 0.47 nm.

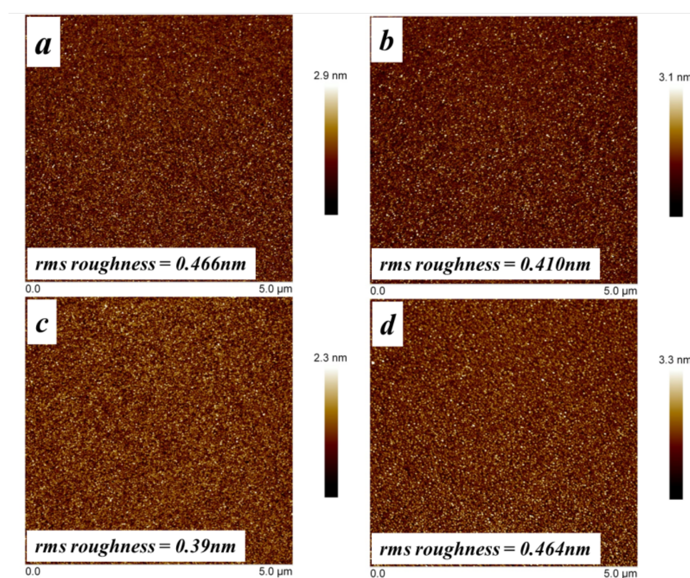

Figure S2. *Atomic force micrographs of ca. 15 nm thick* In_2O_3 *films deposited at (a) 100, (b) 150, (c) 300 and (d) 400°C.*

References

[1] R. K. Ramachandran, J. Dendooven, J. Botterman, S. P. Sree, D. Poelman, J. A. Martens, H. Poelman, and C. Detavernier, *Journal of Materials Chemistry A* **2**, 19232–19238 (2014).
[2] T. T. Van and J. P. Chang, *Applied Surface Science* **246**(1-3), 250–261 jun (2005).
[3] T. T. Van and J. P. Chang, *Surface Science* **596**(1-3), 1–11 (2005).

Paper IV
Plasma enhanced atomic layer deposition of Fe_2O_3 thin films *

Abstract

Atomic layer deposition of Fe_2O_3 is generally performed at temperatures above 350 °C. In this work, Fe_2O_3 thin films were deposited by remote plasma enhanced atomic layer deposition using tertiary butyl ferrocene (TBF) and O_2 plasma in a broad temperature range starting from 150 to 400 °C. A maximum growth rate of 1.2 Å/cycle was achieved between 300 and 350 °C. Below 300 °C, the saturated growth per cycle was found to depend on the temperature of the sample. All the deposited films were pure with no significant amount of carbon contamination. Films deposited at 250 °C and above were crystalline with an α - Fe_2O_3 crystal structure, while the low temperature films were crystallized by a post-deposition annealing in He. Annealing in H_2 induced the formation of metallic iron.

*Published as: Ramachandran, R. K.; Dendooven, J. ; Detavernier, C., *J. Mater. Chem. A*, 2014, 2, 10662-10667.

Introduction

Hematite (α - Fe_2O_3) is the most common form of oxide in the Fe-O_2 system. Its unique combination of stability, nontoxicity and exceptionally low material cost makes it an important candidate for many applications such as magnetic devices,[1–5] hydrocarbon gas sensors,[6–9] photo electrochemical solar cells,[10–15] heterogeneous catalysis,[16–19] and as electro chromic material for smart windows.[20;21]

Fe_2O_3 thin films have been grown for various purposes by a variety of different methods such as sputtering,[1;22] solgel,[4;7] molecular beam epitaxy (MBE),[23–25] metalorganic deposition (MOD),[26;27] spray pyrolysis,[20;28] chemical vapor deposition (CVD)[5;15;29–31] and atomic layer deposition (ALD).[8;32–40] Amongst these methods, ALD is the most powerful method for depositing highly uniform and conformal layers, which is an important requirement for coating nanostructured surfaces. There exist several ALD processes for depositing iron oxide. While the first demonstrated tris-(2,2,6,6-tetramethyl-3,5-heptanedionato)iron(III) [Fe(thd)$_3$)] and ozone process[32] suffers from an exceptionally low growth rate, the processes that use iron(III)tert-butoxide [$Fe_2(OtBu)_6$)][33;34] and bis(2,4-methylpentadienyl)iron[35] are limited by their narrow temperature window and commercial unavailability of the precursors. Most of the other methods use ferrocene [$Fe(Cp)_2$] as Fe precursor in combination with either molecular oxygen or ozone.[36–39] These processes generally use high deposition temperatures[36–38] (above 350 °C) while also suffering from extremely low growth rates[37] and narrow temperature windows for controlled growth.[38] Recently, Martinson et al.[39] reported an ALD process for Fe_2O_3 using $Fe(Cp)_2$ and O_3 in a lower temperature range from 200 to 350 °C with a crystalline phase starting from 250 °C. However, relatively large exposures of both $Fe(Cp)_2$ and O_3 are required to reach saturated growth conditions on planar surfaces.

In this article, we report a novel ALD process for Fe_2O_3 that relies upon sequential pulsing of tert-butyl ferrocene (TBF) and O_2 plasma and allows for the controlled deposition of pure films in a broad temperature range from 150 to 350 °C. TBF is a commercially available liquid with a boiling point of 96 °C (at 1 mmHg) and with sufficient vapor pressure, which makes it a suitable precursor for ALD applications. In comparison with most existing ALD processes for Fe_2O_3, this novel process enables deposition at temperatures as low as 150 °C, which is attractive for applications that require the controlled deposition of iron oxide on temperature sensitive materials. Furthermore, the formation of metallic iron by a post deposition annealing of the films in H_2 is also demonstrated, which makes this novel process more versatile in view of technological applications such as data storage,[41] surface plasmon coupled chemiluminescence[42;43] and biomedicine and magnetic devices.[44]

Experimental methods

All the depositions were performed in a home built experimental cold-wall ALD chamber connected through a gate valve to a turbo pump backed up by a rotary pump.[45;46] A second gate valve was installed for pre-evacuation of the chamber via a bypass line to the rotary pump. The liquid TBF precursor (98%, Strem Chemicals), kept in a stainless steel container, was heated to 65 °C, and the delivery line to the chamber was heated to 70 °C. For the remote plasma process the O_2 gas flowed through the plasma source at a pressure of 0.03 mbar and the RF plasma power was set at 300 W. The precursor was injected through a quarter inch stainless steel tube located at the top of the ALD chamber and a static exposure mode was applied.[47] Unless stated otherwise, the pulse time of the TBF precursor was 15 s, after which the valves to the pumping system were kept closed for another 10 s, resulting in a total exposure time of 25 s at 1 mbar pressure. For O_2 plasma, the pulse time was 15 s. No purge gas was used in the deposition cycle.

The thickness of the growing Fe_2O_3 films was monitored *in situ* using spectroscopic ellipsometry (SE, J. A. Woollam M-2000). Based on SE measurements performed on several Fe_2O_3 layers with a known thickness, the optical constants of the films were found to be appropriately described by a TaucLorentz oscillator model in the wavelength range of 600 to 1000 nm. Good quality fits to the ellipsometric data were obtained, even during the start of the film growth. The determination of film thickness by *in situ* SE was complemented by *ex situ* X-ray reflectivity (XRR) and X-ray fluorescence (XRF) measurements. XRR was carried out using a Bruker D8 Discover system with Cu Kα radiation, while XRF was performed using a Mo X-ray source (at an angle of 45° with sample surface) and a silicon drift detector placed at an angle of 52° with the sample surface. The fluorescence signal was integrated over a period of 100 s. Film thicknesses were extracted as explained in the Supplementary Information.

The chemical composition of the deposited films was determined by X-ray photoelectron spectroscopy (XPS) using a Thermo VG Scientific ESCALAB 220i-XL with a monochromatic Al Kα X-ray source. The reported Binding Energy values (BE) were corrected for charging effects by assigning a BE of 284.6 eV to the C 1s signal. The film crystallinity was investigated by X-ray diffraction (Bruker D8 Discover, Cu Kα radiation) using a point sensitive detector. The diffraction patterns were analyzed with the Scherrer equation to derive the size of the crystallites in the deposited films. The surface roughness of the films was determined by atomic force microscopy (AFM) on a Bruker Dimension Edge system operating in tapping mode in air. The Root Mean Square (RMS) roughness values were calculated on 5 μm x 5 μm micrographs.

The ALD process was characterized by *in situ* mass spectrometry (Hiden Analytical) using the spectrometer in Bar Scan mode with the Faraday detector (source voltage 70 V).

Finally, post-annealing of the deposited films in He and 5% H_2/He was performed in a home-built heating chamber mounted on a Bruker D8 diffractometer[48;49] to enable *in situ* XRD characterization. A linear detector was used to

collect the diffracted X-rays at 2 s time intervals.

Results and Discussion

Characteristics of the Iron Oxide ALD process

The temperature window of the ALD process was investigated on Si substrates covered with 100 nm thermally grown SiO_2. **Figure 1** shows the variation in growth per cycle (GPC) with the temperature of the substrate. The substrate temperature was varied between 150 to 400 °C. The GPC has both temperature dependent and temperature independent regions. In the temperature range of 300 to 350 °C the GPC is temperature independent with a value of 1.2 Å/cycle. Below 300 °C the growth rate was found to decrease with decreasing temperature. Above 350 °C, the growth rate increased significantly, likely due to thermal decomposition of the TBF precursor. The thickness of the films deposited at and above 350 °C was extracted from XRF measurements (see Supporting Information).

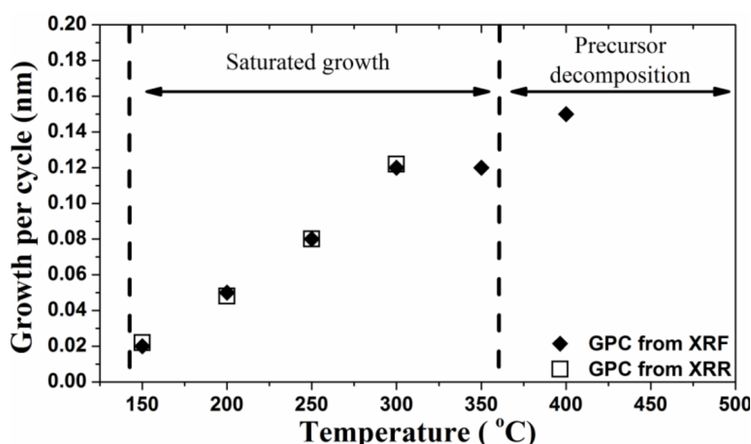

Figure 1. Growth rate as a function of deposition temperature.

Saturation of the ALD process was studied at different deposition temperatures. While both ALD half reactions saturate in the range of 150 °C to 350 °C, no saturated growth was found at 400 °C, indicating thermal decomposition of the precursor at this temperature. **Figure 2**(a) and (b) show the 150 and 350 °C saturation curves for the TBF precursor and O_2 plasma half cycles respectively. The pulse time of the TBF precursor was followed by an additional 10 s static exposure. At 300 and 350 °C a 7 s TBF pulse, resulting in a pressure of 7×10^{-1} mbar in the chamber, was sufficient to have saturated growth. However, at low temperatures, long pulse times were needed to ensure saturation. At the lowest deposition temperature of 150 °C a 15 s TBF pulse, resulting in a pressure of 1 mbar, was

required for saturated growth. In the case of O_2 plasma, a 6 s exposure resulted in saturated growth at 300 °C, while 15 s were needed at 150 °C.

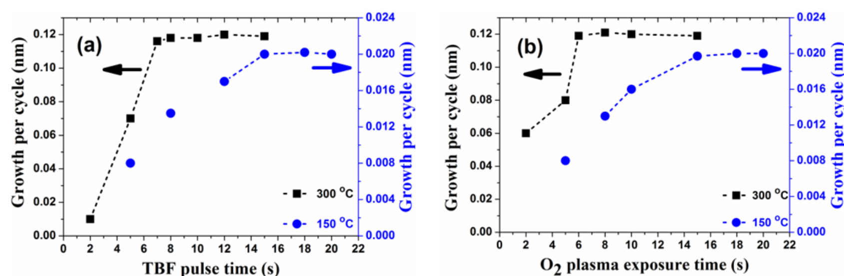

Figure 2. *(a) Growth rate against the TBF pulse time, using a fixed O_2 plasma exposure of 15 s. (b) Growth rate against the O_2 plasma exposure time, using a fixed TBF total exposure of 25 s. The black squares were obtained at 300 °C (left Y-axis) and the blue circles at150 °C (right Y-axis)*

To get more insights in the mechanisms driving the temperature dependent saturation of the growth rate in the TBF/O_2 plasma process, *in situ* mass spectrometry was used to analyze the reaction products formed during both ALD half cycles. As also reported for the ferrocene/O_2 process by J. R. Scheffe *et al.*,[37] CO_2 and H_2O were detected during both the precursor and reactant pulse. The formation of CO_2 and H_2O during the first half reaction indicates the presence of chemisorbed oxygen on the surface that reacts with the TBF ligands upon precursor adsorption. In the subsequent exposure to O_2 plasma, the remaining ligands of the adsorbed precursor molecules are oxidized.[39;50–52] Mass spectrometry revealed no difference in reaction products for the processes at 150 °C and 300 °C respectively, suggesting that similar ligand combustion reactions occur at both temperatures. The reduced growth rate at low temperatures could possibly be due to competing site blocking reactions by organic precursor groups during the TBF pulse. Surface poisoning by precursor fragments followed by removal of the surface carbon during the O_2 reactant step has earlier been proposed to occur during Pt and Ru ALD processes using Cp-based precursors.[53]

The linearity of the ALD process was studied on 100 nm SiO_2 films thermally grown on Si substrates. The thickness after each ALD cycle was followed with in situ spectroscopic ellipsometry measurements. Independent of the deposition temperature, there was a delay in the nucleation of the Fe_2O_3 film. The growth was limited up to about 30 cycles after which the film thickness increased linearly with the number of ALD cycles (**Figure 3**). The final thickness of the film was measured *ex situ* with XRR and was in close agreement with the ellipsometric measurement.

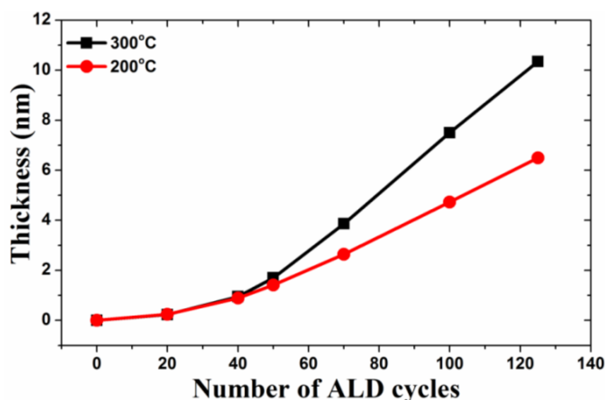

Figure 3. *Thickness of the Fe_2O_3 films deposited at 200 and 300 °C on SiO_2 substrates against the number of ALD cycles. Ellipsometric measurements at certain intervals only are shown for clarity.*

Properties of the Iron Oxide Films

Iron oxide films were deposited on 100 nm SiO_2/Si substrates using the conditions described in the experimental section. All the deposited films were continuous and the thickness uniformity was excellent, with a typical deviation in thickness of less than 2% across a two-inch area. Phase identification of *ca.* 27 nm thick films was performed using XRD measurements. All the films deposited at and above 250 °C were crystalline and the XRD peaks correspond to an α - Fe_2O_3 (Hematite) phase (**Figure 4**). Analysis of the (104) peak with the Scherrer equation yielded crystallite sizes of 16 and 45 nm for the as deposited films at 250 °C and 350 °C respectively. The 3^+ oxidation state of iron (Fe^{3+}) was also confirmed by XPS measurements. **Figure 5** shows the XPS spectra of as-deposited films at 150 and 350 °C. The maximum of the Fe $2p_{3/2}$ peak is at 711 eV and the satellite peak between the $2p_{3/2}$ and $2p_{1/2}$ peaks is clearly visible. To verify the stoichiometry of the films, the O 1s peaks were studied in detail. Irrespective of the deposition temperature, the O 1s spectrum was characterized by the presence of two contributing bands. While the band at BE = 530.2 eV (species I, black, 74% of total oxygen content) could be ascribed to lattice oxygen in Fe_2O_3, the band at 532.2 eV (species II, gray) could be related to the presence of surface hydroxyl groups along with coordinatively unsaturated oxygen species.[31;54] Taking only the lattice oxygen species in to account the Fe/O ratio was found to be 0.62, in agreement with the stoichiometry expected for Fe_2O_3. Comparing these observations with those reported in literature,[8;31;37;54;55] it can be concluded that the iron in the ALD films is in the Fe^{3+} state. XPS also showed a negligible amount of carbon ($< 5\%$) in the deposited films.

All the films deposited below 250 °C were amorphous, but could be converted into the hematite phase with (104) preferential orientation by annealing in He. **Fig-**

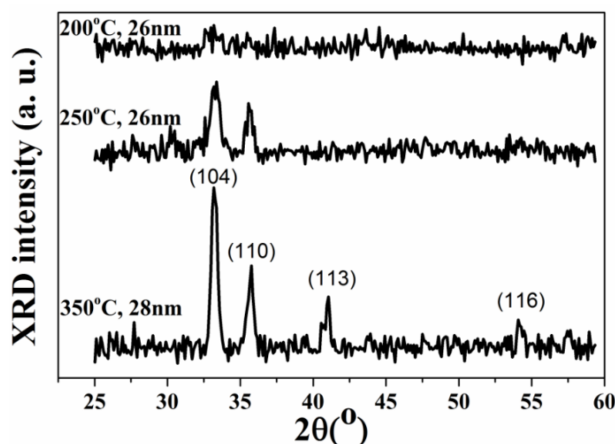

Figure 4. *XRD patterns of the Fe_2O_3 films deposited at different temperatures on SiO_2 substrates.*

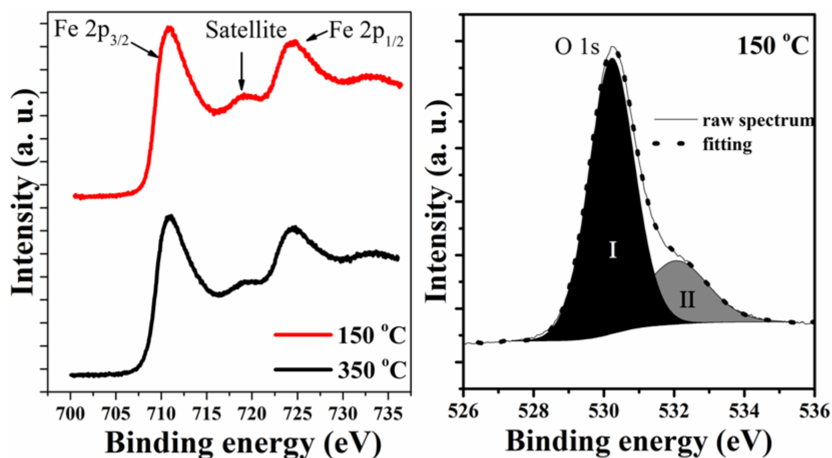

Figure 5. *XPS spectra of Fe 2p (left) from the surface of Fe_2O_3 films deposited at 150 and 350 °C and O1s (right) from the surface of Fe_2O_3 films deposited at 150 °C on SiO_2 substrates.*

ure 6(bottom) shows the XRD patterns for the as-deposited film at 200 °C and for the same film annealed in He to 600 °C at a heating rate of 0.2 °C/s. **Figure 6**(top) shows the evolution of the XRD pattern during this thermal treatment. Crystallization of the film started at 350 °C, as revealed by the intensification of the peak corresponding to α - Fe_2O_3 (104). The Scherrer equation revealed an average crystallite size of 35 nm.

All the deposited Fe_2O_3 films can be reduced to metallic Fe by annealing in H_2

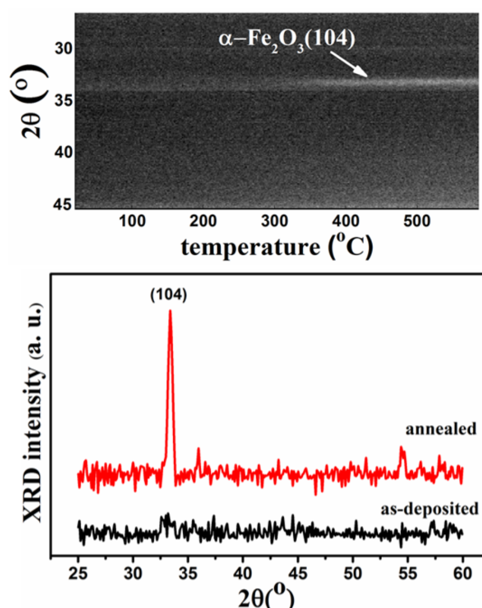

Figure 6. *XRD patterns of a 26 nm thick Fe_2O_3 film deposited at 200 °C on a SiO_2 substrate and of the same film after annealing in He to 600 °C at a heating rate of 0.2 °C/s. The top figure shows the evolution of the XRD pattern during this thermal treatment.*

atmosphere. Upon annealing from room temperature to 650 °C at a heating rate of 0.2 °C/s, the Fe_2O_3 first reduces to Fe_3O_4 at 385 °C and then suddenly reduces to metallic Fe at 430 °C (**Figure 7**). This reduction process could be of interest for applications of metallic ferromagnetic iron in data storage,[41] biomedicine and magnetic devices.[44]

Finally, the morphology of the films was studied using atomic force microscopy (AFM). As also reported for the iron(III) chloride and water process,[40] the surface roughness of the Fe_2O_3 films was found to increase with increasing deposition temperature (**Figure 8**). This increase in surface roughness is related to the higher crystallinity of the films with increasing temperature. The rms roughness of the film deposited at 200 °C, which was measured from a 5 μm x 5 μm scan area, increased from 0.32 to 0.81 nm after annealing in He. Increase in the rms roughness value after annealing can be attributed to the formation of grains upon crystallization.

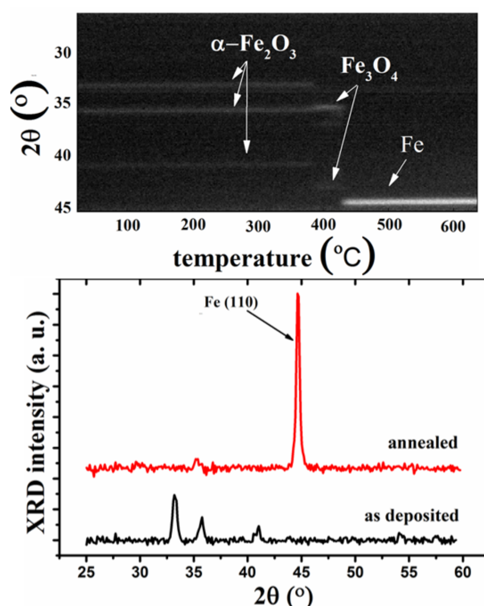

Figure 7. *XRD patterns of a 28 nm thick Fe_2O_3 film deposited at 350 °C on a SiO_2 substrate and of the same film after annealing in H_2 to 650 °C at a heating rate of 0.2 °C/s. The top figure shows the evolution of the XRD pattern during this thermal treatment.*

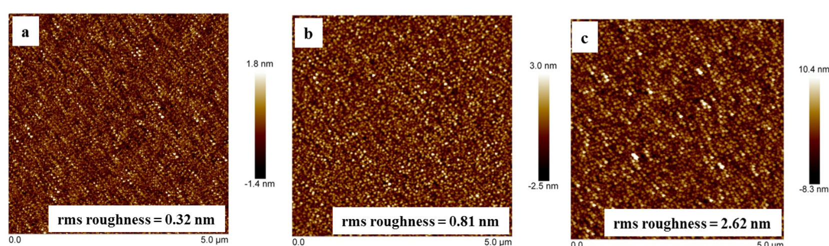

Figure 8. *Atomic force micrographs of 13 nm thick Fe_2O_3 films (a) deposited at 200 °C, (b) the same annealed in He and (c) deposited at 350 °C on SiO_2 substrates.*

Conclusion

A new ALD process for the growth of uniform and pure α - Fe_2O_3 (hematite) thin films has been developed using t-butylferrocene as precursor and O_2 plasma as reactant. Both ALD half reactions are self-saturating in a broad temperature window ranging from 150 to 350 °C. Remarkably, the saturated growth rate increases with increasing temperature. Films deposited at 250 °C and higher temperatures

are crystalline as-deposited, while the low temperature films can be crystallized by post-deposition annealing in He. Annealing in H_2 induces the formation of metallic iron. In comparison with most existing ALD processes for Fe_2O_3, this novel process enables deposition at temperatures as low as 150 °C, which is attractive for applications that require the controlled deposition of iron oxide on temperature sensitive materials. In future work, a detailed study of the growth behaviour on different substrates will be investigated.

Acknowledgments

This research was supported by the European Research Council (Starting Grant no. 239865), by the Flemish Research Foundation (FWO) and by the Special Research Fund BOF of Ghent University (GOA 01G01513).The authors also gratefully acknowledge Nico De Roo (UGent) for performing the XPS measurements.

References

[1] S. Ohta and A. Terada, *Thin Solid Films* **143**(1), 73–82 (1986).

[2] A. Sun, P. Kuo, C. Chou, S. Chen, C. Lie, M. Lin, J. Chen, and H. Huang, *Journal of Magnetism and Magnetic Materials* **272-276**, 1776–1777 (2004).

[3] Y. Huang, J. Lin, X. Ding, C. Tang, C. Gu, and S. Qi, *Materials Letters* **61**(3), 697–700 (2007).

[4] C.-D. Park, D. Magana, and A. E. Stiegman, *Chemistry of Materials* **19**(4), 677–683 (2007).

[5] G. Carraro, D. Barreca, C. Maccato, E. Bontempi, L. E. Depero, C. de Julián Fernández, and A. Caneschi, *CrystEngComm* **15**(6), 1039 (2013).

[6] K. Sirok, J. Jire, and L. Hudec, *Thin solid films* **245**(1-2), 211–214 (1994).

[7] L. Huo, Q. Li, H. Zhao, L. Yu, S. Gao, and J. Zhao, *Sensors and Actuators B* **107**(2), 915–920 (2005).

[8] M. Aronniemi, J. Saino, and J. Lahtinen, *Thin Solid Films* **516**(18), 6110–6115 (2008).

[9] G. Carraro, D. Barreca, E. Comini, A. Gasparotto, C. Maccato, C. Sada, and G. Sberveglieri, *CrystEngComm* **14**(20), 6469 (2012).

[10] J. H. Kennedy and K. W. Frese, *J. Electrochem. Soc.* **125**(5), 709–714 (1978).

[11] S. U. M. Khan and J. Akikusa, *The Journal of Physical Chemistry B* **103**(34), 7184–7189 (1999).

[12] N. Beermann, L. Vayssieres, S.-E. Lindquist, and A. Hagfeldt, *Journal of The Electrochemical Society* **147**(7), 2456–2461 (2000).

[13] A. Kay, I. Cesar, and M. Grätzel, *Journal of the American Chemical Society* **128**(49), 15714–21 (2006).

[14] V. Satsangi, S. Kumari, A. Singh, R. Shrivastav, and S. Dass, *International Journal of Hydrogen Energy* **33**(1), 312–318 (2008).

[15] G. Carraro, C. Maccato, A. Gasparotto, T. Montini, S. Turner, O. I. Lebedev, V. Gombac, G. Adami, G. Van Tendeloo, D. Barreca, and P. Fornasiero, *Advanced Functional Materials* **24**(3), 372–378 (2014).

[16] W. Weiss, D. Zscherpel, and R. Schl, *Catalysis Letters* **52**, 215–220 (1998).

[17] O. Shekhah, W. Ranke, A. Schüle, G. Kolios, and R. Schlögl, *Angewandte Chemie* **42**(46), 5760–3 (2003).

[18] W. Huang, W. Ranke, and R. Schlögl, *The journal of physical chemistry. B* **109**(19), 9202–4 (2005).

[19] A. Schüle, U. Nieken, O. Shekhah, W. Ranke, R. Schlögl, and G. Kolios, *Physical chemistry chemical physics* **9**(27), 3619–34 (2007).

[20] L. Dghoughi, B. Elidrissi, C. Bernède, M. Addou, M. A. Lamrani, M. Regragui, and H. Erguig, *Applied Surface Science* **253**(4), 1823–1829 (2006).

[21] J. Chavez-Galan and R. Almanza, *Solar Energy* **81**(1), 13–19 (2007).

[22] B. Mauvernay, L. Presmanes, S. Capdeville, V. de Resende, E. De Grave, C. Bonningue, and P. Tailhades, *Thin Solid Films* **515**(16), 6532–6536 (2007).

[23] F. Voogt, T. Hibma, P. Smulders, and L. Niesen, *Journal of Crystal Growth* **174**(1-4), 440–445 (1997).

[24] Y. Gao, Y. Kim, and S. Chambers, *Journal of materials research* **13**, 2003–

2014 (1998).
[25] M. Gautier-soyer, S. Gota, E. Guiot, and M. Henriot, *PHYSICAL REVIEW B* **60**(20), 14387–14395 (1999).
[26] B. Pal and M. Sharon, *Thin Solid Films* **379**(1), 83–88 (2000).
[27] S. Trudel, C. H. W. Jones, and R. H. Hill, *Journal of Materials Chemistry* **17**(21), 2206–2218 (2007).
[28] W. Inglerjr and S. Khan, *International Journal of Hydrogen Energy* **30**(8), 821–827 (2005).
[29] S. Park, S. Lim, and H. Choi, *Chemistry of Materials* **18**(22), 5150–5152 (2006).
[30] G. Carraro, D. Barreca, M. Cruz-Yusta, A. Gasparotto, C. Maccato, J. Morales, C. Sada, and L. Sánchez, *Chemphyschem* **13**(17), 3798–801 (2012).
[31] D. Peeters, G. Carraro, C. Maccato, H. Parala, A. Gasparotto, D. Barreca, C. Sada, K. Kartaschew, M. Havenith, D. Rogalla, H.-W. Becker, and A. Devi, *Physica Status Solidi A* **211**(2), 316–322 (2014).
[32] M. Lie, H. Fjellvåg, and A. Kjekshus, *Thin Solid Films* **488**(1-2), 74–81 (2005).
[33] K. Nielsch, J. Bachmann, M. Daub, J. Jing, M. Knez, U. Gosele, S. Barth, S. Mathur, J. Escrig, and D. Altbir, *ECS Transactions* **11**(7), 139–148 (2007).
[34] J. Bachmann, J. Jing, M. Knez, S. Barth, H. Shen, S. Mathur, U. Gösele, and K. Nielsch, *Journal of the American Chemical Society* **129**(31), 9554–5 (2007).
[35] S. C. Riha, J. M. Racowski, M. P. Lanci, J. A. Klug, A. S. Hock, and A. B. F. Martinson, *Langmuir* **29**(10), 3439–45 (2013).
[36] M. Rooth, A. Johansson, K. Kukli, J. Aarik, M. Boman, and A. Hårsta, *Chemical Vapor Deposition* **14**(3-4), 67–70 (2008).
[37] J. R. Scheffe, A. Francés, D. M. King, X. Liang, B. A. Branch, A. S. Cavanagh, S. M. George, and A. W. Weimer, *Thin Solid Films* **517**(6), 1874–1879 (2009).
[38] A. Tamm, M. C. Dimri, J. Kozlova, A. Aidla, T. Tätte, T. Arroval, U. Mäeorg, H. Mändar, R. Stern, and K. Kukli, *Journal of Crystal Growth* **343**(1), 21–27 (2012).
[39] A. B. F. Martinson, M. J. DeVries, J. A. Libera, S. T. Christensen, J. T. Hupp, M. J. Pellin, and J. W. Elam, *The Journal of Physical Chemistry C* **115**(10), 4333–4339 (2011).
[40] J. A. Klug, N. G. Becker, S. C. Riha, A. B. F. Martinson, J. W. Elam, M. J. Pellin, and T. Proslier, *Journal of Materials Chemistry A* **1**(38), 11607 (2013).
[41] X. Zhang, G. Wen, S. Huang, L. Dai, R. Gao, and Z. L. Wang, *Journal of Magnetism and Magnetic Materials* **231**(1), 9–12 (2001).
[42] K. Aslan, M. Weisenberg, E. Hortle, and C. D. Geddes, *Journal of Applied Physics* **106**(1), 014313 (2009).
[43] K. Aslan, Y. Zhang, and C. D. Geddes, *The journal of physical chemistry C* **113**(48), 20535–20538 (2009).
[44] Y. Li, Y. Hu, G. Huang, and C. Li, *Particuology* **11**(4), 460–467 (2013).

[45] Q. Xie, Y.-L. Jiang, C. Detavernier, D. Deduytsche, R. L. Van Meirhaeghe, G.-P. Ru, B.-Z. Li, and X.-P. Qu, *Journal of Applied Physics* **102**(8), 083521 (2007).

[46] J. Musschoot, Q. Xie, D. Deduytsche, K. De Keyser, D. Longrie, J. Haemers, S. Van den Berghe, R. Van Meirhaeghe, J. D'Haen, and C. Detavernier, *Microelectronic Engineering* **87**(10), 1879–1883 (2010).

[47] J. Dendooven, R. K. Ramachandran, K. Devloo-Casier, G. Rampelberg, M. Filez, H. Poelman, G. B. Marin, E. Fonda, and C. Detavernier, *Journal of Physical Chemistry C* **117**(40), 20557–20561 (2013).

[48] W. Knaepen, C. Detavernier, R. Van Meirhaeghe, J. Jordan Sweet, and C. Lavoie, *Thin Solid Films* **516**(15), 4946–4952 (2008).

[49] W. Knaepen, S. Gaudet, C. Detavernier, R. L. Van Meirhaeghe, J. J. Sweet, and C. Lavoie, *Journal of Applied Physics* **105**(8), 083532 (2009).

[50] D. Longrie, K. Devloo-Casier, D. Deduytsche, S. Van den Berghe, K. Driesen, and C. Detavernier, *ECS Journal of Solid State Science and Technology* **1**(6), Q123–Q129 (2012).

[51] I. J. M. Erkens, A. J. M. Mackus, H. C. M. Knoops, P. Smits, T. H. M. van de Ven, F. Roozeboom, and W. M. M. Kessels, *ECS Journal of Solid State Science and Technology* **1**(6), P255–P262 (2012).

[52] S. M. George, *Chem. Rev* **110**, 111–131 (2010).

[53] A. J. M. Mackus, N. Leick, L. Baker, and W. M. M. Kessels, *Chemistry of Materials* **24**(10), 1752–1761 (2012).

[54] F. Visentin, R. Gerbasi, G. Rossetto, C. D. Zorzi, C. S. Uniti, N. E. Habra, D. Barreca, and A. Gasparotto, *Surface science spectra* **18**(1), 29–35 (2011).

[55] T. Yamashita and P. Hayes, *Applied Surface Science* **254**(8), 2441–2449 (2008).

Paper IV - supplementary information

Plasma enhanced atomic layer deposition of Fe_2O_3 thin films *

Thickness determination

A series of depositions were carried out at 200 °C with different number of ALD cyles. The thickness of the films was measured with X-ray reflectivity (XRR). Excellent fit for the XRR spectra were obtained by assuming the film density equal to the one of bulk α - Fe_2O_3 $(5.27g/cm^3)$.[1] X-ray fluorescence measurements were done on each sample and a linear relationship was obtained by plotting the integrated area under the Fe Kα peak against the thickness (**Figure S1**). This linear relationship was used for extracting the thickness, from XRF, of the films deposited at and above 350 °C and the thicker films deposited at 300 °C.

*Published as: Ramachandran, R. K.; Dendooven, J.; Poelman, H.; Detavernier, C.,*J. Phys. Chem. C*, 2015, 119, 11786-11791.

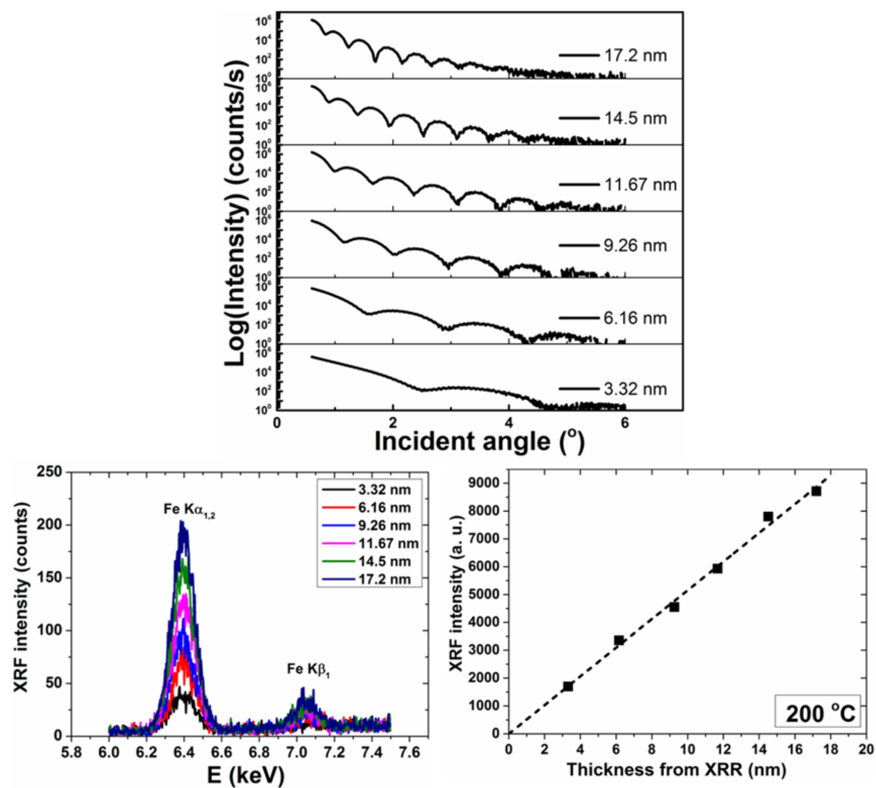

Figure S1. *XRR (top) and XRF (bottom left) signals of Fe_2O_3 thin films with different thicknesses deposited on SiO_2 substrates at 200°C. The thickness against the integrated XRF intensity over Fe Kα signal is plotted in the bottom right figure.*

References

[1] M. Lie, H. Fjellvåg, and A. Kjekshus, *Thin Solid Films* **488**(1-2), 74–81 (2005).

4

ALD based synthesis of noble and non-noble metal containing bimetallic alloys

4.1 Introduction

Bimetallic nanoparticles are an important class of materials, offering enhanced properties that surpass those of their monometallic parent materials due to synergistic effects.[1–6] Traditional synthesis methods[7;8] such as impregnation, electroless deposition, controlled simultaneous reduction, *etc.* often experience difficulties in obtaining a precise control over the size and composition of bimetallic nanoparticles, which are essential for the synthesis of an ideal supported bimetallic catalyst. ALD has proven its potential for reaching these goals, after Elam *et al.* demonstrated the suitability of ALD to deposit mixed metal layers of Ir and Pt.[9] Since then, several researchers have exploited its potential for fabricating different kinds of bimetallic particles, such as core/shell and alloyed nanoparticles, with (sub-)monolayer precision. In these previous studies, typically two noble metal ALD processes were combined, either sequentially or in a supercycle approach, and the nanoparticle morphology emerges as a result of the nucleation controlled growth of noble metals on oxide surfaces.

4.2 ALD for the synthesis of bimetallic materials

For the successful deposition of a bimetallic material, it is preferred that the surface chemistries of different components are mutually compatible and the deposition conditions are similar. Another important requirement is that the second metal should selectively grow on the first metal but not on the support. To this end, noble metals were always an interesting candidate as they prefer to grow selectively on the existing noble metal particles rather than on the oxide supports. The selective growth can also be obtained by different ways such as reducing the partial pressure of a reactant,[9–11] using self-assembled monolayers[12] or by using a lower deposition temperature.[13;14]

However, as discussed in the introductory chapter, section 1.2.2.2, this ALD based approach has to date only been applied for the synthesis of binary noble metal nanoparticles such as PtPd, PtRu *etc.* On the other hand, bimetallic materials consisting of a noble metal along with a non-noble metal, such as Pt-In, Pt-Ga and Pt-Sn, are actively explored in different fields including catalysis, gas sensing and optic and magnetic applications.[15–19] The direct deposition of such bimetallic materials by ALD is challenging because of the lack of favorable ALD chemistries for the deposition of the non-noble metals in their elemental state. As a consequence, a strong need has arisen to develop alternative ALD strategies which can deal with non-noble metals also and facilitate the tailored synthesis of bimetallic nanoparticle containing both noble and non-noble metals.

During this thesis work, a novel ALD based methodology has been developed for the controlled synthesis of bimetallic alloys containing both noble and non-noble metals and thereby adding a new possibility to the ALD based supported catalyst design. In this work, Pt is used as noble metal and the non-noble metals tried were In, Ga and Sn. The method essentially consists of two steps: first, thin films of MO_x and Pt are sequentially deposited using the respective ALD processes, yielding a Pt/MO_x bilayer. These bilayer structures are then subjected to a temperature programmed reduction (TPR) under H_2 atmosphere, which results in the formation of alloyed M_aPt_b particles with size and composition controlled by the selected ALD process conditions. A detailed description on the basic principles of this method, including the bilayer deposition, alloy formation mechanism and the phase and size tunability of the formed alloys, is given in the paper V, by taking the example of Pt-In and Pt-Ga alloy systems. A case study for the catalytic application of this novel approach is also discussed in the paper by taking the Pt-In system as an example. In addition, an extension of this method towards the synthesis of the well-known Pt-Sn bimetallic catalyst system is demonstrated in paper VI, which thereby affirms the generality of this novel approach.

References

[1] G. J. Hutchings and C. J. Kiely, *Accounts of Chemical Research* **46**(8), 1759–1772 (2013).

[2] D. I. Enache, J. K. Edwards, P. Landon, B. Solsona-Espriu, A. F. Carley, A. A. Herzing, M. Watanabe, C. J. Kiely, D. W. Knight, and G. J. Hutchings, *Science* **311**(5759), 362–365 (2006).

[3] R. Mu, Q. Fu, H. Xu, H. Zhang, Y. Huang, Z. Jiang, S. Zhang, D. Tan, and X. Bao, *Journal of the American Chemical Society* **133**(6), 1978–1986 (2011).

[4] S. Alayoglu, A. U. Nilekar, M. Mavrikakis, and B. Eichhorn, *Nature Materials* **7**(4), 333–338 (2008).

[5] J. Greeley, T. F. Jaramillo, J. Bonde, I. B. Chorkendorff, and J. K. Nørskov, *Nature materials* **5**(11), 909–13 (2006).

[6] F. Maroun, F. Ozanam, O. Magnussen, and R. Behm, *Science* **293**(September), 1811–1814 (2001).

[7] P. Munnik, P. de Jongh, and K. de Jong, *Chemical Reviews* **115**, 6687–6718 (2015).

[8] F. Pinna, *Catalysis Today* **41**, 129–137 (1998).

[9] S. T. Christensen and J. W. Elam, *Chemistry of Materials* **22**(8), 2517–2525 (2010).

[10] M. J. Weber, M. A. Verheijen, A. A. Bol, and W. M. M. Kessels, *Nanotechnology* **26**(9), 094002 (2015).

[11] A. J. M. Mackus, M. A. Verheijen, N. Leick, A. A. Bol, and W. M. M. Kessels, *Chemistry of Materials* **25**(9), 1905–1911 (2013).

[12] K. Cao, Q. Zhu, B. Shan, and R. Chen, *Scientific Reports* **5**, 8470 (2015).

[13] H. Wang, C. Wang, H. Yan, H. Yi, and J. Lu, *Journal of Catalysis* **324**, 59–68 (2015).

[14] P. M. Carisson and Jan-Otto, *J. Electrochem. Soc.* **145**(8), 2926–2931 (1998).

[15] F. Somodi, S. Werner, Z. Peng, A. Bean Getsoian, A. N. Mlinar, B. S. Yeo, and A. T. Bell, *Langmuir* **28**, 3345–3349 (2012).

[16] X. Wang, L. Altmann, J. Stöver, V. Zielasek, M. Bäumer, K. Al-Shamery, H. Borchert, J. Parisi, and J. Kolny-Olesiak, *Chemistry of Materials* **25**, 1400–1407 (2013).

[17] G. Onyestyák, *Catalysis Communications* **38**, 50–53 (2013).

[18] H. Zhu, D. H. Anjum, Q. Wang, E. Abou-Hamad, L. Emsley, H. Dong, P. Laveille, L. Li, A. K. Samal, and J.-M. Basset, *Journal of Catalysis* **320**, 52–62 (2014).

[19] E. A. Redekop, V. V. Galvita, H. Poelman, V. Bliznuk, C. Detavernier, and G. B. Marin, *ACS Catalysis* **4**, 1812–1824 (2014).

Paper V
Atomic Layer Deposition Route to Tailor Nanoalloys of Noble and Non-Noble Metals *

Abstract

Since their early discovery, bimetallic nanoparticles have revolutionized various fields, including nanomagnetism and -optics as well as heterogeneous catalysis. Knowledge build-up in the past decades has witnessed that the nanoparticle size and composition strongly impact the nanoparticle's properties and performance. Yet, conventional synthesis strategies lack proper control over the nanoparticle morphology and composition. Recently, atomically-precise synthesis of bimetallic nanoparticles has been achieved by atomic layer deposition (ALD), alleviating particle size and compositional non-uniformities. However, this bimetal ALD strategy applies to noble metals only, a small niche within the extensive class of bimetallic alloys. We report an ALD based approach for the tailored synthesis of bimetallic nanoparticles containing both noble and non-noble metals, here exemplified for Pt-In. First, a Pt/In_2O_3 bilayer is deposited by ALD, yielding precisely defined Pt-In nanoparticles after high temperature H_2 reduction. The nanoparticles' In content can be accurately controlled over the whole compositional range, and the particle size tuned from microns down to the nanometer scale. The size and compositional flexibility provided by this ALD-approach will trigger the fabrication of fully tailored bimetallic nanomaterials, including superior nanocatalysts.

*Published as: Ramachandran, R. K.; Dendooven, J.; Filez, M.; Galvita, V. V.; Poelman, H.; Solano, E.; Minjauw, M. M.; Devloo-Casier, K.; Fonda, E.; Hermida-Merino, D.; Bras, W.; Marin, G. B.; Detavernier, C., *ACS Nano*, 2016, 10, 8770-8777.

Introduction

Bimetallic nanoparticles play a pivotal role in optical, magnetic and electronic applications, and are true workhorses during the catalytic transformation of chemicals.[1–3] The addition of promoting elements to the monometallic host generates possibilities to diversify and tune the nanoparticle's properties and performance.[4] During the past years, breakthroughs in computational high-throughput screening have resulted in the discovery of interesting bimetallic nanomaterials.[5;6] However, such model-guided design is largely impeded by the lack of experimental validation. The rational design of bimetallic nanomaterials is thus dependent on the advent of synthesis methods which offer high control over the nanoparticle size and composition for a broad range of constituent elements. Traditional methods such as sequential or simultaneous wet impregnation[7;8] and ion exchange processes[8] often result in a wide distribution of particle sizes as well as heterogeneously mixed alloy phases. Colloidal synthesis methods enable the synthesis of bimetallic nanoparticles (BMNPs) with precise control over the size and composition,[9;10] but it remains challenging to remove the protecting ligands after deposition on the support without changing the morphology of the BMNPs. Recently, atomic layer deposition (ALD),[11–13] a vapour-phase deposition method, has proven its potential for the size and composition controlled synthesis of supported BMNPs, but has to date only been applied for the synthesis of binary noble metal nanoparticles like Pt-Pd, Pt-Ru and Pd-Ru BMNPs.[14–17] Extension of this approach to BMNPs containing non-noble metals has so far been hampered by unfavorable ALD chemistries to deposit non-noble metals in their elemental state.[13] As a consequence, a strong need has arisen to develop alternative ALD-strategies which can deal with non-noble metals also and facilitate the tailored synthesis of, among others, Pt-X (X = In, Sn, Ga; Cr, Mn, Fe, Co, Ni, Cu, W) and Cu-Y (Y = Zn, Ni) materials for magnetic[2] and (electro-)catalytic applications.[18;19]

This study presents an ALD based methodology for the synthesis of BMNPs containing both noble and non-noble metals, here demonstrated for catalytically important BMNPs containing Pt as noble and In or Ga as non-noble metal. The principle of the approach is depicted in **Figure 1**. First, a metal oxide (MO_x) layer is deposited with sub-monolayer thickness control onto a plasma cleaned silica substrate, followed by the deposition of a well-defined amount of Pt. The as-deposited Pt/MO_x bilayer is then subjected to a temperature programmed reduction (TPR) in hydrogen to induce the formation of M_aPt_b BMNPs. By tuning the deposited Pt/MO_x ratio and total amount of material, the synthesis of BMNPs with well-defined phase and size on planar surfaces is accomplished, as demonstrated by *in situ* X-ray diffraction (XRD), *in situ* grazing incidence small angle X-ray scattering (GISAXS), *ex situ* X-ray absorption spectroscopy (XAS) and *ex situ* scanning electron microscopy (SEM). In addition, successful BMNP synthesis is achieved on mesoporous silica, resulting in high surface area nanocatalysts which show promising high activity for propane dehydrogenation. The BMNP formation and phase and size tuning potential of the ALD strategy have been thoroughly studied for Pt-In. To illustrate the generality of the presented method, results for

Pt-Ga are included in the Supplementary Section 1.

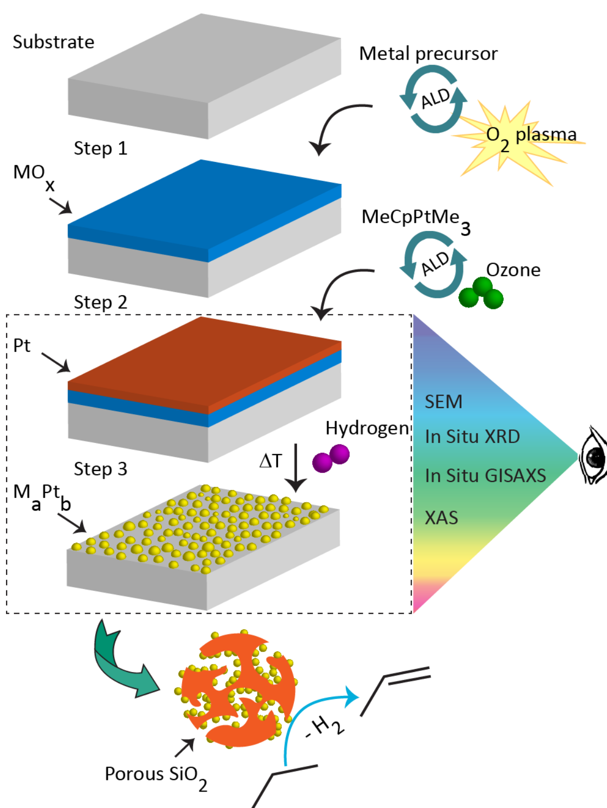

Figure 1. *ALD based synthesis of BMNPs on planar and porous silica supports. The procedure consists of three steps: (Step 1) ALD deposition of a metal oxide, MO_x, layer using a metal precursor and oxygen plasma, (Step 2) ALD deposition of a Pt layer using $MeCpPtMe_3$ and ozone, and (Step 3) temperature programmed reduction in hydrogen to convert the as-deposited Pt/MO_x bilayer into M_aPt_b BMNPs. First, planar silica substrates are used as supports enabling detailed characterization of the BMNP formation and investigation of the phase and size tuning potential by* in situ *grazing incidence small angle X-ray scattering (GISAXS),* in situ *X-ray diffraction (XRD), X-ray absorption spectroscopy (XAS) and scanning electron microscopy (SEM). Second, we demonstrate that this approach can be transferred to mesoporous silica substrates, allowing evaluation of the catalytic performance of the BMNPs in the dehydrogenation of propane.*

Results and Discussion

The mechanism of bimetallic particle formation is illustrated, starting from an ALD-deposited bilayer consisting of 6 nm Pt on top of 5.2 nm In_2O_3 (**Figure 2**a,

left). The Pt/(Pt+In) atomic ratio amounts to 72 %, as confirmed by X-ray fluorescence (XRF) compositional analysis (Supplementary Section 2). As shown by SEM imaging (**Figure 2**a, right) and time-resolved *in situ* XRD (**Figure 2**b), micron-sized $InPt_3$ alloyed particles are obtained after H_2 TPR to 700 °C. Initially, the pattern shows diffractions from In_2O_3 (222) (PDF 44-1087) and metallic Pt (111) (PDF 87-0646). The In_2O_3 (222) peak intensity is moderate at first and intensifies around 300 °C. This observation is in line with the reported increase in crystallinity of low temperature ALD-grown In_2O_3 films upon annealing in inert atmosphere.[20] The disappearance of the In_2O_3 (222) peak around 330 °C is indicative of complete reduction of the In_2O_3 layer. The In_2O_3 reduction is accompanied by a shift of the Pt (111) diffraction towards lower 2θ angle, implying expansion of the Pt fcc lattice due to insertion of In (atomic radius of 167 pm) into the Pt (atomic radius of 139 pm) structure. The stabilization of the shifted diffraction peak suggests the formation of an $InPt_3$ fcc alloy (PDF 50-1615).

To gain insights on the local atomic ordering, *ex situ* XAS measurements at the Pt L_{III} edge are carried out. In **Figure 2**c, the x-ray absorption near edge structure (XANES) spectrum of the reduced Pt-In sample is depicted together with the spectrum of a bulk Pt reference. The higher edge energy and the lower intensity of the white line - the first maximum above the edge - of the Pt-In sample as compared to the Pt reference are characteristic of Pt-In alloying.[21–24] Based on the electronegativity difference (In: 1.78 eV and Pt: 2.28 eV), electron donation takes place from In to Pt and results in the stabilization of Pt-In bonds, eventually yielding Pt-In alloys. Complementary extended x-ray absorption fine structure (EXAFS) data of the reduced Pt-In sample allow for more structural refinement of the local environment around Pt (**Figure 2**c, inset). Modeling of the EXAFS data including a single Pt-In and a Pt-Pt shell yields good agreement in a 2 - 3 Å R-range. Besides the dominant presence of Pt neighbors around Pt (N_{Pt-Pt} = 6.2 ± 3.2), EXAFS modeling evidences that In atoms are also present around Pt (N_{Pt-In} = 4.2 ± 2.4). In addition, the interatomic distances R_{Pt-Pt} and R_{Pt-In} are very similar (2.82 ± 0.04 and 2.81 ± 0.04 Å, respectively) and larger than the R_{Pt-Pt} distance in bulk Pt ($\sim$2.77 Å).[25] The higher shells around Pt ($R > 3$ Å) show strong resemblance with the peak features of fcc packed Pt, implying that the lattice packing inside the Pt-In alloyed phase is fcc-type. These results are in full accord with the formation of an $InPt_3$ alloyed phase, as indicated by *in situ* XRD. $InPt_3$ alloys have an isotropically expanded cubic fcc-type packing in which both Pt (face-centered positions) and In (corner positions) atoms surround Pt in an ordered intermetallic lattice.[26]

Nanoscale $InPt_3$ particles are obtained by downscaling the amounts of deposited Pt and In_2O_3, while keeping the Pt/(Pt+In) atomic ratio constant (**Figure 2**d, right)). By reducing the number of ALD cycles, equivalent thicknesses (Supplementary Section 2) of 1.0 nm Pt and 0.7 nm In_2O_3 are deposited with high control, yielding a Pt/(Pt+In) ratio of 76 %. SEM imaging (**Figure 2**d, left) shows that the as-deposited Pt morphology consists of a large density of sub-10 nm particles, known to be a consequence of the initial nucleation-controlled growth mode for Pt ALD.[27;28] *In situ* XRD characterization during H_2 TPR shows similar trends

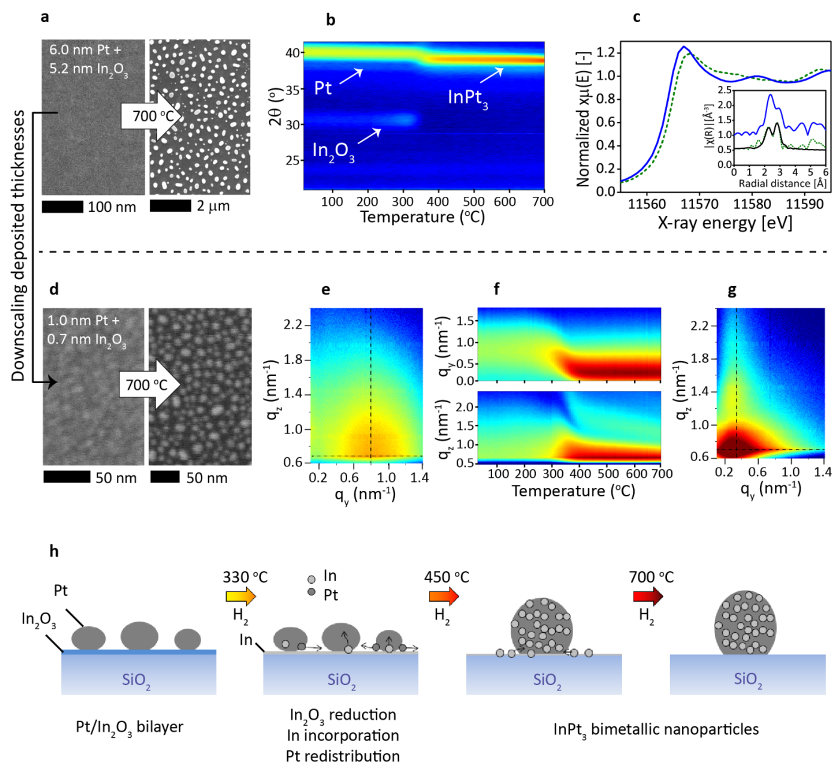

Figure 2. Bimetallic nanoparticle formation on planar silica substrates. (a,d) SEM images of as-deposited Pt/In_2O_3 bilayers (left) and the BMNPs obtained after TPR in 10% H_2/N_2 up to 700 °C (right). Deposited (equivalent) thicknesses are indicated in the image. (b) in situ XRD patterns measured during TPR in 10% H_2/N_2. (c) XANES and k^2-weighted Fourier transformed EXAFS (inset) magnitudes of the BMNPs obtained after TPR in 10% H_2/N_2 up to 700 °C (green, dashed) and metallic Pt fcc reference (blue, full). The black line in the inset is the EXAFS modeling result (Pt-Pt + Pt-In shell). (e,g) Experimental 2D GISAXS patterns of the as-deposited Pt/In_2O_3 bilayer (e) and the BMNPs obtained after TPR in 20% H_2/He up to 700 °C (g). (f) 2D color maps showing the intensity evolution of the horizontal line profile at q_z = 0.69 nm^{-1} (top) and the vertical line profile at $q_{y,max}$ (bottom). The dashed lines in e and g indicate the positions of the line profiles. (h) Schematic representation of the BMNP formation as interpreted from in situ XRD and GISAXS.

as for the above discussed thicker variant and confirms the formation of an $InPt_3$ alloyed phase (Supplementary Figure S3). *In situ* GISAXS characterization during TPR monitors the evolution of the nanoscale morphology of the sample (**Figure 2**e-g). Comparison of the scattering pattern observed for the as-deposited sample (**Figure 2**e) with simulations (Supplementary Figure S4a, right) confirms that the Pt ALD process results in particles with an average size of 3-4 nm and center-to-center distance of *ca.* 5.5 nm. The temporal evolution of the scattering features is

clearly visible in the 2D color plots representing horizontal (**Figure 2**f, top) and vertical intensity (**Figure 2**f, bottom) line profiles. A stable scattering pattern is observed up to a temperature of *ca.* 300 °C. The horizontal profiles reveal that the onset of alloying - observed at 330 °C in *in situ* XRD (Supplementary Figure S3) - is accompanied by a gradual peak shift to lower q_y-values. In addition, an intensification of the main scattering peak is observed, followed by a stabilization of the scattering pattern at *ca.* 450 °C. In the vertical profiles, a clear shift of the scattering minimum is observed to lower q_z-values between 300 and 450 °C (**Figure 2**f, bottom). These results indicate that the insertion of In in the Pt fcc lattice, as monitored by XAS and XRD, is accompanied by the migration and redistribution of Pt atoms across the surface. Based on GISAXS simulations, on average 7-9 as-deposited Pt nanoparticles coalesce into a larger BMNP between 300 and 450 °C. Above 450 °C, the lateral morphology remains stable, while the increase in $InPt_3$ crystallinity - indicated by intensification of the diffraction peak (Supplementary Figure S3) induces a gradual increase in particle height (*ca.* 1 nm from 450 to 700 °C) as concluded from the slow continuous decrease of the $q_{z,min}$ -value in **Figure 2**f (bottom). Analysis of the GISAXS pattern measured at 700 °C (**Figure 2**g and Supplementary Figure S4b, right) indicates an average size of the BMNP of 7-8 nm and a center-to-center particle distance of *ca.* 21 nm. As schematically illustrated in **Figure 2**h, in situ XRD and GISAXS thus allow to conclude that the alloyed phase and particle morphology are formed simultaneously during the TPR.

Tuning of the composition is achieved by controlling the ratio of the deposited (equivalent) thickness of Pt (dPt) to the thickness of In_2O_3 (dIn_2O_3). In addition to the sample with an as-deposited Pt/(Pt+In) atomic ratio of 72% that was discussed above (**Figure 2**b and repeated in **Figure 3**a, left), the phase formation is studied in detail for three other Pt/In_2O_3 bilayers with a total thickness above 10 nm and Pt/(Pt+In) atomic ratios of 58%, 38% and 11% (**Figure 3**b-d, left). Because for these three samples dIn_2O_3 is larger than for the first sample, the In_2O_3 (222) diffraction peak is more intense in the initial XRD patterns and additional peaks corresponding to In_2O_3 (332) and (400) respectively, are visible for the In-rich samples. The Pt (111) peak, on the other hand, is less intense for the 38% sample and is below the detection limit for the 11% sample due to the smaller values of dPt. The larger broadness of this peak for the 38% sample is related to the morphology of the deposited Pt layer, being a dense collection of small Pt nanoparticles. The color plots in **Figure 3** reveal a striking difference in evolution of the diffraction peaks with temperature between the 72% sample and the other ones. For the latter, In is incorporated into the Pt lattice before the In_2O_3 layer is completely reduced, which is indicated by the shift of the Pt (111) peak and appearance of Pt-In diffractions before the disappearance of the In_2O_3 diffractions. Once the whole In_2O_3 layer is reduced, the high availability of In enables the further enrichment and saturation of the Pt phase, resulting in In_9Pt_{13} (PDF 31-0598), In_2Pt (PDF 65-2989) and In_7Pt_3 (PDF 65-4560) intermetallic compounds for the 58%, 38% and 11% sample, respectively. For the 11% sample, $InPt_3$ is formed as an intermediate phase next to In_2O_3 between 300 and 500 °C. Although the intermediate Pt-In phases are less obvious to identify for the 58% and 38% samples,

it is likely that in both cases there is a small temperature window following the downward shift of the Pt (111) peak where $InPt_3$ is formed. For the 58% sample, this phase is shortly present next to the In_9Pt_{13} phase. For the 38% sample, the downward shift of the broad Pt peak and intermediate formation of $InPt_3$ is followed by diffraction at a 2θ angle of 40.7°, suggesting the temporal formation of In_9Pt_{13} before the final In_2Pt phase is formed. The wider 2θ scans measured after TPR up to 700 °C and subsequent cooldown in H_2 flow to room temperature (**Figure 3**a-d, right) confirm the formation of phase pure Pt-In alloys for the 72%, 58% and 38% samples, while metallic In is observed next to the bimetallic In_7Pt_3 phase for the 11% sample.

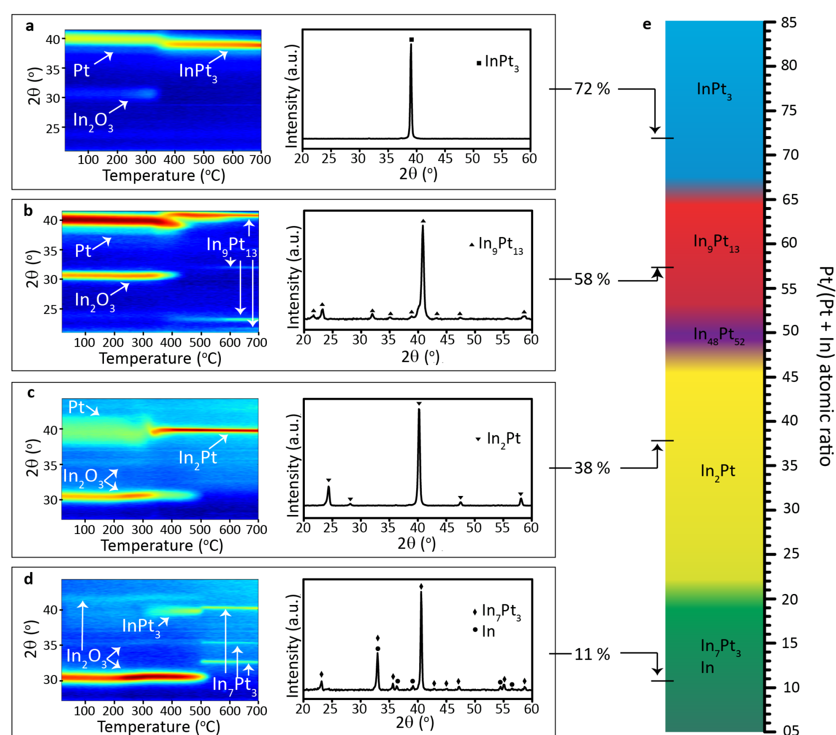

Figure 3. Phase tuning by ALD on planar silica substrates. (a-d) (Left) In situ *XRD patterns measured during TPR in 10% H_2/N_2 of Pt/In_2O_3 bilayers with a Pt/(Pt+In) atomic ratio of (a) 72%, (b) 58%, (c) 38%, and (d) 11%. The color plot in a is identical to that in Figure 2b. Note the different 2θ range for the color plots in panels a,b vs. panels c,d. (Right) 20 - 60° 2θ scans measured after TPR in 10% H_2/N_2 up to 700 °C. (e) Color bar visualizing the relation between the as-deposited Pt/(Pt+In) atomic ratio and the alloy phase(s) obtained after TPR up to 700 °C independent of the total deposited thickness.*

Figure 3e presents the relation between the as-deposited Pt/(Pt+In) atomic ratio and the alloy phase(s) obtained after TPR up to 700 °C, as resulting from the characterization of more than 40 samples with different Pt/(Pt+In) atomic ratios in

the range 5 - 85%. These phases are found to be independent of the total deposited thickness of the as-deposited bilayer, as is further also demonstrated in **Figure 4** and Supplementary Figure S5. In total 4 different phase-pure alloys are achievable, with wide Pt/(Pt+In) atomic ratio windows for $InPt_3$, In_9Pt_{13} and In_2Pt, and only a small window for $In_{48}Pt_{52}$. In between the phase-pure windows, XRD indicates mixtures of the adjoining phases as represented by the graded color zones. For Pt/(Pt+In) atomic ratios below 20%, metallic In is observed next to the most In-rich phase, In_7Pt_3. Compositional analysis of reduced samples with as-deposited Pt/(Pt+In) ratios between 33 and 5% furthermore reveals a 10 to 50% In loss during TPR. This is a consequence of the low melting point of metallic In (156.6 °C) and indicates that not all reduced In can be incorporated in In-rich Pt-In alloys. On the other hand, for as-deposited Pt/(Pt+In) ratios above 33% all available In is used in the alloy formation. In summary, these experiments show that, in spite of the complex nature of the Pt-In phase diagram,[29;30] the proposed ALD based approach offers a high level control over the phase of the In_aPt_b alloy that is formed upon reduction.

As discussed before for $InPt_3$, decreasing the size of the bimetallic particles from the micro- to the nanoscale is achieved by reducing the total deposited thickness of the Pt/In_2O_3 bilayer (dTotal = dPt + dIn_2O_3), while keeping the Pt/(Pt+In) atomic ratio constant. To investigate the size tuning potential at the nanoscale more systematically, three series of samples with Pt/(Pt+In) atomic ratios of *ca.* 75%, 60% and 40%, and different values of dTotal in the range 1 - 5 nm are deposited. TPR of the samples up to 700 °C leads to the formation of the expected $InPt_3$, In_9Pt_{13} and In_2Pt phases respectively, as confirmed by XRD for samples with dTotal $>$ 1.5 nm, the thinner ones being below the XRD detection limit (Supplementary Figure S5). The SEM images and particle size distributions of the reduced samples can be found in the Supplementary Figure S6, while **Figure 4** displays the average particle size against the total thickness dTotal for the three series of samples. Two trends are observed: (i) the average particle size decreases linearly with decreasing dTotal, and (ii) for the same value of dTotal, larger BMNPs are obtained for the most Pt-rich phase, $InPt_3$, than for the other phases. Linear fits to the data points demonstrate that the atomic-level control of ALD over the deposited Pt and In_2O_3 thicknesses can be exploited to accurately tune the average particle size, while ensuring the formation of a specifically targeted Pt-In alloy phase.

To evaluate the applicability of the ALD based BMNP synthesis approach for catalysis, consecutive In_2O_3 and Pt ALD are applied on mesoporous silica powder as a proof-of-principle experiment. Inductively coupled plasma mass spectrometry (ICP-MS) confirms the successful deposition of both Pt and In_2O_3 on the mesoporous material. The nanoparticle nature of the ALD-deposited material after TPR in hydrogen is evidenced by scanning transmission electron microscopy (STEM) in **Figure 5**.

The catalytic activity of a reduced Pt-In loaded porous silica with Pt/(Pt+In) atomic ratio of 75% is tested in the industrially important dehydrogenation of propane and compared to the activity of an ALD-prepared monometallic reference sample containing the same amount of Pt (Supplementary Figure S7). Both Pt and

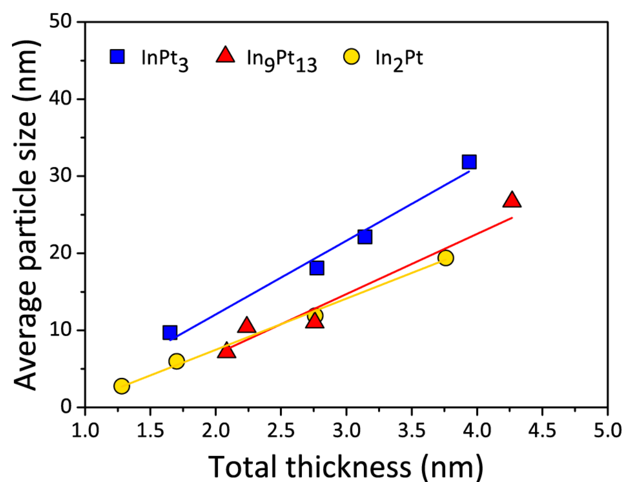

Figure 4. *Size tuning by ALD on planar silica substrates. Average size of the BMNPs formed after TPR in 10% H_2/N_2 up to 700 °C as determined from SEM analysis against the total deposited thickness (dTotal) for three different Pt-In phases, $InPt_3$ (blue squares), In_9Pt_{13} (red triangles), and In_2Pt (yellow circles). The lines are linear fits to the data points and highlight the observed trends.*

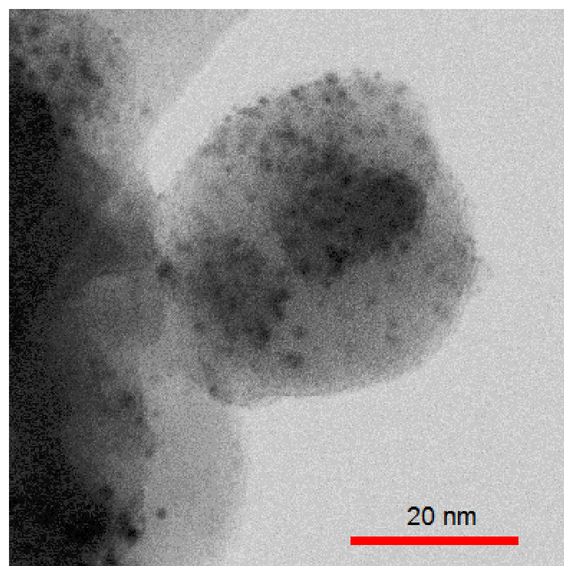

Figure 5. *Bimetallic nanoparticle formation on porous silica support. STEM bright field micrograph showing the overall morphology of the supported BMNPs after TPR in 5% H_2/Ar up to 650 °C.*

Pt-In catalysts display a propylene turnover frequency (TOF) which is comparable to state-of-the-art synthesized Pt and Pt-In dehydrogenation catalysts. More specifically, the steady-state propylene TOF for Pt/SiO_2 (ALD) and $Pt/Mg(Al)O_x$ (conventional) monometallic catalysts amount to 0.95 s^{-1} and 0.90 s^{-1}, respectively, while the $Pt\text{-}In/SiO_2$ (ALD) and $Pt\text{-}In/Mg(In)(Al)O_x$ (conventional) bimetallic catalysts have a $\sim$2.5 times larger propylene TOF of 3 s^{-1}.[31–33] In addition to a high activity, both ALD-prepared catalysts exhibit good selectivity with a steady-state value close to 100%. Determination of the amount of coke accumulation on both materials reveals the bimetallic catalyst to be far less prone to deactivation through coking (Supplementary Section 3.4).[34] After surface coke removal and regeneration of the catalysts by an oxidation-reduction cycle, the initial activity of both ALD-prepared catalysts is fully restored, indicating their resilience in harsh conditions (600 °C). Complementary *in situ* XRD during cyclic oxidation and reduction of BMNPs on planar substrates shows the repetitive segregation of Pt-In bimetal into Pt and In_2O_3 under oxidative environment and re-alloying under reducing environment, while *in situ* GISAXS measurements confirm the stability of the particle morphology (Supplementary Section 3.5). Such an environment-dependent mobility of the modifying element on the catalyst surface appears to be a general feature of supported Pt-based bimetallic catalysts.[35–38] It is concluded that the ALD-prepared Pt-In nanocatalyst can compete with existing outstanding propane dehydrogenation catalysts in activity, selectivity and durability, while the capability of ALD for tuning the size and phase of BMNPs will allow pursuing high level optimization. Hence, ALD has strong potential to deliver the next generation of rationally designed and tailor-made bimetallic catalysts.

Conclusion

In summary, an ALD based recipe is established for the fully-tailored synthesis of supported bimetallic nanoparticles, allowing accurate control over particle size and alloy composition. In contrast to previously reported ALD synthesis strategies, our approach extends to nanoparticles containing both noble and non-noble metals, here demonstrated in detail for Pt-In alloys. The self-limiting nature of ALD allows for the deposition of a Pt/In_2O_3 bilayer with atomically-precise control over the individual Pt and In_2O_3 layer thicknesses. When subjected to a thermal reduction treatment in hydrogen, the ALD-deposited bilayer transforms into alloyed Pt-In particles as a result of atomic migration and coalescence at the support surface. The particle size can be tuned with high precision in a range from 1 to 30 nm by changing the total thickness of the ALD-grown Pt/In_2O_3 bilayer. The control over the deposited Pt/In ratio provided by ALD offers tools at hand to manipulate the Pt-In alloy phase, independent of the initial total film thickness. As a proof-of-principle, mono- and bimetallic Pt and Pt-In nanocatalysts have been produced, exhibiting similar performance as existing state-of-the-art propane dehydrogenation catalysts. Further optimization efforts have strong potential to generate greatly improved bimetallic nanocatalysts which outperform the current alternatives. In

addition, the presented method is expected to create opportunities for fields in search of bimetallic materials containing non-noble metals, for example, Pt-Fe or Pt-Co particles for magnetic applications.

Methods

Sample preparation. All depositions were performed at 150 °C in a ALD chamber with a base pressure of 10^{-6} mbar and a remote plasma configuration.[39;40] For the planar model systems, O_2 plasma cleaned Si wafers with a 100 nm thermally grown SiO_2 layer on top were used as substrates. M_2O_3 [M = In or Ga] and Pt were deposited using alternating exposures of $M(TMHD)_3$ (99%, Strem Chemicals) and O_2 plasma for M_2O_3 ALD[20;41] and $(MeCp)PtMe_3$ (99%, Strem Chemicals) and O_3 for Pt ALD.[27;28] Ar with 99.999% purity was used as a carrier gas for all precursors. For the plasma process, O_2 gas flowed through the plasma source at a pressure of 0.01 mbar and the RF plasma power was set at 300 W. O_3 was produced from a 99% O_2/N_2 mixture with an AC-2025 (USA Inc.) generator, resulting in an O_3 concentration of 200 μg/ml. A typical M_2O_3 ALD cycle lasted 20 s with 5 s pulse time for both the precursor and reactant, and 5 s pumping after each pulse. For Pt ALD, a static exposure mode was applied during both ALD half-cycles,[27] resulting in a total cycle time of 50 s. For the depositions on high surface area supports, *ca.* 100 mg of mesoporous SiO_2 powder was spread on the bottom of a Mo cup, and four times longer precursor and reactant pulse times were applied. Thermal reduction of the as-deposited samples in hydrogen was achieved by heating the sample to 700 °C using a ramp rate of 0.2 °C/s.

Composition determination. For the planar model systems, Pt and M_2O_3 film thicknesses were determined by X-ray reflectivity measurements using a Bruker D8 Discover system with Cu Kα radiation. Alternatively, the thickness was extracted from calibrated X-ray fluorescence data obtained with a Bruker Artax system with Mo X-ray source. Pt/(Pt+M) atomic ratios were calculated from the thicknesses by assuming bulk densities for Pt and M_2O_3 (Supplementary Section 2). For the mesoporous samples, inductively coupled plasma atomic emission spectroscopy (ICP-AES, ICAP 6500, Thermo Scientific) was performed to determine the bulk chemical compositions. The samples were mineralized using peroxide and alkaline fusion with a mix of Li-tetraborate and Li-metaborate.

In situ X-ray diffraction. The TPR treatment of the Pt/M_2O_3 bilayers was performed under 10% H_2/N_2 atmosphere in a home-built heating chamber mounted on a Bruker D8 diffractometer[42;43] to enable in situ XRD characterization. A linear detector covering 20° in 2θ was used to collect the diffracted X-rays with a 2 s time resolution.

In situ grazing incidence small angle x-ray scattering. In situ GISAXS measurements during TPR treatment of the Pt/M_2O_3 bilayers were performed in a home-built heating chamber positioned in the path of a 12.0 keV X-ray beam at the DUBBLE beamline of the ESRF synchrotron facility (Grenoble, France).[44] The samples were irradiated at an incidence angle of 0.5° and the scattered x-rays were recorded with a Dectris Pilatus 1M detector placed at a sample-detector distance of approximately 4.1 m. A H_2 in He reducing gas mixture was used. During the annealing, data were collected with 30 s time resolution. Details on the GISAXS modeling are available in Supplementary Section 3.2.

X-ray absorption spectroscopy. XAS measurements were performed at the SAMBA beamline of the SOLEIL synchrotron (Saint-Aubin, France) operating at 450 mA. All experiments were performed in fluorescence mode at the Pt L_{III} edge (E = 11564 eV) using a 35-element Ge detector (Canberra). XAS data reduction and analysis were executed with the Demeter 0.9.13 software package by following the methodology of Koningsberger *et al.*.[45–47] For EXAFS modeling, the FEFF 6.0 code was applied to calculate the phase shifts and backscattering amplitude functions of Pt-In and Pt-Pt contributions to the EXAFS signal.[47] The minimization of the objective function, carried out by IFEFFIT, yielded estimates for the structural parameters by multiple shell fitting in R-space using multiple k-weightings.[45]

Electron microscopy. SEM analysis of the planar model systems was performed on a FEI Quanta 200F and a FEI Sirion instrument. On the porous sample, HR-TEM and BF-STEM were performed using a JEOL JEM-2200FS Cs-corrected microscope operated at 200 kV, and equipped with a Schottky-type field-emission gun and EDX JEOL JED-2300D. The samples were fixed by immersion onto a lacey carbon film on a copper support grid.

Catalytic testing. Experimental details are available in Supplementary Section 3.4.

Acknowledgments

This research was supported by the European Research Council (Starting Grant no. 239865), by the Flemish Research Foundation (FWO-Vlaanderen) (Project G.0209.11, research fellowships of J.D. and M.M.M.), the Flemish Government (Long-term structural fundingMethusalem funding), the Special Research Fund BOF of Ghent University (GOA 01G01513), and the IAP7/05 Interuniversity Attraction Poles Programme, Belgian State, Belgian Science Policy. The authors received funding from the European Community's Trans National Access Program CALIPSO for financing beam time at the SAMBA beamline of SOLEIL and travel costs, and from the Fund for Scientific Research Flanders (FWO-Vlaanderen) for

financing beam time at the DUBBLE beamline of the ESRF and travel costs. We are also grateful to the ESRF and SOLEIL staff for smoothly running the facilities.

References

[1] B. Lim, M. Jiang, P. H. C. Camargo, E. C. Cho, J. Tao, X. Lu, Y. Zhu, and Y. Xia, *Science* **324**(5932), 1302–1305 (2009).

[2] A. K. Nayak, M. Nicklas, S. Chadov, P. Khuntia, C. Shekhar, A. Kalache, M. Baenitz, Y. Skourski, V. K. Guduru, A. Puri, U. Zeitler, J. M. D. Coey, and C. Felser, *Nature Materials* **14**(7), 679–684 (2015).

[3] J. A. Schuller, E. S. Barnard, W. Cai, Y. C. Jun, J. S. White, and M. L. Brongersma, *Nature materials* **9**(3), 193–204 (2010).

[4] A. Franceschetti and A. Zunger, *Nature* **402**(6757), 60–63 (1999).

[5] J. Greeley, T. F. Jaramillo, J. Bonde, I. Chorkendorff, and J. K. Nørskov, *Nature Materials* **5**(11), 909–913 (2006).

[6] G. Ceder, Y.-M. Chiang, D. R. Sadoway, M. K. Aydinol, Y.-I. Jang, and B. Huang, *Nature* **392**(6677), 694–696 (1998).

[7] S. Duan and R. Wang, *Progress in Natural Science: Materials International* **23**(2), 113–126 (2013).

[8] E. Marceau, X. Carrier, M. Che, O. Clause, and C. Marcilly, *Handbook of Heterogeneous Catalysis* , 467–484 (2008).

[9] C.-J. Jia and F. Schüth, *Physical chemistry chemical physics : PCCP* **13**(7), 2457–2487 (2011).

[10] X. Wang, L. Altmann, J. Stöver, V. Zielasek, M. Bäumer, K. Al-Shamery, H. Borchert, J. Parisi, and J. Kolny-Olesiak, *Chemistry of Materials* **25**, 1400–1407 (2013).

[11] S. M. George, *Chem. Rev* **110**, 111–131 (2010).

[12] C. Detavernier, J. Dendooven, S. Pulinthanathu Sree, K. F. Ludwig, and J. A. Martens, *Chemical Society Reviews* **40**(11), 5242 (2011).

[13] V. Miikkulainen, M. Leskelä, M. Ritala, and R. L. Puurunen, *Journal of Applied Physics* **113**(2), 021301 jan (2013).

[14] B. J. O'neill, D. H. K. Jackson, J. Lee, C. Canlas, P. C. Stair, C. L. Marshall, J. W. Elam, T. F. Kuech, J. A. Dumesic, and G. W. Huber, *ACS Catalysis* **5**, 1804–1825 (2015).

[15] J. Lu, K.-B. Low, Y. Lei, J. A. Libera, A. Nicholls, P. C. Stair, and J. W. Elam, *Nature Communications* **5**, 3264 (2014).

[16] S. T. Christensen, H. Feng, J. L. Libera, N. Guo, J. T. Miller, P. C. Stair, and J. W. Elam, *Nano Letters* **10**(8), 3047–3051 (2010).

[17] K. Cao, Q. Zhu, B. Shan, and R. Chen, *Scientific Reports* **5**, 8470 (2015).

[18] G. Prieto, J. Zečević, H. Friedrich, K. P. de Jong, and P. E. de Jongh, *Nature materials* **12**(1), 34–39 (2013).

[19] W. Yu, M. D. Porosoff, and J. G. Chen, *Chemical Reviews* **112**(11), 5780–5817 (2012).

[20] R. K. Ramachandran, J. Dendooven, H. Poelman, and C. Detavernier, *The Journal of Physical Chemistry C* **119**(21), 11786–11791 (2015).

[21] L.-S. Hsu, G. Guo, J. Denlinger, and J. Allen, *Physical Review B* **63**(15), 155105 (2001).

[22] E. Bus and J. A. V. Bokhoven, *Journal of Physical Chemistry C* **111**, 9761–

9768 (2007).

[23] M. Filez, E. A. Redekop, H. Poelman, V. V. Galvita, R. K. Ramachandran, J. Dendooven, C. Detavernier, and G. B. Marin, *Chemistry of Materials* **26**, 5936–5949 (2014).

[24] M. Filez, E. A. Redekop, H. Poelman, V. V. Galvita, and G. B. Marin, *Analytical Chemistry* **87**(6), 3520–3526 (2015).

[25] B. Roldan Cuenya, M. Alcántara Ortigoza, L. K. Ono, F. Behafarid, S. Mostafa, J. R. Croy, K. Paredis, G. Shafai, T. S. Rahman, L. Li, Z. Zhang, and J. C. Yang, *Physical Review B* **84**(24), 1–14 (2011).

[26] H. Ipser, *Pure and Applied Chemistry* **79**(10), 1675–1689 (2007).

[27] J. Dendooven, R. K. Ramachandran, K. Devloo-Casier, G. Rampelberg, M. Filez, H. Poelman, G. B. Marin, E. Fonda, and C. Detavernier, *Journal of Physical Chemistry C* **117**(40), 20557–20561 (2013).

[28] M. Filez, H. Poelman, R. K. Ramachandran, J. Dendooven, K. Devloo-Casier, E. Fonda, C. Detavernier, and G. B. Marin, *Catalysis Today* **229**, 2–13 (2014).

[29] T. Biggs, S. S. Taylor, and E. Van Der Lingen, *Platinum Metals Review* **49**(1), 2–15 (2005).

[30] H. Okamoto, *Journal of Phase Equilibria & Diffusion* **26**(4), 399–399 (2005).

[31] J. Zhu, M. L. Yang, Y. Yu, Y. A. Zhu, Z. J. Sui, X. G. Zhou, A. Holmen, and D. Chen, *ACS Catalysis* **5**(11), 6310–6319 (2015).

[32] M. Filez, E. A. Redekop, H. Poelman, V. V. Galvita, M. Meledina, S. Turner, G. Van Tendeloo, C. Detavernier, and G. B. Marin, *Catal. Sci. Technol.* **6**(6), 1863–1869 (2016).

[33] P. Sun, G. Siddiqi, W. C. Vining, M. Chi, and A. T. Bell, *Journal of Catalysis* **282**(1), 165–174 (2011).

[34] G. Siddiqi, P. Sun, V. Galvita, and A. T. Bell, *Journal of Catalysis* **274**(2), 200–206 (2010).

[35] M. Filez, E. A. Redekop, V. V. Galvita, H. Poelman, M. Meledina, S. Turner, G. Van Tendeloo, A. T. Bell, and G. B. Marin, *Phys. Chem. Chem. Phys.* **18**(4), 3234–3243 (2016).

[36] J. Im and M. Choi, *ACS Catalysis* **6**, 2819–2826 (2016).

[37] H. Zhu, D. H. Anjum, Q. Wang, E. Abou-Hamad, L. Emsley, H. Dong, P. Laveille, L. Li, A. K. Samal, and J.-M. Basset, *Journal of Catalysis* **320**, 52–62 (2014).

[38] E. A. Redekop, V. V. Galvita, H. Poelman, V. Bliznuk, C. Detavernier, and G. B. Marin, *ACS Catalysis* **4**, 1812–1824 (2014).

[39] Q. Xie, Y.-L. Jiang, C. Detavernier, D. Deduytsche, R. L. Van Meirhaeghe, G.-P. Ru, B.-Z. Li, and X.-P. Qu, *Journal of Applied Physics* **102**(8), 083521 (2007).

[40] J. Musschoot, Q. Xie, D. Deduytsche, S. Van den Berghe, R. Van Meirhaeghe, and C. Detavernier, *Microelectronic Engineering* **86**(1), 72–77 (2009).

[41] R. K. Ramachandran, J. Dendooven, J. Botterman, S. P. Sree, D. Poelman,

J. A. Martens, H. Poelman, and C. Detavernier, *Journal of Materials Chemistry A* **2**, 19232–19238 (2014).

[42] W. Knaepen, C. Detavernier, R. Van Meirhaeghe, J. Jordan Sweet, and C. Lavoie, *Thin Solid Films* **516**(15), 4946–4952 (2008).

[43] W. Knaepen, S. Gaudet, C. Detavernier, R. L. Van Meirhaeghe, J. J. Sweet, and C. Lavoie, *Journal of Applied Physics* **105**(8), 083532 (2009).

[44] W. Bras, I. Dolbnya, D. Detollenaere, R. van Tol, M. Malfois, G. Greaves, A. Ryan, and E. Heeley, *Journal of Applied Crystallography* **36**(3), 791–794 (2003).

[45] B. Ravel and M. Newville, *Journal of Synchrotron Radiation* **12**(4), 537–541 (2005).

[46] D. Koningsberger, B. Mojet, G. van Dorssen, and D. Ramaker, *Topics in Catalysis* **10**(3), 143–155 (2000).

[47] J. J. Rehr, J. Mustre de Leon, S. I. Zabinsky, and R. C. Albers, *Journal of the American Chemical Society* **113**(14), 5135–5140 (1991).

Paper V - supplementary information

Atomic Layer Deposition Route to Tailor Nanoalloys of Noble and Non-Noble Metals *

1. Pt-Ga phase tuning

Pt-Ga phase tuning is achieved by controlling the ratio of the thickness of Pt (dPt) to the thickness of Ga_2O_3 (dGa_2O_3). Three different samples are prepared with a constant Ga_2O_3 thickness of 11.8 nm, while the Pt thickness is varied. With Pt thicknesses of 12.9, 5.7 and 1.4 nm, the as-deposited bilayers have a Pt/(Pt+Ga) atomic ratio of 66, 46 and 17%, respectively. **Figure S1**a (left) shows the time-resolved *in situ* XRD patterns recorded during TPR of the 66% sample. Initially the pattern shows a single diffraction peak at 39.8° corresponding to metallic Pt (111), as the as-deposited Ga_2O_3 is amorphous. With increasing temperature, the crystallinity of the metallic Pt increases as evidenced by the intensification of the Pt (111) peak above 350 °C. Moreover, additional peaks appear symmetrically around the diffraction peak, which suggests that the reducing treatment induces the formation of smooth grains whose width is much larger than their thickness.[1] At 500 °C, we observe an upward shift of the Pt peak, implying contraction of the Pt fcc lattice due to insertion of Ga (atomic radius of 135 pm) into the Pt (atomic radius of 139 pm) structure. The stabilization of the intense diffraction peak at 40.2° suggests the formation of a $GaPt_2$ (PDF 65-4771) structure. The purity of the formed phase is confirmed in the 20° to 60° 2θ scan measured after the reducing experiment (**Figure S1**a (right)). The *in situ* XRD patterns recorded during TPR of the 46% sample (**Figure S1**b (left)) show a shift of the Pt (111) peak to the $GaPt_2$ diffraction at 40.2° around 350 °C, followed by formation of the GaPt,[2;3] phase at 500 °C as evidenced by the appearance of diffractions at 36.8° and 41.2°. For the 17% sample, XRD shows the consecutive formation of $GaPt_2$

*Published as: Ramachandran, R. K.; Dendooven, J.; Filez, M.; Galvita, V. V.; Poelman, H.; Solano, E.; Minjauw, M. M.; Devloo-Casier, K.; Fonda, E.; Hermida-Merino,D.; Bras, W.; Marin, G. B.; Detavernier, C., *ACS Nano*, 10, 8770-8777 (2016).

at ~300 °C, GaPt at 450 °C, Ga_2Pt (PDF 03-1007) at 600 °C and finally Ga_3Pt_2 (PDF 65-7105) at 670 °C (**Figure S1**c (left)). This evolution is in line with the lower stability of the Ga2Pt and Ga_3Pt_2 phases at low temperature compared to GaPt, as concluded from the Ga-Pt phase diagram.[4] The right graph of **Figure S1**c includes 2θ scans measured after reducing the sample up to 650 (red) and 700 °C (black). *Ex situ* XRF measurements on these reduced samples show lower amounts of Ga compared to the as-deposited sample, with Ga atomic ratios of 29 and 39% for the 650 and 700 °C sample respectively, evidencing the increasing evaporation of Ga that cannot be bound in the alloys. These experiments show that, similar to Pt-In, the ALD of Pt/Ga_2O_3 bilayers followed by thermal reduction in hydrogen enables a high level of Ga_aPt_b phase control.

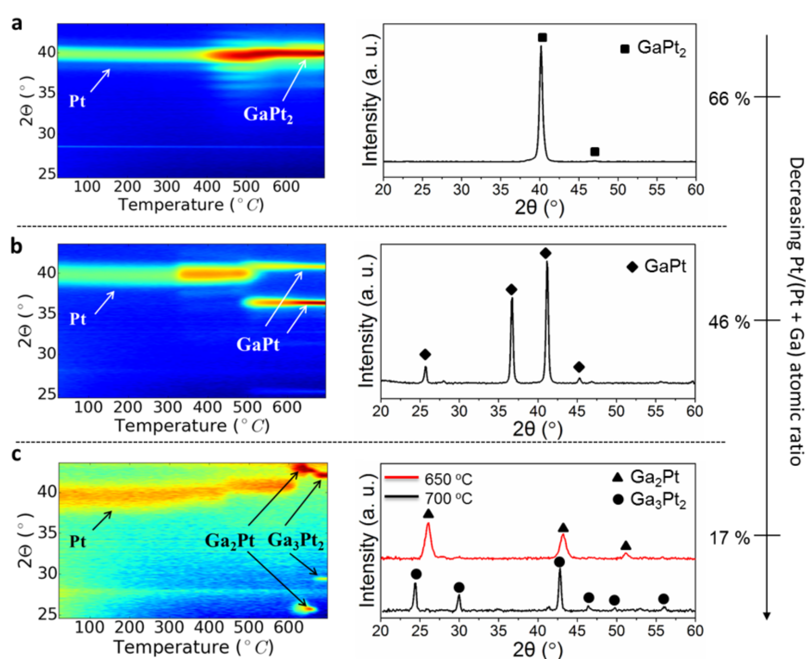

Figure S1. *(Left) In situ XRD patterns measured during TPR in 10% $H_2/N_2$of Pt/Ga_2O_3 stacks with a Pt/Ga atomic ratio of a) 66%, b) 46%, and c) 17%. (Right) 20-60° 2θ scans measured after TPR in 10% H_2/N_2up to 700 °C (and 650 °C).*

2. Composition determination

A series of pure films of Pt and M_2O_3 (M = In, Ga) with different thicknesses were deposited on planar SiO_2 substates and their thickness was determined by X-ray reflectivity (XRR). From the thickness, the specific weight of the Pt and M was calculated by assuming the densities of the films equal to that of bulk Pt and M_2O_3,

respectively. XRF measurements were performed on each film and the respective fluorescence signal (Pt Lα, In Lα and Ga Kα) was integrated over a period of 100 s. The XRF intensity counts and specific weight of materials were plotted against the thickness of the films (**Figure S2**), yielding a relationship that was used for determining the composition of the bilayer materials.

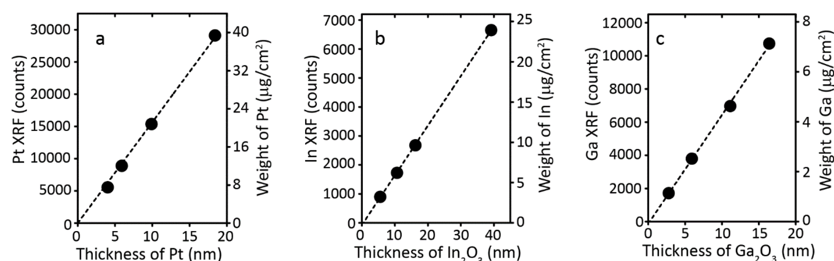

Figure S2. *Variation of Pt (a), In (b) and Ga (c) XRF intensity (left y-axis) and weight (right axis) against the Pt (a), In_2O_3 (b) and Ga_2O_3 (c) film thickness.*

As a consequence of the nucleation-controlled growth mode of Pt ALD on oxide surfaces, a 3D island morphology is observed for low amounts of Pt ($< 5\mu g/cm^2$) (*Figure 2d* (left)). In this case, the Pt thickness obtained from the relation should therefore be considered as an equivalent thickness. The equivalent thickness equals the thickness of a 2D Pt thin film containing the same number of Pt atoms as the real deposited 3D Pt morphology.

3. Pt-In

3.1 Additional *in situ* XRD data

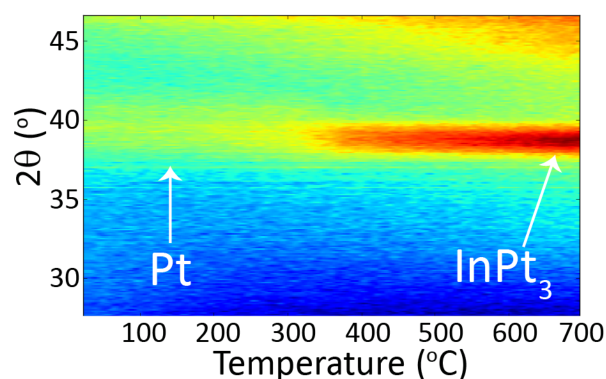

Figure S3. *In situ XRD patterns measured during TPR of a Pt/In_2O_3 bilayer with a Pt/(Pt+In) atomic ratio of 76% in 10% H_2/N_2.*

3.2 GISAXS simulations

Figure S4 and **Table S1** provide the simulation results for the 2D GISAXS patterns presented in *Figure 2.* The simulated patterns were calculated using the software IsGISAXS assuming truncated spheres arranged on a regular 2D lattice.[5] For form factor calculation, the distorted-wave Born approximation (DWBA) was used, including the model of the graded interface used to describe the perturbation caused by densely packed particles on a surface.[6] The interference function was calculated based on the 2D paracrystal model, which is a regular 2D lattice with a loss of long-range order. The distance distribution was described by a Gaussian function, while a log-normal distribution function was assumed for the particle dimensions.

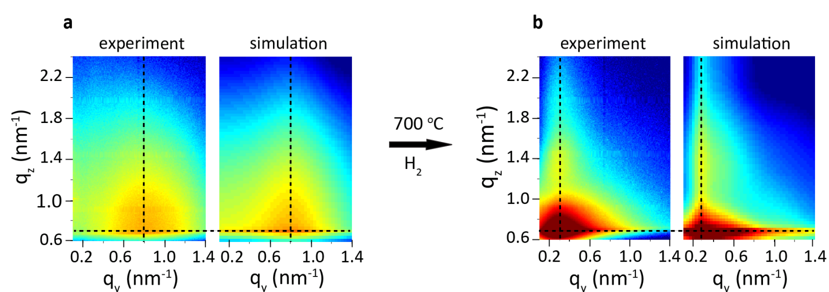

Figure S4. *Experimental and simulated 2D GISAXS pattern of the as-deposited Pt/In_2O_3 bilayer (a) and the BMNPs obtained after TPR in 20% H2/He up to 700 °C (b).*

	W (nm)	σw (nm)	H (nm)	D (nm)	(nm)
As-deposited	4.2	5.5	2.8	5.5	2.6
700 °C	7.0	14.0	7.2	21.0	7.0

Table S1. *Morphological parameters extracted from the 2D GISAXS simulations assuming truncated spheres to describe the cluster shape (W and σw are the particle width and width of the width distribution, H is the particle height, D is the correlation distance and is the disorder parameter for D).*

3.3 SEM and XRD characterization of the "size tuning" samples

Figure S5 shows the 20° - 60° XRD patterns measured for the samples for which the average particle sizes are depicted in *Figure 4.* The patterns confirm the expected alloy phase formation. **Figure S6** displays the SEM images and extracted particle size distributions that yielded the average particle sizes depicted in *Figure 4.*

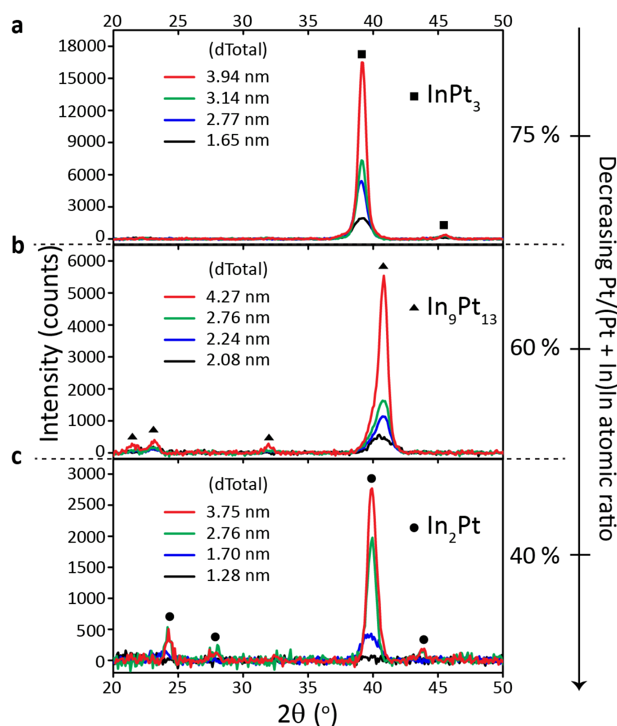

Figure S5. *XRD patterns measured after TPR up to 700 X°C of Pt/In$_2$O$_3$ bilayers with Pt/(Pt+In) atomic ratios of ca. 75 % (a), 60 % (b) and 40 % (c) and different values of dTotal (same samples as in Figure 4 and Figure S6).*

3.4 Catalytic testing

The catalytic activity of the ALD-prepared monometallic Pt and bimetallic Pt-In loaded porous silica with Pt wt% of 0.21 and 0.13 [Pt/(Pt+In) ratio = 0.75] respectively is tested in the dehydrogenation of propane at 600 °C (Eq. 1), an important industrial process which gained tremendous interest during the past decade:[7]

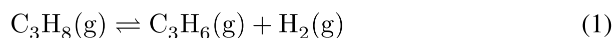

$$C_3H_8(g) \rightleftharpoons C_3H_6(g) + H_2(g) \quad (1)$$

Catalytic activity measurements were performed at atmospheric pressure in a quartz micro reactor with an internal diameter of 10 mm, placed inside an electric furnace. Typically, 120 mg of catalyst was packed between quartz wool plugs. The temperature of the catalyst bed was measured with K-type thermocouples touching the outside and inside of the reactor at the position of the catalyst bed. The inlet gas flow rates were maintained by means of calibrated Brooks mass flow controllers. The feed and product gas streams were monitored online using a calibrated OmniStar Pfeiffer mass spectrometer (MS). MS signals were recorded for all major fragments of C_3H_8, C_3H_6, C_2H_6, C_2H_4 and CH_4 species. A carbon balance with a

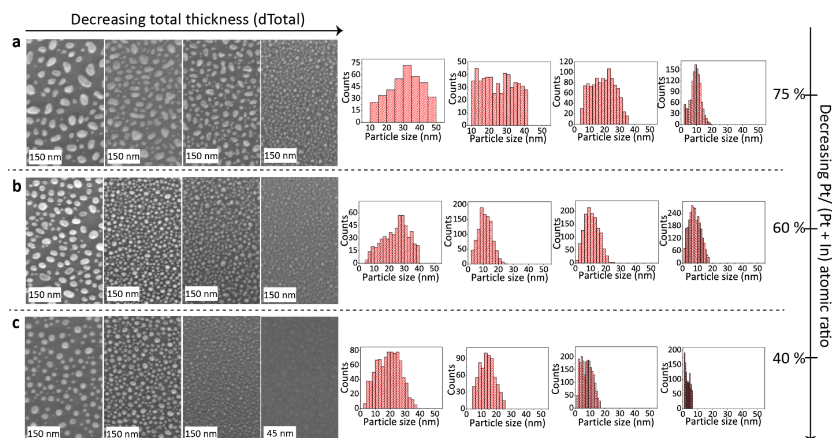

Figure S6. *SEM (left) and particle size distributions (right) measured after TPR up to 700 °C of Pt/In$_2$O$_3$ bilayers with Pt/(Pt+In) atomic ratios of ca. 75 % (a), 60 % (b) and 40 % (c) and different values of dTotal (same samples as in Figure 4 and Figure S5)*

maximum deviation of 15% was obtained.

The as-deposited samples were reduced in 1 ml/s flow of 5 % H_2/Ar at 650 °C for 0.5 h. Then, the temperature was decreased to 600 °C, while purging with He. At 600 °C, an activity measurement was conducted for 10 min at $W_{cat}/F_{C_3H_8,0}$ = 19 $kg_{cat.s.mol^{-1}}$ and $P_{C_3H_8,0}$ = 20 kPa (20 vol% C_3H_8/He mixture at a total pressure of 101.3 kPa).

The turnover frequency (TOF, s^{-1}) was calculated from the difference in the inlet and outlet molar flow rates, as measured relative to an internal standard (Ar) using the online MS, i.e.

TOF (s^{-1}) = $(F_{0,i} - F_i)/N_{Pt,s}$

where $F_{0,i}$ and F_i, in mol.s^{-1}, are the inlet and outlet molar flow rates of component i, and $N_{Pt,s}$, in $mol_{Pt,s}$, is the amount of exposed (surface) Pt atoms in the sample. The latter was determined by H_2 chemisorption using an AutoChem II 2920 (Micromeritics Instrument Corporation). About 100 mg of catalyst was loaded into a quartz reactor and reduced in flowing 10% H_2/Ar (1 ml/s). The temperature of the sample was raised by 10 °C/min to 625 °C and then maintained at this level for 30 min. Hereafter, the sample was flushed with flowing Ar for 30 min, while cooling down to 20 °C. Eventually, the chemisorption of hydrogen was measured by determining the uptake of H_2 from well-defined pulses using a thermal conductivity detector (TCD).

In **Figure S7**, the TOF of propylene production is shown as a function of time-on-stream (TOS) for both samples. Following a decrease in activity of both catalysts during the first 40 min of use, the steady-state TOF over the Pt-In catalyst is more than 2.5 times larger than for the Pt catalyst and reaches a value of $\sim 3s^{-1}$.This result is in line with earlier findings by Sun *et al.*,[8] who reported that the activity of Pt-In catalysts for propane dehydrogenation passes through a maxi-

mum for a bulk In/Pt ratio of 0.48, and then rapidly declines to nearly zero above a bulk In/Pt ratio of 2. An In/Pt ratio of 0.48 corresponds to a Pt/(Pt+In) ratio of 0.67. The above arguments support the higher activity exhibited by the Pt-In catalyst, which possesses a composition close to this optimal value [Pt/(Pt+In) ratio = 0.75]. The selectivity to propylene as gas phase product increases with time of reaction, reaching a value of close to 100% after 40 min for both catalysts. The amount of coke accumulation on both catalysts is calculated from the amount of CO_2 generated after two hours TOS oxidation. It is found to be 6 times larger on the monometallic catalyst (120 mol_C/mol_Pt) than on the bimetallic catalyst (20 mol_C/mol_Pt), suggesting the latter one is far less prone to deactivation through coking.

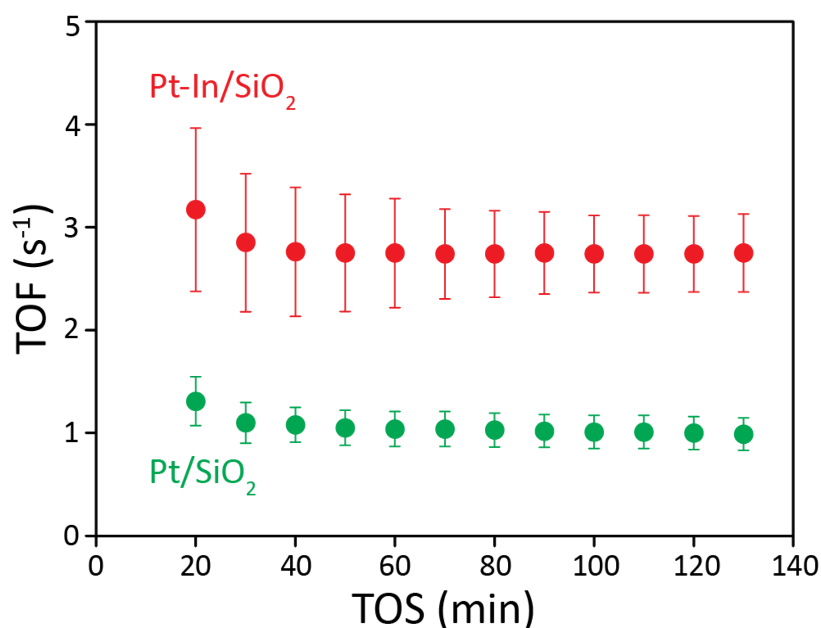

Figure S7. *Catalytic testing in propane dehydrogenation at 60°C. Turnover frequency (TOF) of propylene production as a function of time-on-stream (TOS) for reaction over supported Pt nanoparticles (in green) and Pt-In BMNPs (in red). ($W_{cat}/F_{C_3H_8,0}$ = 20 $kg_{cat.s.mol^{-1}}$ and $P_{C_3H_8,0}$ = 20 kPa at a total pressure of 101.3 kPa). The error bars represent twice the standard deviation.*

3.5 *In situ* XRD and GISAXS during oxidation/reduction cycling of $InPt_3$ BMNPs

A series of *in situ* XRD measurements are performed during isothermal oxidation/reduction cycling of bimetallic particles supported on planar silica substrates

at 700 °C (**Figure S8**). Following the bilayer ALD deposition, initially the temperature is increased from room temperature to 700 °C with a ramp rate of 0.2 °C/s under H_2/N_2atmosphere, which results in the formation of $InPt_3$ particles. Then, the temperature is maintained at 700 °C and the gas environment is periodically changed between H_2/N_2 and O_2. In between each reduction and oxidation cycle the heating chamber is purged with He in order to prevent direct mixing of H_2 and O_2. The XRD pattern clearly shows a periodic switching behavior. When the BMNPs are exposed to O_2, diffraction peaks of Pt (39.8°) and In_2O_3 (30.6° and 35.5°) are observed. During H_2/N_2exposure, the peak corresponding to the bimetallic alloy $InPt_3$ (39°) appears. This type of repetitive segregation of PtIn alloy into Pt and In_2O_3 under oxidative environment, has been observed earlier for $Pt/In_2O_3/Al_2O_3$ catalysts.[9]

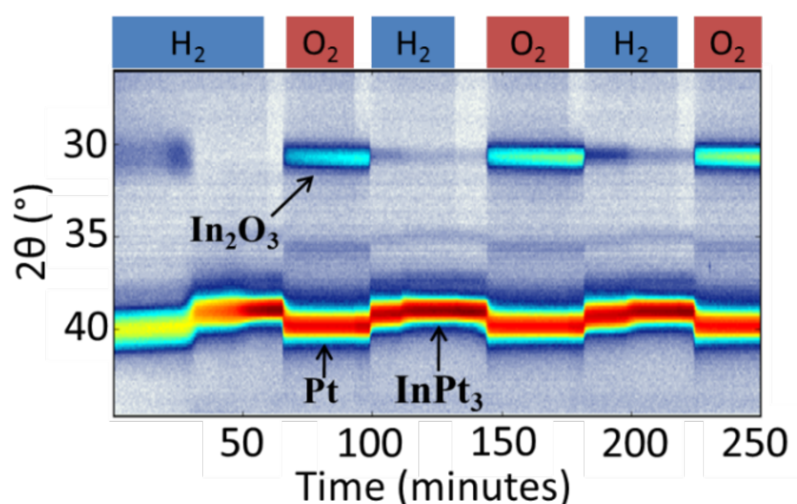

Figure S8. *In situ XRD patterns measured during TPR of a Pt/In_2O_3 bilayer with a Pt/(Pt+In) ratio of 72 % followed by reduction/oxidation cycling at 700 °C (alternating 10% H_2/N_2, He, andO_2). The sequence of gas environments is shown at the top.*

Insights in the morphological evolution of the BMNPs during oxidation/reduction cycling are obtained by an *in situ* GISAXS study. The left 2D color plots in **Figure S9** are identical to those in Figure 2f and show the horizontal and vertical GISAXS line profiles recorded during the initial thermal reduction of the as-deposited Pt/In_2O_3 bilayer in 20% H_2/He, inducing the formation of InPt3 BMNPs. After evacuation of the annealing chamber and cooldown of the sample to room temperature, the chamber is slowly filled with 20% O_2/He and the sample is heated again to 700 °C using the same ramp rate of 0.2 °C/s. The middle 2D color plots in Figure SS9 show the recorded *in situ* GISAXS data. No distinct changes are observed in the scattering pattern, indicating a stable sample morphology during the oxidative treatment. Finally, the sample is exposed again to a reductive

treatment while *in situ* GISAXS data are acquired (right 2D color plots in **Figure S9**). Again a stable scattering is observed. This result proves the stability of the $InPt_3$ BMNP morphology during one oxidation/reduction cycle.

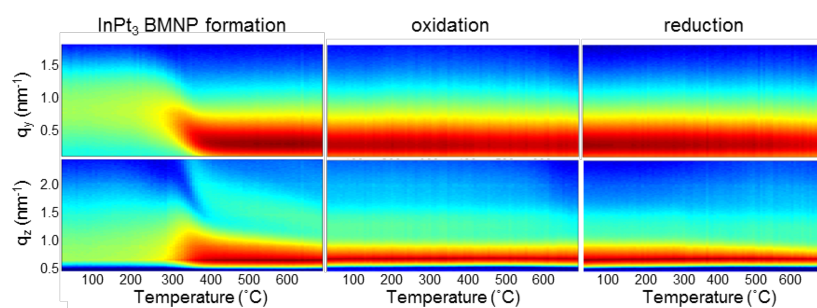

Figure S9. *In situ GISAXS horizontal (top) and vertical (bottom) line profiles measured during TPR in 20% H_2/He of a Pt/In_2O_3 bilayer with a Pt/(Pt+In) atomic ratio of 76% (dPt = 1.0 nm, dIn_2O_3 = 0.7 nm), followed by a temperature programmed oxidation/reduction cycle. The left color plots are identical to those in Figure 2f.*

References

[1] J. Dendooven, R. K. Ramachandran, K. Devloo-Casier, G. Rampelberg, M. Filez, H. Poelman, G. B. Marin, E. Fonda, and C. Detavernier, *Journal of Physical Chemistry C* **117**(40), 20557–20561 (2013).

[2] Y. K. Kim, D. A. Baugh, D. K. Shuh, R. Stanley Williams, L. P. Sadwick, and K. L. Wang, *Journal of Materials Research* **5**(10), 2139–2151 (1990).

[3] E. A. Redekop, V. V. Galvita, H. Poelman, V. Bliznuk, C. Detavernier, and G. B. Marin, *ACS Catalysis* **4**, 1812–1824 (2014).

[4] T. Biggs, S. S. Taylor, and E. Van Der Lingen, *Platinum Metals Review* **49**(1), 2–15 (2005).

[5] R. Lazzari, *Journal of Applied Crystallography* **35**, 406–421 (2002).

[6] R. Lazzari, G. Renaud, J. Jupille, and F. Leroy, *Physical Review B* **76**, 125412 (2007).

[7] J. J. H. B. Sattler, J. Ruiz-Martinez, E. Santillan-Jimenez, and B. M. Weckhuysen, *Chemical Reviews* **114**(20), 10613–10653 (2014).

[8] P. Sun, G. Siddiqi, W. C. Vining, M. Chi, and A. T. Bell, *Journal of Catalysis* **282**(1), 165–174 (2011).

[9] R. L. Barbosa, V. Papaefthimiou, Y. T. Law, D. Teschner, M. Hävecker, A. Knop-Gericke, R. Zapf, G. Kolb, R. Schlögl, and S. Zafeiratos, *The Journal of Physical Chemistry C* **117**(12), 6143–6150 (2013).

Paper VI

Size- and Composition-Controlled Pt - Sn Bimetallic Nanoparticles Prepared by Atomic Layer Deposition *

Abstract

Pt-Sn bimetallic nanoparticles (BMNPs) are used in a variety of catalytic reactions and are widely accepted as model system for Pt-based bimetallics in fundamental catalysis research. Here, Pt-Sn BMNPs were prepared *via* a two-step synthesis procedure combining atomic layer deposition (ALD) and temperature programmed reduction (TPR). In situ X-ray diffraction measurements during TPR and *ex situ* X-ray absorption spectroscopy at the Pt L_{III}-edge revealed the formation of Pt-Sn bimetallic alloys with a phase determined by the Pt/(Pt+Sn) atomic ratio of the as-deposited bilayer. The size of the BMNPs could be tuned by changing the total thickness of the bilayers, while keeping the Pt/(Pt+Sn) atomic ratio constant. Due to the exceptional control over BMNP size and crystalline phase, the proposed method will enable highly systematic studies of the relation between the structure and the performance of Pt-Sn bimetallic catalysts.

*Published as: Ramachandran, R. K.; Filez, M.; Dendooven, J.; Galvita, V. V.; Poelman, H.; Solano, E.; Fonda, E.; Marin, G. B.; Detavernier, C., *RSC Adv.*, 2017, 7, 20201-20205.

Introduction

Pt-Sn bimetallic catalysts are highly performant in a variety of catalytic reactions, including (de)hydrogenation and oxidation of hydrocarbons.[1] In industry, for example, they are used worldwide in the Oleflex (UOP) process for the on-purpose production of propylene.[2] Besides their wide applicability, Pt-Sn catalysts have become quintessential model systems in catalysis science as a result of several decades of intense research. In this research history, academia as well as industry have tried to understand the role of the promoting element (Sn) on the overall performance of Pt-based bimetallic catalysts in particular, and metal catalysts in general.[3;4] Despite their merits, full elucidation of structure-performance relationships has only been obtained in rare cases, due to the non-uniform nature of the alloyed nanoparticle phase.[5;6] More particularly, conventional methods for bimetallic catalyst synthesis - wet impregnation and precipitation - introduce compositional and particle size heterogeneities, hindering unambiguous disentanglement of structure-performance relationships. This missing link between nano-alloy structure, reaction mechanism and the catalyst performance impedes the redesign of current bimetallic catalysts. The fabrication of fundamentally improved bimetallic catalysts therefore relies on the synthesis of bimetallic catalysts which allows for control over the bimetallic nanoparticle (BMNP) composition and particle size. Recently, there have been reports on the controlled synthesis of Pt-Sn nanoparticles employing solution phase methods. While Wang *et al.*[7] reported on controlling the shape of colloidal PtSn nanoparticles, DeSario *et al.*[8] focussed on the low temperature crystallization and ordering in alloys with different compositions.

Here, we demonstrate the simultaneous control on both size and composition of the Pt-Sn nanoparticles *via* a vapor phase method called atomic layer deposition (ALD).[9;10] A crucial advantage of ALD is that the amount of deposited material can be controlled at the monolayer level by changing the number of ALD cycles. This is a consequence of the self-limiting nature of the surface reactions determining the ALD process. Moreover, this unique surface chemistry enables conformal depositions on 3D substrates, including mesoporous supports with large surface areas.[11]

Until recently, the ALD based synthesis of BMNPs was limited to combinations of two noble metals.[12–15] Several groups exploited two characteristics typical of noble metal ALD processes, in casu the island growth mode[16;17] and their selective deposition onto other noble metal over oxide sites,[13;18;19] to grow Pt-Pd, Pt-Ru and Pd-Ru BMNPs. To broaden the range of possible alloying elements for Pt-based BMNPs, we recently reported an ALD based synthesis strategy that allows for the size- and composition-controlled preparation of BMNPs containing a non-noble metal next to a noble metal, namely Pt-In and Pt-Ga systems.[20] In this work, the generality of the method is further demonstrated by providing proof for its applicability to Pt-Sn BMNPs. Future fundamental catalysis studies, generally employing the Pt-Sn model system, will highly benefit from the atomically precise control over composition and size offered by the ALD method.

Figure 1 schematically describes the steps involved in the fabrication process

of the Pt-Sn BMNPs. First, thin films of SnO_2 and Pt are sequentially deposited on a silica substrate by means of ALD, using alternating exposures of tetrakis(dimethylamido)tin and H_2O for SnO_2 ALD[21] and trimethyl(methylcyclopentadienyl)platinum and O_3 for Pt ALD,[16;22] yielding a Pt/SnO_2 bilayer structure. These bilayers are then subjected to a temperature programmed reduction (TPR) to 700 °C in 10% H_2/N_2 at a heating rate of 0.2 °C/s, which results in the formation of alloyed Pt-Sn particles. The composition and size of the BMNPs can be controlled by profiting from the atomic level thickness control of the ALD technique.

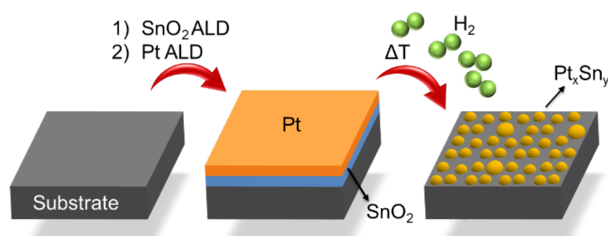

Figure 1. *Schematic representation of the ALD based Pt-Sn BMNPs synthesis.*

1. Experimental methods

Sample preparation. All depositions were performed at 150 °C in a home-built cold-wall ALD chamber[16;23;24] with a base pressure of 10^{-6} mbar. For the planar model systems, Si wafers with a 100 nm thermally grown SiO_2 layer on top were used as substrates. SnO_2 and Pt were deposited using alternating exposures of TDMASn (99%, Strem Chemicals) and H_2O for SnO_2 ALD[21] and (MeCp)$PtMe_3$ (99%, Strem Chemicals) and O_3 for Pt ALD.[16] Ar with 99.999% purity was used as a carrier gas for all precursors. O_3 was produced from a 99% O_2/N_2 mixture with an AC-2025 (USA Inc.) generator, resulting in an O_3 concentration of 200 μg/ml. A typical SnO_2 ALD cycle lasted 20 s with 5 s pulse time for both the precursor and reactant, and 5 s pumping after each pulse. For Pt ALD, a static exposure mode was applied during both ALD half-cycles, resulting in a total cycle time of 50 s.

Composition determination. Pt and SnO_2 film thicknesses were determined by X-ray reflectivity measurements using a Bruker D8 Discover system with Cu Kα radiation. Alternatively, the thickness was extracted from calibrated X-ray fluorescence data obtained with a Bruker Artax system with Mo X-ray source. From the thickness, the specific weight of the Pt and Sn was calculated by assuming the densities of the films equal to that of bulk Pt and SnO_2, respectively. (see ESI for the details)

***In situ* X-ray diffraction.** The TPR treatment of the Pt/SnO_2 bilayers was performed under 10% H_2/N_2 atmosphere in a home-built heating chamber mounted on a Bruker D8 diffractometer[25;26] to enable *in situ* XRD characterization. A linear detector covering 20° in 2θ was used to collect the diffracted X-rays with a 2 s time resolution.

X-ray absorption spectroscopy. XAS measurements were performed at the SAMBA beamline of the SOLEIL synchrotron (Saint-Aubin, France) operating at 450 mA. All experiments were performed in fluorescence mode at the Pt L_{III} edge (E = 11564 eV) using a 35-element Ge detector (Canberra). XAS data reduction and analysis were executed with the Demeter 0.9.13 software package by following the methodology of Koningsberger *et al.*[27]

Electron microscopy. SEM analysis of the planar model systems was performed on a FEI Quanta 200F and a FEI Sirion instrument. The analysis of the SEM images was done using the ImageJ software, providing particle size distributions. The reported average particle sizes and standard deviations were calculated from a Gaussian fit to the particle size distributions (see ESI for the details).

Results and Discussion

A series of bilayer samples with different Pt/(Pt+Sn) atomic ratios was prepared by using the atomic level control of ALD to precisely define the thickness of SnO_2 and Pt layers (**Table 1**, samples a-f). *In situ* XRD patterns collected during H_2 TPR of the as-deposited bilayers a - d show similar phase evolution behaviour (**Figure 2**A). Initially, the patterns show a diffraction peak which corresponds to metallic Pt(111). No diffractions corresponding to SnO_2 are observed, as a consequence of its amorphous structure. As the temperature increases, a gradual shift of the Pt(111) peak towards a lower 2θ angle occurs around 250 °C, resulting from the incorporation of reduced Sn into the Pt fcc lattice.[28] The diffraction peaks at higher temperatures show that the uptake of reduced Sn results in the formation of PtSn intermetallic alloys. For sample e with a Pt/(Pt+Sn) atomic ratio of 47%, the formation of the crystalline alloy phase happens more abrupt at a temperature of 200 °C. In the case of the most Sn rich sample, sample f, there are no diffraction peaks visible initially, as the amount of Pt is under the detection limit of XRD. When the temperature reaches 500 °C, two diffractions corresponding to the $PtSn_4$ phase appear and disappear as this phase is not stable above 522 °C. The absence of diffractions from SnO_2 in the *in situ* XRD patterns indicates that the as-deposited amorphous SnO_2 is reduced to Sn before being crystallized. Sn is also not visible as it is liquid at higher temperatures.[29]

The *ex situ* XRD measurements after TPR and cool down (**Figure 2**B) allow to pinpoint the exact Pt-Sn alloy phases for differently composed bilayers at room temperature (**Table 1**). There is a clear relation between the Pt/(Pt+Sn) atomic ratio of the as-deposited bilayers and their eventual Pt-Sn alloy composition/phase. A

Sample ID	SnO_2 thickness (nm)	Pt thickness (nm)	Pt/(Pt+Sn) atomic ratio(%)	Phase(s) formed after TPR	n_{Pt-Pt}	n_{Pt-Sn}
a	2.1	5.5	87	Pt*, Pt_3Sn	0.81	0.19
b	4.4	5.5	75	Pt_3Sn	0.62	0.38
c	7.9	5.5	63	Pt_3Sn*, PtSn	0.58	0.42
d	7.9	3.8	54	Pt_3Sn, PtSn*	0.45	0.55
e	4.4	1.7	47	PtSn	0.20	0.80
f	7.9	1.0	22	$PtSn_4$, Sn	-	-

Table 1. *Characterization of Pt-Sn samples prepared for demonstrating the composition control. The atomic ratio was determined by XRF (see ESI), the crystalline phase by XRD and the fractional Pt coordination numbers (n_{Pt-Pt} and n_{Pt-Sn}) by EXAFS analysis (the error on the EXAFS coordination numbers is ~ 10%). Dominant phases are marked (*).*

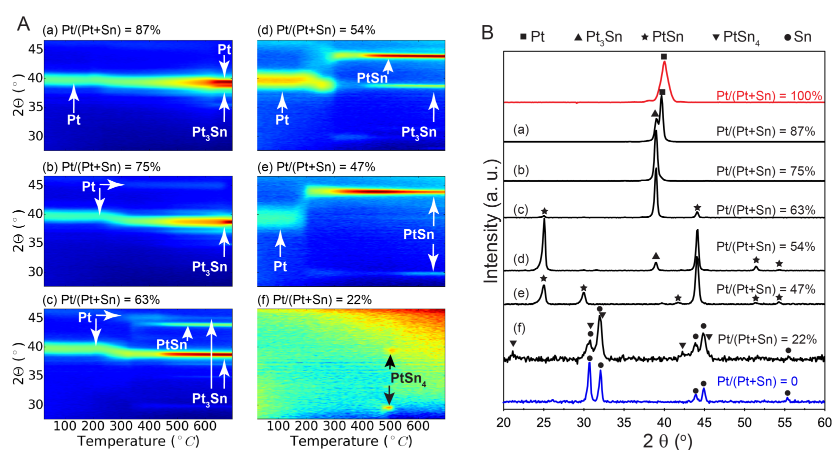

Figure 2. *(A) In situ XRD patterns during TPR in 10% H_2/N_2 of Pt/SnO_2 bilayer samples with Pt/(Pt+Sn) atomic ratios of (a) 87%, (b) 75%, (c) 63%, (d) 54%, (e) 47% and (f) 22%. (B) Ex situ XRD patterns measured after the TPR experiment. The red and blue patterns are measured after TPR of pure Pt and SnO_2 layers, respectively.*

gradual transformation from Pt towards metallic Sn is observed, demonstrating the exceptional ability of ALD to tune the phase of bimetallic Pt-Sn alloys. For sample f, diffractions corresponding to metallic Sn are observed in addition to the $PtSn_4$ peaks.

Ex situ Pt L_{III} edge extended X-ray absorption fine structure (EXAFS) data of the reduced samples (**Figure 3**) furnish a detailed insight into the local atomic structure of the alloys, except for sample f for which the quality of the measured EXAFS data was too low for analysis. Qualitative analysis of the features in the higher R-range (R > 3 Å) reveals an fcc structure for samples a and b which gradually disappears for samples with lower Pt content. Because Pt and Pt_3Sn have fcc lattice stacking, this result is in agreement with the long-range XRD data. Quantitative modeling of the EXAFS data with a Pt-Pt and Pt-Sn shell yields good

agreement with the experimental signal for R in the 2 - 3 Å range. Pt-Sn alloying was assessed by deriving the fractional Pt coordination numbers (n_{Pt-Pt} = N_{Pt-Pt}/(N_{Pt-Sn} + N_{Pt-Pt}) and n_{Pt-Sn} = NPt-Sn/(N_{Pt-Sn} + N_{Pt-Pt}) in **Table 1**). A clear decrease [increase] in the fraction of Pt-Pt [Pt-Sn] bonds is observed with decreasing Pt content. More specifically, quasi phase pure Pt_3Sn (sample b) and PtSn (sample e) display 62 [38] and 20 [80] % Pt [Sn] coordination around the Pt central absorber, respectively. This is in close accord with the theoretical 67 [33] and 25 [75] % Pt-Pt [Pt-Sn] bond abundance for Pt_3Sn and PtSn alloy structures. The short-range information derived from EXAFS therefore fully corroborates with the long-range XRD data, proving the high phase-tuning potential of ALD for Pt-Sn alloys.

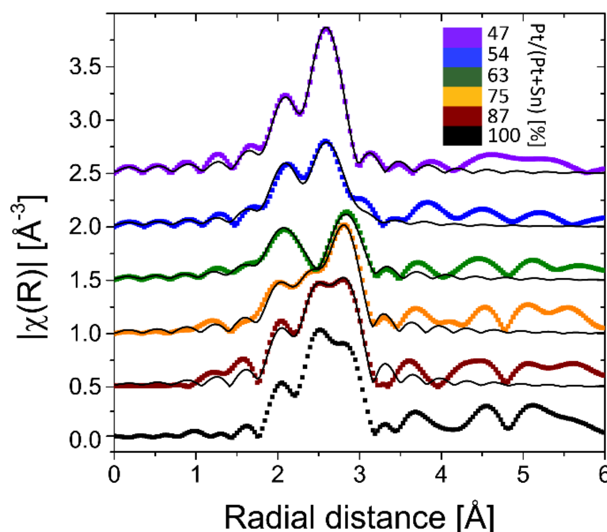

Figure 3. *k^2-weighted Fourier transformed EXAFS magnitudes of the BMNPs obtained after TPR in 10% H_2/N_2 up to 700C. The thin black lines are the EXAFS modeling results (Pt-Pt + Pt-Sn shell).*

In addition to phase control, the presented method enables tuning of the Pt-Sn BMNP size. More particularly, particle size control is achieved by scaling the total bilayer film thickness, while keeping the Pt/(Pt+Sn) atomic ratio constant. This is demonstrated by the preparation of a series of bilayer films with a constant Pt/(Pt+Sn) atomic ratio of *ca.* 75%, but different total thickness, ranging from 1.4 to 5.8 nm (**Table 2**). The films were subjected to a TPR up to 700 °C in 10% H_2/N_2 and the formation of Pt_3Sn was confirmed by XRD measurements (see ESI). The morphology of the films was studied by scanning electron microscopy (SEM). The SEM images are shown in **Figure 4** together with a plot of the average particle size against the total deposited thickness. A linear relation is observed, proving that the average BMNP size can indeed be tuned *via* the total thickness of the

bilayer ALD-film. While a wide distribution of nanoparticle sizes is observed for the largest nanoparticles in the SEM image of sample V, a narrow particle size distribution is obtained for the smallest nanoparticles that are of highest interest in the field of catalysis (see ESI).

Sample ID	**SnO_2 thickness (nm)**	**Pt thickness (nm)**	**Total thickness (nm)**	**Average particle size (nm)**
I	0.7	0.7	1.4	5
II	0.9	1.1	2	10
III	1.3	1.4	2.7	17
IV	1.5	1.7	3.2	25
V	2.8	3	5.8	58

Table 2. *Characterization of Pt-Sn samples with Pt/(Pt+Sn) atomic ratio of* ca. *75% prepared for demonstrating the size control. The standard deviation obtained from the particle size distribution is about 25% of the average particle size.*

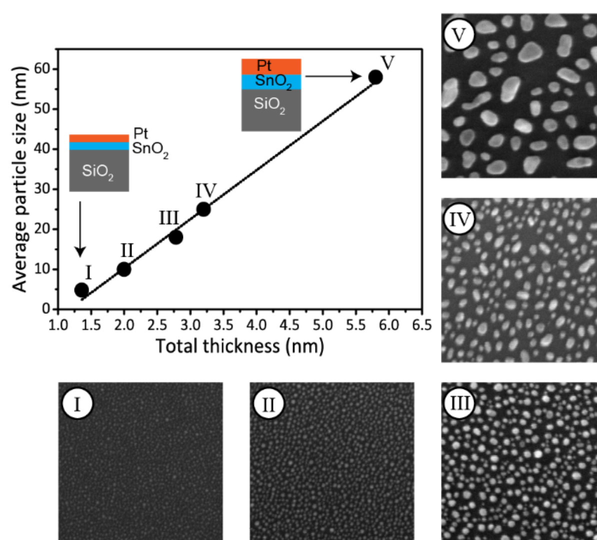

Figure 4. *SEM images (full width of 500 nm) measured after TPR in 10% H_2/N_2 up to 700 °C of Pt/SnO_2 bilayers with Pt/(Pt+Sn) atomic ratio of* ca. *75%. The graph shows the average BMNP size formed after TPR as determined from SEM analysis versus the total deposited thickness. The line is a linear fit to the data points. The schematics show how the thickness of the Pt and SnO_2 layers is scaled to tune the particle size.*

Conclusion

In summary, this work demonstrates that a reductive treatment of Pt/SnO_2 bilayers deposited with ALD results in the formation of alloyed Pt-Sn particles for which

the crystalline phase and average particle size can be controlled *via* the ALD process. The crystalline phase is determined by the as-deposited Pt/(Pt+Sn) atomic ratio, while the average particle size is defined by the total (SnO_2 + Pt) thickness. Therefore, this approach highly takes advantage of the unique monolayer-level thickness control of ALD. Since the phase and size of the Pt-Sn bimetallic nanoparticles can be rationally tuned, we believe that the synthesis method we present here will open up a new way for constructing model systems that enable in-depth investigations of the relation between the Pt-Sn bimetallic particle structure and the catalytic efficiency and selectivity. In a first effort to validate the catalytic applicability of the presented Pt-Sn BMNP synthesis approach during propane dehydrogenation, activities comparable to conventionally synthesized Pt-Sn catalysts were observed. Detailed investigation towards optimization is ongoing.

Acknowledgments

This research was supported by the European Research Council (Starting Grant no. 239865), by the Flemish Research Foundation (FWO-Vlaanderen) (Project G.0209.11, postdoctoral fellowship of J.D.), the Flemish Government (Long-term structural fundingMethusalem funding and Medium-scale research infrastructure funding-Hercules funding), the Special Research Fund BOF of Ghent University (GOA 01G01513), and the IAP7/05 Interuniversity Attraction Poles Programme, Belgian State, Belgian Science Policy. We are also grateful to the SAMBA-SOLEIL staff for smoothly running the facilities.

References

[1] W. Yu, M. D. Porosoff, and J. G. Chen, *Chemical Reviews* **112**(11), 5780–5817 (2012).

[2] J. J. H. B. Sattler, J. Ruiz-Martinez, E. Santillan-Jimenez, and B. M. Weckhuysen, *Chemical Reviews* **114**(20), 10613–10653 (2014).

[3] J. Wu, Z. Peng, and A. T. Bell, *Journal of Catalysis* **311**, 161–168 (2014).

[4] M. Filez, E. A. Redekop, H. Poelman, V. V. Galvita, M. Meledina, S. Turner, G. Van Tendeloo, C. Detavernier, and G. B. Marin, *Catal. Sci. Technol.* **6**(6), 1863–1869 (2016).

[5] A. Sapi, F. Liu, X. Cai, C. M. Thompson, H. Wang, K. An, J. M. Krier, and G. A. Somorjai, *Nano Letters* **14**(11), 6727–6730 nov (2014).

[6] C. Cui, M. Ahmadi, F. Behafarid, L. Gan, M. Neumann, M. Heggen, B. R. Cuenya, and P. Strasser, *Faraday Discussions* **162**, 91–112 (2013).

[7] X. Wang, L. Altmann, J. Stöver, V. Zielasek, M. Bäumer, K. Al-Shamery, H. Borchert, J. Parisi, and J. Kolny-Olesiak, *Chemistry of Materials* **25**, 1400–1407 (2013).

[8] D. Y. Desario and F. J. Disalvo, *Chemistry of Materials* **26**(8), 2750–2757 (2014).

[9] S. M. George, *Chem. Rev* **110**, 111–131 (2010).

[10] V. Miikkulainen, M. Leskelä, M. Ritala, and R. L. Puurunen, *Journal of Applied Physics* **113**(2), 021301 jan (2013).

[11] C. Detavernier, J. Dendooven, S. Pulinthanathu Sree, K. F. Ludwig, and J. A. Martens, *Chemical Society Reviews* **40**(11), 5242 (2011).

[12] S. T. Christensen, H. Feng, J. L. Libera, N. Guo, J. T. Miller, P. C. Stair, and J. W. Elam, *Nano Letters* **10**(8), 3047–3051 (2010).

[13] J. Lu, K.-B. Low, Y. Lei, J. A. Libera, A. Nicholls, P. C. Stair, and J. W. Elam, *Nature Communications* **5**, 3264 (2014).

[14] K. Cao, Q. Zhu, B. Shan, and R. Chen, *Scientific Reports* **5**, 8470 (2015).

[15] B. J. O'Neill, D. H. K. Jackson, J. Lee, C. Canlas, P. C. Stair, C. L. Marshall, J. W. Elam, T. F. Kuech, J. A. Dumesic, and G. W. Huber, *ACS Catalysis* **5**(3), 1804–1825 (2015).

[16] J. Dendooven, R. K. Ramachandran, K. Devloo-Casier, G. Rampelberg, M. Filez, H. Poelman, G. B. Marin, E. Fonda, and C. Detavernier, *Journal of Physical Chemistry C* **117**(40), 20557–20561 (2013).

[17] J. Lu, J. W. Elam, and P. C. Stair, *Surface Science Reports* **71**(2), 410–472 (2016).

[18] M. J. Weber, M. A. Verheijen, A. A. Bol, and W. M. M. Kessels, *Nanotechnology* **26**(9), 094002 (2015).

[19] M. J. Weber, A. J. M. MacKus, M. a. Verheijen, C. Van Der Marel, and W. M. M. Kessels, *Chemistry of Materials* **24**(15), 2973–2977 (2012).

[20] R. K. Ramachandran, J. Dendooven, M. Filez, V. V. Galvita, H. Poelman, E. Solano, M. M. Minjauw, K. Devloo-Casier, E. Fonda, D. Hermida-Merino, W. Bras, G. B. Marin, and C. Detavernier, *ACS Nano* **10**, 8770–8777 (2016).

[21] M. N. Mullings, C. Hagglund, and S. F. Bent, *Journal of Vacuum Science &*

Technology A: Vacuum, Surfaces, and Films **31**(6), 061503 (2013).
[22] M. Filez, H. Poelman, R. K. Ramachandran, J. Dendooven, K. Devloo-Casier, E. Fonda, C. Detavernier, and G. B. Marin, *Catalysis Today* **229**, 2–13 (2014).
[23] Q. Xie, Y.-L. Jiang, C. Detavernier, D. Deduytsche, R. L. Van Meirhaeghe, G.-P. Ru, B.-Z. Li, and X.-P. Qu, *Journal of Applied Physics* **102**(8), 083521 (2007).
[24] J. Musschoot, Q. Xie, D. Deduytsche, S. Van den Berghe, R. Van Meirhaeghe, and C. Detavernier, *Microelectronic Engineering* **86**(1), 72–77 (2009).
[25] W. Knaepen, C. Detavernier, R. Van Meirhaeghe, J. Jordan Sweet, and C. Lavoie, *Thin Solid Films* **516**(15), 4946–4952 (2008).
[26] W. Knaepen, S. Gaudet, C. Detavernier, R. L. Van Meirhaeghe, J. J. Sweet, and C. Lavoie, *Journal of Applied Physics* **105**(8), 083532 (2009).
[27] D. Koningsberger, B. Mojet, G. van Dorssen, and D. Ramaker, *Topics in Catalysis* **10**(3), 143–155 (2000).
[28] M. Filez, E. A. Redekop, V. V. Galvita, H. Poelman, M. Meledina, S. Turner, G. Van Tendeloo, A. T. Bell, and G. B. Marin, *Phys. Chem. Chem. Phys.* **18**(4), 3234–3243 (2016).
[29] T. Biggs, S. S. Taylor, and E. Van Der Lingen, *Platinum Metals Review* **49**(1), 2–15 (2005).

Paper VI - supplementary information

Size- and Composition-Controlled Pt - Sn Bimetallic Nanoparticles Prepared by Atomic Layer Deposition *

Composition determination

The thickness of the bilayer sample was determined by X-ray reflectivity measurements, as shown in **Figure S1** for a bilayer consisting of 7.9 nm SnO_2 and 5.5 nm Pt. From the thickness, the specific weight of Pt and Sn was calculated by assuming the densities of the films equal to those of bulk Pt and SnO_2, respectively. Alternatively, and especially for thinner samples for which XRR analysis becomes difficult, the thickness was extracted from calibrated X-ray fluorescence data. For this, a series of pure films of Pt and SnO_2 with different thicknesses were deposited on planar SiO_2 substrates and their thickness was determined by XRR. XRF measurements were performed on each film and the respective fluorescence signal (Pt Lα and Sn Lα) was integrated over a period of 100 s. The XRF intensity counts and specific weight of Pt and Sn were plotted against the thickness of the films (**Figure S2**), yielding calibration curves that could be used for determining the composition of the bilayer materials.

As a consequence of the nucleation-controlled growth mode of Pt ALD on oxide surfaces, a 3D island morphology is observed for low amounts of Pt ($< 5\mu g/cm^2$). In this case, the Pt thickness obtained from the relation should therefore be considered as an equivalent thickness. The equivalent thickness equals the thickness of a 2D Pt thin film containing the same number of Pt atoms as the real deposited 3D Pt morphology.

*Published as: Ramachandran, R. K.; Filez, M.; Dendooven, J.; Galvita, V. V.; Poelman, H.; Solano, E.; Fonda, E.; Marin, G. B.; Detavernier, C., *RSC Adv.*, 2017, 7, 20201-20205.

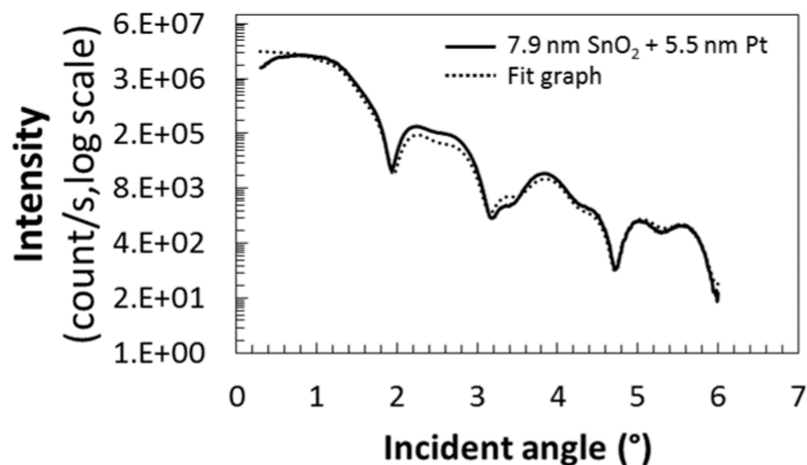

Figure S1. *X-ray reflectivity measurement for a bilayer sample with 7.9 nm SnO_2 and 5.5 nm Pt.*

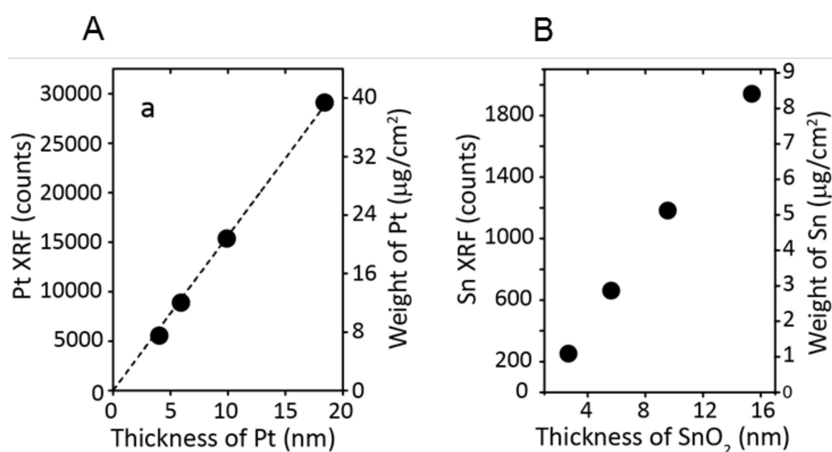

Figure S2. *Variation of Pt (A) and Sn (B) Lα XRF intensity (left y-axis) and weight (right axis) against the Pt and SnO_2 film thickness.*

Pt_xSn_y size tuning experiment

A series of bilayer films with a constant Pt/(Pt+Sn) atomic ratio of *ca.* 75%, but different total thickness, ranging from 1.4 to 5.8 nm, was subjected to a TPR up to 700 °C in 10% H_2/N_2 and the formation of Pt_3Sn was confirmed by XRD measurements (**Figure S3** (A)). The morphology of the films was studied by scanning electron microscopy (SEM), where the particle size distribution was obtained us-

ing the ImageJ software. A Gaussian fit to the particle size distribution was made for determining the average particle size and half of the full width at half maximum (FWHM) was taken as the standard deviation of the particle size. **Figure S3** (B) shows the particle size distributions and the corresponding Gaussian fits.

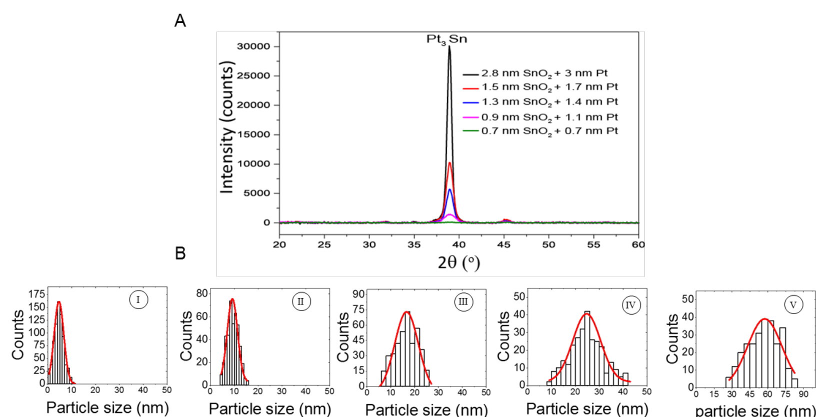

Figure S3. *(A) XRD patterns and (B) particle size distribution calculated from the SEM images, measured after TPR in 10% H_2/N_2 up to 700 °C, of Pt/SnO_2 bilayers with Pt/(Pt+Sn) atomic ratios of* ca*. 75% and total thickness of 1.4, 2, 2.7, 3.2 and 5.8 nm.*

5

Conclusions and suggestions for future work

5.1 Summary and general conclusions

The goal of this work was to develop new ALD processes for the deposition of metals and metal oxides, which are relevant for catalysis, and finally, establish a synthesis strategy for the fabrication of bimetallic materials containing both noble and non-noble metals. Initially different ALD processes were developed for the deposition of metallic platinum and oxides of Ga, In and Fe. Since different ALD processes have to be eventually combined for the deposition of bimetallic materials, processes with wide temperature windows were targeted and developed.

For Pt ALD, the well-known $MeCpPtMe_3$ precursor was used together with ozone as reactant, resulting in an ALD process for Pt with a constant growth rate of 0.45 Å/cycle in a broad temperature range of 100 - 300 °C. Normally, a high temperature (>300 °C) is required for the thermal ALD of Pt and even with O_2 plasma, obtaining a metallic Pt film was found to be difficult at low temperatures. Interestingly, the newly developed ALD process yielded high purity metallic Pt films at a temperature as low as 100 °C. This is highly attractive for the deposition of Pt on heat-sensitive materials.

Iron oxide ALD was accomplished by using a cyclopentadienyl based precursor, named tir-butylferrocene (TBF) with O_2 plasma as reactant. Generally, Fe_2O_3 ALD is performed at very high temperatures (>350 °C) and uses ferrocene as precursor. In our experience, we often encountered problems related to condensation of the precursor when using solid metallocene precursors (Cobaltocene and Nicke-

locene). The newly introduced TBF based process enables the deposition of Fe_2O_3 at low and broad temperature range (150 - 350 °C) using a liquid precursor.

Gallium and indium oxides were deposited by using β-diketonate based precursors, $Ga(TMHD)_3$ and $In(TMHD)_3$ respectively, with O_2 plasma reactant. Even though these processes show low growth rates, the very broad temperature window ranging from 100 to 400 °C could be of interest for doping applications, where the deposition temperatures for different ALD processes have to be compatible.

Bimetallic nanoparticle (BMNP) synthesis using ALD is an emerging method for the fabrication of bimetallic catalyst with controlled size and composition. A key advantage of ALD is that size and composition control can be obtained by simply playing with the number of ALD cycles. However, so far this method has been limited to the synthesis of bimetals with noble metals only, which is a very limited subset in the class of bimetallic materials. During this thesis work, a successful extension of the ALD based approach towards the synthesis of bimetallic nanoparticles containing both noble and non-noble metals has been accomplished. In this method, a bilayer consisting of the desired materials is deposited by ALD, which is then subjected to temperature programmed reduction (TPR) under hydrogen atmosphere to form the BMNPs. The size and composition of the obtained BMNPs can be precisely controlled by tuning the number of ALD cycles in a proper way.

Finally, some preliminary experiments were conducted to demonstrate the catalytic applications of the developed methods. Individual ALD processes were exploited for the introduction of catalytically active metal and metal oxide species into zeolite supports for the application in decane hydroconversion reactions. On the other hand, the newly developed BMNPs synthesis method was employed for the synthesis of Pt-In bimetallic catalyst in a mesoporous silica materials and was tested for catalytic activity towards the propane dehydrogenation reaction. These initial catalytic tests revealed some encouraging results and a detailed investigation in exploring the ALD based methods in different aspects of catalysis is ongoing.

To conclude, atomic layer deposition has emerged as a powerful method for the tailored synthesis of catalyst materials. The self-limiting surface chemistry of ALD provides sub-nanometer control over the amount of material deposited and allows nanoporous, high surface area materials to be coated uniformly. These unique features of ALD render it a potential tool for fine tuning various determining factors of heterogeneous catalysts, including the particle size, density, stability and activity. Highly dispersed catalytically active acid sites can be introduced on porous supports by applying very few (or even only one) metal oxide ALD cycles, while a conformal coating of metal oxides can be applied for precisely tuning the pore size of different porous supports. Metal oxide ALD can also provide a protective overcoating, which can effectively reduce the deactivation of the supported metal nanoparticle catalysts by preventing sintering and coke formation. The invention of ALD processes for noble metals has revolutionized the applicability of ALD in the supported metal catalyst synthesis. Noble metal ALD can be used for preparing highly dispersed nanoparticles, with the size controlled easily at the nanometer scale by adjusting growth parameters such as the number of ALD cycles. By combining the ALD processes for two different materials, bimetallic

nanoparticles can be synthesized where the size and composition is tuned by the total and relative number of ALD cycles used for the two components. In summary, ALD has proven to be an ideal tool for producing model catalysts materials, which could make a huge impact in catalysis related research. The development of dedicated reactor concepts for ALD coating of powders [1–3] can be expected to lead to a growing interest in atomic level tailoring of catalyst powders through ALD over the next decade.

5.2 Suggestions for future work

Synthesis of other Pt containing BMNPs: Based on the new ALD based methodology for the synthesis of BMNPs, there are plenty of opportunities for fabricating different bimetallic materials for catalysis and several other applications. For example Pt-Ni, Pt-Co and Pt-Fe bimetallic systems are interesting candidates in many catalytic reactions such as (de)hydrogenation and reforming reactions. Apart from their catalytic activity, Pt-Co and Pt-Fe are interesting candidates in the field of magnetism. Magnetic BMNPs with high areal density, which is of great importance for magnetic recording devices, can be synthesized using this novel approach.

Replacement of Pt with other noble metals: Apart from the Pt based BMNPs synthesis, this method can be extended towards the synthesis of other noble metal based BMNPs such as Pd-X, Ru-X *etc.* (X = non-noble metal).

Synthesis of noble metal free BMNPs: Another interesting area to be explored is the deposition of noble metal free BMNPS such as Fe-Co, Ni-Co and Fe-Ni, which can be promising substitutes for noble metal catalysts.

Synthesis of Trimetallic catalysts: Recently, there has been some studies which show that trimetallic catalysts such as Pt-Ir-Sn, Pt-Fe-Au and Au-Pd-Pt exhibit better catalytic performance than both their monometallic and bimetallic counterparts. Several groups have already investigated the mechanism of the promoted reactivity in trimetallic catalysts and found an influence of size and shape of the nanostructures in the increased activity. An extension of the ALD based approach towards the synthesis of trimetallic alloys can trigger new opportunities in the respective field.

Extension of the catalysis related work: In chapters 3 and 4 some preliminary catalytic experiments have been demonstrated. An extension of this work for a detailed investigation for different catalytic systems is ongoing. In the propane dehydrogenation experiments only a single Pt-In composition was tested. A detailed investigation will be conducted by preparing different compositions and sizes for

the Pt-In system, and will be extended to Pt-Ga and Pt-Sn systems. For the bifunctional catalysis discussed in chapter 3, a detailed investigation will be carried out to understand the catalytic chemistry involved. In the synthesis of bifunctional catalysts, so far only one functionality at a time (Pt metal or acidic M^{3+} ion) has been introduced by ALD. The synthesis of a fully bifunctional catalyst using the combination of metal and metal oxide ALD is under consideration.

References

[1] D. Longrie, D. Deduytsche, and C. Detavernier, *Journal of Vacuum Science & Technology A: Vacuum, Surfaces, and Films* **32**(1), 010802 (2014).

[2] D. Longrie, D. Deduytsche, J. Haemers, P. F. Smet, K. Driesen, and C. Detavernier, *ACS Applied Materials and Interfaces* **6**(10), 7316–7324 (2014).

[3] A. Goulas and J. Ruud van Ommen, *Journal of Materials Chemistry A* **1**(15), 4647 (2013).

List of abbreviations

acac	Acetyl Acetonate
AFM	Atomic Force Microscopy
ALD	Atomic Layer Deposition
ALE	Atomic Layer Epitaxy
BMNP	BiMetallic NanoParticle
CVD	Chemical Vapor Deposition
EDX	Energy-Dispersive X-ray Spectroscopy
EXAFS	Extended X-ray Absorption Fine Structure
GISAXS	Gracing-Incidence Small-Angle X-ray Spectroscopy
MBE	Molecular Beam Epitaxy
ML	Molecular Layering
PLD	Pulsed Laser Deposition
PVD	Physical Vapor Deposition
sccm	Standard cubic centimeter per minute
SE	Spectroscopic Ellipsometry
SEM	Scanning Electron Microscopy
SMT	Semiconductor-Metal Transition
slm	Standard liter per minute
TBF	TertiaryButylFerrocene
TDMASn	Tetrakis(DiMethylAmino)Tin
TEM	Transmission Electron Microscopy
TMA	TriMethylAluminum
TMHD	TetraMethylHeptanedionate
TPR	Temperature Programmed Reduction
UHV	Ultra-High Vacuum
XANES	X-ray Absorption Near-Edge Spectrum
XAS	X-ray Absorption Spectroscopy
XPS	X-Ray Photoelectron Spectroscopy
XRD	X-Ray Diffraction
XRF	X-Ray Fluorescence
XRR	X-Ray Reflectivity

List of Figures

Chapter 1: Introduction **1**

1.1 Schematic illustration of ALD reaction cycle. 2
1.2 Saturation and Linearity. 3
1.3 Real ALD growth. 4
1.4 Temperature window. 5
1.5 Conformality. 6
1.6 Shematics for ALD in supported catalyst design. 9
1.7 Frame work of -COK-14. 10
1.8 Photocatalysis - SEM and TEM images. 11
1.9 Photocatalysis. 12
1.10 Tuning substrate morphology - TEM image of HfO_2 coated mesoporous titania film 13
1.11 Tuning substrate morphology - XRF. 14
1.12 SEM image of Pt islands. 15
1.13 Pt ALD in MIL-101. 17
1.14 Pd/Pt core/shell nanoparticles 19
1.15 Possibilities of ALD in supported catalyst design - one step forward 20

Chapter 2: Experimental **29**

2.1 Shematic drawing of the ALD reactor 31
2.2 Schematic representation of a basic ellipsometer system 31
2.3 Mass spectrum of methane 32
2.4 Schematic representation of a SEM 33
2.5 Schematic illustration of the operation principle of AFM 34
2.6 Schematic illustration of the operation principle of AFM 35
2.7 Shematic illustration of X-ray absorption spectrum 36
2.8 Shematic illustration of XRF 36
2.9 Shematic representation of *in situ* XRD chamber 37
2.10 XRR pattern and its interpretation 38
2.11 GISAXS geometry 39
2.12 Schematic outline of the arrangement of the various STEM detectors 40

Chapter 3: Process development for the ALD of Pt and MO_x (M = Ga, In and Fe) 43

3.1 Overview of the newly developed Pt ALD process 45
3.2 Overview of the newly developed gallium oxide ALD process . . 49
3.3 Overview of the newly developed indium oxide ALD process . . . 49
3.4 Overview of the newly developed iron oxide ALD process 50
3.5 HR SEM images of ZSM-5 catalysts 52
3.6 TEM images of ZSM-5 catalysts 52
3.7 Hydroconversion using Pt loaded parent ZSM5 53
3.8 Hydroconversion using Pt loaded desilicated ZSM5 53
3.9 HR SEM images of -COK-14/Al catalysts 55
3.10 HR SEM images of -COK-14/Al catalysts 56
3.11 Hydroconversion using ALD modified -COK-14 56

Paper I: Low Temperature Atomic Layer Deposition of Platinum using (methylcyclopentadienyl)Trimethylplatinum and Ozone 63
1 Temperature window 66
2 ALD characteristics on sputtered Pt substrates 67
3 ALD characteristics on native SiO_2/Si substrates 68
4 XRD spectra of Pt ALD films 69
5 Conformality 70
6 XRF growth curve 70

Paper II: Plasma enhanced atomic layer deposition of Ga_2O_3 thin films 75
1 Temperature window 78
2 Saturation 79
3 *In situ* mass spectrometry results 80
4 Linearity 81
5 XRD spectra of Ga_2O_3 films 82
6 XPS spectra of Ga_2O_3 film 82
7 Transmittance spectrum 83
8 Ellipsometric measurements 84
9 Atomic force micrographs of 30 nm thick Ga_2O_3 films 84
10 XRF growth curves 85

Paper III: Low temperature atomic layer deposition of crystalline In_2O_3 films 91
1 Temperature window 94
2 Saturation 95
3 Linearity 96
4 XRF growth curves 96
5 XPS spectrum of In_2O_3 films 97
6 XRD spectra of In_2O_3 films 98
7 Transmittance spectrum 99

Paper III - supplementary information: Low temperature atomic layer deposition of crystalline In_2O_3 films **103**
S1 *In-situ* mass spectrometry results . . . 104
S2 Atomic force micrographs of *ca.* 15 nm thick In_2O_3 films . . . 105

Paper IV: Plasma enhanced atomic layer deposition of Fe_2O_3 thin films **107**
1 Temperature window . . . 110
2 Saturation . . . 111
3 Linearity . . . 112
4 XRD patterns of the Fe_2O_3 films . . . 113
5 XPS spectra of the Fe_2O_3 films . . . 113
6 *In-situ* XRD during annealing in He . . . 114
7 *In-situ* XRD during annealing in H_2 . . . 115
8 Atomic force micrographs of 13 nm thick Fe_2O_3 films . . . 115

Paper IV - supplementary information: Plasma enhanced atomic layer deposition of Fe_2O_3 thin films **121**
S1 XRR and XRF signals of Fe_2O_3 thin films with different thicknesses 122

Paper V: Atomic Layer Deposition Route to Tailor Nanoalloys of Noble and Non-Noble Metals **129**
1 ALD based synthesis of BMNPs on planar and porous silica supports 131
2 Bimetallic nanoparticle formation on planar silica substrates . . . 133
3 Phase tuning by ALD on planar silica substrates . . . 135
4 Size tuning by ALD on planar silica substrates . . . 137
5 Bimetallic nanoparticle formation on porous silica support . . . 137

Paper V - supplementary information: Atomic Layer Deposition Route to Tailor Nanoalloys of Noble and Non-Noble Metals **145**
S1 Pt-Ga phase tuning . . . 146
S2 Composition determination . . . 147
S3 *In situ* XRD during TPR of a Pt/In_2O_3 bilayer . . . 147
S4 GISAXS pattern . . . 148
S5 XRD characterization of the Pt-In “size tuning” samples . . . 149
S6 SEM characterization of the Pt-In “size tuning” samples . . . 150
S7 Propane dehydrogenation . . . 151
S8 *In situ* XRD during oxidation/reduction cycling of $InPt_3$ BMNPs . 152
S9 *In situ* GISAXS during oxidation/reduction cycling of $InPt_3$ BMNPs 153

Paper VI: Size- and Composition-Controlled Pt-Sn Bimetallic Nanoparticles Prepared by Atomic Layer Deposition **155**
1 Schematic representation of the ALD based Pt-Sn BMNPs synthesis 157
2 Pt-Sn phase tuning . . . 159
3 EXAFS spectra . . . 160
4 Pt-Sn size tuning . . . 161

Paper VI - supplementary information: Size- and Composition-Controlled Pt-Sn Bimetallic Nanoparticles Prepared by Atomic Layer Deposition **165**

S1 XRR measurement for a Pt/SnO_2 bilayer sample 166

S2 Pt-Sn composition determination 166

S3 XRD patterns and particle size distribution of Pt-Sn size tuning samples 167

List of Tables

Chapter 1: Introduction **1**

1.1 Feasiblitiy of ALD. 6
1.2 Supported monometallic nanoparticles by ALD. 16
1.3 Supported bimetallic nanoparticles by ALD. 18

Chapter 3: Process development for the ALD of Pt and MO_x (M = Ga, In and Fe) **43**

3.1 Pt ALD processes 44
3.2 Gallium oxide ALD processes 47
3.3 Indium oxide ALD processes 47
3.4 Properties of GZO and IZO prepared by ALD 48
3.5 Iron oxide ALD processes 50

Paper I: Low Temperature Atomic Layer Deposition of Platinum using (methylcyclopentadienyl)Trimethylplatinum and Ozone **63**
1 Thickness, RMS roughness and resistivity of Pt ALD films 68

Paper III: Low temperature atomic layer deposition of crystalline In_2O_3 films **91**
1 Thickness, RMS Roughness, and Resistivity of In_2O_3 ALD films . 99

Paper V - supplementary information: Atomic Layer Deposition Route to Tailor Nanoalloys of Noble and Non-Noble Metals **145**
S1 Morphological parameters extracted from the 2D GISAXS simulations 148

Paper VI: Size- and Composition-Controlled Pt-Sn Bimetallic Nanoparticles Prepared by Atomic Layer Deposition **155**
1 Characterization of Pt-Sn samples prepared for demonstrating the composition control 159

2 Characterization of Pt-Sn samples prepared for demonstrating the size control 161

List of publications

- **Size- and Composition-Controlled Pt-Sn Bimetallic Nanoparticles Prepared by Atomic Layer Deposition**
  R. K. Ramachandran, M. Filez, J. Dendooven, V. V. Galvita, H. Poelman, E. Solano, E. Fonda, G. B. Marin and C. Detavernier
  RSC Adv. 7, 20201-20205 (**2017**)
  (Contribution of RKR: Designed experiments, prepared materials and samples, analyzed the XRD results, helped in XAS measurements and prepared manuscript)

- **Atomic Layer Deposition Route To Tailor Nanoalloys of Noble and Non-noble Metals**
  R. K. Ramachandran, J. Dendooven, M. Filez, V. V. Galvita, H. Poelman, E. Solano, M. M. Minjauw, K. Devloo-Casier, E. Fonda, D. Hermida-Merino, W. Bras, G. B. Marin and C. Detavernier
  ACS Nano 10, 8770-8777 (**2016**)
  (Contribution of RKR: Designed experiments, prepared materials and samples, analyzed the XRD results, helped in XAS and GISAXS measurements and prepared manuscript)

- **Atomic Layer Deposition of Pt Nanoparticles within the Cages of MIL-101: A Mild and Recyclable Hydrogenation Catalyst**
  K. Leus, J. Dendooven, N. Tahir, R. K. Ramachandran, M. Meledina, S. Turner, G. Van Tendeloo, J. Goeman, J. Van der Eycken, C. Detavernier and P. Van Der Voort
  Nanomaterials 6, 45 (**2016**)
  (Contribution of RKR: Performed ALD on MIL-101 samples and helped in preparing manuscript)

- **Direct Imaging of ALD Deposited Pt Nanoclusters inside the Giant Pores of MIL-101**
  M. Meledina, S. Turner, M. Filippousi, K. Leus, I. Lobato, R. K. Ramachandran, J. Dendooven, C. Detavernier, P. Van Der Voort and G. Van Tendeloo
  Part. Part. Syst. Charact. 1 (**2016**)

(Contribution of RKR: Performed ALD on MIL-101 samples and helped in preparing manuscript)

- **Low Temperature Atomic Layer Deposition of Crystalline In_2O_3 Films**
  R. K. Ramachandran, J. Dendooven, H. Poelman and C. Detavernier
  J. Phys. Chem. C 21, 11786-11791 (**2015**)
  (Contribution of RKR: Designed experiments, prepared materials and samples, analyzed the results and prepared manuscript)

- **Plasma Enhanced Atomic Layer Deposition of Ga_2O_3 Thin Films**
  R. K. Ramachandran, J. Dendooven, J. Botterman, S. P. Sree, D. Poelman, J. A. Martens, H. Poelman and C. Detavernier
  J. Mater. Chem. A 2, 19232-19238 (**2014**)
  (Contribution of RKR: Designed experiments, prepared materials and samples, analyzed the results and prepared manuscript)

- **Plasma Enhanced Atomic Layer Deposition of Fe_2O_3 Thin Films**
  R. K. Ramachandran, J. Dendooven and C. Detavernier
  J. Mater. Chem. A 2, 10662-10667 (**2014**)
  (Contribution of RKR: Designed experiments, prepared materials and samples, analyzed the results and prepared manuscript)

- ***In situ* XAS and XRF Study of Nanoparticle Nucleation during O_3 - Based Pt Deposition**
  M. Filez, H. Poelman, R. K. Ramachandran, J. Dendooven, K. Devloo-Casier, E. Fonda, C. Detavernier and G. B. Marin
  Catal. Today 229, 2-13 (**2014**)
  (Contribution of RKR: Helped in designing and performing experiments, helped in analyzing XRF results and preparing manuscript)

- **Unravelling the Formation of Pt - Ga Alloyed Nanoparticles on Calcined Ga-Modified Hydrotalcites by *In Situ* XAS**
  M. Filez, E. A. Redekop, H. Poelman, V. V Galvita, R. K. Ramachandran, J. Dendooven, C. Detavernier and G. B. Marin
  Chem. Mater. 26, 5936-5949 (**2014**)
  (Contribution of RKR: Helped in performing XAS measurement)

- **Low-Temperature Atomic Layer Deposition of Platinum Using (Methylcyclopentadienyl)trimethylplatinum and Ozone**
  J. Dendooven#, R. K. Ramachandran#, K. Devloo-Casier, G. Rampelberg, M. Filez, H. Poelman, G. B. Marin, E. Fonda and C. Detavernier
  J. Phys. Chem. C 117, 20557-20561 (**2013**)
  (#Equally contributed: JD designed the experiments and wrote the manuscript. RKR performed all the experiments and helped in the manuscript preparation)